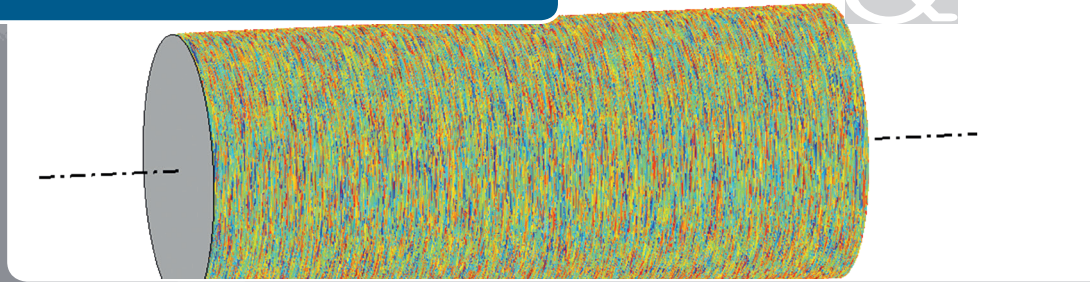


Philipp Arnecke

mts



## A measurement method for characterising micro lead on ground shaft surfaces

Berichte aus dem Lehrstuhl für Messtechnik und Sensorik  
Band 4

Herausgeber: Prof. Dr.-Ing. Jörg Seewig



Philipp Arnecke

**mts**  
&



## **A measurement method for characterising micro lead on ground shaft surfaces**

**Berichte aus dem Lehrstuhl für Messtechnik und Sensorik  
Band 4**

Herausgeber: Prof. Dr.-Ing. Jörg Seewig

### **Bibliografische Information der Deutschen Nationalbibliothek**

Die Deutsche Nationalbibliothek verzeichnet diese Publikation in der Deutschen Nationalbibliografie; detaillierte bibliografische Daten sind im Internet über <http://dnb.d-nb.de> abrufbar.

Berichte aus dem Lehrstuhl für Messtechnik und Sensorik - Band 4

Herausgeber: Prof. Dr.-Ing. Jörg Seewig  
Lehrstuhl für Messtechnik und Sensorik  
Fachbereich Maschinenbau und Verfahrenstechnik  
Technische Universität Kaiserslautern  
Gottlieb-Daimler-Straße  
67663 Kaiserslautern

Verfasser: Philipp Arnecke  
Verlag: Technische Universität Kaiserslautern

Druck: Technische Universität Kaiserslautern  
Hauptabteilung 5 | Abteilung 5.6 Foto-Repro-Druck  
D-386

© Philipp Arnecke · Kaiserslautern 2017

Alle Rechte vorbehalten, auch das des auszugsweisen Nachdrucks, der auszugsweisen oder vollständigen Wiedergabe (Photographie, Mikroskopie), der Speicherung in Datenverarbeitungsanlagen und das der Übersetzung.

Als Manuskript gedruckt. Printed in Germany.

ISSN 2365-9742  
ISBN 978-3-95974-047-0



## **Kurzfassung**

Bei der Herstellung von Wellenoberflächen als Gegenlaufflächen für Radialwellendicht-  
ringe in dynamischen Dichtsystemen können Strukturen auftreten, die Einfluss auf die  
Funktion des Dichtsystems haben können. Diese Strukturen werden als Drall bezeich-  
net und können entsprechend ihrer Ausprägung und Entstehung in die Drallarten Makro-  
und Mikrodrall eingeteilt werden. Im Optimalfall wird Drall bereits während der Herstel-  
lung vermieden, zumindest soll er aber erkannt und bezüglich seiner Ausprägung an  
Hand von Parametern quantifiziert werden. Während Messmethoden und Verfahren  
zum Nachweis von Makrodrall existieren, wird in dieser Arbeit eine Methode zur Cha-  
rakterisierung von Mikrodrall, also der Hauptrichtung der Bearbeitungsstruktur bezo-  
gen auf die Umfangsrichtung, beschrieben. Aus der Definition von Mikrodrall folgt di-  
rekt, dass sowohl die Umfangs- als auch die Bearbeitungsrichtung hochgenau erfasst  
werden müssen. Zu diesem Zweck werden geeignete Messsysteme und zugehörige  
Kalibrierverfahren beschrieben, welche neben der Messung der Wellenoberfläche die  
Kalibrierung der Umfangsrichtung mit hoher Genauigkeit und niedriger Unsicherheit  
ermöglichen. Auf Basis dieser flächenhaften Messungen wird ein Verfahren zur Ermitt-  
lung der Texturrichtung, dem die Radontransformation zu Grunde liegt, vorgestellt und  
parametrisiert. Mit der Ermittlung der Texturrichtung und der Kalibrierung der Achsla-  
ge können damit beide Anforderungen an die Messmethode zur Mikrodrallmessung an  
geschliffenen Wellenoberflächen erfüllt werden.

## **Abstract**

The detection and characterisation of undesired lead structures on shaft surfaces is a  
concern in production and quality control of rotary shaft lip-type sealing systems. The  
potential lead structures are generally divided into macro and micro lead based on  
their characteristics and formation. Macro lead measurement methods exist and are  
widely applied. This work describes a method to characterise micro lead on ground  
shaft surfaces. Micro lead is known as the deviation of main orientation of the ground  
micro texture from circumferential direction. Assessing the orientation of microscopic  
structures with arc minute accuracy with regard to circumferential direction requires  
exact knowledge of both the shaft's orientation and the direction of surface texture.  
The shaft's circumferential direction is found by calibration. Measuring systems and  
calibration procedures capable of calibrating shaft axis orientation with high accuracy  
and low uncertainty are described. The measuring systems employ areal-topographic  
measuring instruments suited for evaluating texture orientation. A dedicated evaluation  
scheme for texture orientation is based on the Radon transform of these topographies  
and parametrised for the application. Combining the calibration of circumferential di-  
rection with the evaluation of texture orientation the method enables the measurement  
of micro lead on ground shaft surfaces.



# **A measurement method for characterising micro lead on ground shaft surfaces**

Vom Fachbereich Maschinenbau und Verfahrenstechnik  
der Technischen Universität Kaiserslautern  
zur Verleihung des akademischen Grades

**Doktor-Ingenieur (Dr.-Ing.)**

genehmigte

**Dissertation**

vorgelegt von

Dipl.-Ing. Philipp Arnecke  
aus Würzburg

Kaiserslautern 2017

D 386

Dekan:

Prof. Dr.-Ing. Jörg Seewig

Vorsitzender:

Prof. Dr.-Ing. Bernd Sauer

Berichterstatter:

Prof. Dr.-Ing. Jörg Seewig

Prof. Dr.-Ing. habil. Peter Lehmann

Tag der mündlichen Prüfung:

22. August 2016



# Preface and Acknowledgements

The presented thesis is the outcome of my time as research assistant at the Institute for Measurement and Sensor Technology at the University of Kaiserslautern. Funding was received from the Stiftung Rheinland-Pfalz für Innovation through research grant 987 "Anwenderorientierte Charakterisierung von Mikrodrall auf Basis optischer Messeinrichtungen".

The completion of this thesis would not have been possible without the support from my colleagues, friends and family.

First, I would like to cordially thank my doctoral adviser Mr Prof. Dr.-Ing. Jörg Seewig for the trust he placed in me over the years first as student assistant and then as research assistant. I benefited from the unconstrained atmosphere at his institute and the scientific freedom to follow own ideas together with his very competent advice and suggestions at the right places. All of this together with his personal straightforward and humane attitude had their share in succeeding the work.

I would also like to thank both members of the board of examiners, Mr Prof. Dr.-Ing. habil. Peter Lehmann and Mr Prof. Dr.-Ing. Bernd Sauer, for the interest in my work, the rewarding discussions and the overall smooth procedure.

The great colleagues at MTS contributed a lot to the work. Not only as great partners in research related discussions with many valuable suggestions drawn from their vast experience in metrology and related subjects but also in off-research activities. I would especially like to highlight the enriching contributions of student assistances and supervised students to the thesis related work.

The largest share in the successful graduation has my family. I am infinitely grateful not only for the freedom to chose my own path and the opportunity of unburdened studies but also for precious advice and unconditional support.

Further, great thanks goes to all friends and supporters who encouraged me and made the successful completion of this thesis possible. Nearly everybody I know was involved in one or another way.

Munich, February 2017

Philipp Arnecke



# Summary

Lead structures can appear on shaft surfaces in dynamic sealing systems and enhance axial fluid transport under the sealing lip of rotary shaft lip-type seals. This generally undesirable behaviour can cause the sealing system to fail by generating leakage or dry run. Besides macro lead micro lead is one of the lead types that can be present on ground shaft surfaces. It is also known as setting lead and defined as the deviation between the main texture orientation of the ground micro texture and circumferential direction. It follows from this definition that the two characteristics that need to be assessed in order to quantify micro lead are main texture orientation of the ground micro texture  $\psi_t$  and axial direction/circumferential direction  $\psi_{circ}$ .

Assessing micro lead starts with measuring the shaft surface. An areal measurement method is required to sample directional processing traces. Three optical areal-topographic measuring systems and the corresponding calibration procedures for shaft axis orientation are presented and discussed. A concern is the relation of the chosen coordinate system to the measuring instrument's internal coordinate system to correctly estimate orientation with regard to the signed lead angle.

One of the systems is a stationary measuring instrument with its optical axis aligned horizontally. The instrument is fixed to a support frame for axial, radial, and tangential positioning. The shaft is mounted on a rotary table in a vertical position enabling simple measurements around its circumference. Positioning of the instrument relative to the shaft can lead to angular deviations caused by the support frame but the effects are found to be small. The effects of eccentricity and tilt on texture orientation are studied on a model of the rotating shaft and the stationary instrument. The vertical alignment of the shaft makes adjustment of eccentricity and tilt possible and their effects are therefore negligible. To calibrate the measuring instrument's orientation to the shaft's circumferential direction a calibration shaft is designed. Among several alternatives a circumferential groove is found to be well suited but requires a dedicated calibration procedure. The procedure uses areal-topographic measurements and iteratively fitted models of the groove bottom to detect the groove's orientation within a topography. Sub-arc minute deviations as small as a quarter arc minute can be resolved easily by the presented procedure. The suitability of the calibration procedure is examined by regarding the metrological properties measurement resolution, sensitivity,

accuracy, precision, and uncertainty.

An alternative to the above system is measuring the horizontal workpiece in a v-block under the upright instrument. In this case, calibration can be performed on the v-block's edges or with the help of the calibration shaft. Using the v-block's edges suffers from a high variability, mainly caused by insufficient edge detection. The calibration shaft yields good results with low variability. An effort to simplify calibration with the help of a grating acting as memory for shaft orientation is not successful mainly because the mounting of the grating is not repeatable enough.

A mobile measuring system is designed as further alternative. It is supposed to enable measurements of large shafts that cannot be practically positioned relative to a common measuring instrument. The system has a v-block support and a coherence scanning interferometer as instrument. As before, calibration is conducted with the help of a calibration shaft. In an uncertainty study of the calibration procedure the shaft employed in this case is exposed as the main contributor to the system's considerably high calibration uncertainty. The study also reveals that other contributions are small, rendering the system capable of the task.

Besides calibrating the orientation of the instrument to the shaft axis characterising micro lead requires knowledge of the main texture orientation of the ground texture  $\psi_t$ . The discussed measuring instruments generate a microscopic topographic representation of the shaft surface. This topography is preprocessed to extract the relevant processing traces from the measurement and to minimise artefacts evoked by the instrument. To characterise  $\psi_t$  in topographic measurements the available standardised parameter for surface texture orientation cannot be used because it is found to have – at least in its current implementation – an insufficient resolution. A Radon transform-based method is employed instead to estimate texture orientation. Several implementations of the Radon transform are examined and compared and a scheme employing cubic spline interpolation is found suitable. Texture orientation is calculated from the Radon domain in an integral way. The method is made computational in reasonable time by an iterative scheme stepping from coarse to fine orientation. With adequate sampling of the discrete parameters the method is capable of assessing texture orientation of unidirectional topographies in the low sub-arc minute range. Quarter arc-minute deviations can be resolved easily. Some practical applications are studied on simulated and measured topographies with regard to texture orientation, including the effects of varying topography sizes, effects of different apertures, and effects of superposed periodic structures and surface imperfections. Ways to decompose a topography into different scales are shown.

With both texture orientation  $\psi_t$  and circumferential direction  $\psi_{circ}$  known, the micro lead angle  $\psi_{ml}$  can be calculated as difference between  $\psi_t$  and  $\psi_{circ}$ . To demonstrate the method's capability, exemplary evaluations of test shafts and macro lead standards



are presented. The test shafts are found to be free of micro and macro lead but a circumferential waviness is detected. Implications of these structures are not known and further research appears indicated. It is shown empirically in another test that measurements in a v-block are better taken around the circumference rather than axially. The benefit of scale limiting for micro lead orientation estimation in the presence of macro lead structures is demonstrated on two ground macro lead measurement standards. Finally, some approaches on the way to the development of micro lead measurement standards are presented and discussed.

The described methods and procedures enable users to take objective measurements of micro lead on ground shaft surfaces. They are a step towards replacing the demand 'lead free' with objective limits on the extend of micro lead tolerable on shaft surfaces. Micro lead will always be observable to some extend due to statistical variations of the involved quantities  $\psi_{circ}$  and  $\psi_t$ . The aim of this thesis is to develop the ability in the form of a practical method and procedures to measure these structures in an objective way. A functional correspondence between micro lead and its influences on the sealing system as well as realistic tolerances should be established in future research.

# Zusammenfassung

Drall bezeichnet in der Oberflächenmess- und Dichtungstechnik Strukturen, die auf Wellenoberflächen in dynamischen Dichtsystemen auftreten können. Unter Umständen können diese Strukturen eine Bewegung des abzudichtenden Fluids in axialer Richtung unter der Dichtkante hervorrufen und die technische Dichtheit oder die Lebensdauer des Systems durch das Auftreten von Leckage oder Trockenlaufen negativ beeinflussen. Neben Makrodrall kann auf geschliffenen Wellenoberflächen auch Mikrodrall auftreten. Bei Mikrodrall weist die Hauptstrukturrichtung der Mikroschleifstruktur eine Rechtwinkligkeitsabweichung von der Bauteilachse auf, was beispielsweise aus einer Parallelitätsabweichung (Schrägung) zwischen Schleifscheibe und Werkstück resultieren kann. Dieser Dralltyp ist in der Literatur auch unter der Drallart Schrägungsdrahl bekannt und die Mikroschleifstrukturen stehen also schräg zur Umfangsrichtung. Der Nachweis und die quantitative Messung von Mikrodrall erfordern deshalb genaue Kenntnis sowohl von der Werkstückachse/Umfangsrichtung  $\psi_{circ}$  als auch von der Hauptstrukturrichtung der Mikroschleifstruktur  $\psi_t$ .

Zum Erfassen der Richtung der gerichteten Schleifstrukturen ist eine flächenhafte Messung der Wellenoberfläche notwendig. In dieser Arbeit werden drei Messsysteme einschließlich der zugehörigen Kalibrierverfahren vorgestellt und besprochen, deren Messgeräte auf der flächenhaften Topographiemethode basieren. Dabei wird auch auf die unterschiedlichen Koordinatensysteme von Messgerät und Auswertung eingegangen, um den Winkel des Mikrodralls mit korrektem Vorzeichen anzugeben.

Das zuerst besprochene Messsystem besteht aus einem stationären, um  $90^\circ$  in die horizontale Lage gekippten Messgerät, das relativ zur vertikal auf einem Drehtisch aufgespannten Welle ausgerichtet werden kann. Bei schrittweiser Rotation des Drehtischs lassen sich Messungen um den Umfang des Werkstücks leicht durchführen. Das Portal, das zur Positionierung des Messgeräts dient, wird zur Erhöhung der Stabilität an einen Rahmen geklemmt, was bei der Repositionierung zu Abweichung der relativen Lage von Bauteil und Messgerät führen kann. In experimentellen Untersuchungen wird gezeigt, dass diese Einflüsse nur geringe Auswirkungen auf das Messergebnis haben. Durch die vertikale Lage der Welle ist das Justieren von Exzentrizität und Taumel der Wellenachse zur Rotationsachse möglich und sinnvoll. Es wird ein Modell des Messsystems aufgestellt, an dem diese Effekte bequem studiert werden können. Um die

Lage des Messgeräts zur Wellenachse zu kalibrieren, wird eine Kalibriermethode bestehend aus einer Kalibrierwelle und der dazugehörigen Signalverarbeitung entwickelt. Aus verschiedenen Möglichkeiten der Strukturierung der Kalibrierwelle wird eine umlaufend eingestochene Rille ausgewählt. Ein Ausschnitt der Rille kann mit dem Messgerät erfasst werden und in den Rillengrund werden Kurven eingepasst, die die Lage der Rille innerhalb des Ausschnitts wiedergeben. Mit diesem Verfahren können Unterschiede in der Rillenorientierung im Bereich einer viertel Bogenminute problemlos aufgelöst werden. Die Eignung des Kalibrierverfahrens wird an Hand der metrologischen Eigenschaften Auflösung, Empfindlichkeit, Genauigkeit, Präzision und Unsicherheit untersucht.

Eine Alternative zum obigen Messsystem stellt die Messung der horizontal ausgerichteten Welle mit einem vertikal ausgerichteten Messgerät dar. Dabei wird die Welle in ein Messprisma eingelegt und die Kalibrierung kann an den Kanten des Prismas oder wieder mit der Kalibrierwelle erfolgen. Die Kalibrierung an der Prismenkante zeigt dabei Schwächen, die auf die unzureichende Qualität der Kantenerkennung zurückzuführen sind. Das oben beschriebene Kalibrierverfahren mit der Kalibrierwelle ergibt eine niedrige Streuung und zeigt schon bei relativ wenigen Messungen um den Umfang gute Ergebnisse. Zur Vereinfachung der Kalibrierung wird ein geometrisches Merkmal entwickelt, aus dessen bekannter Lage zur Wellenachse die Kalibrierung mit einer minimalen Anzahl von Messungen erfolgen soll. In Versuchen zeigt sich die Repositionierbarkeit der entwickelten Halterung am Prisma jedoch als nicht stabil genug.

Als weitere Alternative wird ein mobiles Messsystem vorgestellt, um Messungen an großen Wellen zu ermöglichen, deren Handhabung und Positionierung relativ zum Messgerät ansonsten nicht leicht möglich ist. Eine Prismenaufgabe ermöglicht die repositionierbare Auflage und Ausrichtung des Messsystems auf der Welle. Ein Weißlichtinterferometer ist auf der Prismenaufgabe montiert und diverse Stellmöglichkeiten ermöglichen die Ausrichtung zur Wellenoberfläche. Auch hier wird die Kalibrierung an einer Kalibrierwelle durchgeführt. In Versuchen ergibt sich hierbei eine große Variabilität der Orientierungen mehrerer Rillenausschnitte. Eine Unsicherheitsuntersuchung zeigt, dass diese auf das Kalibrierverfahren und darin vermutlich auf die unzureichende Qualität der eingestochenen Rille zurückzuführen ist. Die Studie zeigt außerdem, dass weitere Einflüsse klein genug sind, um das System als geeignet anzusehen.

Neben der Kenntnis der Achslage/Umfangsrichtung relativ zum Messgerät aus der Kalibrierung ist zur Mikrodrallmessung auch die genaue Kenntnis der Hauptstrukturrichtung der Mikroschleifstruktur in Koordinaten des Messgeräts notwendig. Die vorgestellten Messgeräte liefern eine flächenhafte Darstellung der Wellenoberfläche. Eine solche Topographie muss nach der Messung vorverarbeitet werden, um einerseits Artefakte aus dem Messprozess möglichst zu unterdrücken und gleichzeitig die Mikroschleifstruktur hervorzuheben. Auf Basis dieser vorverarbeiteten Oberfläche kann auch

eine genormte Kenngröße zur Charakterisierung der Texturrichtung ermittelt werden. In Versuchen zeigt sich jedoch, dass dieser Kennwert, zumindest in seiner derzeitigen Implementierung, eine zu geringe Empfindlichkeit aufweist und die erforderlichen Strukturrichtungsunterschiede im Subbogenminutenbereich nicht auflösen kann. Deshalb wird ein, auf der Radontransformierten der vorverarbeiteten Oberfläche basierendes Verfahren angewandt. Dazu werden unterschiedliche Implementierungen der Radontransformation untersucht und verglichen. Dabei zeigt sich, dass die Berechnung der Radontransformierten mit Hilfe der kubischen Splineinterpolation der Zwischengitterstellen für die Anwendung geeignet ist. Die Texturrichtung wird aus der Radontransformierten anschließend integral ermittelt.

Mit Hilfe eines iterativen Verfahrens, das zuerst die Texturrichtung grob schätzt und anschließend Schritt für Schritt genauer auswertet, wird diese rechenintensive Methode ausführbar. In Verbindung mit geeigneter Abtastung der unidirektionalen vorverarbeiteten Topographie ermöglicht das Verfahren die Ermittlung der Texturrichtung im Subbogenminutenbereich. Unterschiede in der Texturrichtung im Bereich einer viertel Bogenminute können problemlos aufgelöst werden. Einige praktische Anwendungen des Verfahrens und dabei auftretende Charakteristika in Bezug auf die zu ermittelnde Texturrichtung werden an simulierten und gemessenen Oberflächen untersucht. Dazu zählen Effekte durch unterschiedliche Topographiegrößen und Aperturen, von überlagerten periodischen Strukturen sowie von Oberflächenunvollkommenheiten und Makrodrall. Außerdem werden zwei Möglichkeiten der Zerlegung der vorverarbeiteten Oberfläche in Wellenlängen- und Strukturgrößenbereiche demonstriert.

Nachdem sowohl die Orientierung der Schleifstrukturen  $\psi_t$  in Koordinaten des Messgeräts als auch die Orientierung des Messgeräts zur Welle  $\psi_{circ}$  bekannt sind, kann der Mikrodrallwinkel  $\psi_{ml}$  aus der Differenz der beiden Größen ermittelt werden. Die Methode wird an Hand von Untersuchungen an zwei geschliffenen Testwellen und zwei Makrodrallnormalen demonstriert. Die Testwellen weisen weder Mikro- noch Makrodrall, dafür aber eine umlaufende Welligkeit auf. Die Bedeutung dieser, vermutlich aus Schwingungen im Schleifprozess resultierenden Strukturen und die Eignung damit behafteter Wellenoberflächen für dynamische Dichtsysteme ist jedoch weitgehend unbekannt und ergibt einen möglichen Anknüpfungspunkt für weitere Forschung. Weiterhin ergeben empirische Untersuchungen, dass Mikrodrallmessungen, bei denen die Welle in ein Prisma eingelegt wird, um den Umfang der Wellenoberfläche statt axial erfolgen sollten. Die Vorteile der Limitierung der vorverarbeiteten Topographie auf bestimmte Wellenlängenbereiche zeigen sich an den beiden Makrodrallnormalen. Abschließend werden bisherige Arbeiten zur Entwicklung von Mikrodrallnormalen dargelegt und besprochen.

Die beschriebene Methode der flächig-topographiehaften Mikrodrallmessung unter Berücksichtigung der Achslage und die dazu beschriebenen Mess- und Kalibrierver-

fahren ermöglichen es Anwendern, objektive Messungen bezüglich des Vorhandenseins und der Ausprägung von Mikrodrall als Abweichung der Hauptstrukturrichtung der Mikroschleifstruktur von der Umfangsrichtung an geschliffenen Wellenoberflächen durchzuführen. Diese Fähigkeit stellt einen weiteren Schritt in der Bemühung dar, die veraltete Angabe drallfrei gegen objektive und tolerierbare Grenzen einer möglichen Mikrodrallausprägung zu ersetzen. Mikrodrall wird auf gemessenen Bauteiloberflächen immer erkennbar sein. Dies ergibt sich alleine aus dem statistischen Charakter der beteiligten Größen  $\psi_t$  und  $\psi_{circ}$ .

Das Ziel dieser Arbeit ist es, objektive und praktisch anwendbare Verfahren zur Messung von Mikrodrall zur Verfügung zu stellen. Die Ermittlung eines Zusammenhangs zwischen Mikrodrallausprägung und einem möglichen Einfluss auf die Funktion des Dichtsystems sowie die Ermittlung realistischer Toleranzen können mögliche Anwendungen dieser Messmethode sein.



# Contents

- Glossary** **xix**
  
- 1 Introduction** **1**
  
- 2 Lead in rotary shaft lip-type sealing systems** **3**
  - 2.1 Lead types . . . . . 3
    - 2.1.1 Macro lead . . . . . 4
    - 2.1.2 Micro lead . . . . . 5
  - 2.2 Rotary shaft lip-type sealing systems . . . . . 6
    - 2.2.1 Rotary shaft lip-type seals . . . . . 6
    - 2.2.2 The role of the shaft surface . . . . . 8
  - 2.3 Evaluation of lead and surface imperfections . . . . . 12
    - 2.3.1 Macro lead . . . . . 12
    - 2.3.2 Micro lead . . . . . 15
    - 2.3.3 Surface imperfections . . . . . 18
    - 2.3.4 Thread method . . . . . 19
    - 2.3.5 State of the art of lead evaluation . . . . . 20
  
- 3 Measuring systems** **21**
  - 3.1 Rotating measuring system . . . . . 23
    - 3.1.1 Practical set-up . . . . . 23
    - 3.1.2 Eccentricity and tilt . . . . . 28
    - 3.1.3 Calibration . . . . . 32
    - 3.1.4 Results . . . . . 40
    - 3.1.5 Discussion . . . . . 46
    - 3.1.6 Summary . . . . . 49
  - 3.2 Non-rotating measuring system . . . . . 50
    - 3.2.1 Practical set-up . . . . . 50
    - 3.2.2 Calibration . . . . . 52
    - 3.2.3 Results . . . . . 55
    - 3.2.4 Discussion . . . . . 59

|          |  |            |
|----------|--|------------|
| 3.2.5    | Summary . . . . .  | 60         |
| 3.3      | Mobile measuring system . . . . .                                  | 61         |
| 3.3.1    | Practical set-up . . . . .   | 61         |
| 3.3.2    | Calibration . . . . .  | 64         |
| 3.3.3    | Uncertainty considerations . . . . .                               | 66         |
| 3.3.4    | Discussion . . . . .   | 74         |
| 3.3.5    | Summary . . . . .  | 75         |
| 3.4      | Summary . . . . .  | 75         |
| <b>4</b> | <b>Texture orientation</b>   | <b>77</b>  |
| 4.1      | Preprocessing of measurement data . . . . .                        | 79         |
| 4.1.1    | Handling non-measured points . . . . .                             | 79         |
| 4.1.2    | Noise removal . . . . .  | 80         |
| 4.1.3    | S-filter . . . . .   | 80         |
| 4.1.4    | F-operation . . . . .  | 81         |
| 4.1.5    | L-filter . . . . .   | 81         |
| 4.1.6    | Summary . . . . .  | 81         |
| 4.2      | Radon transform-based method . . . . .                             | 82         |
| 4.2.1    | Implementations based on different interpolation schemes . . . . . | 83         |
| 4.2.2    | Main texture orientation . . . . .                                 | 89         |
| 4.2.3    | Comparison with regard to orientation estimation . . . . .         | 91         |
| 4.2.4    | Sampling considerations . . . . .                                  | 94         |
| 4.2.5    | Summary . . . . .  | 96         |
| 4.3      | Practical realisations . . . . .                                   | 97         |
| 4.3.1    | Evaluation procedures . . . . .                                    | 97         |
| 4.3.2    | Practical considerations and effects . . . . .                     | 98         |
| 4.3.3    | Summary . . . . .  | 107        |
| 4.4      | Discussion . . . . .   | 108        |
| 4.5      | Summary . . . . .  | 110        |
| <b>5</b> | <b>Results and Discussion</b>                                      | <b>111</b> |
| 5.1      | Exemplary evaluations . . . . .                                    | 112        |
| 5.1.1    | Ground test shafts . . . . .                                       | 112        |
| 5.1.2    | Macro lead standards . . . . .                                     | 119        |
| 5.1.3    | Measurement standards for micro lead . . . . .                     | 121        |
| 5.2      | Discussion . . . . .   | 123        |
| 5.3      | Summary . . . . .  | 126        |



- 6 Conclusion** **127**
- 6.1 Summary . . . . . 127
- 6.2 Further development . . . . . 129
  
- A Model of rotating shaft with stationary measuring instrument** **132**
  
- B Groove model for uncertainty evaluation** **135**
  
- C Modelling directional surface texture** **139**
  
- Bibliography** **147**



# Glossary

|                  |  |
|------------------|--|
| CMM              | coordinate measuring machine   |
| CSI              | coherence scanning interferometer  |
| MTS              | Institute for Measurement and Sensor-Technology at the University of Kaiserslautern                  |
| NMP              | non-measured point   |
| $\alpha_g$       | inclination angle limiting the evaluated section of the calibration groove                           |
| $\alpha_{g,max}$ | maximal wall inclination angle of the calibration groove   |
| $\alpha_{NA}$    | acceptance angle of the measuring instrument's objective   |
| $\alpha_V$       | half v-block opening angle   |
| $L_V$            | axial v-block length   |
| $M$              | number of measurements of circumferential direction  |
| $M_t$            | number of topography samples in $y_t$ direction  |
| $m_t$            | lateral topography coordinate in samples   |
| $N$              | number of measurements of texture orientation and micro lead   |
| $NA$             | numerical aperture   |
| $N_t$            | number of topography samples in $x_t$ direction  |
| $n_t$            | lateral topography coordinate in samples   |
| $\phi$           | orientation angle of straight lines used in the Radon transform                                      |
| $\psi_{ax}$      | axial direction  |
| $\psi_{circ}$    | circumferential direction  |
| $\psi_{ml}$      | micro lead angle   |
| $\psi_t$         | texture orientation  |
| $\bar{q}$        | arithmetic mean of independent observations $q_i$ of randomly varying quantity                       |
| $q$              |  |
| $\rho$           | distance from origin of straight lines used in the Radon transform                                   |
| $s(q_i)$         | experimental standard deviation from independent observations $q_i$ of randomly varying quantity $q$ |

$s(\bar{q})$  experimental standard deviation of the mean  $\bar{q}$  of randomly varying quantity  $q$

$x_t$  lateral coordinate of topography

$y_t$  lateral coordinate of topography

$z_t$  height coordinate of topography

# 1 Introduction

In many mechanical machines rotating shafts pass through the machine's housing connecting the machine's inside to its outside. The inside is often lubricated and the lubricating fluid is supposed to be sealed off from the machine's environment. Although different options exist to achieve the sealing function, a commonly employed dynamic sealing system is the rotary shaft lip-type sealing system [71] which seals in radial direction. It often consists of an elastomer sealing ring fixed to the housing and a shaft with a finished surface rotating in its middle. The seal has a sealing lip under which a thin fluid film can form and separate sealing lip and shaft surface given some conditions are met [98, p. 79]. Due to its design the sealing lip prevents fluid from leaking to the machine's outside [7]. But if structures on the shaft surface are present that disturb the sealing lip's work, the sealing system might fail to seal properly. Consequences could be dry run when the fluid under the sealing lip flowed to the inside of the machine or leakage if it flowed to the outside. In general, the shaft surface is supposed not to facilitate fluid transport in either direction. But during production of the shaft unwanted structures on the shaft surface might be generated that actively facilitate fluid pumping. These structures are referred to as lead on the shaft surface<sup>1</sup>.

The generation of lead structures needs to be controlled during or after production in the first place. It can be very expensive for manufacturers and suppliers to disassemble complete machines to exchange a leaking sealing system which failed in operation. And a car employs about 80 dynamic sealing systems [127]. Environmental considerations are also a concern when lubricating fluid, e.g. oil, leaks to the environment. Old standards and guidelines on rotary shaft lip-type sealing systems demand shaft surfaces not to *"exhibit lead whose fluid transport generates leakage depending on the direction of rotation"* [40]. Today, the notion 'lead reduced' is common view [118, 95]. In order to tolerate the characteristics of lead structures measurement methods capable of detecting and characterising these structures are required. At this point the current work comes into play.

Lead structures can be classified into macro and micro lead. For macro lead dedicated measurement procedures have long been in the focus of research and accepted meas-

---

<sup>1</sup>Surface imperfections can also play a role.

urement methods exist and found their way into standardisation [46, 127, 128, 95, 47]. The appearance of micro lead structures is fundamentally different from macro lead and no standardised methods exist yet. Micro lead is the deviation of the main texture orientation of the ground micro texture from the circumferential direction of the shaft [95]. Grinding is commonly used to finish the shaft surfaces and so the micro texture consists of the grinding marks of individual grits on the grinding disc.

The aim of this work is to develop and design measurement methods to characterise micro lead on ground shaft surfaces. It can be deduced from the definition of micro lead that this involves assessing the main texture orientation of the ground micro texture as well as the axial or circumferential direction of the shaft. These fundamental tasks also govern the structure of the work.

After giving an overview of the functionality of radial lip-type sealing systems while paying particular attention to the shaft surface in chapter 2, measurement methods for lead are surveyed and the current state of the art is outlined. Three measurement systems based on areal-topographic surface texture measurement methods capable of taking measurements with regard to circumferential direction and the corresponding calibration procedures are presented in chapter 3. The three systems target different demands and are characterised in detail regarding several metrological properties. A method to characterise texture orientation based on the Radon transform is designed in chapter 4. It is shown that the method's angular resolution is very high and several tests with practical application in mind are performed. Exemplary evaluations of ground shaft surfaces connect the two parts of micro lead evaluation in chapter 5. Additionally, evaluations of macro lead and a circumferential structure are shown and first steps towards measurement standards for micro lead are presented. A final summary and an outlook in chapter 6 conclude the work.

## **2 Lead in rotary shaft lip-type sealing systems**

The Mercedes-Benz company standard on lead measurement procedures MBN 31007-7 [95] defines lead (also known as twist in older publications) as a texture occurring around the whole circumference of the shaft sealing surface. Lead can disturb the proper operation of the sealing system and cause leakage by influencing axial fluid transport or other effects [95].

Some authors adopt a slightly different wording, describing lead as all surface features occurring on the shaft contact surface of rotary shaft lip-type sealing systems that influence axial fluid transport [127, 128, 8, 13]. This two definitions agree on major points but they differ on the extent of structures they include, especially surface imperfections, e.g. scratches, dents etc. The standard seems to exclude them, which is reasonable given today's insufficient knowledge both regarding their effects on sealing applications and standardised characteristics and evaluation methods found in surface metrology. The former definition, which is used by the standard, is adopted in this work, regarding isolated features on the shaft surface not as lead.

With this definition in mind the chapter on the theoretical foundations of lead and its characterisation starts by explaining lead types in section 2.1 before taking a look into the technology and operation of rotary shaft lip-type sealing systems with focus on the shaft surface in section 2.2. A description of methods and procedures to detect and characterise lead and other potentially disruptive structures on ground shaft sealing surfaces is given in section 2.3. The chapter is concluded by the current state of the art of lead evaluation.

### **2.1 Lead types**

In older publications, e.g. by Kersten [78], three lead categories were regarded on ground shaft sealing surfaces: dressing lead as a coarse or macro structure that could superpose the micro structure of setting lead. Kersten regarded structures from pre-processing (turning) and postprocessing (assembly) as third category [78, pp. 31 sq.].

He also reported on dressing lead-like shaped structures caused by oscillations in the grinding process, which he accordingly sorted into the first category [78, pp. 29 sq.]. With development of a dedicated measurement procedure for macro lead by Rau et al. [118, 119] and the systematic investigation of these structures additional lead structures could be observed. Today, lead structures are classified according to MBN 31007-7

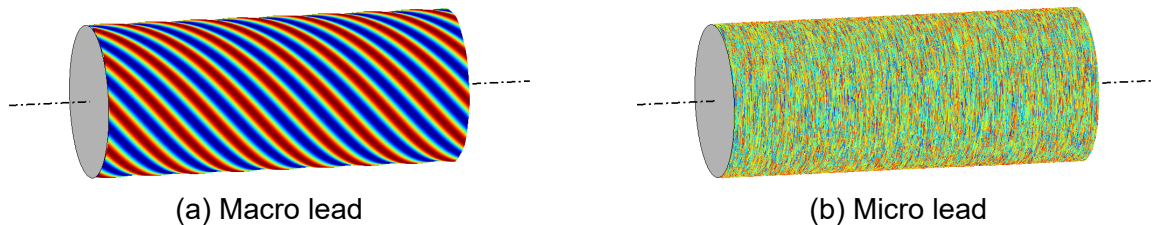


Figure 2.1: Simplified and exaggerated illustration of lead types

based on their characteristics and formation into the lead types macro and micro lead which themselves are subdivided into lead categories. Macro structures are of larger spatial extent and superposed to micro structures. A schematic of a macro and micro lead structure on a shaft is depicted in fig. 2.1.

### 2.1.1 Macro lead

Axially periodic circumferential structures with one or multiple thread starts are termed macro lead [128, p. 530]. Macro lead is subdivided by its formation into four categories: dressing lead, feeding lead, periodic zero lead, and non-periodic zero lead [95]. Figure 2.2 shows the corresponding simplified and exaggerated lateral surfaces. Details on their generation are given in [78, pp. 17-20, 95]. Apparently, non-periodic zero lead disagrees with the definition of axial periodicity. It nevertheless belongs to macro lead due to its macro structure and was denoted circumferential waviness [117, p. 96] in older publications.

Macro lead is characterised by a set of lead parameters defined in MBN 31007-7. These are lead angle  $D\gamma$ , lead depth  $Dt$ , number of thread starts  $DG$ , theoretical pumping cross section  $DF$ , theoretical pumping cross section per rotation  $DFu$ , axial period length  $DP$ , and contact length ratio in percentage  $DLu$ . The parameters are visualised in fig. 2.3. The lead angle is a signed parameter value. MBN 31007-7 defines lead structures from down right to top left as right-handed with positive sign and lead structures from down left to top right as left-handed with negative sign [95]. In terms of screw threads right-hand threads correspond to a positive lead angle and left-hand threads to a negative lead angle [37].



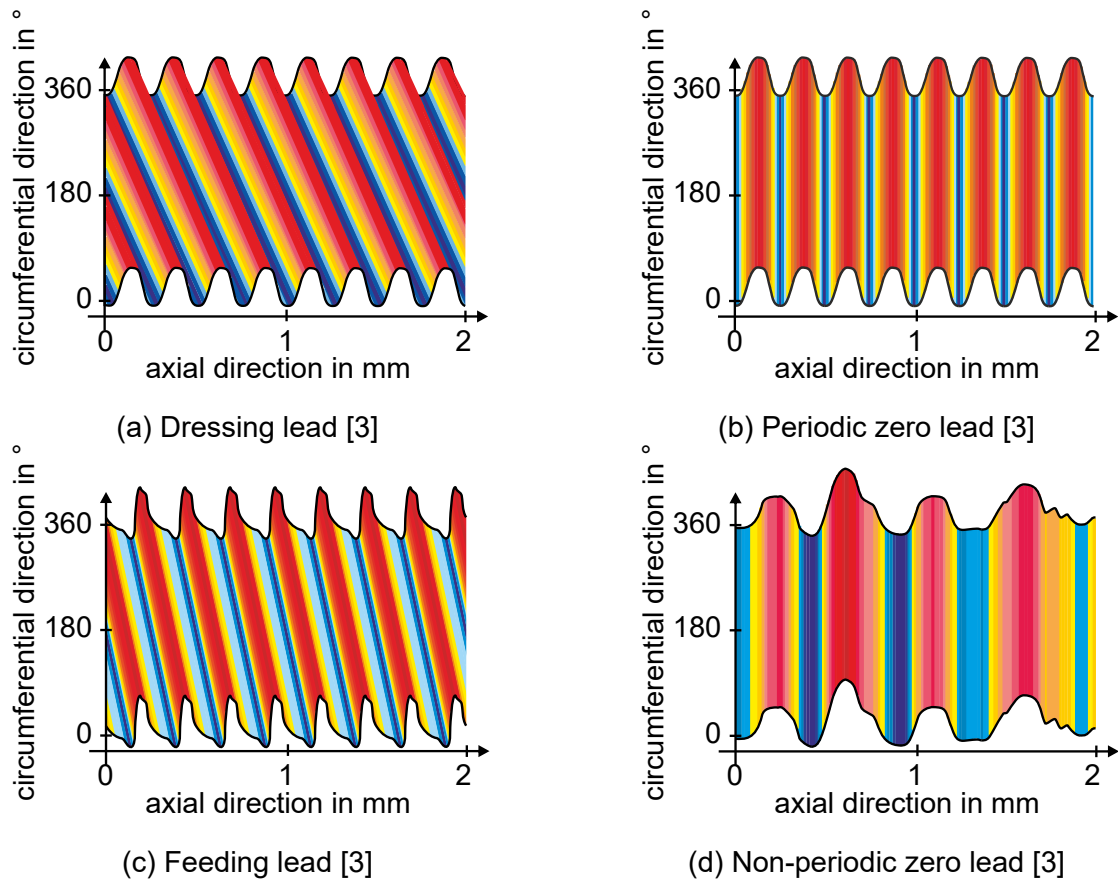


Figure 2.2: Simplified and exaggerated macro lead structures as developed lateral shaft surfaces according to [95]

### 2.1.2 Micro lead

Micro lead is also known by its only subgroup: setting lead. It is a deviation of the main texture orientation of the ground micro texture from the shaft's circumferential direction [78, p. 16, 118, p. 1014, 95, p. 5]. The only parameter defined in MBN 31007-7 is the setting lead angle  $DS\gamma$ . It is the signed angle between the main orientation of the processing traces' micro texture  $\psi_t$  and circumferential direction  $\psi_{circ}$ , whose projection is perpendicular to shaft axis  $\psi_{ax}$  [95]. Its sign convention is identical to the macro lead angle, i.e. positive from bottom right to top left and negative from bottom left to top right. In this work the micro lead angle is defined identically to  $DS\gamma$  and therefore to MBN 31007-7 but referred to as  $\psi_{ml}$ . The situation is depicted in fig. 2.4.

The name setting lead stems from a setting or skew between workpiece and grinding disc during production which is an undesired state [121, p. 7]. Obviously, if present, it will always be very small. If it was large, i.e. in the range of several degrees, it would easily be detected and adjusted by the operator. Besides the setting, another mechanism possibly producing tilted textures is grinding with axial feed. Details and formulae on these two mechanisms of micro lead generation can be found in [78, pp. 14-17].

Seewig and Hercke describe micro lead as *"all structures which are tilted with respect*

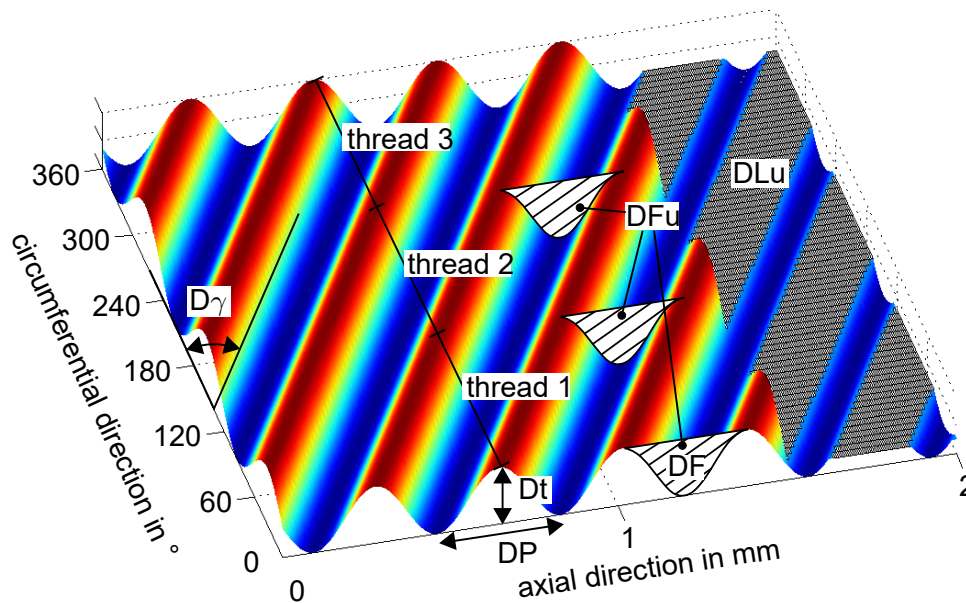


Figure 2.3: Macro lead parameter according to MBN 31007-7 and [3]

to the workpiece axis” [128, p. 530]. This definition includes scratches as well. The definition used in this work regards micro lead only as the deviation of the ground texture. Surface imperfections, e.g. scratches, bumps, holes, are generally possible on all technical surfaces and independent of lead and regarded as an own category.

## 2.2 Rotary shaft lip-type sealing systems

Lead on a shaft surface can be problematic if the surface is the contact surface of a rotary shaft lip-type seal. Its presence can influence the sealing function and – by outbalancing the seal’s inherent sealing mechanisms – cause the sealing system to fail.

This section provides a short introduction to sealing systems with ordinary elastomer rotary shaft lip-type seals. Attention is paid to the shaft surface and structures that can influence the sealing system.

### 2.2.1 Rotary shaft lip-type seals

A rotary shaft lip-type seal is regarded as dynamic seal because the sealing lip and the shaft surface exhibit a “*significant relative sliding motion*” [98, p. 1]. Its purpose is the sealing of unpressurised and low pressure fluid on the inside of a machine to the air side [98, p. 86]. According to Baart the seal has to provide static and dynamic sealing, lubrication between sealing lip and shaft, and pumping of fluid to the fluid side [7].

A typical elastomer rotary shaft lip-type seal is displayed in fig. 2.5. It is normally fitted to a static housing while the shaft rotates. In static case the sealing lip is in contact

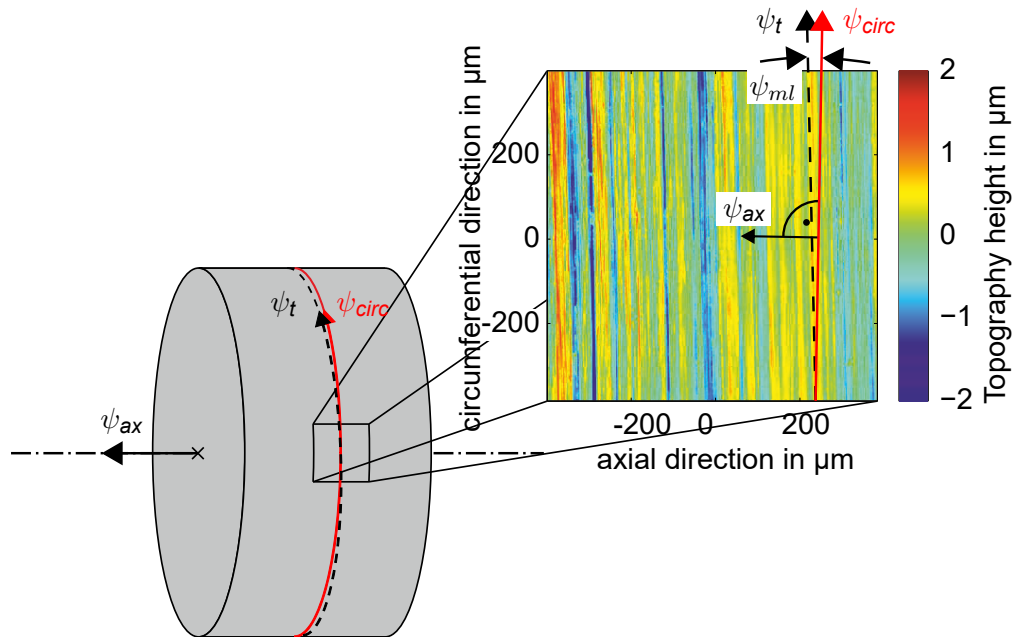


Figure 2.4: Positive micro lead angle  $\psi_{ml}$  as deviation of main texture orientation of the ground micro texture  $\psi_t$  from circumferential orientation  $\psi_{circ}$  according to [4]

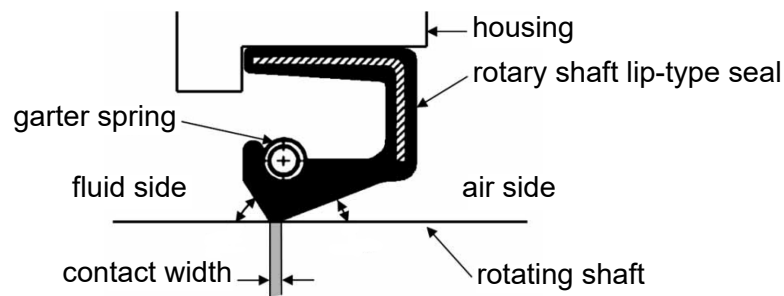


Figure 2.5: Axial section through a typical rotary shaft lip-type seal based on [7, p. 348]

with the shaft's surface with a radial load applied by a stretch of the elastomer and a garter spring [98, p. 74]. In operation the shaft surface and the sealing lip move at relative speed in circumferential direction. Depending on several conditions the shaft surface and the sealing lip might be separated by a fluid film some tenth microns thick [98, p. 79]. The fluid film separating both surfaces in optimal operation is generated by hydrodynamic effects from the roughness of the sealing lip. Asperities on the sealing lip moving relative to the shaft surface form pressure generating pads. Each pad can be thought of as a converging gap generating a radial force. The surfaces separate when the sum of radial forces exceeds the radial load of the seal [98, p. 79]. This is a desired condition because friction and wear are low [7].

The seal exhibits inherent dynamic sealing mechanisms causing pumping effects that counteract leakage [98, pp. 80 sq.]. These will now be summarised briefly.

## Hypotheses on the seal's functional behaviour

Several hypotheses regarding microscopic structures are available to account for the behaviour of the seal. But *"none of them gives a conclusive understanding of how radial lip seals work"* [7, p. 348].

The seal's behaviour can be explained in large parts by two primary mechanisms [7, p. 356] both regarding the micro structure of the sealing lip. One goes by the name of cascade pumping side flow concept [7, p. 351]. Due to the different angles at the fluid and air side between sealing lip and shaft surface (see fig. 2.5) the radial pressure under the sealing lip is not distributed symmetrically in axial direction. The angle at the air side is lower and so is the pressure gradient. The pressure maximum lies closer to the fluid side. In operation the fluid moves over and sideways of the asperities on the sealing lip. Because of the different angles more asperities at the air side are in contact with the shaft than at the fluid side with its lower pressure gradient [28, p. 34]. This is thought to result in a stronger pumping between the asperities at the air side that in total transports fluid from the air to the fluid side of the seal [7, p. 351].

In the non-symmetrical tangential deformation hypothesis asperities and axially extended undulations on the sealing lip are deformed in circumferential direction by shear stress from the relative motion between sealing lip and shaft surface [7, pp. 351 sq.]. The non-symmetric contact pressure in axial direction deforms the asperities non-symmetrically V-shaped. These deformed asperities deflect the fluid sideways. As more deformed asperities appear on the air side [98, p. 82] because of its longer axial extension [99, p. 10] and the pressure maximum is closer to the fluid side more fluid is pumped from the air to the fluid side.

Other microscopic and macroscopic mechanisms are secondary mechanisms [7, p. 356]. Depending on the operating conditions effects from one or the other hypotheses will be predominant [28, p. 31]. In literature, macroscopic hydrodynamic sealing aids are often referred to as lead (e.g. [55]).

### 2.2.2 The role of the shaft surface

The shaft surface plays an important role in the proper behaviour of the sealing system [98, pp. 77 sqq.]. A certain level of shaft roughness is required to ensure that roughness on the sealing lip develops and sustains in operation. Surface roughness or axial waviness with heights of a few microns forms on the sealing lip during the first few rotations of running in by wear mechanisms [98, p. 77]. Unused sealing lips have a contact width (see fig. 2.5) of 100 to 150  $\mu\text{m}$ . It broadens to 200 to 300  $\mu\text{m}$  in use and can reach more than 700  $\mu\text{m}$  in abrasive environments [98, p. 76]. A very rough shaft surface can lead to increased wear of the sealing lip. Shaft surface roughness is commonly specified

by height parameters<sup>1</sup> and the production method. Mostly plunge grinding<sup>2</sup> with a long spark out time is recommended [99, p. 7, 145, pp. 6-8, 8, p. 14]. For different production methods differing parameters and values apply [23, 108, pp. 40 sqq.]. Here, only shafts with ground surface finish are regarded.

### Specification of ground shaft surfaces

Specifications of the shaft's geometric and surface texture tolerances are provided by national and international standards and recommendations of seal manufacturers.

The standards DIN 3761-2 [40], DIN 3760 [39], RMA OS-1-1 [122] and ISO 6194-1 [71] tolerate the shaft surface. Roughness of the contact surface measured as arithmetic mean deviation of the assessed profile  $R_a$  and maximum height of the profile  $R_z$  is specified in all standards (see table 2.1). Each standard demands slightly different additional specifications. These are maximum height of the profile of one sampling length  $R_{max}$ <sup>3</sup> (DIN 3761-2, DIN 3760) to ensure absence of surface imperfections [40, p. 3], average peak to mean height  $R_{pm}$ <sup>4</sup> (RMA OS-1-1), roundness tolerances (DIN 3761-2, RMA OS-1-1), grinding chatter (RMA OS-1-1), and limits on lead angles (RMA OS-1-1) or absence of lead (DIN 3760, ISO 6194-1). Due to the number of surface finishing methods, the latest international standard ISO 6194-1 from 2007 demands agreement of seal manufacturer and user on surface texture and roughness parameters [71, p. 6].

Publications by sealing manufactures add recommendations regarding the production

Table 2.1: Overview of roughness parameters found in different standards

|            | $R_a$ in $\mu\text{m}$ | $R_z$ in $\mu\text{m}$ |
|------------|------------------------|------------------------|
| DIN 3760   | 0.2 to 0.8             | 1 to 5                 |
| DIN 3761-2 | 0.2 to 0.8             | 1 to 4                 |
| RMA OS-1-1 | 0.2 to 0.43            | 1.65 to 2.9            |
| ISO 6194-1 | 0.2 to 0.5             | 1.2 to 3               |

processes. For ground surfaces Freudenberg [145, p. 8] recommends a spark out time of not less than 30 s.

In addition to those documents, multiple scientific publications recommend various surface texture parameters to describe the shaft surface as well as its visual appearance. Among those is Symons who examined periodic components on the shaft's circumference. He recommended absence of grinding chatter and a minimal number of

<sup>1</sup>See ISO 4287 [50], ISO 4288 [51], and [35] for definitions of profile-based surface texture parameters.

<sup>2</sup>Also known as peripheral-transverse outside diameter grinding between centres [59].

<sup>3</sup>Older standards and publications specify  $R_{max}$  defined in [52]. Today's equivalent is  $R_{z1}$  or  $R_{z1max}$  defined in [51].

<sup>4</sup>Definition similar to maximum profile peak height  $R_p$  in ISO 4287 [50].

periods around the circumference with limited height [137, p. 373]. Qu [111] studied influences on short time leakage and found influences of the parameters skewness of the assessed profile  $R_{sk}$ , kurtosis of the assessed profile  $R_{ku}$ , and maximum profile valley depth  $R_v$  (see footnote 1). Shuster et al. [132] proposed the normalised volume under a plane parallel to the topography's reference plane and touching the highest peak to describe the topography in a functional way. Rau et al. [117] gave a description of the visual appearance of a well ground contact surface for rotary shaft lip-type sealing applications: a non-uniform distribution of similarly shaped grooves without sharp edges oriented perpendicular to shaft axis. The surface was supposed to be free of continuous structures and superposed structures with an axial component. The grinding marks' length of their surfaces was  $\approx 0.7 \mu\text{m}$  [117, p. 93]. Marquart et al. [92] gave an overview of 3D surface parameters from ISO 25178-2 [44] and Jung and Haas [77] found a correlation between pumping rate of ground shafts and mean dales volume  $S_{dv}^5$ . Rau et al. [116] gave some insight into macro lead parameters' values (cf. fig. 2.3) and their relevance to fluid transport. Applying the first generation macro lead measurement procedure they found a highly proportional correlation between pumping rate and theoretical pumping cross section  $DF$  and to a smaller extent with lead depth  $D_t$  and axial period length  $DP$ . An increase in the related parameter  $D_\gamma$  and  $DG$  also yielded a higher pumping rate [116, p. 398]. Buhl [27] proposed new parameters for the shaft surface. Kunstfeld [83] developed another set of parameters and Baitinger [8] developed parameters to characterise micro lead. Baumann et al. extended Baitinger's method to larger scales which they termed micro waviness structures [12].

A goal during recent years of research was to assess the shaft sealing surface and its influences on pumping rate by a single parameter (e.g. [116, p. 398, 28, pp. 56 sqq.]). This is not yet possible [83, p. 110, 8, pp. 107 sq.].

### Effects of lead structures

Both seal and shaft surface have the ability to pump fluid axially. Many sources demand the shaft surface to be free of lead [98, p. 79, 40, p. 3, 39, p. 7, 71, p. 6, 55, p. 45]. According to Baitinger it is impossible to encounter completely 'lead free' rotary shaft lip-type sealing systems [8, p. 127]. The lead parameters in MBN 31007-7 [95] are designed to replace the specification 'lead free' by 'lead reduced' together with a functional description of lead structures on the shaft surface. With an objective measurement and characterisation method at hand critical and non-critical structures can be defined [118, p. 1013, 117, p. 97].

Buhl regarded lead structures as having an active pumping ability [28, p. 56]. They could outbalance the sensitive equilibrium of back-pumping and lubrication provided

---

<sup>5</sup>See ISO 25178-2 [45] and [35] for definitions of areal surface texture parameters.

by the seal's inherent dynamic sealing mechanisms [118, p. 1014]. The seal's inherent pumping mechanisms generate pumping from air to fluid side for both directions of rotation (see section 2.2.1). Lead structures on the shaft pump fluid in differing axial directions for each direction of rotation. The sealing system works properly as long as the inherent pumping of the seal is higher than the pumping of structures on the shaft surface from fluid to air side [83, p. 91]. If the axial pumping direction of shaft surface and seal coincide, dry run can occur because the seal's lubrication mechanisms are outbalanced by the shaft surface's pumping rate.

Several researchers investigated the effects of micro structures on the shaft surface: As one of the first (and only) Kersten [78] examined the effects of minute deviations of texture orientation of the ground micro texture from circumferential direction on leakage. He reported that an inclination of micro structures to circumferential direction below 5' resulted in no leakage. From only 5' to 10' some sealing systems showed leakage. And above 10' leakage occurred in all measurements [78, pp. 101 sq.]. Raab compared lead structures to a screw thread that pumped oil in axial direction depending on the orientation and direction of rotation [112, pp. 11 sq.]. This behaviour included all structures skew to circumferential direction. Observing that the visible orientation of macro lead did not match the expected pumping direction he suggested the presence of other than periodic lead structures to have a significant effect on the pumping rate of the shaft [112, p. 87]. Buhl explained that the fluid is dragged along in the direction of rotation and skew structures deflect it in axial direction [28, pp. 47 sq.]. He showed that very fine structures under 45° to circumferential direction with a height of  $\approx 150$  nm can double the pumping rate compared to a turned shaft with an amplitude of 12  $\mu\text{m}$  without a fine micro structures. He concluded from another experiment exhibiting an overlay of fine and coarse structures that a fine lead structure can even prevent the formation of the fluid film under the sealing lip [28, p. 54]. Kunstfeld came to the same conclusion as he did similar studies [83, pp. 87 sqq.]. Studies by Buhl [28], Kunstfeld [83], and Baitinger [8] focused on micro structures at angles of several degrees (up to e.g. 80°) to circumferential direction. These examinations are relevant for the development of new textures of the shaft contact surface. But common grinding processes result in texture orientations that are more or less orientated in circumferential direction (except for quickpoint grinding, cf. [117, p. 96]). According to Rau et al. lead angle values are generally far below 5° – mostly in the range of arc minutes [119, p. 7]. Only Kersten regarded such structures in his experiments [78, pp. 100 sqq.].

### **Imperfections of the shaft surface**

Surface imperfections on the shaft surface can also disturb the proper function of the sealing system. Guides and standards generally demand absence of surface imperfections on the shaft contact surface e.g. [40, p. 3, 55, p. 45]. A variety of possible surface

imperfections is described in ISO 8785 [72].

Some literature resources on the topic are available: Buhl showed an example of protruding defects on hard turned shafts that could act as directional structures and deflect the fluid axially [28, p. 53]. Rau et al. mentioned some surface imperfections on turned sealing surfaces from material inhomogeneities [117]. According to [145, p. 8] an inhomogeneous texture could even be produced by grinding processes. Grooves could be smeared by grits or parts of the surface be ripped out. These inhomogeneities decreased the axial resistance for the fluid and could therefore lead to leakage, which increased with the number of inhomogeneities. Yet, rotary shaft lip-type seals could compensate for minor inhomogeneities [145, p. 9].

Leis and Hollen [86, 66] examined the effects of dents and grooves on axial fluid transport in an objective way. Their dents were impressions from hardness tests shaped as pyramids and balls. Grooves were manufactured with a diamond marker and by laser texturing. Depth, width and orientation varied. They observed that grooves generated a visible and measurable fluid transport depending on their orientation to circumferential direction. Leakage caused by dents correlated mainly with their depth [86, p. 65].

## **2.3 Evaluation of lead and surface imperfections**

Various measurement techniques, systems, and procedures were developed and often exist in parallel today. The following section gives an overview of lead evaluation and the current state of the art. Each subsection contains an overview of literature resources regarding methods and procedures for lead evaluation together with the respective author or company sorted by the first relevant publication discovered. In some cases the methods did not focus on lead evaluation but rather developed versatile methods that can find their application in lead evaluation. Many, especially older publications do not explicitly distinguish between macro or micro lead or surface defects. These methods are included according to their best agreement.

### **2.3.1 Macro lead**

All macro lead measurement procedures make use of the periodicity of macro lead structures.

- The objective evaluation of lead with roughness measurement methods was first approached by Kersten [78]. He took axial profiles at defined circumferential positions. Orientation of lead structures was calculated from their cross correlation. Their auto correlation provided him with properties of the grinding process and possibly present axially periodic components on the shaft surface. Additionally, he developed two optical sensor concepts for macro lead evaluation. Both sensors



illuminated the surface under a flat incident angle in axial direction with coherent light [78, pp. 92,95].

- Rau et al. [118, 119] presented a measurement procedure to detect and characterise periodic macro lead. It is referred to as macro lead evaluation of the first generation [127] or sometimes as CARMEN method [109, p. 117, 80, p. 29, 110, p. 459, 8, p. 21, 12, p. 10]. The procedure is the predecessor of today's Mercedes Benz standard MBN 31007-7 [95] with its second generation lead evaluation. Lead parameters defined in Rau et al.'s work for dressing lead are still widely used in science and industry. In two subsequent publications they gave an overview of parameter values found by their measurement procedure [116] and described superposed structures that appeared as macro lead with a high number of threads on turned shafts [117]. The same phenomenon was observed by Kunstfeld [83, p. 53] and Kersten noted related structures on ground surfaces [78, pp. 29 sq.].
- A method to detect and characterise periodic lead structures on ground shaft surfaces based on visual inspection was developed by Krahe and Beyerer [81, 80, 20, 19]. They used a magnified grey scale image of the surface taken by a camera. Illumination occurred under a flat incidence angle to enhance the contrast of structures on the surface. Based on the work of Krahe and Beyerer Puente and Rau improved robustness of macro lead parameter estimation on grey scale images from ground surfaces around the shaft [109, 110, 33].
- Daimler Chrysler patented a hand-held sensor developed by Baumgart et al. [15]. The sensor was designed to detect periodic structures on the surface. A laser source illuminated the surfaces under a flat incidence angle perpendicular to circumferential direction and thus perpendicular to the lead structures. The periodic components (i.e. macro lead) acted, if present, as diffraction grating.
- Rau et al. presented a successive patent to the handheld sensor [120]. It worked on the same physical principle but the surface was illuminated parallel to circumferential direction (and thus to lead structures). Due to the nearly tangential illumination the maxima were transformed to lines on the focussing screen. A commercial measuring device based on this principle was introduced as Shaft Twist Tester by Matesy GmbH [63, 16].
- Shuster et al. [132] used a coherence scanning interferometer as areal-topographic system to measure shaft surfaces around the circumference. The shaft axis appears to be oriented horizontally in a rotary unit.

- In addition to adopting the macro lead evaluation according to MBN 31007-7 Mahr developed its own lead evaluation [146, 91, 10]. It consisted of a combination of several measurements on the lateral surface of the shaft.
- Draft international standards E DIN EN ISO 25178-3:2008-03 [46] and E DIN EN ISO 25178-3:2010-03 [47] both described macro lead evaluation and parameters similar to MBN 31007-7 in their annexes as example for surface texture. However, the example is not present in the final standard from 2012 [49].
- Krenn [82] described the application of areal-topographic measurements with focus variation microscopy to characterise macro lead. Predominant texture orientation was visualised with the help of the autocorrelation function.
- Besides describing the macro lead evaluation of MBN 31007-7 in [127, 128], Seewig et al. took measurements with a confocal chromatic probe at a high axial measurement speed. The measurement time was reduced significantly to 4 min for 136 profiles with essentially the same results as the tactile reference. Another modification to reduce measurement time is a procedure patented by Jenoptik that estimated lead structures from only a few axial profiles and improved the estimate with each new measurement [125].
- Confovis GmbH [31] presented a measuring system for shafts based on structured illumination – a technology related to focus variation. The shaft was mounted horizontally. The large lateral measuring range enabled profile measurements with the default upper limit of the valid axial wavelength range of 2 mm according to MBN 31007-7.
- Innovent e.V. offered a measuring system with a rotary table for circumferential measurements of shafts based on the same physical principle (scattering light with coherent illumination) as the handheld sensor discussed above [64, 65, 70, 62].
- Novak and Schmit of Bruker Nano showed application of 3D microscopes to macro lead measurements [102].

The many different procedures can also be arranged by the underlying surface texture measurement method according to ISO 25178-6 [48]. This is done in table 2.2. The measurement methods from Krahe, Beyerer, and Puente ([81, 80, 20], [109, 33, 110]) contained no height information and are therefore not listed.

### **State of the art and review of macro lead evaluation methods**

The state of the art lead evaluation procedure is standardised in the latest version of MBN 31007-7 [95]. It is also described in [127, 128] and referred to as second gener-

Table 2.2: Macro lead measurement methods sorted by surface texture measurement methods

| Measurement method | Related publications   |
|--------------------|--|
| profile            | [78], [118, 119, 116, 96], [117], [146, 91, 10], [46, 47], [127, 128, 95], [125] |
| areal-topographic  | [132], [82], [31], [102]   |
| area-integrating   | [78], [15], [120, 63, 93, 16], [64, 65, 62, 70]                                  |

ation lead evaluation. The measurement data consists of two grids of 72 axial profiles each over the two circumferential ranges of  $36^\circ$  and  $360^\circ$ . Measurement of both grids is mandatory on ground shaft surfaces because they meet different sampling requirements [127, p. 1958]. Lead parameters (cf. fig. 2.3) obtained by this method are widely accepted [129, p. 49, 33, p. 12, 115, p. 285] and serve as reference in many publications. Agreement of the results obtained with instruments from different manufacturers is guaranteed because only a single implementation is distributed. Measured with a high speed optical probe, as detailed in [129], the measurement time is very short. When looking at older publications, it is important to remember that the evaluation procedure changed between the 2002 and 2009 version of MBN 31007-7. No comparative study is available but the values are most likely not comparable to the latest detail. Area-integrating methods are fast and can give an indication of macro lead structures. However, not all relevant parameters can be calculated directly.

When surface texture is sampled optically and used to calculate lead parameters according to MBN 31007-7 two prerequisites have to be fulfilled. First, the topography has to be sufficient long in axial direction to measure at least a profile length of five times the default upper axial wavelength limit of 0.4 mm. This can be accomplished by either a point sensor coupled to an axial feed axis, a large sensor length or stitching. Care must be taken as latter can result in misaligned topographies. And second the axial sampling distance has to be sufficiently small as demanded in [95]. While measurements by a point sensor were proven successful [129] no scientific publication is known that examines areal-topographic measurements on their suitability for macro lead measurements. The areal extent of topographies offers no additional information relevant to macro lead evaluation.

### 2.3.2 Micro lead

Several approaches were published to measure and characterise micro lead structures and their orientation. The irregular micro structures cannot be characterised by macro lead methods because the grinding marks are neither continuous in circumferential direction nor periodic. Due to the irregularity of structures line-profiling measurements

fail as they cannot convey information about texture orientation. Thus all methods are either areal-topographic or area-integrating. Kersten showed the necessity to detect deviations from circumferential direction as small as a few arc minutes [78, pp. 102 sqq.]. In the following the methods from Kersten, Beyerer, Puente, Buhl, Kunstfeld, Baitinger, Cohen, and Baumann will be explained shortly without going into details. As before they are sorted in order of the first relevant publication.

- Ruling out areal measurements with contact stylus scanning instruments because the instrument's axial starting position varied too much and structures were affected by effects of a  $\lambda_s$  smoothing filter (which both lead to undesirable high uncertainties of assessed lead angles [78, pp. 62 sq.]), Kersten [78] developed an optical sensor to examine the scattering light of micro structures skew to circumferential direction. The directional grinding marks produced a broad scattering distribution in transverse direction (axial direction). Taking two sections of the distribution he could determine the distribution's orientation and calculate the direction of micro structures with an uncertainty of 1' [78, p. 82]. The shafts were mounted between centres of a gear wheel testing machine and measured around the circumference. Averaging rendered angular run-out harmless [78, p. 90].
- Beyerer [17] developed models for machined surfaces and described methods to estimate the surfaces' parameters from magnified grey scale images. He did not mention lead or lead analysis but rather developed a toolkit for surface texture related image analysis. The images were taken with illumination at a flat incidence angle to enhance their contrast. Some of his parameters are also applicable to ground surfaces, e.g. groove orientation, groove density, cutting depth/appearance of single grits, and average groove profile. The groove angle is of interest for micro lead evaluation. Basis for its calculation is the discrete 2D Fourier spectrum. Multiplication of the image by a circular window was followed by integration along radial lines of the squared magnitude spectrum with bilinear interpolation. The angle's step size, i.e. the angular resolution of the scheme was  $0.5^\circ$ .
- Puente [109, 110, 120] calculated the orientation of grinding marks in the course of his macro lead evaluation. He took a series of grey scale images around the circumference of the shaft under flat illumination. The maximum of the radial projection of each image's power spectrum gave the orientation in each image. By taking the average over all images he received an estimate of the overall orientation.
- Buhl [27, 28] proposed a scheme to decompose topographies measured by a contact stylus scanning instrument into orders of form deviation. The form was removed by a least-squares fit of a second order polynomial. A Gaussian rough-

ness filter with an 80  $\mu\text{m}$  cut-off wavelength then separated the waviness and a cut-off wavelength of 25  $\mu\text{m}$  the roughness. In an example with a ground shaft he found lead on the waviness scale by visual inspection [28, pp. 75 sqq.].

- Kunstfeld [83] took areal-topographic surface texture measurements with a confocal chromatic probe and a lateral scanning table. Periodic texture was removed by averaging perpendicular to the grooves and histogram equalisation. The resulting topography was converted to binary representations by thresholding. Connected structures were found in each of the binary images and characterised individually after small structures were excluded. They were related to a reference direction and grouped according to their aspect ratio.
- Baitinger [9, 8] developed an evaluation procedure to assess micro lead on ground shaft sealing surfaces called Micro-structure Analysis and incorporated a series of image processing operations. Grooves and marks were characterised individually by lateral and height parameters. These were then related to the orientation angle. Topographies were measured with a confocal and a confocal chromatic instrument. In a first step he removed the form of the shaft by subtracting a least-squares fitted 2nd order polynomial. Roughness and waviness were separated by an areal Gaussian filter with nesting index 10  $\mu\text{m}$  [8, pp. 76 sq.]. The roughness surface was processed and resulted in a binary mask with locations of micro structures and a reference surface for height parameters. Connected regions representing single micro structures were then extracted to compute common lateral descriptors, e.g. an ellipse fit led to the structure's orientation angle, and several spatial parameters. For height parameters the reference surfaces was obtained from the roughness surface by an elastic areal rolling ball filter.
- Cohen et al. and Bruker Nano presented a 'self-referencing' procedure to measure lead angles of 3' and less [30]. Measurements were taken by Bruker's coherence scanning interferometer (CSI). After the shaft was clamped horizontally to a rotary unit in a three jaw chuck, the shaft's axis was obtained by fitting a cylinder into the measured topographies of the rotated shaft. The calibration procedure required approx. 250 measurements. The calibrated shaft axis was then subtracted as reference from the calculated lead angle. The lead angle was calculated from the power spectrum of the measured surface but no details were provided.
- Baumann et al. [14, 12] presented an extension to Baitinger's micro structure analysis for which they used Bruker's CSI as measuring system. They introduced micro waviness as additional lead type to micro and macro lead and surface imperfections [12, p. 630]. Micro waviness exhibited a lateral width of more than 20  $\mu\text{m}$

and could be oriented arbitrarily and be circumferential or non-circumferential (e.g. peened surfaces). After passing a test for scratches the topography was separated into micro structures and micro waviness by a Gaussian filter. Micro structures were processed as described by Baitinger [9, 8]. Waviness structures were segmented by a watershed transform and several height and spatial parameters to characterise micro structures were calculated.

### **Review of micro lead evaluation methods**

No standardised measurement method or procedure for micro lead analysis exists today. A lot of effort was put into sophisticated evaluation procedures to assess lead angle and several lateral and spatial parameters often with regard to a reference orientation (circumferential direction or axis orientation). Not so much attention was paid to the crucial calibration of shaft axis or circumferential direction. Kunstfeld [83, pp. 97,100] and Buhl [28] did not detail how they aligned shaft axis and instrument and Baitinger aligned them manually [8, p. 94]. Only Kersten [78] and Cohen et al. [30] approached this problem. Kersten also produced reference shafts with known orientation by tilting the centres of the workpiece in a grinding machine to test his optical sensor. He observed a good correspondence of the measured values with the adjusted tilt [78, p. 91]. The sign convention on positive and negative lead angles is not consistent throughout literature sources. Buhl defined the orientation angle of the manufactured structures as  $0^\circ$  in circumferential direction. Positive angles were orientated from down left to top right [28, p. 61] and thus just opposite to MBN 31007-7 (see section 2.1.1) whose method he employed for macro lead evaluation. Neither did Baitinger's sign convention agree with MBN 31007-7 [8, p. 94]. Generally, an agreement with MBN 31007-7 would be desirable.

### **2.3.3 Surface imperfections**

Not many researchers characterised surface imperfections on ground shaft surfaces in dynamic sealing systems.

- Beyerer and Krahe developed signal processing procedures to detect surface imperfections on honed surfaces [18, 17, 80, pp. 86 sqq., 95 sqq., 105 sqq., 118 sqq.].
- Rau et al. found imperfections on turned shaft surfaces. In their study they were mainly concerned with imperfections on shafts made of cast iron.
- Kunstfeld showed the extraction of a single structure using the example of pittings and classified them individually into four different classes according to their aspect ratio [83, p. 101].

- Hollen and Leis conducted a detailed study on dents and scratches on ground shaft sealing surfaces [86, 66]. They detected the imperfections' locations alternatively with a camera or a scattering light sensor in a multi-sensor coordinate measuring machine (CMM) set-up. The structures' topographies were then measured by a confocal chromatic probe. Both dents and scratches were characterised by several lateral and spatial parameters. The scattering light sensor was also found to be particularly suited for visualising wear tracks on the shaft surface [86, p. 39].
- Novak and Schmit [102] showed the application of Bruker's CSI to the measurement of imperfections.
- Bauer et al. [11] proposed methods to detect and characterise scratches and dents based on CSI measurements.

#### 2.3.4 Thread method

The so called thread method does not assess lead types separately but rather indicates the presence of any structures inducing axial fluid transport – at least in theory. Even though descriptions of this method were published in the 1970s this method is still widely applied in industry. Execution is always similar with small but decisive variations.

A loop of thread with a weight attached is placed around the horizontally clamped and aligned shaft. Often, the shaft surface is lubricated by a drop of oil. The shaft is then rotated at a predefined speed. An axial movement of the thread indicates lead on the surface. Manufacturers and suppliers have their own company standards on measurement procedures, e.g. Freudenberg, Schaeffler, and Volkswagen. Procedures and conditions are based on experience and specify even minute details. The outcome is said to depend on many factors [78, p. 5, 30], e.g. the type and colour of the thread, speed, weight, operator etc., which makes the method not very objective and reliable [118] and the results of different implementations hard to compare. The additional obstacle of handling the thread in modern machine tools was described in [16]. Some authors note a low resolution below certain lead angles [78, p. 5, 30].

Table 2.3 lists some known literature sources describing the thread method. Tests of two ground macro lead standards showed no thread movement even though the method was conducted according to a company standard by experienced personnel. It is generally unclear, how thread and shaft surface interact and which structures exactly influence the thread and to what extent.

Table 2.3: Overview of publicly available literature on thread methods sorted by time of publication

| Author or company                | Related publications |
|----------------------------------|----------------------|
| Otto                             | [104]                |
| Rubber manufacturers association | [122]                |
| Bearing Specialists Association  | [26]                 |

### 2.3.5 State of the art of lead evaluation

Lead structures can be divided into macro and micro lead and the same is true for lead evaluation. The only exception might be the thread method but presumably it can be tuned to the detection of macro or micro structures by selecting appropriate threads and adapting other conditions. Unfortunately, hardly any research on the thread method and its influencing factors is publicly available.

Measurement methods and procedures for macro lead characterisation make use of macro lead's characteristic occurrence and are highly specialised. The MBN 31007-7 method serves as reference and is widely applied. Measurements can be taken with tactile instruments or optically. Employing different instruments for this task the requirements of sampling distances have to be regarded. Further optical methods, e.g. based on scattering light, can offer a quick indication on the presence of macro lead.

The appearance of micro lead is fundamentally different from macro lead. It cannot be assessed with any of the macro lead procedures. Several approaches are available but either they lack a detailed description on their implementation or they leave out crucial requirements. Combining the different approaches might be an option. The most promising concept is Kersten's optical sensor which is both fast and possesses the resolution necessary to evaluate minute lead angles.



## 3 Measuring systems

After theoretical foundations were laid in chapter 2, the way micro lead can be evaluated will be described in this and the following chapter. Micro lead is defined in MBN 31007-7 [95] as deviation of the main texture orientation of the ground micro texture from the shaft's circumferential direction (cf. section 2.1.2). Besides gaining knowledge of texture orientation relative to the measuring instrument a crucial part in micro lead evaluation is therefore the calibration of the instrument's orientation to either circumferential direction or shaft axis. The shaft's orientation is either referred to as shaft axis orientation or circumferential direction. The projections of these two orientations are perpendicular to each other and either of them is used as synonym depending on the context.

This chapter introduces three practical measuring systems that allow measurements with regard to the shaft's orientation and describes corresponding calibration procedures. After shortly motivating the use of optical areal measurement methods, the three systems are presented. All three systems are based on optical areal-topographic surface texture measurement methods. The measurement and calibration procedures are explained in each section and accompanied by a discussion.

### Why optical areal measuring systems?

The ground surface texture, whose main orientation needs to be assessed, is formed in an outside diameter grinding process by individual grits in and on the surface of the grinding disc and the topography of the disc itself. Many process parameters influence the outcome (cf. e.g. [79, 24]). The ideal ground shaft surface texture for sealing applications was described by Rau et al. to exhibit uniformly shaped and non-uniformly distributed grinding marks that were oriented perpendicular to the shaft's axis and the texture was free of sharp edges [117]. Micro lead structures formed evenly around the circumference [95] and the circumferential length of the marks of Rau et al. was around 0.7 mm [117]. Raab described a maximal circumferential length of  $\approx 1$  mm [112, p. 80] while Kersten expected circumferential lengths between 0.2 mm and 0.5 mm [78, p. 14]. Kersten found axial widths in average between 10  $\mu\text{m}$  and 20  $\mu\text{m}$  and cited literature sources that suggested similar values. But he noted that the values were av-

erages and that finer structures might well occur [78, p. 14]. These descriptions on the spatial characteristics of micro lead structures define the requirements the measuring instruments have to meet.

Detecting a direction demands a minimum number of sample points which depends on the characteristics of the texture. The structures of a ground texture are not regular so an areal method that captures many structures in one measurement is beneficial. The measurement method needs to be able to measure a sufficiently large area of the surface and provide sufficiently dense lateral and vertical sampling and high optical resolution. Areal-topographic and area-integrating methods [48] both take measurements of an areal section of the surface and are therefore basically suited. The possible measurement principles are not limited to optical instruments only. ISO 25178-6 [48] specifies several principles like contact stylus scanning, atomic force microscopy, scanning electron microscopy, or parallel-plate capacitance that can be considered, too. But in contrast to these methods optical measuring instruments enable relatively quick measurements with manageable preparation and are readily available. Depending on the individual instrument they often offer identical sampling distances in both lateral directions and are well described in literature and technically mature. References to areal-topographic and area-integrating methods within this work always refer to optical methods.

Areal-topographic measuring instruments take surface measurements through microscope objectives. Generally speaking, the larger the measured topography the better because more grinding marks and other features are contained in one measurement, i.e. the sample size is larger. An option to increase lateral sample size is stitching several measured topographies together. Test results on page 58 in section 3.2.3 regard stitching and its suitability for assessing surface texture orientation.

Regardless of topography size the instrument's lateral and vertical resolution have to be high enough to resolve ground structures. Vertical resolution is determined by the vertical step size, the evaluation procedure, and the measured surface. An experienced user will most likely adjust vertical step size properly. For confocal microscopes and CSI it ranges from several nm to more than 100 nm. Smaller step sizes increase measuring time and this costs are often not reflected in better results. Lateral optical resolution, i.e. the minimal distinguishable lateral distance of two points on the surface, is a function of  $NA$  and illumination wavelength. It can be assessed by the Rayleigh criterion [113, pp. 52 sq., 144, p. 22]. In the case of the applied instruments the lowest  $NA$  is 0.4 of the CSI. The maximum of its illumination wavelength spectrum is somewhere in the range of 525 nm<sup>1</sup> resulting in an optical resolution of around 0.8  $\mu\text{m}$ . The confocal microscope employs objectives with a higher  $NA$  and its optical resolution is slightly

---

<sup>1</sup>The instrument was examined at the Institute for Measurement and Sensor-Technology (MTS) in connection with a different project.

better. Lateral sampling distance of the image sensor has to be adapted to the optical resolution which is the case for the applied instruments. The coarsest lateral sampling distance is  $1.5625\ \mu\text{m}$  and therefore less than a sixth of the smallest expected average width of the structures.

## 3.1 Rotating measuring system

Multiple circumferential measurements at different spots on the shaft surface can either be accomplished by rotating the shaft or the measuring instrument. The former concept is taken up here. The shaft is rotated on a high-quality rotary table and measured at various spots around its circumference by an areal-topographic measuring instrument. The section first explains the practical set-up before discussing the effects of radial run-out. Next, the calibration procedure is introduced, including the selection of a suitable calibration shaft, before some results are presented and analysed. Finally, the system is discussed.

### 3.1.1 Practical set-up

The measuring system consists of an areal-topographic measuring instrument and its support frame and a rotary table to mount and rotate the workpiece for circumferential measurements. Measuring instruments that commonly come with rotation units for cylindrical workpieces are roughness and roundness measuring instruments. Roughness measuring instruments often have their rotation unit aligned horizontally, i.e. parallel to probe scanning direction. Roundness measuring instruments rotate a shaft around its vertically aligned axis. The major difference between the horizontal and vertical alignment of the shaft is that a vertical shaft can easier be adjusted for eccentricity and tilt than a horizontal shaft. Keeping eccentricity and tilt small is beneficial in this application for two reasons: First, the height axis of the instrument does not need to be adjusted previous to the each measurement around the circumference. And second, the tilt can possibly manifest in a higher frequency deviation (see section 3.1.2).

The set-up resembles a roundness measuring instrument with a vertically aligned shaft. Due to the vertical alignment, the shaft can be adjusted for eccentricity and tilt. The instrument is tilted  $90^\circ$  from its upright position, so that the optical axis is horizontal, and fixed to a support frame. A picture of the system is shown in fig. 3.1.

The set-up allows for various degrees of freedom of positioning and aligning both the shaft and the instrument. The support frame was designed at MTS and makes positioning of the instrument in all three translational axes and tilting in the plane incorporating both the shaft axis and the optical axis possible (see fig. 3.2a). It can be clamped to a frame of aluminium profiles for better resistance to vibrations. The rotary table is

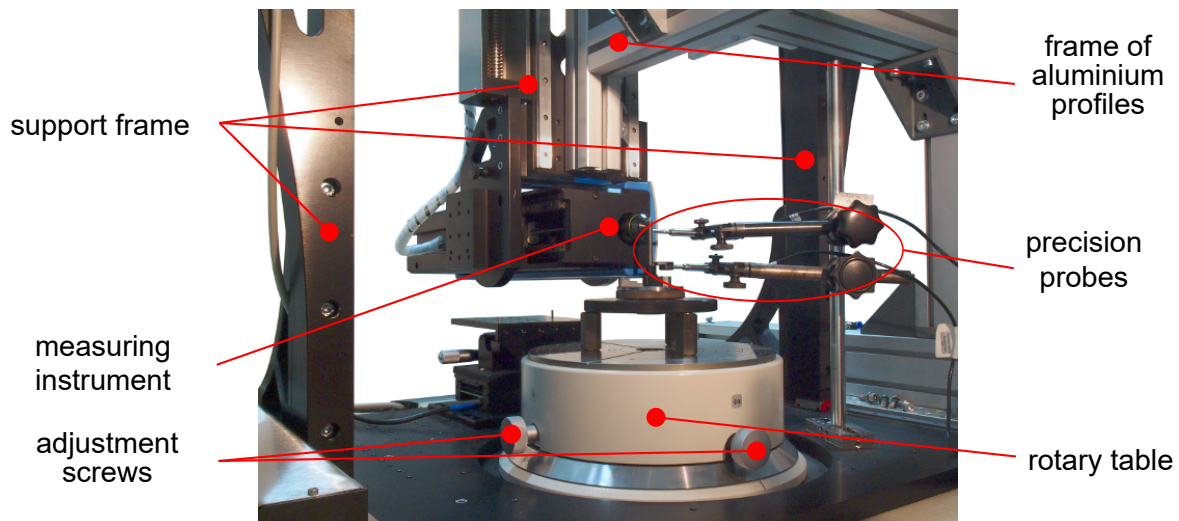
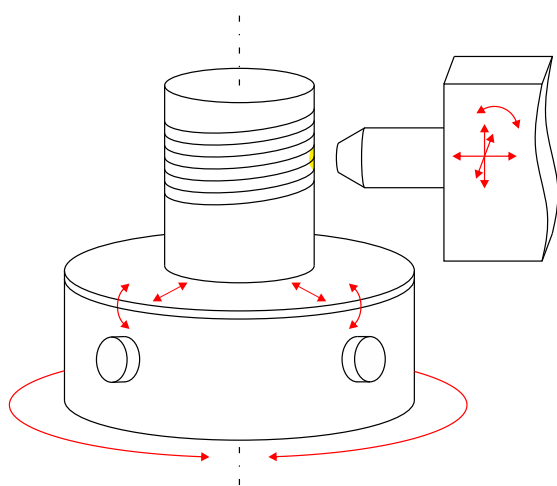
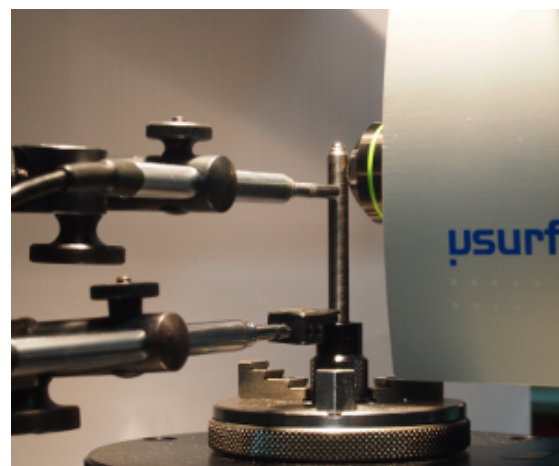


Figure 3.1: Picture of the complete set-up including the rotary table with the adjustment screws, the horizontal measuring instrument, two precision probes, the support frame, and a frame of aluminium profiles.

equipped with four adjustment screws to adjust eccentricity and tilt relative to the axis of rotation. For this purpose roundness measuring instruments are usually equipped with a motorised vertical stage to calibrate radial run-out at several axial positions. Here, the lack of a vertical stage is compensated by two electronic precision probes (see fig. 3.2b) connected to the table manufacturer's proprietary software. Alternatively, one probe can be replaced by the confocal measuring instrument itself and deviations be adjusted manually.



(a) Sketch of the rotating measuring system with a shaft with positive lead angle and degrees of freedom according to [6]



(b) Picture of the rotating measuring system with probes for adjustment and a fine-threaded screw as workpiece

Figure 3.2: Set-up of the rotating measuring system

### Areal-topographic measuring instrument

The areal-topographic measuring instrument used is the confocal microscope NanoFocus  $\mu$ surf explorer. The confocal principle of preventing out-of-focus light from passing through the pinhole applies only to a point [113, pp. 31 sq.]. In order to measure a topography the surface has to be scanned. Scanning is achieved in this case by a rotating multi pinhole disc [100, 144]. The device comes with several objectives. Here, only magnification factors of 20 and 50 are used and the objectives are  $20\times/0.45$ ,  $20\times/0.6$ , and  $50\times/0.5$  with the second number being the  $NA$ . Unless stated otherwise the  $20\times/0.6$  objective is applied throughout this work. The instrument's camera has a resolution of 8 bit gray scale and provides  $512 \text{ pixel} \times 512 \text{ pixel}$ . The resulting lateral properties are tabulated in table 3.1. Optical resolution is calculated as the minimal distinguishable distance between two points according the Rayleigh criterion [113, pp. 48 sq.]. The wavelength of the LED light source is given as 505 nm [100]. Posi-

Table 3.1: Objectives and lateral properties of the confocal microscope

| Objective       | Field of view                            | Optical resolution  | Lateral sampling distance                      |
|-----------------|--|---------------------|--|
| $20\times/0.45$ | $800 \mu\text{m} \times 800 \mu\text{m}$ | $0.685 \mu\text{m}$ | $1.5625 \mu\text{m} \times 1.5625 \mu\text{m}$ |
| $20\times/0.6$  | $800 \mu\text{m} \times 800 \mu\text{m}$ | $0.513 \mu\text{m}$ | $1.5625 \mu\text{m} \times 1.5625 \mu\text{m}$ |
| $50\times/0.5$  | $320 \mu\text{m} \times 320 \mu\text{m}$ | $0.616 \mu\text{m}$ | $0.625 \mu\text{m} \times 0.625 \mu\text{m}$   |

tioning along the optical axis is achieved by a piezo drive with a range of  $250 \mu\text{m}$  and a stepping motor for longer distances. The sampling distance along the optical axis can be set freely. It commonly varies between 62 nm and 125 nm for the  $20\times/0.6$  objective. The reference file correcting the image field curvature is kept up to date. The camera gain is switched off to decrease noise.

### Topography orientation

Evaluating measurements of anisotropic surfaces with areal-topographic instruments requires agreement on a coordinate system. Throughout this work the  $(x_t, y_t, z_t)^T$  coordinate system of fig. 3.3 is used unless stated otherwise. The coordinates of the confocal microscope and a major evaluation software, however, rely on pixel coordinates similar to image coordinates or row-column coordinates of a matrix with the origin in the upper left corner. Lateral indices are  $m_t, n_t$ , and  $M_t$  and  $N_t$  the respective number of pixels.  $z_t$  denotes topography height. The relationship between lateral pixel coordi-

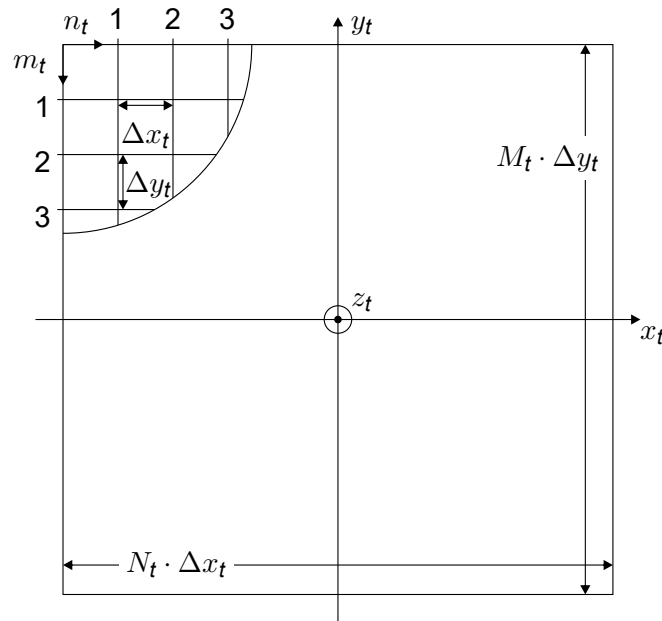


Figure 3.3: Coordinate system within a topography

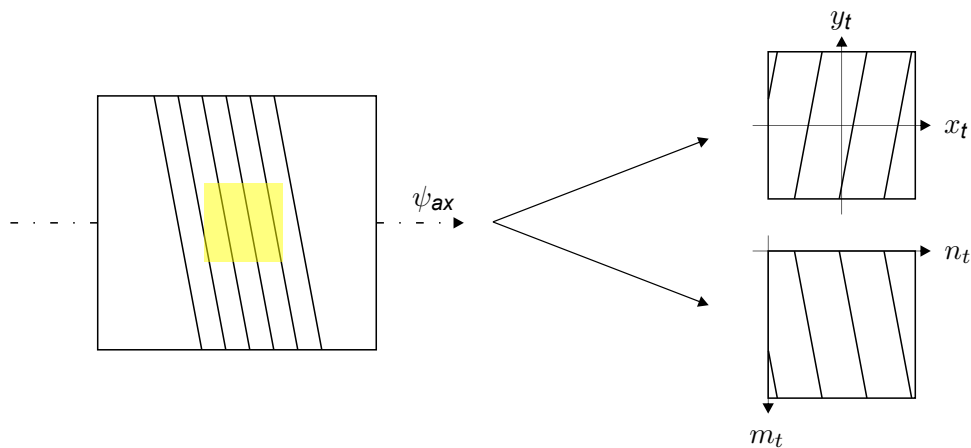


Figure 3.4: Coordinate system of a topography with structures with a positive lead angle (right-handed lead) and their appearance in different coordinate systems

ates and  $(x_t, y_t, z_t)^T$  coordinates is

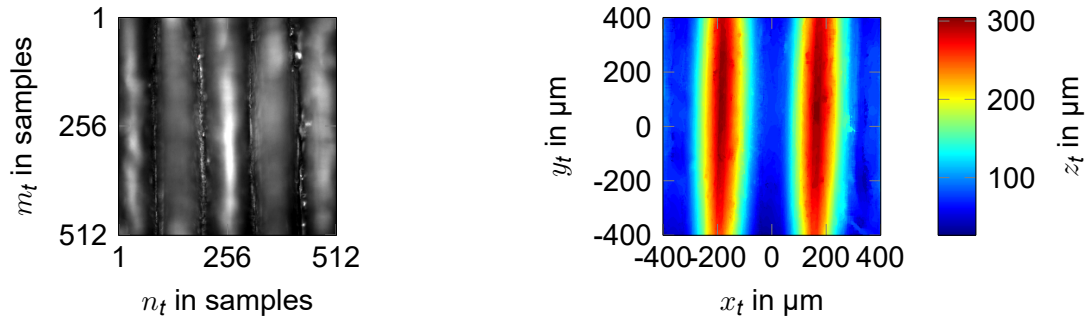
$$x_t = n_t - \frac{N_t + 1}{2} \tag{3.1a}$$

$$y_t = -m_t + \frac{M_t + 1}{2} \tag{3.1b}$$

$$z_t = z_t . \tag{3.1c}$$

This relationship is outlined on a shaft measurement in fig. 3.4. It can be seen that structures are swapped around the  $x_t$  axis and structure orientation is different, too. The example of a real measurement of a right-hand threaded screw with fine thread in fig. 3.5 confirms the effect. The right-handed thread in fig. 3.5a corresponds to right-handed lead structures (positive lead angle). However, due to the minus sign in eq. (3.1b), the

surface is flipped over the  $x_t$  axis exhibiting left-handed lead structures (negative lead angle) in fig. 3.5b. But this effect can easily be taken care of in the evaluation and all results are presented in the  $(x_t, y_t, z_t)^T$  coordinate system.



(a) Microscopic picture of a right-hand threaded screw with fine thread from fig. 3.2b (b) Areal-topographic measurement of fig. 3.5a in  $(x_t, y_t, z_t)^T$  coordinates

Figure 3.5: Measurement of a right-hand threaded screw measured similar to fig. 3.2 to determine topography orientation

### Positioning and repositioning

The support frame enables free positioning of the measuring instrument within a large volume to measure large objects like crank and cam shafts as well as non rotating parts. The system is located on the ground floor of a university building without special attention to vibration damping and several laboratories with test facilities are present on the floor below. Due to the large positioning range and therefore large measuring circuit the instrument exhibits vibrations that require clamping to a frame of stiff aluminium profiles visible in fig. 3.1. An undesirable side effect of additional clamping is that it inevitable wraps the support frame and shifts the instrument from its previous position. While a small shift is tolerable a rotation around the optical axis is not. A test with six successive series of 50 measurements each looks at the effects of several positioning and clamping operations on the calculated orientation. The experimental standard deviation  $s(\psi_{t,i})$  is defined as

$$s(\psi_{t,i}) = \sqrt{\frac{1}{N-1} \cdot \sum_{i=1}^N (\psi_{t,i} - \bar{\psi}_t)^2} \quad (3.2)$$

and indicates the variability within a series, which is very low.  $\Delta\bar{\psi}_t$  is the difference between the means  $\bar{\psi}_t$  of two successive series of measurements with

$$\bar{\psi}_t = \frac{1}{N} \cdot \sum_{i=1}^N \psi_{t,i} \quad (3.3)$$

Between each series the support frame was handled in a different way described together with the results in table 3.2. For high sensitivity and minimal measurement precision the measurements were taken on a grating of high quality (see fig. 3.23a).

It follows that even though the radial position along the optical axis ranged in a large in-

Table 3.2: Description and results of six series of 50 repeated measurements each after positioning and clamping of the support frame

| Series | description  | $\bar{\psi}_t$ | $s(\psi_{t,i})$ | $\Delta\bar{\psi}_t$ |
|--------|--|----------------|-----------------|----------------------|
| 1      | very lightly clamped   | -7.90'         | 0.08'           | —                    |
| 2      | very strong clamping ( $z_t$ position shifted $\approx 360 \mu\text{m}$ )                                    | -7.36'         | 0.03'           | 0.54'                |
| 3      | unclamped, laterally moved, repositioned, and reclamped ( $z_t$ position shifted $\approx 800 \mu\text{m}$ ) | -7.50'         | 0.04'           | 0.14'                |
| 4      | clamping with additional bracket ( $z_t$ position shifted $\approx 50 \mu\text{m}$ )                         | -7.77'         | 0.03'           | 0.27'                |
| 5      | small traverse movement without unclamping   | -8.23'         | 0.04'           | 0.46'                |
| 6      | traverse moved back  | -7.64'         | 0.03'           | 0.59'                |

terval the rotation varied much less. Still, the differences observed between the series are significant larger than the measurement precision within each series. Encouraging is the fact that the variation between two positioning operations with clamping and unclamping (2 to 3) is rather small. A traverse movement without unclamping should be avoided (4 to 5 to 6) and the clamping should be the same for all measurements (i.e. clamping each time with one bracket or two brackets (3 to 4) and with approximately the same torque (1 to 2)). For practical applications of measuring at different axial positions the case of 2 to 3 will be the most common. It is therefore examined further by another ten series of ten measurements each. Lacking a shaft of high reproducibility in axial direction measurements are taken on the grating again. The support frame was unclamped, the instrument moved down and up approximately 10 mm, and reclamped. Of the ten series only the first eight can be used because evaluation shows a significant shift in the last two, indicating an involuntary movement of the grating. The experimental standard deviation of the eight mean values of each series is 0.17'. This value is in the range of the result (2 to 3) from table 3.2.

### 3.1.2 Eccentricity and tilt

Eccentricity and tilt are inevitable caused by clamping the shaft in a three (or more) jaw chuck. Taking topography measurements with a tactile roughness measuring instrument Raab noted that due to tilted clamping in the three-jaw chuck the orientation of



structures within a circumferential segment could be distorted [112, pp. 77 sq.]. Here, the stationary instrument takes areal-topographic measurements of the incrementally rotated shaft. Figure 3.6 depicts an exemplary vertically clamped shaft that is affected by eccentricity and tilt. It is supposed to rotate around its  $z_c$  axis but does actually rotate around an axis displaced parallel to  $z_c$  by eccentricity  $\mathbf{e}_c = (e_x, e_y, 0)^\top$  and tilted to  $z_c$  around the  $x$  and/or  $y$  axis by  $\alpha_{c,x/y}$ . The effects of tilt and eccentricity are visible in the measured topographies and affect them in two ways. First, the form component of the shaft appears differently in each measurement because the shaft moves sideways and back and forth relative to the instrument. And second, the orientation of directional structures varies throughout circumferential measurements and they even can appear distorted within a topography.

The first effect results in non-equidistant lateral sampling due to the higher gradient

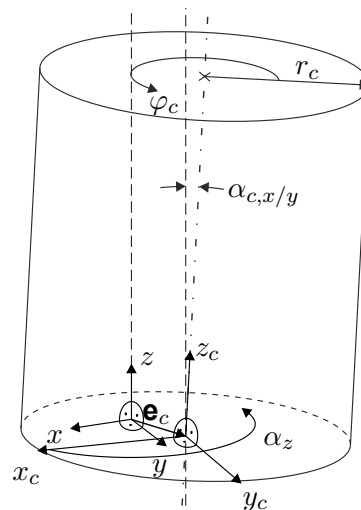


Figure 3.6: Eccentricity and tilt to the axis of rotation in a vertical rotating measuring system

within a topography. But these effects are negligible here because of good adjustment of eccentricity and tilt<sup>2</sup>. But this can not be guaranteed for horizontally aligned (i.e. with significant eccentricity and tilt) and especially thin shafts. A careful study on the effects is required in such cases.

The second effect leads to an estimation of texture orientation around the shaft following a sinusoidal curve. Additionally, it can distort the direction within each individual topography, i.e. straight lines can appear bent. To investigate this behaviour a model is set up in appendix A. It consists of the rotating shaft affected by eccentricity and tilt as it is seen through a stationary window (the aperture of the areal-topographic measuring instrument). Its basis is the illustration of fig. 3.6. The resulting surface represents the form component of a measured topography. The values of the axial height coordinate

<sup>2</sup>A shaft with diameter of 80 mm, a displacement between the clamped end and the measurement position in 60 mm height of 10  $\mu\text{m}$ , and an eccentricity of 10  $\mu\text{m}$  results in a maximal deviation in lateral sampling distance of less than 0.01 %.

$z_c$  are of constant  $z$  on a shaft rotating deviation-free. On a shaft affected by eccentricity and tilt the height values will appear sloped in the global  $z$  coordinate. Factors that are assumed to influence this slope are tilt, eccentricity, diameter of the shaft, and the distance from the clamping position in  $z$  direction. Average texture orientation is then the average slope of all sample points with equal height on a topography. Maximal and minimal slope measure the different directions within a topography. The slope angle is evaluated row-wise, i.e. in tangential direction, by the central difference.

Simulated texture orientation of circumferential structures on a shaft with the properties from footnote 2 is displayed in fig. 3.7. The differences between maximal and min-

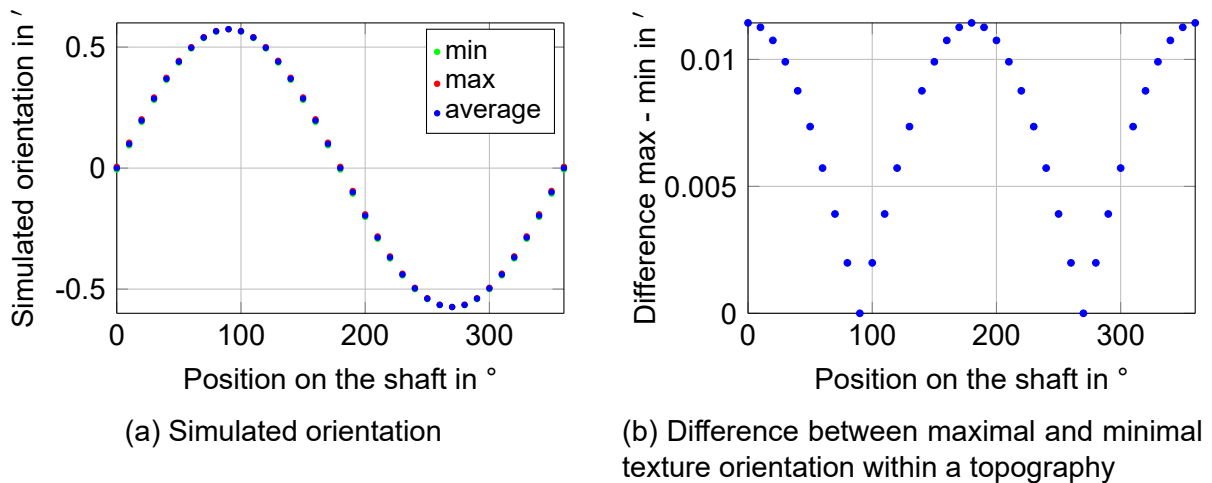


Figure 3.7: Simulated orientation of circumferential structures on a rotated shaft with properties from footnote 2

imal texture orientation within a topography are minute in this example (see fig. 3.7b). A reason is the small field of view of  $0.8 \text{ mm} \times 0.8 \text{ mm}$  and the thick shaft. It can be established from fig. 3.7 that the curves can be assumed to be sinusoidal for small values of eccentricity and tilt and the variation between minimal and maximal orientation within a single topography is very small.

The diagrams in fig. 3.8 show the average texture orientation based on the parameters from footnote 2 for several circumferential positions on the shaft with the parameter under question varied while the other parameters are kept constant. In this configuration only the tilt  $\alpha_{c,x/y}$  has a significant – and for all positions apparently linear – effect on texture orientation. The amplitude  $A_\alpha$  of the sinusoid can thus be estimated simply as

$$A_\alpha \approx \alpha_{c,x/y} . \quad (3.4)$$

For larger values of tilt and eccentricity or a very large axial distance from the clamping position, the situation changes, as fig. 3.9 shows. Here, the distance from the clamping position is varied up to the limit imposed by the radius, i.e. the radial run-out is so large

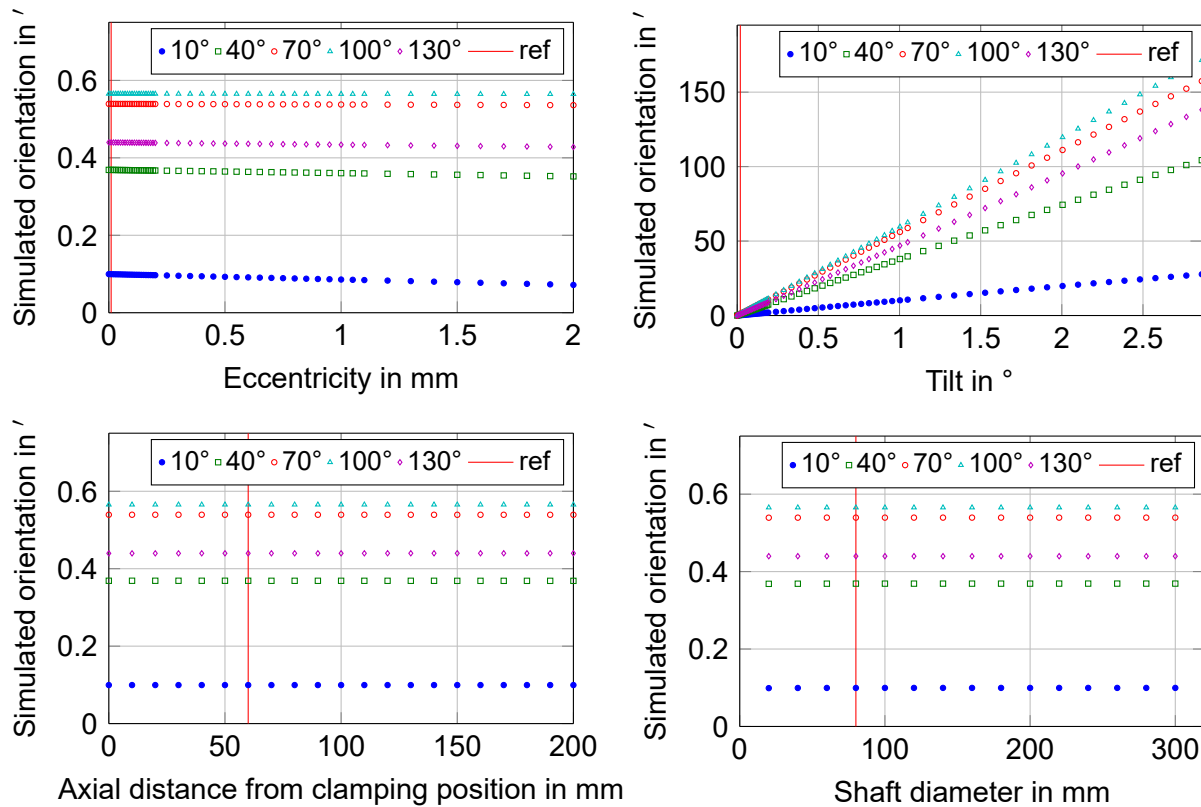


Figure 3.8: Individual variation of either eccentricity, tilt, distance from clamping position, or shaft diameter of the shaft parameters from footnote 2 (regarded as ref) at five exemplary circumferential positions

that the optical axis does not intersect with the shaft any more<sup>3</sup>. As a result texture orientation can differ significantly from the sinusoidal curve of eq. (3.4). The reason is that eccentric structures can appear steeper than on the cylinder's zenith. With larger distance from the centre of rotation and more tilt and eccentricity this effect intensifies. A large topography can also contain a larger section of bended structures than a small one. The effects depend further on shaft diameter because it also intensifies the steeper appearance. The model allows for comfortable assessment of all these parameters. Enlarging the aperture to a stitched field of view of  $1.35 \text{ mm} \times 1.35 \text{ mm}$  on a shaft of 20 mm diameter with eccentricity of 0.25 mm and tilt of  $0.191^\circ$  measured at 150 mm from the rotation centre the difference becomes clearer in fig. 3.10a. The pure sinusoid with an amplitude according to eq. (3.4) is plotted as comparison (theoretical). Differences between min and max are larger than  $1.5'$ . A clearly non-purely sinusoidal propagation of orientations is shown in fig. 3.10b of a shaft of 30 mm diameter, 1 mm eccentricity,  $2^\circ$  tilt measured 150 mm from clamping with a measuring field as before. The effects of eccentric structures are clearly visible at positions  $90^\circ$  and  $270^\circ$ . At least in the latter case estimation by eq. (3.4) is not sufficient.

<sup>3</sup>The limit at  $z \approx 240 \text{ m}$  with this parameters will very unlikely be met in practical applications.

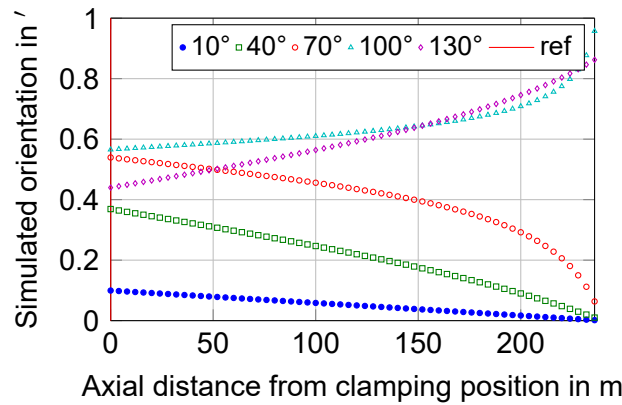
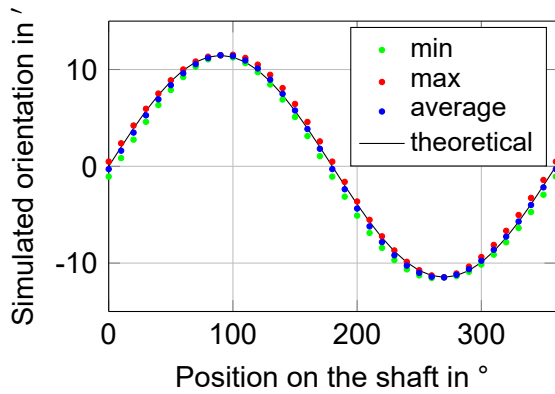
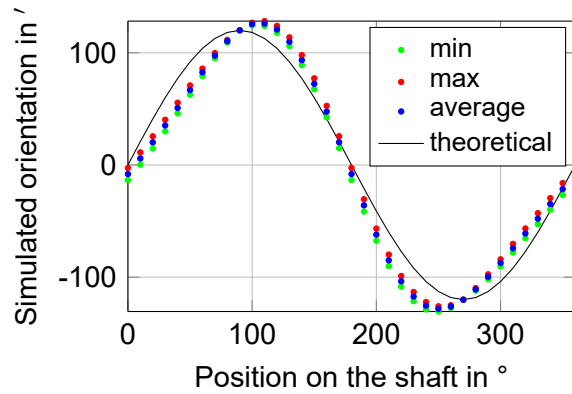


Figure 3.9: Individual variation of distance from clamping position up to the maximal limit

In addition to the above model the values are verified via analytical calculation of the



(a) Simulated orientation with larger field of view



(b) Simulated orientation with significant tilt

Figure 3.10: Two simulated orientations of circumferential structures on a rotated shaft (theoretical curve (black line) calculated as sinusoid with amplitude according to eq. (3.4))

slope of ellipses representing the tilted shaft's cross section at various stages of rotation.

### 3.1.3 Calibration

Calibrating axis orientation of the rotated shaft relative to the measuring instrument's field of view is a mandatory step in micro lead evaluation. Conclusions on deviations from circumferential direction as small as a few arc minutes are only possible with exact knowledge of the shaft's orientation.

Here, the fact is exploited that after adjusting eccentricity and tilt the axis of rotation is – with negligible deviations caused by run-out – identical for all shafts and coincides with the shaft axis. The basic idea is to estimate the orientation of the measuring instrument to the axis of rotation via the known orientation of structures on a calibration shaft. The

selection and design of suitable structured calibration shafts is outlined first before an easy-to-use method to assess the structures' orientation from areal-topographic measurements with low uncertainty is developed.

### Calibration shafts

Several shapes of structures are imaginable. These include a ground surface finish, thread-shaped structures with and without pitch, and axial and circumferential structures. Each structure offers advantages and disadvantages in some categories. The regarded categories are the ability and difficulty of production, the expected variability of the results (a small standard deviation is highly desirable), and the ease of application for the user. The properties of the structures are rated in five steps from very good (++) to very bad (--). The results are summarised in table 3.3.

**Ground shafts** can be easily manufactured and form deviations can be avoided by calibrating and adjusting the grinding machine regularly. Production of ideal circumferential structures is made very likely by adjusting the machine but it is not guaranteed (+). The standard deviation is expected to be considerably high because of the stochastic nature of the grinding process (--). Once a reference shaft with known structure orientation is available, calibration is just as easy to apply as the measurement itself (++).

**Thread shaped structures** are easily produced by turning. Regarding form deviations they share all advantages with ground shafts. As a result from the turning process their reference direction will always be different from circumferential direction. A difficulty can arise if the pitch is not known exactly. Regarding an exemplified axial feed  $f_{ax}$  of 0.16 mm/turn [24, p. 331] illustrates that a deviation of only  $\pm 5\%$  from  $f_{ax}$  and a shaft diameter  $d$  of 60 mm can result in a considerable interval between  $\psi_{calib}^{-5\%} = 2.77'$  and  $\psi_{calib}^{+5\%} = 3.06'$ <sup>4</sup>. It is therefore important to either measure  $f_{ax}$  manually or run the machine tool in closed-loop mode. An alternative is to measure the pitch or the structure inclination after production. A possible measurement procedure is the macro lead evaluation from MBN 31007-7 [95]. A problem can arise as the number of displayed digits is not sufficient in the standard software implementation. A specially designed implementation of the algorithm avoids this issue. Calculating texture orientation similar to ground shafts is also an option. Overall, production is simple (+). In contrast to ground shafts the structures are regular thus yielding a low variability of the estimated orientation (cf. section 5.1.3) (++)). Evaluation is identical to the evaluation of ground surface texture orientation in chapter 4. Calibration can take place in any height on the machined shaft (++)). **Threaded structures without pitch** consist of a periodic pattern running in circumferential direction. The properties are generally identical to thread shaped structures. A benefit is that they are strictly circumferential thus the reference

---

<sup>4</sup> $\psi_{calib}^{\pm 5\%} = \arctan \frac{f_{ax} \cdot (1 \pm 0.05)}{d \cdot \pi}$

direction is always known without further tests. However, these patterns are much more difficult to manufacture [149] (—). **Axial structures** can be manufactured on top of arbitrarily finished shafts. Production appears difficult because first the shaft and the tool have to be aligned parallel with low sub-arc minute tolerances. And second the tool has to produce structures of high quality that are easily evaluable (—). Depending on the shape of structures a dedicated evaluation scheme appears necessary. No forecast on its variability and ease of use can be made. **Circumferential structures** added to arbitrarily finished shafts offer the advantage that no additional reference direction has to be assessed or taken into account. Manufacturing the structures by turning in one setting guarantees that structures are exactly orthogonal to the axis of rotation. Even stochastic run out, which could be present in the machine tool's ball bearings and results in a small tilt of the workpiece, is disregarded because it cancels out with an increasing number of rotations. The outcome is only governed by the quality of the turning process (++). The evaluation procedure depends on the shape of structures. Here, a circumferential cut-in with round groove bottom is regarded that can be evaluated with low variability (++). Ease of use is high but measurements can only be done at axial positions with a groove present (+). Table 3.3 summarises the advantages and disadvantages discussed. Concluding from table 3.3 both threaded with non-zero pitch

Table 3.3: Expected advantages and disadvantages of shapes on calibration shafts (rating ranges from very good to very bad denoted by symbols: ++, +, o, -, --)

| Property    | ground | thread w/ pitch | thread w/o pitch | axial | circ. |
|-------------|--------|-----------------|------------------|-------|-------|
| Production  | +      | +               | --               | --    | ++    |
| Variability | --     | ++              | ++               |       | ++    |
| Ease of use | ++     | ++              | ++               |       | +     |

and circumferential structures are eligible. The latter is presented in the following.<sup>5</sup>

A shaft with circumferential cut-in is used. The cut-in is a groove with round groove bottom comparable to that of a depth-setting standard (cf. [61]). As outlined before the groove is orthogonal to shaft axis as a result of turning without reclamping. First tests were conducted on shafts made of well-machinable stainless steel. The shafts exhibit low groove quality and optical artefacts resulting in a relatively high variability. One of these grooves is presented in section 3.3.2 and appendix B and [4]. Subsequent designs were made from aluminium and brass focusing on higher quality grooves through better machinability. All these tests were produced on standard industrial-grade turning machines. Best results were obtained with a brazen ultra-precision turned shaft with a diameter of  $\approx 47$  mm that was manufactured by the Institute for Manufacturing Technology and Production Systems at the University of Kais-

<sup>5</sup>Measurements on turned shaft surfaces are regarded in section 5.1.3.

erslautern. Its three grooves were designed with widths  $b_g$  of approx. 330  $\mu\text{m}$ , 600  $\mu\text{m}$ , and 800  $\mu\text{m}$ . Figure 3.11 displays groove shape and corresponding parameters and an image of the actual shaft can be seen in fig. 3.12. Care was taken to provide axial space for adjusting eccentricity and tilt. The grooves were produced by a cutting tool with a cutting edge radius of  $r_g = 1 \text{ mm}$  resulting in e.g. groove  $b_{g,2}$  with a maximal groove wall inclination  $\alpha_{g,max} \approx \pm 18^\circ$  and a depth  $t_g \approx 50 \mu\text{m}$ .

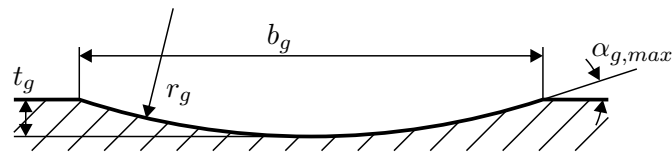


Figure 3.11: Sketch of an axial section through the calibration groove

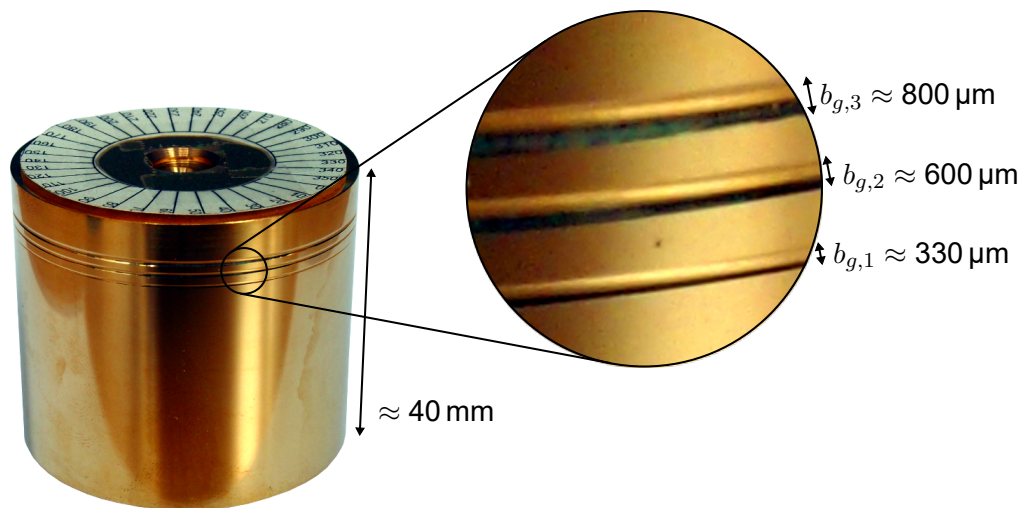


Figure 3.12: Image of brazen ultra-precision turned calibration shaft with three grooves and sufficient space for adjusting eccentricity and tilt above and below the grooves

### Calibration procedure

The orientation of circumferential direction  $\psi_{circ}$  relative to the instrument is assessed with the help of measurements of the calibration shaft groove. Measurements are taken with the same optical areal-topographic measuring instrument used for texture orientation. Groove orientations  $\psi_{circ,j}$ , with  $j = 1, 2, \dots, M$  and  $M$  being the number of calibration measurements, are calculated as samples of  $\psi_{circ}$  from the topographies after preprocessing. The following description is concerned with calculating a single  $\psi_{circ,j}$  from a measurement of the groove.

The idea of preprocessing is to remove high frequency fluctuations but keep the low frequency content as it contains the directional information of the groove. Measurement data is treated first by removing unrealistic high spikes and replacing them

by non-measured points (NMPs). NMPs are filled and an areal median filter with a  $3 \text{ pixel} \times 3 \text{ pixel}$  filter mask is applied once followed by an areal Gaussian low pass filter [43] with nesting index of  $8 \mu\text{m}$  acting as S-filter according to [45]. These steps are similar to sections 4.1.1 to 4.1.3.

Calculation of groove orientation by fitting geometric primitives based on the groove model follows these preprocessing steps. As mentioned above, the groove bottom is round and replicates the cutting tool's shape. An axial profile section through a topography approx. perpendicular to the groove looks similar to fig. 3.11. Evaluating the topography profile by profile and connecting the profiles by a straight line is the first of two approaches described in the following and will be referred to as 'profile' method. Instead of evaluating profiles separately it is also possible to approximate the groove by an areal shape, e.g. an areal second order polynomial. With grooves following the curvature of the shaft, an areal polynomial will always take the shape of a hyperbolic paraboloid. The approach with an areal second order polynomial will be referred to as 'areal' method.

The prerequisite for both approaches is that only 'good' data points are considered. One situation in which optical measuring instruments are known to generate incorrect height values are measurements on surfaces tilted to the optical axis. The reason is that with increasing tilt less light is reflected back into the objective. This leads to a decrease in modulation depth for CSI measurements [107, p. 98] and a lower and asymmetric peak in confocal microscopes [58]. These effects decrease the signal to noise ratio [58, 90, 107, pp. 95 sqq.] and start to appear at inclinations below the absolute limit of the acceptance angle  $\alpha_{NA}$  imposed by the objective's NA. With the diffraction index of air of  $\approx 1$  [139, p. 1032] NA and  $\alpha_{NA}$  of dry objectives are related by [113, p. 64]

$$\alpha_{NA} = \arcsin NA . \quad (3.5)$$

Additionally, technical surfaces with a considerable surface roughness exhibit higher gradients than very smooth surfaces. This can further decrease the light reflected back into the objective from already tilted spots. It is therefore advisable to limit the evaluated surface axially to a central groove section with an inclination angle  $\alpha_g$  well below the absolute limit set by  $\alpha_{NA}$ . In this work approximately half the acceptance angle is selected:

$$\alpha_g = \left\lceil \frac{\alpha_{NA}}{2} \right\rceil . \quad (3.6)$$

Regardless of the approach used to calculate groove orientation the preceding limiting procedure in axial direction is always profile based. It is summarised in the flow chart in fig. 3.13 and described in detail in the following.

The groove topography is sliced up into axial profiles parallel to the regular grid of the image sensor. Each profile contains a cross section of the groove. If the measuring



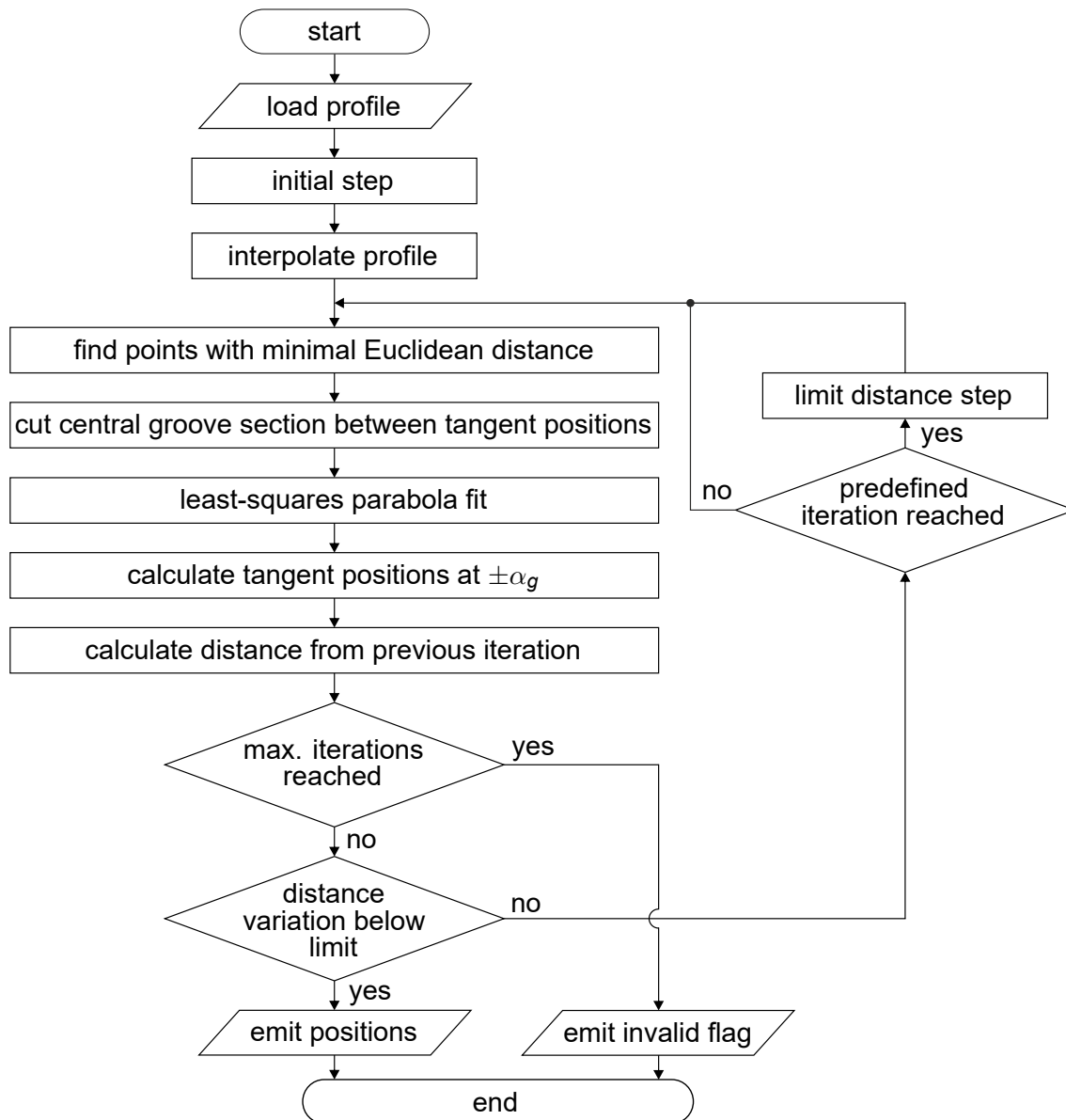


Figure 3.13: Limiting procedure for one profile

instrument is aligned parallel to the shaft's circumferential direction, the groove profile will have the groove's original width. Any deviation will make it appear broader and alter the perceived angle, thus also slightly changing the central groove section.

In the initial step, a parabola is fitted to a predefined interval centred around an initial point of the profile. A parabola was chosen because of its similarity to a cutting tool's shape. The fit is a least-squares approximation. With groove orientation parallel to  $y_t$  direction the parabola  $\mathbf{x}_p(t)$  is defined parametrically with parameter  $t \in [-1, 1]$  in the topography's coordinates (cf. fig. 3.3) as

$$\mathbf{x}_p(t) = \begin{pmatrix} x_p(t) \\ z_p(t) \end{pmatrix} = \begin{pmatrix} 2 \cdot t \cdot a_1 + x_{p,0} \\ t^2 \cdot a_2 + z_{p,0} \end{pmatrix}. \quad (3.7)$$

Additionally a rotation of  $\mathbf{x}_p$  around the coordinate centre by the angle  $\alpha_p$  is included:

$$\mathbf{x}_{\alpha_p}(t) = \begin{pmatrix} b_1 \cdot t^2 + 2 \cdot b_2 \cdot t + b_3 \\ b_4 \cdot t^2 + 2 \cdot b_5 \cdot t + b_6 \end{pmatrix}. \quad (3.8)$$

This can be written as a linear system of equations with the profile coordinates  $\mathbf{x}_{\alpha_p} = (x_t, z_t)^\top$ , the unknown  $\mathbf{b}_p = (b_1, b_2, b_3, b_4, b_5, b_6)^\top$ , and the matrix

$$\mathbf{M}_p = \begin{pmatrix} t^2 & 2 \cdot t & 1 & 0 & 0 & 0 \\ 0 & 0 & 0 & t^2 & 2 \cdot t & 1 \end{pmatrix} \text{ as:}$$

$$\mathbf{M}_p \cdot \mathbf{b}_p = \mathbf{x}_{\alpha_p}. \quad (3.9)$$

The least-squares solution for  $\mathbf{b}_p$  is then found by minimising the squared distances between the groove profile and the estimated parabola (cf. e.g. [54, pp. 302 sqq.]). The positions with a positive and negative tangent with slope  $\alpha_g$  are calculated on the approximated parabola.

After this initial step the whole profile is considered and interpolated using cubic spline interpolation. The interpolated profile samples with the closest Euclidean distance to the tangent positions are calculated and the interval between these two positions is cut out. Now approximation starts again in the selected interval followed by the calculation of the tangent positions and an interval between the tangent points is cut out again and again. The loop exits either after a maximum number of iterations is reached or the stop criterion is met. The stop criterion is met when the Euclidean distance of the tangent positions between successive iterations falls below a predefined limit. In other words the tangent positions are stable. In rare cases the procedure can get stuck jumping between two tangent positions and groove sections yielding identical Euclidean distances. To facilitated convergence in these cases the distance step (i.e. the lateral tangent positions defining the interval in which the groove is cut out) is limited after a predefined number of iterations. The result of the iteration are two axial positions in  $(x_t, z_t)^\top$  coordinates for each profile representing the positive and negative tangent of the groove with inclination  $\pm\alpha_g$ . If the iteration does not converge, invalid positions would be emitted and the positions of this profile section would be disregarded in all further calculations. On medium and high quality grooves, and if no further limitations on the step size are imposed, it will generally take less than ten iterations per profile until convergence is reached.

Instead of the least-squares approximation in eq. (3.8) other approximations of the parabola are possible (e.g. minimising the orthogonal distances according to [2], the extension to weighted least squares according to [94, pp. 4-82 sqq.] or robust least-squares using bisquare weighting according to [94, pp. 4-84 sqq., 101, p. 2.6.5.2.2])<sup>6</sup>. The

<sup>6</sup>Minimising the orthogonal distances provides a more realistic approximation of the groove because

second and third method mentioned were implemented but the results were of little difference or even higher variability and the speed of ordinary least-squares approximation prevails over more complex methods.

Running the limiting procedure on all profiles results in the central axial groove section with wall inclination below  $\pm\alpha_g$  (see fig. 3.14). This central groove section is the basis for calculating orientation by profile and areal methods.

As mentioned above calculation of groove orientation  $\psi_{circ,j}$  uses either the separate

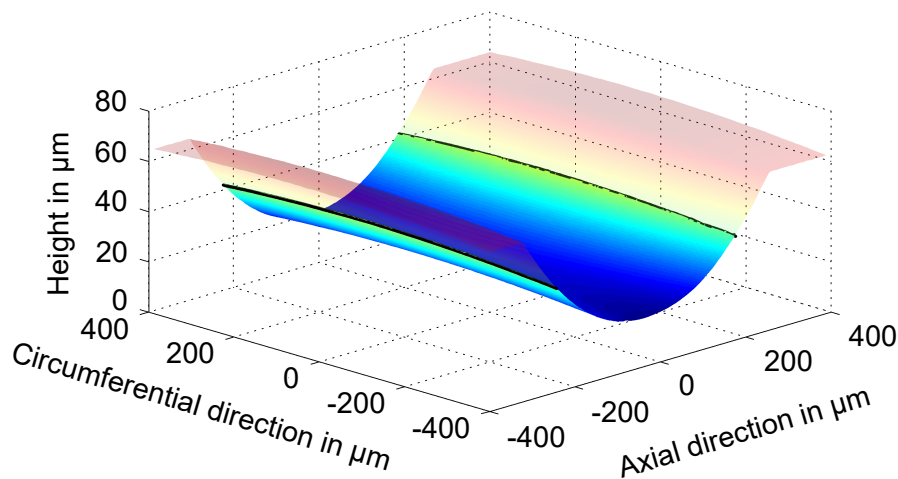


Figure 3.14: Central groove section (non-transparent) with  $\alpha_g = 12^\circ$  of ultra-precision turned shaft (delimited by black line, colours represent height)

profiles or an areal approximation. In the former, the parabola from eq. (3.8) is fitted to the last profile section by the known least-squares approximation of eq. (3.9). The direction of the groove is then found as the displacement of the parabolas along the groove. Several ways to estimate the displacement are possible. It could be the position at  $t = 0$  or the horizontal tangent position. A simple correlation with e.g. a parabola with averaged parameters might also be possible. Here, the horizontal tangent is established analytically and the shift of its contact point is used as measure of horizontal displacement. The positions of the horizontal tangent of each profile are approximated by a geometric line fit [1]. The geometric fit minimises the orthogonal distances in  $x_t$  and  $y_t$ . The desired circumferential direction  $\psi_{circ}$  is then the line's direction. This method is referred to as 'profile'.

The areal method as alternative does not try to fit the profiles separately but considers the central groove section as one continuous surface. This surface can be represented by e.g. a cylinder section or a second-order polynomial. Initial tests showed that a

distances are minimised in  $x_t$  and  $z_t$  alike. Its drawbacks are implementation complexity and iterative calculations. Weighted least-squares were implemented using a triangular weighting function to provide higher influence on the groove bottom and less weight on the sloped walls. The weight is fixed to the parameter  $t$  in eq. (3.8). Robust bisquare weighting uses the  $z_t$  distance of each sample to the fitted model to assign each sample an individual weight. Samples further away from their expected position in the model are given nearly zero weights so they are effectively deleted from the data influencing the model. As a consequence of successive approximations and re-weighting the scheme is iterative.

cylinder fit did not provide stable results – at least not with a variable radius. For this reason the cylinder was not pursued further but an areal second-order polynomial is used. Its formulation is that of a quadric surface with some coefficients set to zero [97, pp. 224 sqq.]

$$z_t(x_t, y_t) = p_1 \cdot x_t + p_2 \cdot x_t^2 + p_3 \cdot y_t + p_4 \cdot y_t^2 + p_5 + p_6 \cdot x_t \cdot y_t . \quad (3.10)$$

Approximation is possible as least-squares fit referred to as 'areal' or as bisquare weighted least-squares fit, then denoted 'areal robust' (see also footnote 6). A geometric fit, e.g. [134], was not implemented. Before calculating the actual approximation, the edges of the central groove section are smoothed by a geometric line fit [1]. Having obtained the parameters of the areal second-order polynomial its orientation of the main axis is assessed by a principal axis transformation via its eigenvalues [97, pp. 230 sqq.]. The main axis orientation is then the desired  $\psi_{circ,j}$ .

### 3.1.4 Results

The calibration scheme is tested on several grooves. Tests are made regarding the available resolution, i.e. the ability to distinguish small differences in groove orientation, the correctness of the resolved value (measurement accuracy), the variability of the values (measurement precision), and measurement uncertainty [36]. In all tests regarding grooves on circumferentially rotated shafts the grooves are assumed to be perfectly parallel to circumferential direction and so all deviations stem from the calibration procedure. As mentioned in section 3.1.3 this perfect alignment can be guaranteed by a stable turning process.

#### Sufficient measurement resolution and sensitivity

The ability of the calibration procedure to resolve small angular steps is verified by measuring the rotated groove of a depth-setting standard with round groove bottom [60]. The highest groove wall angle  $\alpha_{g,max}$  is  $\approx 5^\circ$ . The standard is aligned horizontally and placed on an angular adjustment stage with a graduation of the adjusting scale micrometer of 16.91' per increment [105] (see fig. 3.15a).

Rotating the standard 20 increments results in 21 linearly increasing orientation values. In fig. 3.16a the set rotation is plotted against the estimated groove orientation for all three orientation estimation approaches (profile, areal, and areal robust) with  $\alpha_g = 4.5^\circ$  applied to one dataset. A linear correlation assuming identically set increments (which is an idealised assumption because the steps were adjusted manually) is plotted for comparison. The curves are not altered except for subtracting a constant offset. The offset is the average difference between the manually set rotation read from

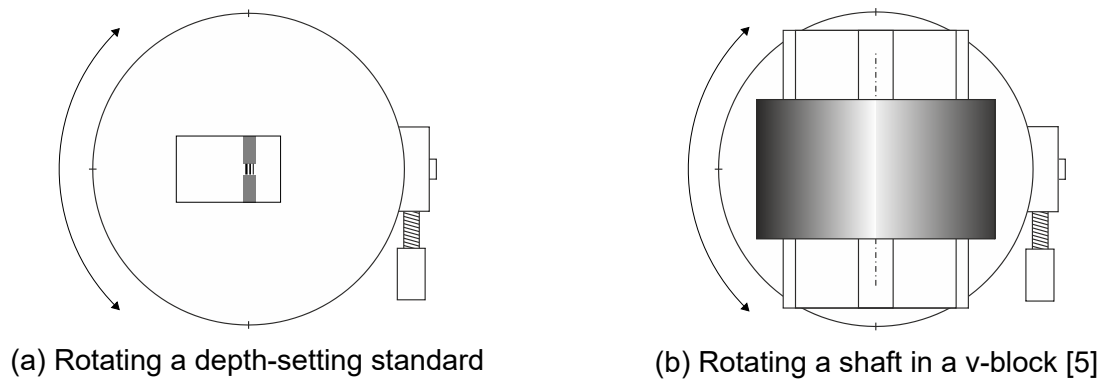


Figure 3.15: Set-ups with angular adjustment stage to investigate distinguishable variations in structure orientation

the scale micrometer and the identified orientations. Figure 3.16b shows the deviation

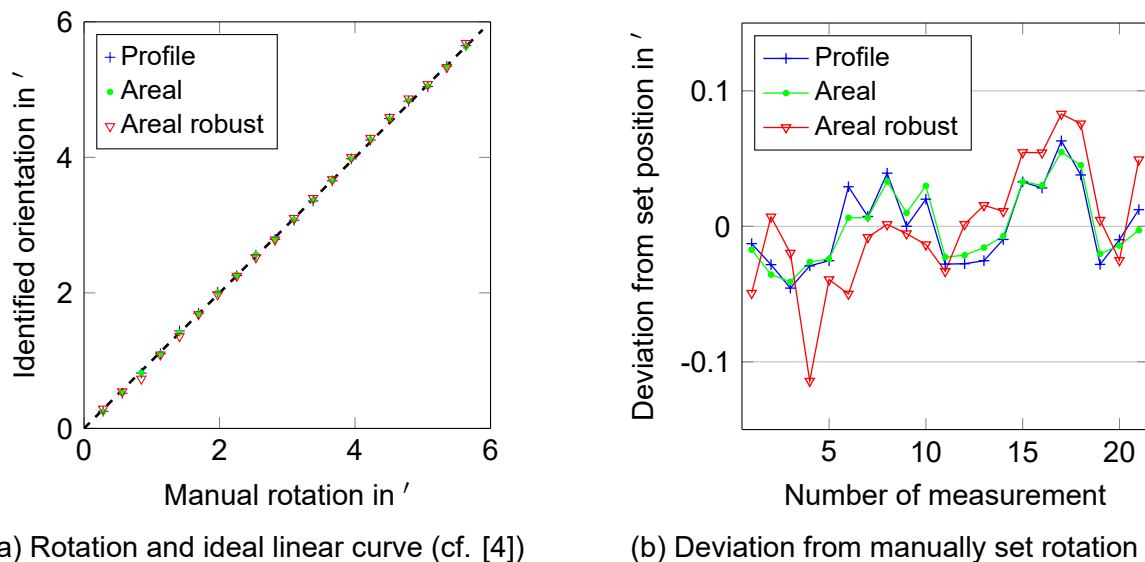


Figure 3.16: Incremental rotation of depth setting standard vs. identified orientation and deviation from set position with  $\alpha_g = 4.5^\circ$

for all 21 increments as the difference between the idealised curve and the identified orientation. The curves are centred around the middle because the mean is subtracted. The result of this test makes it clear that all three evaluation methods discussed above can easily resolve a groove orientation as small as  $\approx 1/4'$  and no significant differences between the methods exist in this context. The correlation coefficient of the ideally linear curve and the measured orientation is 0.9999, 0.9999, and 0.9998 for profile, areal, and areal robust, respectively. The slopes of the curves are 1.006, 1.007, and 1.018. It follows that the methods' sufficient resolution could be verified and the sensitivity is very close to one.

## Measurement accuracy

Although orientations on the depth setting standard obtained by the three methods are highly linear their absolute values differ. The mean differences (the offsets subtracted in fig. 3.16) are presented in the first column of table 3.4. Additionally, 72 circumferential

Table 3.4: Calculated absolute orientations of the depth setting standard and arithmetic mean  $\bar{\psi}_{circ}$  of circumferential measurements of calibration grooves

| Method       | Depth setting standard | $b_{g,1}$ | $b_{g,2}$ | $b_{g,3}$ |
|--------------|------------------------|-----------|-----------|-----------|
| Profile      | 2.002'                 | 10.5'     | 13.7'     | 14.0'     |
| Areal        | 1.997'                 | 10.0'     | 13.2'     | 13.5'     |
| Areal robust | 1.270'                 | 9.2'      | 12.3'     | 12.6'     |

measurements on the ultra-precision turned calibration shaft are examined and their arithmetic mean  $\bar{\psi}_{circ}$  with

$$\bar{\psi}_{circ} = \frac{1}{M} \cdot \sum_{j=1}^M \psi_{circ,j} \quad (3.11)$$

is calculated and presented in column 2, 3, and 4 in table 3.4. They are evaluated with  $\alpha_g = (8^\circ, 16^\circ, 18^\circ)$  for  $b_{g,1}$ ,  $b_{g,2}$ , and  $b_{g,3}$ , respectively. Absolute values of  $b_{g,1}$ ,  $b_{g,2}$ , and  $b_{g,3}$  are not identical because they were not measured successively. The orientations calculated with the areal robust method differ far more from their non-robust counterparts than the profile and areal method among each other. The deviations between profile and areal method are 0.5' for all grooves and the areal and areal robust method differ by nearly another arc minute. The reason for this significant disagreement is not known. The central groove section and the evaluation of the parameters is identical in the areal robust and non-robust case.

To investigate the differences, topographies containing grooves are modelled according to eq. (B.3) and evaluated by all three methods. The models resemble the calibration grooves from fig. 3.12 with the parameters from section 3.1.3:  $r_g = 1$  mm,  $b_g = (330 \mu\text{m}, 600 \mu\text{m}, 800 \mu\text{m})$ , and  $\alpha_{g,max} = (9.5^\circ, 17.5^\circ, 23.6^\circ)$ . The model's groove orientations vary from  $-10$  to  $10'$  in  $1'$  increments and serve as estimates of the true quantity values  $\psi_{circ,true}$ . The evaluated orientations match the modelled values for all three methods with deviations being smaller than  $6''$ . More realistic groove models  $b_{g,1,sim}$ ,  $b_{g,2,sim}$ , and  $b_{g,3,sim}$  add a two-axis rotation around the  $x_t$  and  $y_t$  axis (i.e. a tilt to the optical axis), the form of the shaft (with the radius of the calibration shaft), a circumferential translation from the shaft's zenith, and significant noise (7 pixel  $\times$  7 pixel median filtered white noise with a standard deviation of  $1 \mu\text{m}$ ). The resulting deviations  $\Delta\psi_{circ,true,j} = \psi_{circ,j} - \psi_{circ,true,j}$  in fig. 3.17 for the three groove models confirm the high noise level by significant variations. The curves show a difference mainly between pro-

file and areal methods. But the method's absolute variations on the calibration shaft from table 3.4 can not be reproduced. It rather suggests a sensitivity deviation of the areal methods.

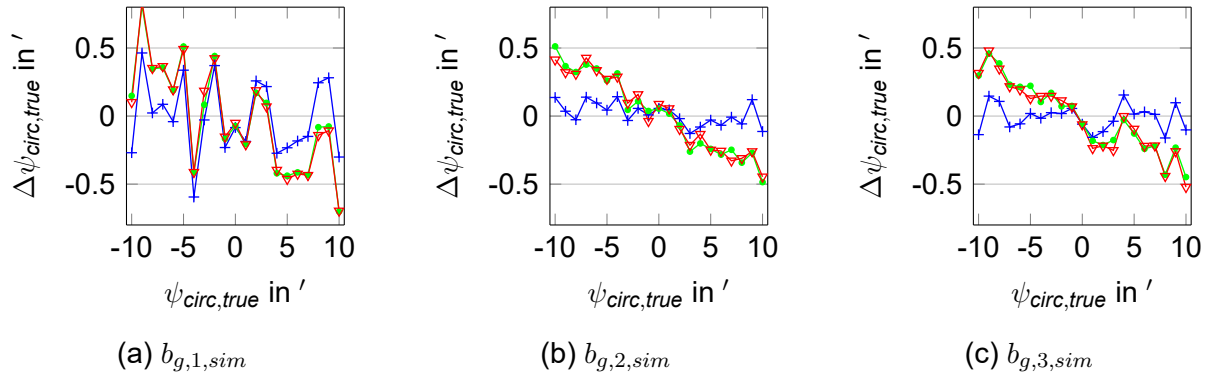


Figure 3.17: Deviations from true orientations for three realistic groove models and all three evaluation methods (legend identical to fig. 3.16b)

In any case does the profile method produce the smallest deviations. The bias between the methods can not be categorised as systematic measurement error because it does not *"remain constant or varies in a predictable manner"* [36, p. 34]. It is therefore classified as random measurement error.

In connection with measurement accuracy it is worth mentioning that all topographies are treated in the  $(x_t, y_t, z_t)^T$  coordinate system. Topographies in the lateral  $(m_t, n_t)$  system calculate the orientation inverted, i.e. right-handed lead appears as left-handed lead and vice versa.

### Measurement precision

Looking at measurements around the circumference of a shaft, the variability defines the uncertainty of the overall calibration procedure. A single measurement is not sufficient for a reliable estimation of  $\psi_{circ}$  because variations naturally occur and can only be handled statistically. Averaging groove orientation of several individual measurements  $\psi_{circ,j}$  around the circumference significantly decreases the resulting variability.  $\psi_{circ}$  is then found as the arithmetic mean over all  $\psi_{circ,j}$ . Uncertainty can be estimated by the experimental standard deviation of the mean [75, p. 10], which naturally decreases with an increasing number of measurements:

$$s(\bar{\psi}_{circ}) = \frac{s(\psi_{circ,j})}{\sqrt{M}} \quad (3.12)$$

with the experimental standard deviation  $s(\psi_{circ,j})$  defined as

$$s(\psi_{circ,j}) = \sqrt{\frac{1}{M-1} \cdot \sum_{j=1}^M (\psi_{circ,j} - \bar{\psi}_{circ})^2}. \quad (3.13)$$

When using the standard deviation of the mean as estimate for the variability of  $\psi_{circ}$  on a shaft, it is important to keep the effects of tilt in mind. Assuming only small tilt angles and measurements close to the centre of rotation the mean will stay the same as in the tilt-adjusted case but the variability will change due to the oscillation. Here, this challenge is circumnavigated by adjusting eccentricity and tilt to levels beyond recognition in the evaluated orientation. This is only possible (without considerable effort) on vertically aligned shafts.

Table 3.5 presents variabilities found measuring the ultra-precision turned calibration shaft from fig. 3.12 72 times around the circumference in 5° increments. Not only are the experimental standard deviations  $s(\psi_{circ,j})$  on groove  $b_{g,1}$  small but by regarding the experimental standard deviation of the mean  $s(\bar{\psi}_{circ})$  of 72 measurements the values decrease to single-digit arc second range. The corresponding curves for the calibration

Table 3.5: Measurement precision on circumferentially measured calibration shaft from fig. 3.12

| Method       | $b_{g,1}$          |                        | $b_{g,2}$          |                        | $b_{g,3}$          |                        |
|--------------|--------------------|------------------------|--------------------|------------------------|--------------------|------------------------|
|              | $s(\psi_{circ,j})$ | $s(\bar{\psi}_{circ})$ | $s(\psi_{circ,j})$ | $s(\bar{\psi}_{circ})$ | $s(\psi_{circ,j})$ | $s(\bar{\psi}_{circ})$ |
| Profile      | 0.32'              | 0.04'                  | 0.63'              | 0.07'                  | 1.29'              | 0.15'                  |
| Areal        | 0.29'              | 0.03'                  | 0.60'              | 0.07'                  | 1.30'              | 0.15'                  |
| Areal robust | 0.32'              | 0.04'                  | 0.61'              | 0.07'                  | 1.28'              | 0.15'                  |

groove  $b_{g,1}$  are plotted in fig. 3.18. The curves are almost identical except for the bias found in table 3.4. Figure 3.19 shows four series of measurements of  $b_{g,1}$  and  $b_{g,2}$  with

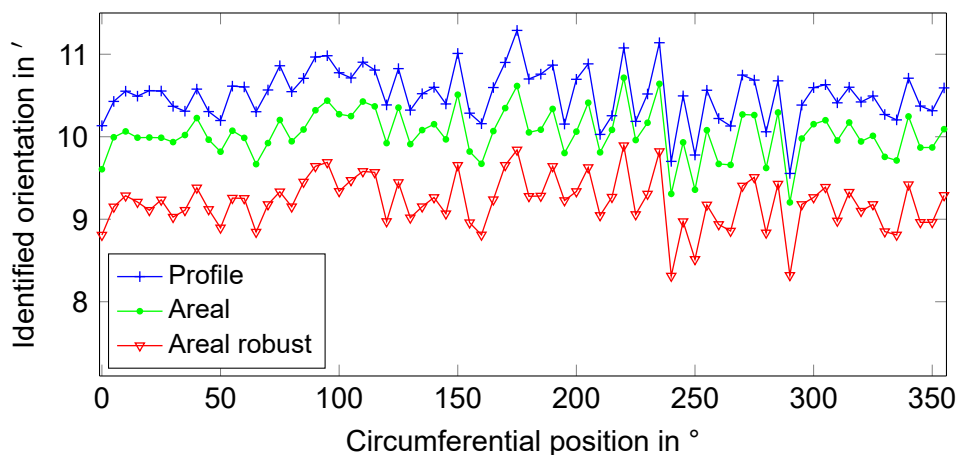
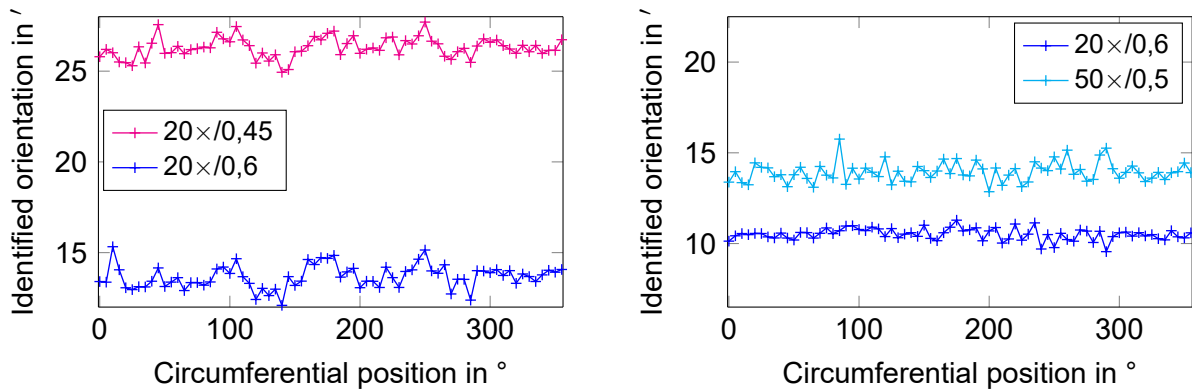


Figure 3.18: Results for groove  $b_{g,1}$  of the calibration shaft for all three methods





(a) Results for groove  $b_{g,2}$  measured successively with the  $20\times/0,45$  and  $20\times/0,6$  objective

(b) Results for groove  $b_{g,1}$  measured with the  $20\times/0,6$  and  $50\times/0,5$  objective

Figure 3.19: Results for grooves  $b_{g,1}$  and  $b_{g,2}$  measured with two objectives and evaluated by the profile method (y-axes identically scaled)

different objectives all evaluated by the profile method. A bias separates the curves but in fig. 3.19a their progression is similar. The bias' origin is not known. Measurements with the  $20\times/0,45$  objective have a standard deviation of  $0,55'$ , which is even smaller than with the  $20\times/0,6$  objective in table 3.5. This can hardly be said of fig. 3.19b, where the higher standard deviation of  $0,54'$  of the measurements with the  $50\times/0,5$  objective compared to the  $20\times/0,6$  objective is visible.

Overall, measurements of grooves  $b_{g,1}$  and  $b_{g,2}$  with any objective are sufficient for the precise estimation of circumferential orientation. Groove  $b_{g,3}$  exhibits a higher variability which might still be acceptable.

### Measurement uncertainty

Applying the rotating measuring system to assess shaft orientation requires knowledge of its measuring uncertainty as an input quantity to the final uncertainty of the micro lead angle. Measurement results from the previous analyses can be used directly in the Type A evaluation [75, pp. 10 sq.]. Due to the deviations appearing in the application of the areal methods only the profile method is regarded here. The experimental standard deviation of the mean  $\bar{\psi}_{circ}$  in one axial position is  $0,04'$  at groove  $b_{g,1}$ . It is this quantity that expresses how well  $\bar{\psi}_{circ}$  estimates the expectation of  $\psi_{circ}$  [75, p. 10] and therefore expresses the desired standard uncertainty  $u(\psi_{circ})$ . The value was derived from  $M = 72$  measurements, so the corresponding degree of freedom  $\nu$  is  $\nu = M - 1 = 71$ . For measurements without repositioning, reclamping or other manipulation on the instrument and the support frame no additional uncertainty components are regarded and the combined uncertainty  $u_c(\psi_{circ})$  equals  $u(\psi_{circ})$ . For the expanded uncertainty  $U$  a level of confidence of 99.73 % is desirable. The effective degree of freedom is equal

to  $\nu$ . The corresponding coverage factor  $k$  is  $\approx 3.125$  [75, p. 78].  $U$  is then:

$$U = \frac{s(\psi_{circ,j})}{\sqrt{M}} \cdot k = \frac{0.32'}{\sqrt{71}} \cdot 3.125 = 0.12' . \quad (3.14)$$

Table 3.2 shows that this value is only applicable when measurements are taken at one axial position without reclamping. If repositioning occurred because the shaft is for example measured at different axial positions, the corresponding uncertainty would have to be considered, too. In section 3.1.1 eight measurements yielded the experimental standard deviation of  $0.17'$  and therefore a significant contribution to uncertainty. Using an additive model the two uncertainties need to be combined to  $u_c(\psi_{circ})$  and corrected by the effective degree of freedom from [75, p. 73].

### 3.1.5 Discussion

For better overview the items of discussion are grouped under a corresponding heading.

**Uncertainty considerations** After looking at table 3.4 and table 3.5 a conflicting picture remains. On the one hand the measurement precision of all three methods is extremely small when considering  $s(\bar{\psi}_{circ})$  but on the other hand, the low accuracy between the methods renders estimation of  $\bar{\psi}_{circ}$  difficult and the shortcomings in accuracy are by no means covered by the variability expressed in  $s(\psi_{circ,j})$ , which is almost equal for all evaluations. The question arises if all three methods (profile, areal, and areal robust) were affected by the low accuracy, and the true orientation might lie somewhere between all three values (idea 1), or if one was correct, and the other two might deviate for unknown reasons (idea 2). This leads to two possible solutions regarding measurement uncertainty:

1. The first idea has to take the unpredictable effects of low accuracy into account by considering the combined arithmetic mean of all three evaluation methods (which equals the arithmetic mean of  $3 \cdot M = 216$  evaluations) for each groove measurement (i.e. combining the rows of table 3.4). The idea is illustrated in fig. 3.20. In the case of groove  $b_{g,2}$  in table 3.4  $\bar{\psi}_{circ}(b_{g,2}) = 13.1'$ . The combined experimental standard deviation of all  $3 \cdot M$  observations is then  $0.83'$ . The combined experimental standard deviation of the mean ranges in similar regions as the values from table 3.5 or is even smaller because the value under the square root in the denominator in eq. (3.14) is higher.
2. Arguments for the second idea can be found in the simulation of grooves, where deviations for both areal methods are clearly visible. Figure 3.17 finds the profile method to be free of accuracy deviations – even though the simulation could not reproduce the differences between the methods. With increasing  $|\psi_{circ}|$  the

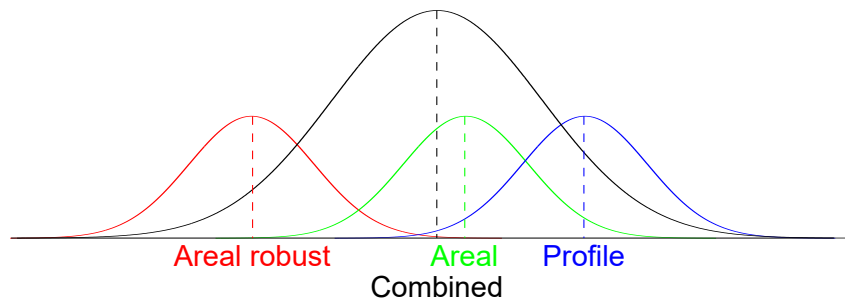


Figure 3.20: Combined uncertainty of all three evaluation methods (different sizes represent the different number of samples)

calculated orientations are smaller for both areal methods as it is the case in the evaluated calibration grooves in table 3.4. However, this effect is not observable on the depth setting standard in fig. 3.16 or in evaluations in section 3.3.

Overall, there is no indication that the profile method leads to inaccurate results. It is therefore straightforward to use it as the preferred method to evaluate groove orientation and consider its accuracy to be high. Using this assumption, the uncertainty consideration for  $\psi_{circ}$  in eq. (3.14) is valid. But it is so only for calibration measurements taken without repositioning or adjusting the set-up or changing the objective (as the offsets in section 3.1.1 and fig. 3.19 illustrate). If repositioning occurs because e.g. the shaft is measured at different axial positions, the corresponding combined uncertainty will have to be considered.

Generally, the GUM states that *"the uncertainty of a result of a measurement is not necessarily an indication of the likelihood that the measurement result is near the value of the measurand"* but *"it is simply an estimate of the likelihood of nearness to the best value that is consistent with presently available knowledge"* [75, p. 51].

**Measurement results** Looking at measurement with different objectives the source of the bias between them is unknown. If the instrument had accidentally been knocked against while changing the objective, could not be reconstructed. However, it accentuates the method's high resolution. The higher standard deviation on measurements made with the 50×/0.5 can have its origin also in the significantly smaller field of view of only 16 % of the area of the 20× objectives.

**Eccentricity and tilt** The effects of eccentricity and tilt affect texture orientation  $\psi_t$  on ground shafts and calibration measurements  $\psi_{circ}$  alike. A general prerequisite for applying the average as measure of  $\psi_{circ}$  or  $\psi_t$  in the presence of tilt is that measurements are taken around the complete circumference. Otherwise, the arithmetic mean will not estimate the orientation correctly. In circumferential measurements small eccentricity and tilt lead to a small variability of the values. In case eccentricity and tilt are present

in circumferential measurements, a modification to the orientation estimation is beneficial. It is straightforward to subtract a filtered curve from the measured orientation. Possible filters are digital filter with zero phase shift or a Fourier series approximation. The latter is plotted in fig. 3.21. The curves are the residuals of the first two Fourier

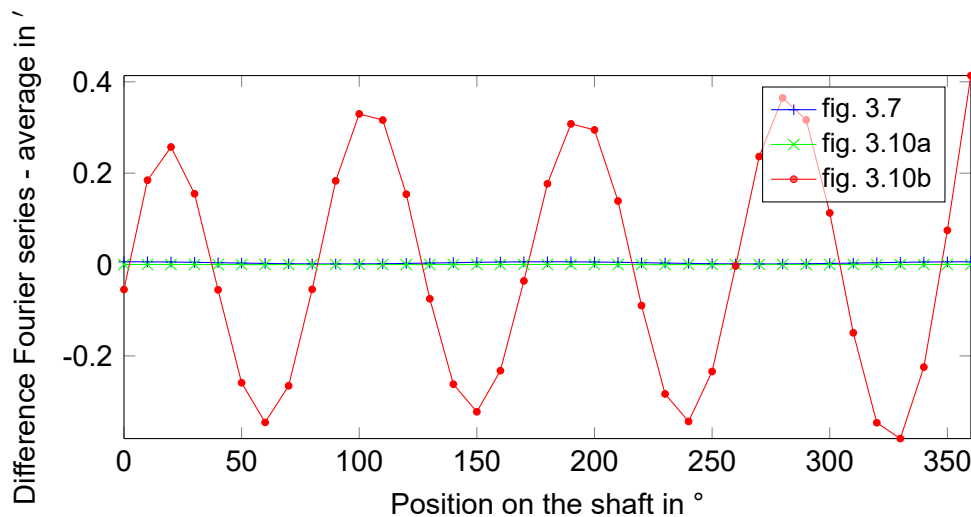


Figure 3.21: Residuals of a Fourier series with two terms of average curves from figs. 3.7 and 3.10 subtracted from the corresponding curves

series terms of the average curves in figs. 3.7 and 3.10 subtracted from the respective curves. It is clearly visible that the residuals are very small despite the large deviations from circumferential direction in the simulated curves. The mean absolute deviation is  $0.0037'$ ,  $0.000\ 082'$ , and  $0.22'$  for fig. 3.7, fig. 3.10a, and fig. 3.10b, respective. The first two Fourier series terms are therefore sufficient to represent the deviations in texture orientation caused by eccentricity and tilt as long as they are small. Although the example uses texture orientation this applies to calibration curves as well as long as the groove is not distorted significantly.

**Alignment of the grooves** The evaluation procedure assumes that groove orientation is almost parallel to  $y_t$  direction. Grooves in  $x_t$  direction can be processed by rotating the topography by  $90^\circ$ . Grooves should always be aligned approx. along either edge to avoid a distortion of the groove in the profile and incorrect values of  $\alpha_g$ .

Even though good results could be achieved with calibration shafts with a circumferential groove other structures, e.g. a turned texture, might work equally well.

**Extension of the measuring system's model** The rotary bearing is an air bearing and its run-out is negligible for the present application. For a higher quality model of the measuring system the bearing could be taken into account by adding stochastic eccentricity and tilt to the constant contributions.

**Rotating measuring system** The effects of clamping and positioning may be studied in more details. The current procedure has the disadvantage that measurements are only evaluated on a lateral region of  $10\text{ mm} \times 10\text{ mm}$ . If results are different at other spots, is not known. A tool to assess the uncertainty at different axial positions can be a high quality turned shaft. With it, variations could be estimated more realistic because it performs the same movement as a workpiece in an actual measurement. However, significant deviations are not expected because clamping is similar at all positions and the linear guides are very stiff. To decrease variability and provide more flexibility and easier measurements at different axial positions a stiffer support frame or a CMM would be beneficial. A multi-sensor CMM is available at the chair but both the machine and the measuring instrument were being worked on and it lacks an adjustable vertical rotary axis. The idea of a larger topography naturally occurs because measuring a longer circumferential section of the groove can only be advantageous to variability. Taking a longer field of view with the current instrument requires stitching. This can not be performed on vertical shafts because the instrument is clamped to the supporting aluminium frame and can not be positioned laterally.

**Further application of the calibration procedure** The presented methods for orientation detection can also be beneficial in other contexts such as the evaluation of depth-setting standards with round groove bottom by areal-topographic measuring instruments. Preliminary tests show that the groove bottom is described well by the fitted parabolas.

### 3.1.6 Summary

A measuring system consisting of a vertically aligned shaft, a horizontally positioned confocal microscope and its support frame was presented. The set-up allows for areal-topographic measurements of the shaft surface at multiple circumferential and axial positions. Eccentricity and tilt of the workpiece can be adjusted relative to its axis of rotation and the measuring instrument can be positioned relative to the workpiece. Due to the large measuring circuit the instrument requires clamping to a stiff frame. The effects of repositioning were studied and found to be within reasonable limits for similar clamping conditions. Any positioning after clamping should be omitted as it causes a rotation around the optical axis directly affecting the calculated orientation.

Eccentricity and tilt of the shaft caused an inclination of the measured surface texture. The propagation of topography orientations around the circumference was modelled. It appeared sinusoidal for small eccentricity and tilt. For higher values deviations from the purely sinusoidal curve became visible.

An ultra-precision turned shaft with a circumferential groove with round groove bottom

was used for calibration. Its evaluation considered only the axial groove region with a slope below half the limit set by the numerical aperture. Among several methods to evaluate groove orientation a profile-wise approximation by parabolas connected by a straight line was found to be first choice. It possessed a high sensitivity, measurement accuracy and precision, and a resolution below a quarter arc minute. The expanded uncertainty of circumferential direction of one of the calibration shaft's grooves without reclamping was as low as  $0.12'$  at a level of confidence of 99.73 % from 72 measurements.

## 3.2 Non-rotating measuring system

Measuring the shaft surface with the rotating measuring system described in section 3.1 is fast and convenient. However, systems with a high-quality rotary bearing are expensive and not readily available. Another solution can be using a common areal-topographic measuring instrument and placing the shaft in a supporting part, where its orientation can be assessed easily or is previously known. This concept using a v-block as support together with an areal-topographic measuring instrument is detailed in this section.

The practical set-up is followed by two applicable calibration procedures, some results and a final discussion. Parts of this section were already outlined in [5].

### 3.2.1 Practical set-up

A v-block offers repeatable and stable positioning of the shaft. Gravity pulls the shaft into the linearly converging v-shape. Two contact lines form between cylinder barrel and tilted v-block walls and the shaft axis is oriented parallel to these contact lines. The shaft can be rotated around its axis, repositioned, or exchanged and will always centre repeatably in the v-block. Furthermore, the v-block can be placed under commonly available areal-topographic measuring instruments and allows simple, cost-effective, and yet highly-accurate measurements of the shaft surface with regard to axis orientation. A sketch of the system with highlighted contact lines is given in fig. 3.22a. The v-blocks used are high-quality v-blocks for measuring purposes some of accuracy class 0 according to DIN 2274 [38].

Once axis orientation is known by calibration and any relative movement between instrument and v-block is prohibited no recalibration is required. If instrument and support are not fixed, axis orientation will have to be recalibrated before each series of measurements. The effort of recalibration can be decreased significantly by a reference landmark that is fixed to the v-block (fig. 3.22). The landmark acts as memory and has to enable calibration with minimal effort. Additionally, it has to work for all objectives

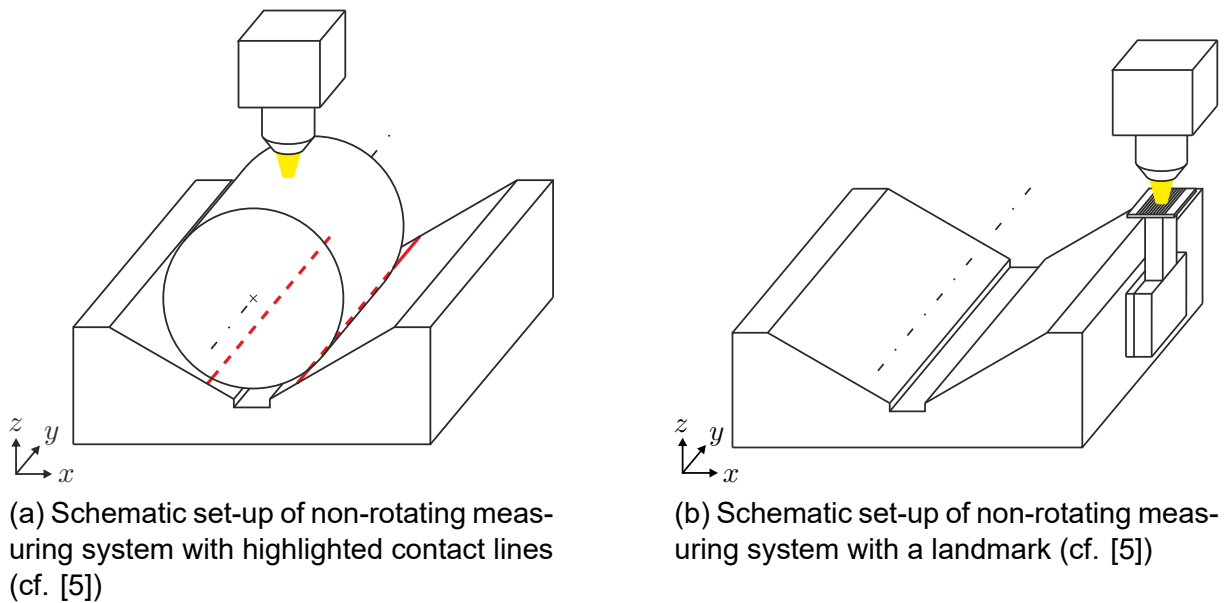


Figure 3.22: Schematic set-up of non-rotating measuring system

with different  $NA$  and magnification factors. Among a variety of possible structures simulated, a grating with multiple parallel lines was found to fulfil all requirements. The lines' pitch is chosen small enough to be measurable with the  $50\times$  magnification factor and still have several lines visible in the field of view. Among several microstructuring technologies available at the University of Kaiserslautern lithographic is applied here. Instead of generating structures with a defined wall slope [123, pp. 20 sqq.] an easier to produce alternative are parallel lines with almost rectangular cross section. A high quality mask for this grating is available at the Nano Structuring Center at the University of Kaiserslautern. The production technique is a lift-off process [32, pp. 218 sqq.] and essentially follows the steps: coating the silicon wafer with a negative tone photo resist, exposure through the mask, development of the photo resist, deposition of a 100 nm thick film of chromium, and finally removal of the remaining photo resist and its superposed chromium regions. The grating then consists of parallel lines of chromium on the silicon wafer with steep walls, a pitch of  $30\ \mu\text{m}$  and a height of 100 nm. A measurement with the confocal microscope with its  $20\times/0.6$  objective on the grating is presented in fig. 3.23a. The grating is glued to a table that is attached to a bracket mounted to the v-block (see fig. 3.23b<sup>7</sup>) by a magnet and secured against rotation and translation by a three-point bearing set-up. The three-point bearing consists of a plate, bearing balls, and cylindrical bearing rollers adjustable by fine-threaded screws. Rotations around all three axes are made possible. The contact surfaces are smooth to minimise negative effects of surface roughness on contact reproducibility.

The confocal microscope from section 3.1.1 is used as areal-topographic measur-

<sup>7</sup>The CAD model of this second attempt was derived by a student assistant based on a first model by the author.

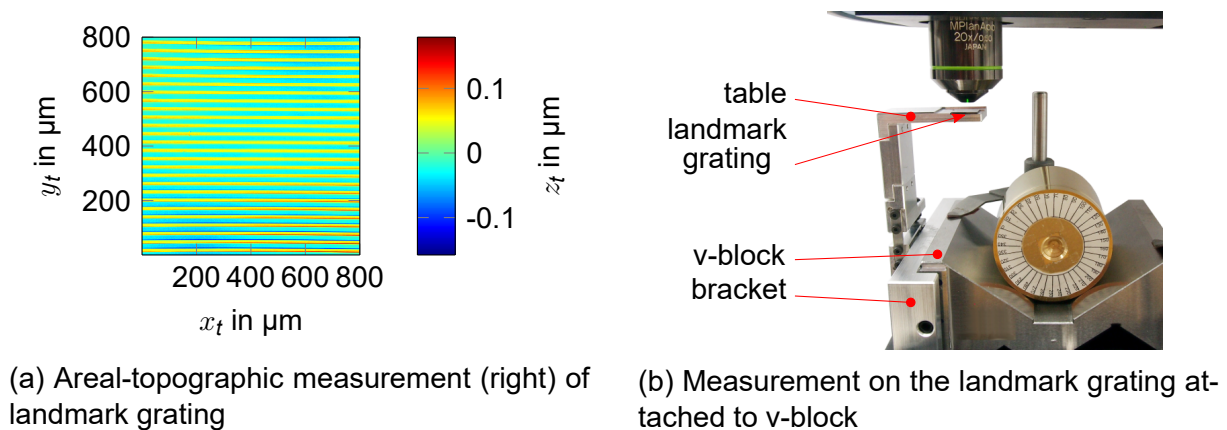


Figure 3.23: Landmark grating and the actual set-up

ing instrument but a CSI (e.g. from section 3.3.1 together with a suitable support for spatial positioning) could be employed equally well. The instrument is positioned upright and lateral positioning is enabled by an x-y stage under the v-block. As described in section 3.1.1 topography orientation is swapped because the confocal microscope displays and measures in the  $(m_t, n_t)^T$  coordinate system. X-y stage and v-block are aligned approximately parallel to topography borders.

### 3.2.2 Calibration

Calibration is needed to assess the orientation of the measuring instrument/measured topography to shaft axis. It is not possible to adjust shaft or v-block manually. Rotations on the scale of a few arc minutes are indistinguishable without specialised detection methods.

Two calibration procedures are presented. The first uses geometric features of the v-block, which are parallel to shaft axis, to assess axis orientation within limits set by the v-block's production tolerances. An additional requirement for a v-block with one cutting in DIN 2274 [38] is that it has to possess a finished and flatness tolerated upper surface. In the second, the axis is found by measuring a calibration shaft. In both cases the landmark described above can 'save' the calibration results to make them accessible quickly, without carrying out another calibration procedure.

#### Calibration on the v-block's geometry

The v-block is first adjusted with its upper surface perpendicular to the areal-topographic measuring instrument's optical axis. The edge between the v-block's contact surface and upper surface is measured at several positions along its length and the global  $(x, y, z)^T$  positions of each measurement are recorded. The edges are parallel to the contact lines and therefore to shaft axis. The edge points are detected row- or column-wise (depending on the v-blocks orientation) within each areal-topographic measure-



ment by an edge detection algorithm. The single points are then transformed into the  $(x, y, z)^T$  coordinate system and represent the two edges that can be approximated by two straight lines. Orientation is estimated either by averaging two independent geometric line fits [1] or by a least-squares approximation representing two parallel lines. The described procedure calibrates the orientation of the shaft to the x-y positioning system. A rotation between the topography's  $(x_t, y_t)^T$  and the positioning movement in  $(x, y)^T$  has to be previously known. Any deviation between these axes results in a systematic measurement error that can be significant but is almost impossible to detect. One method to calibrate this deviation is to take measurements along the edges and to calculate the orientation of the edge in each topography. Averaging and correcting it with the fitted line's orientation of the overall edge then provides an estimate of this deviation. Due to their minute dimensions, results are greatly affected by the quality of the edge in the measured topography, the edge detection procedure, and the straightness and wobble of the x-y positioning system. A CMM is beneficial in this application because it provides accurate guidance and high quality positioning.

Several production tolerances according DIN 2274 [38] can further affect measurement accuracy. The topic was already discussed in [5] and the results are briefly summarised here. DIN 2274 specifies three accuracy classes. Rotation of the two contact lines of an ideal cylinder (cf. fig. 3.22a) can result in a rotation  $\Delta\alpha_z$  around the  $z$  axis and therefore directly influence the measured orientation of structures on a shaft. It can be caused by a parallelism deviation  $t_3$  [38] of the contact lines to the centre plane of the two lateral surfaces. The possible rotation can be as large as  $0.22'$  for a v-block with  $L_V = 50$  mm of the highest accuracy class and  $0.89'$  for the lowest accuracy class. In [5] this error was underestimated.

At first glance, a tilt of the cylinder around the  $x$  axis has no influence on the result because the shaft axis is only tilted. But as in section 3.1.2 it can lead to a perceived inclination of the texture that – in contrast to eccentricity and tilt – does not vary around the ideal cylinder but is stable for all measurements taken at this  $(x, y)^T$  coordinate position. As outlined in [5] the effects are negligible for reasonably well aligned shafts.

With the edge points between contact and upper surface serving as orientation it is important to consider the flatness tolerances  $t_1$  of these surfaces as they can affect the edge's orientation (see fig. 3.24). A flatness deviation  $t_1$  increasing linearly from one side to the other over the whole axial v-block length  $L_V$  is considered for simplicity but other shapes are possible [76, p. 87] and can lead to increased effects. In addition to [5], where only the tolerance of the upper surface is considered, the perceived maximal skew of the line  $\Delta\alpha_e$  can be calculated for one edge as

$$\Delta\alpha_e = \arctan \frac{\frac{t_1}{\cos \alpha_V} \cdot (1 + \sin \alpha_V)}{L_V} \quad (3.15)$$

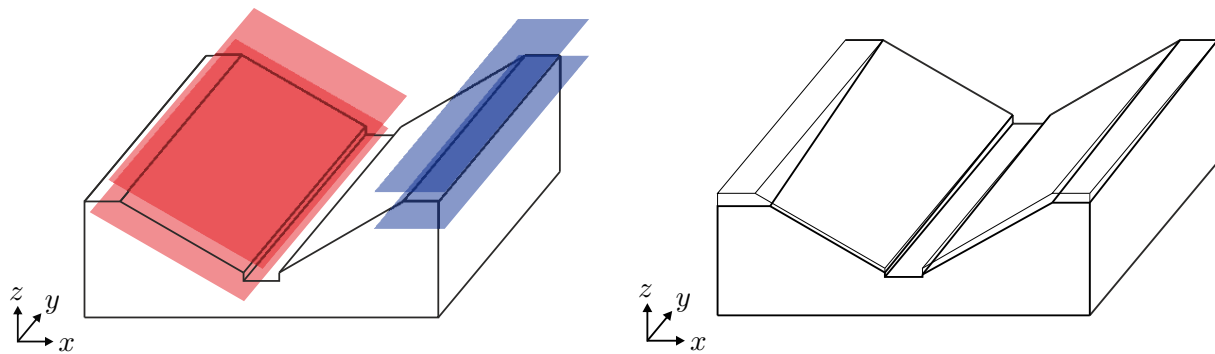


Figure 3.24: Flatness tolerances of the upper and contact surfaces affecting edge orientation according to [5]

The maximal  $\Delta\alpha_e$  for the above v-block with the highest accuracy class with a half v-block opening angle  $\alpha_V = 45^\circ$  is then  $0.35'$  and for the lowest accuracy class it is  $1.74'$ . These are of course only maximal values and apply only to one edge. In the worst case they can apply to both edges and then fully affect the perceived axis orientation after averaging both lines. In the best case they cancel out or are absent at all. The calculations hold true only for a flatness tolerance of the upper surface which is specified in [38] only for v-blocks with two opposite cuttings.

From the above and in accordance with [5] it follows that a v-block of the highest accuracy class should be used.

### Calibration with a calibration shaft

Another way of calibration is taking the v-block purely as support and calibrating axis orientation with a calibration shaft. A high-quality calibration shaft is the ultra-precision turned shaft from section 3.1.3. Production tolerances of the contact lines discussed above apply here, too. To minimise their effects calibration shafts resembling the workpiece in size can be measured at approximately the same position as the workpiece in the v-block.

Prior to measuring, the v-block should be adjusted with its upper surface perpendicular to the measuring instrument's optical axis. Also, the v-block's parallelism of shaft axis to topography edges should not exceed very few degrees to avoid a distortion of the groove.

### Using a pre-calibrated landmark

The landmark works only as memory after being calibrated by either of the above procedures. The landmark is attached to the bracket fixed to the v-block (cf. fig. 3.23b), and after evaluating one or several measurements the orientation of the grating to shaft orientation is known. Prior to further measurements, the landmark can be reattached to obtain axis orientation without time-consuming calibration.

### 3.2.3 Results

Tests are conducted on v-blocks of the highest accuracy class according to DIN 2274 [38] with an opening angle of  $90^\circ$  and an uncalibrated yet high quality v-block for measurement purposes with  $2 \cdot \alpha_V \approx 110^\circ$ . The x-y stage provides a lateral positioning range of  $45 \text{ mm} \times 45 \text{ mm}$ . If necessary, positioning was aided by the support frame (cf. fig. 3.1) because the v-blocks are longer and wider than the maximal positioning range of the stage.

#### Calibration on the v-block's geometry

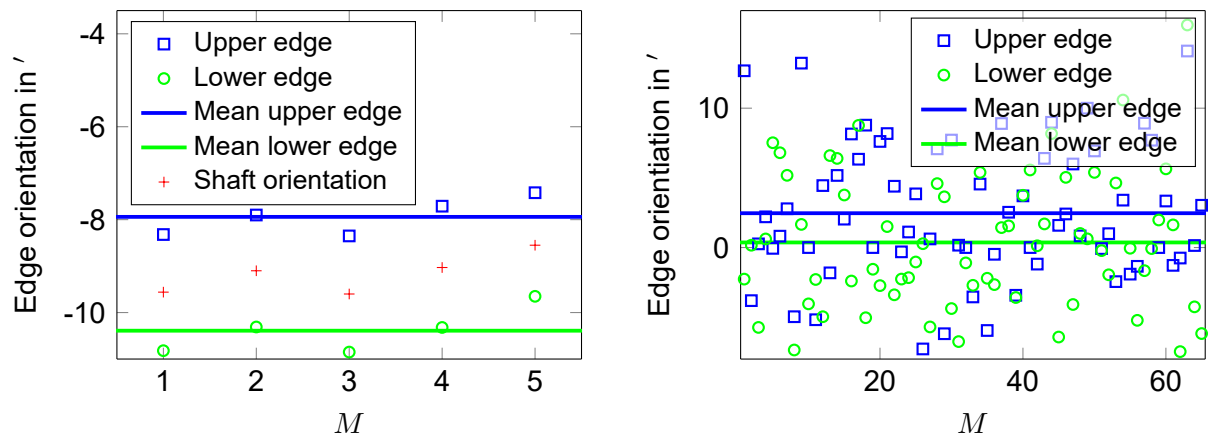
It is of interest, how well axis orientation can be assessed from the v-block's edges and how much the estimates vary. Here, five estimates of orientation are taken on a grade 0 v-block. An estimate consists of 26 measurements each. This are 13 measurements per edge (five measurements along the edge in increments of 2.5 mm starting at both ends of the x-y stage's positioning range and three measurements in the middle with identical increments, cf. fig. 3.26a, no. 1). When the edge had been visibly damaged, the nearest intact position was found. To estimate orientation at different axial sections of the v-block's edge (the v-block is longer than the positioning range of the x-y stage) it was shifted manually with its side locating surfaces in contact with a flat external edge. For easier positioning the v-block's base was lubricated by a whiff of oil. With this procedure, measurements at different positions along the edge were possible, without affecting the v-block's orientation or using the support frame for positioning. Axis orientation yields a mean of  $-9.17'$  and an experimental standard deviation of  $0.43'$  from the five samples. Additionally, orientation of the two edges is calculated separately and their mean differs by  $2.45'$  with each edge's experimental standard deviation being smaller than  $0.5'$ . The measurement results are plotted in fig. 3.25a.

Averaging the orientations of edge points from each measured topography separately for all five estimates affirms a difference in orientation between the v-block's two edges of  $2.10'$ . Figure 3.25b depicts the results together with the edges' respective mean. The edge orientation's experimental standard deviation is around  $5'$ . Other measurements confirm such a high variability.

The difference between the mean orientation of each topography's edge and shaft axis obtained in x-y stage's coordinates is found to be  $10.59'$ . However, this value appears not stable throughout different measurement series. In another two measurements without shifting the v-block it was found to be  $13.53'$  and  $13.17'$  from 19 measurements per edge<sup>8</sup>. Clearly, the high variability of the edge's orientation estimate of individual edges in single measurements affects the overall axis orientation.

---

<sup>8</sup>As both measurements were taken directly one after the other they can be described by their mean of  $13.35'$  but hint a low repeatability.



(a) Orientation of edge orientation measured with the x-y stage

(b) Orientation of edge orientation in individual topographies

Figure 3.25: Calibration results on the v-block's geometry (lines represent the mean of the respective colour)

The question arises how many measurements are required to provide a reliable estimate of axis orientation. This question could simply be addressed by regarding the confidence bounds of the approximated coefficients representing axis orientation and iteratively finding the number of measurements  $M$  that provide this value at the defined level of confidence [94, pp. 7-64 sqq., 101, p. 4.5.1.1]. However, due to the distribution of measurements along a length of 45 mm the standard deviation of the fit's orientation parameter is always smaller than  $0.02'$ . Generally, only two measurements at the most distant points of each line are enough and provide minimal variability through the minimum variance estimator [101, p. 4.3.2]. In an effort to verify the assumption for this realistic measuring system the 13 measurements per edge of the five estimates described above are reduced in five steps (see fig. 3.26a). Leaving out all measurements except for the two outermost changes the arithmetic mean only very slightly in the second position after decimal point (see fig. 3.26b). The experimental standard deviation between the five estimates increases from  $0.43'$  to  $0.50'$ . It follows that, if only points on undamaged edges are measured, two measurements at the outermost positions will be sufficient. Still, with the deviation between the x-y stage and the instrument unknown, four measurements at the whole v-block come at the cost of a very high variability of the edges obtained from the single measurements.

### Calibration with a calibration shaft

Placing the shaft at four positions in the non-specified v-block and measuring groove  $b_{g,2}$  (see fig. 3.12) twelve times around the circumference in increments of  $\approx 30^\circ$  yields an average experimental standard deviation of  $0.51'$  and an experimental standard deviation of the four means of  $0.15'$ . This shows that measurements at different axial

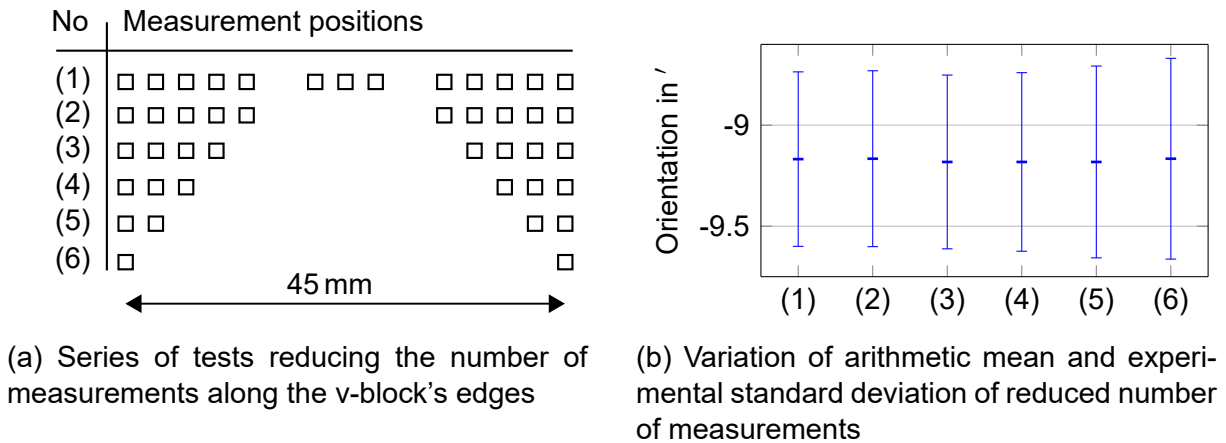


Figure 3.26: Considerations on the required number of measurements on the v-block

position in the v-block yield comparable results.

Estimating the required number of measurements  $M$  is straightforward. The uncertainty is the experimental standard deviation of the mean  $s(\bar{\psi}_{circ})$  corrected by the coverage factor for a limited number of samples. Assuming a level of confidence of 99.73 %  $M$  is then found by iteratively calculating  $U_{99,73}$  for different values of  $M$ . On the basis of  $s(\psi_{circ,j}) = 0.5094'$  from 24 circumferential measurements the first  $U_{99,73}$  to decrease below  $0.2'$  is at  $M = 64$ . The corresponding curve, where the value can be read off, is plotted in fig. 3.27. The assumption made here is that  $s(\psi_{circ,j})$  does describe the distribution of  $\psi_{circ}$  adequately.

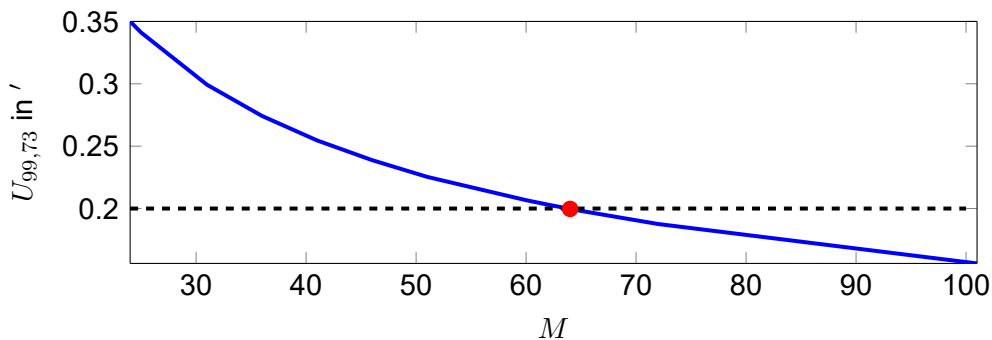


Figure 3.27: Relation between the number of measurements  $M$  and the expanded uncertainty of axis orientation  $U_{99,73}$  from measurements on the calibration shaft

Additionally, the effects of stitching on  $\psi_{circ}$  are examined in the same set-up. Eleven circumferential measurements of the shaft positioned in the v-block are taken around its circumference. The orientation of stitched groove measurements consisting of two measurements in circumferential direction with a stitched size of  $1457 \mu\text{m} \times 800 \mu\text{m}$  is  $-13.06'$  with an experimental standard deviation of  $0.22'$ . Taking only half the stitched field minus the overlap yields  $-9.28'$  and  $-8.81'$  with standard deviations  $0.86'$  and  $0.36'$ , respectively. The values for half the stitched measurement field agree well with the 24

non-stitched measurements around the shaft with  $-8.82'$  and standard deviation  $0.51'$ . The soft spot is, presumably, the assembly of the stitched topographies. The results clearly show that stitching (at least with the default overlap between the topographies) is not an option for high accuracy orientation evaluation.

### Comparing both calibration methods

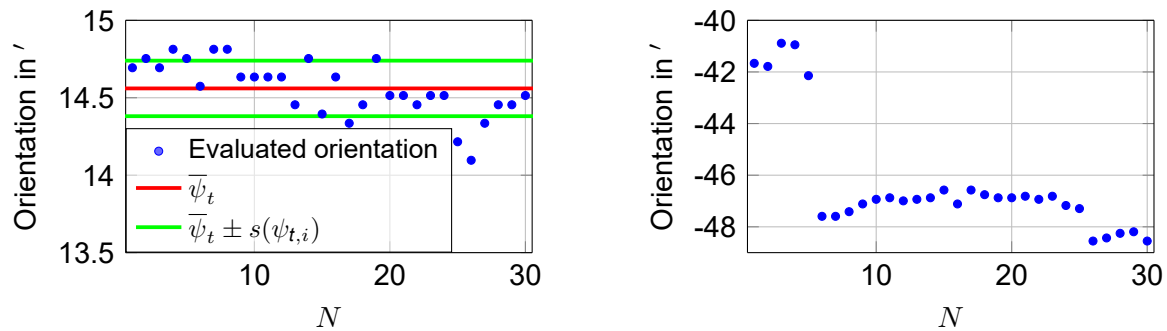
It is clear that both calibration methods are supposed to agree. This can also be seen as an indication of high measurement accuracy. Two measurements of orientation  $\psi_{circ}$  of the v-block with 19 measurements along each edge in distances of  $\approx 2.5$  mm (38 measurements per v-block) yield an orientation of  $-0.71'$  and  $-3.26'$ , respectively. This value is corrected with  $13.35'$  – the averaged deviation between the topographies' individual edges and the edges measured with the x-y stage. The results differ from the arithmetic mean from the calibration shaft by  $1.32'$  and  $1.52'$ , respectively.

In another series the v-block is rotated manually four times in an overall range of  $1^{\circ}52.73'$  (similar to fig. 3.15b). The calibration shaft is measured twelve times around its circumference and each edge six times. This results in differences of up to  $3.5'$  between the methods with neither of the two methods estimating the set rotation correctly.

### Landmark grating

The landmark is attached to the v-block and adjusted perpendicular to the instrument's optical axis with the help of its three-point bearing. The set-up is tested for repeatability in one and multiple spots on the grating and for the quality of reattaching the table. Measurement repeatability in one spot of the grating is high. The experimental standard deviation of 50 measurements is only  $0.07'$ . 30 measurements are taken at different spots on the grating and result in an experimental standard deviation of  $0.18'$  (see fig. 3.28a). The value indicates the high quality of the grating. However, it becomes clear that a single measurement on the grating is not sufficient. Rather, several measurements have to be averaged. The exact number depends on the desired uncertainty of the mean.

A repeatable attaching and detaching is important for the application. Only a high repeatability allows the user to apply the stored information. A series of 30 measurements is conducted with the table being detached and reattached to the bracket on the v-block via the magnet and the three-point bearing. The results are plotted in fig. 3.28b. The plot shows that the repeatability of reattaching is not sufficient for the application. The experimental standard deviation is as high as  $2.28'$ . An unknown event occurred after measurement five and before measurement 26. Between these events the standard deviation is only  $0.29'$ .



(a) Plot of 30 measurements at different positions on the landmark grating

(b) Plot of 30 measurements detaching and reattaching the landmark

Figure 3.28: Measurements at the landmark

### 3.2.4 Discussion

The discussion is separated into parts covering individual topics for better overview.

**Calibration on the v-block's geometry** Calibration on the v-block's geometry shows variabilities that are larger than desired. An example is the high experimental standard deviation of orientations at different positions on the edge. Each of the five estimates with 26 measurements each is supposed to produce a stable result. A minute variation in orientation during the test is of course possible but unlikely because the flat external edge and the side locating surfaces were in close contact at all times. Measuring only a part of the edge in an alternative attempt runs into the problem of straightness deviations of the x-y stage's guides, although this might be tackled with a high-quality positioning stage. A serious issue leading to a very high variability is the orientation deviation between the positioning axes and the measuring instrument/topography edges. This deviation cannot be estimated precisely. A dedicated procedure on the basis of a high quality edge on a glass or silicon substrate could be a remedy. It is also possible to combine the two calibration methods: the calibration shaft is measured in the v-block and the deviation between the edges and the shaft is the desired value. Still, a combination of both methods provides no advantage over the calibration shaft method alone.

Another problem in the detection of the edge could arise with v-blocks with two opposite cuttings because they are designed in a way that the upper side of one orientation is the base side of the respective other orientation. Taking measurements of the edges the base can become affected by scratches.

**Calibration with a calibration shaft** Using the calibration shaft results in an identical set-up for calibration and workpiece measurements. Its variability was found to be almost in the range of table 3.5 in section 3.1.4. An advantage is that it can also be

used with a limited x-y positioning range. A disadvantage is the necessity of rotating the calibration shaft for each measurement. Doing so carefully can avoid damage to the shaft.

As in the case of the rotating measuring system, shafts with other textures might be applicable as well.

**Comparing both calibration methods** Even though 38 measurements per v-block are a lot the resulting experimental standard deviation of the mean of edge orientations within the topographies of one block is  $\approx 0.8'$ .

Of course, the calibration shaft method is affected by variations, too. The deviation between the methods could just be statistical variations. Yet, the reason why neither of the two methods could resolve the rotated orientations correctly is not known. Further tests on this matter appear indicated. All other tests conducted in this work regarded smaller angular ranges, where the calibration shaft method performed well (e.g. fig. 3.16).

Looking at the observed variability and previous results from section 3.1.4 and because it calibrates circumferential direction directly the calibration shaft method is preferred.

**Landmark grating** Calibration with either of the above methods requires a considerable effort. The idea to use the landmark to facilitate this procedure failed due to its insufficient performance. But despite the low repeatability of reattaching, the grating in its current shape can still be used to calibrate orientation in a different set-up, e.g. mounted and locked to a base plate.

Finally, it is clear that the presented set-up is only applicable to short workpieces that fit into the v-block. While the principle stays the same longer shafts require a larger lateral positioning range. A possible solution can be a multi-sensor CMM. The idea of a mobile measuring system for longer or thicker shafts is taken up in section 3.3.

### 3.2.5 Summary

This section introduced a simpler alternative to the rotating measuring system above. Two methods to calibrate the shaft were examined. The method using a grooved calibration shaft that is incrementally rotated around the circumference has some advantages and is – in its current implementation and with the current set-up – more stable. A microscopic grating was selected that can facilitate the calibration procedure. While its properties are well suited for this task the way it is attached to the v-block is not satisfactory because of its high variability. A different design would be required if this idea was pursued.



## 3.3 Mobile measuring system

The procedure from section 3.2 and [5] requires high accuracy v-blocks that are standardised in DIN 2274 [38] up to shaft diameters of about 104 mm for v-blocks with one cutting. For v-blocks with two cuttings the available shaft diameters range only up to about 54 mm. Custom-made v-blocks are required to measure larger diameters. Measuring the shaft on a rotary table is limited by the load carrying capacity of the bearing and mounting options. Additionally, with growing diameter and length shafts become increasingly difficult to handle. Extraordinary diligence must be taken placing them either on a rotary table or in a v-block without causing damage to either the system or the delicate shaft surface. Instead of transporting the shaft to the measuring system the solution for large shafts can lie in a mobile measuring system that is placed on the horizontally positioned shaft.

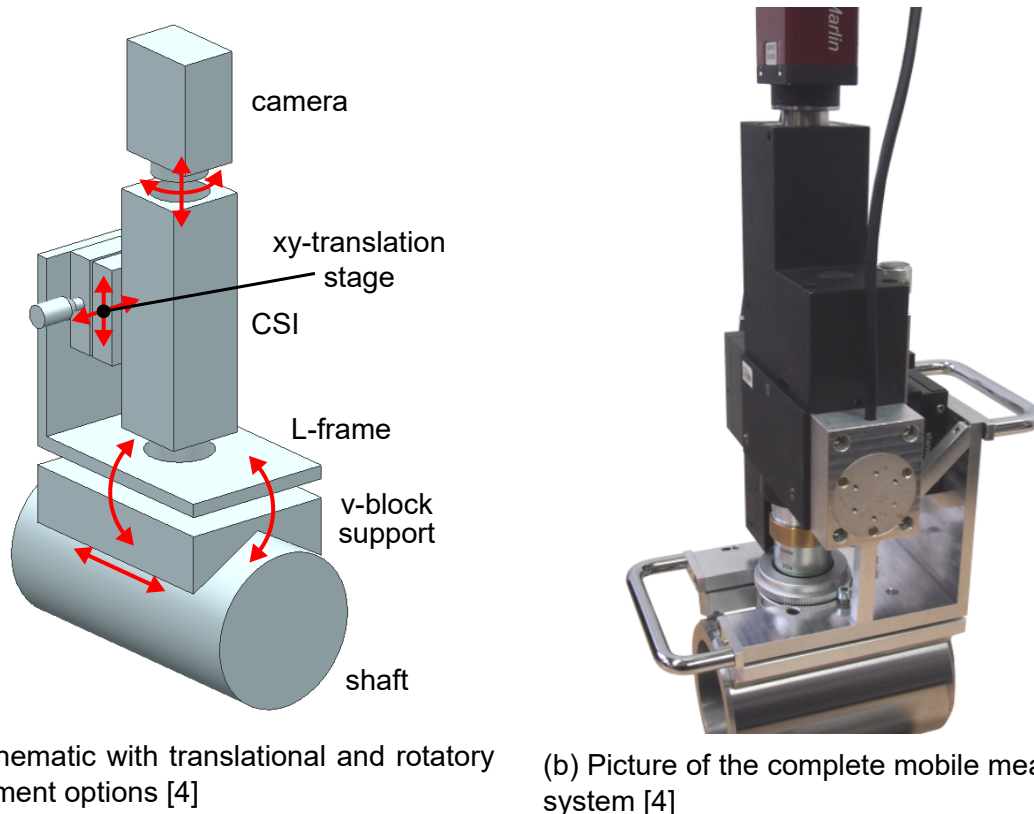
In this section a prototype of a mobile measuring system is described. Its modular structure consists of an areal-topographic measuring instrument mounted onto a v-shaped support. The system is self-centring on the shaft. A calibration strategy using a calibration shaft's circumferential groove – comparable to section 3.1.3 – is employed to assess shaft orientation.

First, a prototype of the mobile measuring system is presented and followed by the calibration procedure, an uncertainty study, and a discussion. The topic was already presented in a condensed form in [4] but is extended here.

### 3.3.1 Practical set-up

The goal of the measuring system is to provide areal-topographic measurements in close proximity to production, possibly even with the shaft still mounted inside the machine tool. Its desirable properties are a high mobility and accurate self-centring without the need for prolonged adjustments. To produce valid results a high measurement repeatability between calibration cycles is mandatory. A high measurement reproducibility would be an asset as it increases the time between calibration cycles. A deviation in shaft axis orientation results directly in an incorrect micro lead angle. Only by guaranteeing a low measurement uncertainty of both calibration and texture measurements the results are of any use for quality control purposes.

An overview of the system is given in fig. 3.29, where fig. 3.29a shows a schematic. An picture of the system is displayed in fig. 3.29b and its parts will now be described. In this prototype a CSI is used as areal-topographic measuring instrument. It originates from a multi-sensor CMM and so its external dimensions are adapted to limited space. The instrument is configured as Mirau interferometer, a type that incorporates the reference path (consisting of semi-reflecting mirror and reference mirror) into the



(a) Schematic with translational and rotatory adjustment options [4]

(b) Picture of the complete mobile measuring system [4]

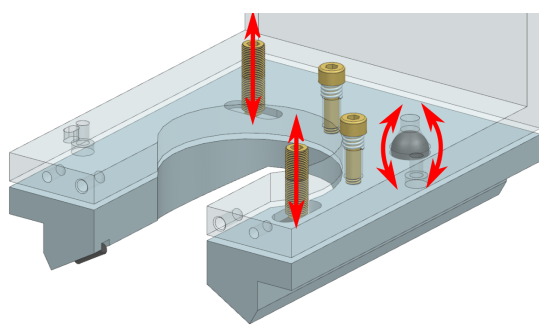
Figure 3.29: Schematic and prototype of the mobile measuring system

objective. The advantage of this type of configuration is its compactness and little or no need for adjustment [85, p. 146]. The device is mainly used with a  $20\times/0.4$  objective. With the 8 bit gray scale camera with its  $640 \text{ pixel} \times 480 \text{ pixel}$  the lateral field of view is  $530 \mu\text{m} \times 400 \mu\text{m}$  with sampling distance of  $0.83 \mu\text{m} \times 0.83 \mu\text{m}$ . The optical resolution was found with the Rayleigh criterion as  $0.8 \mu\text{m}$  on page 22. The piezo drive for the z-scan has a range of  $100 \mu\text{m}$ . The step size is set to  $10 \text{ nm}$  or  $50 \text{ nm}$ . The image stack of each measurement is evaluated by detecting the maximum of the envelope according to Seewig et al. [126].

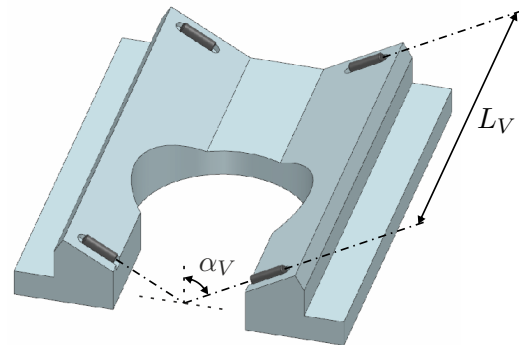
As it is the case with any areal-topographic measurements, it is highly desirable to have the surface aligned perpendicular to the optical axis, i.e. only minimal tilt of the surface is present. One reason for this is that after removing the topography's form by subtracting a fitted form element such as a cylinder lateral sampling steps are not equidistant any more. Also signal to noise ratio (expressed in modulation depth in CSI measurements) decreases as less light is reflected back into the objective with increasing tilt to the optical axis [58, 107, p. 98]. Various other effects and optical artefacts can occur during CSI measurements (see e.g. [58, 56, 107] for details). The desired minimal-tilt alignment is adjustable by separating the v-block support from the L-frame holding the instrument. The two parts are pulled together by tension springs. A three-point bearing allows for adjusting the upper frame in axial and tangential direction while preventing

relative rotational movement (see fig. 3.30a). Fine threaded adjustment screws with ball ends push onto a plate and a groove formed by two cylindrical bearing rollers and rotate the frame around a ball.

The vital part is the v-block support displayed in fig. 3.30b. Its axial length  $L_V = 100$  mm



(a) Three-point bearing between L-frame (transparent) and v-block support for adjusting axial and tangential tilt [4]



(b) V-block support with four cylindrical bearing rollers [4]

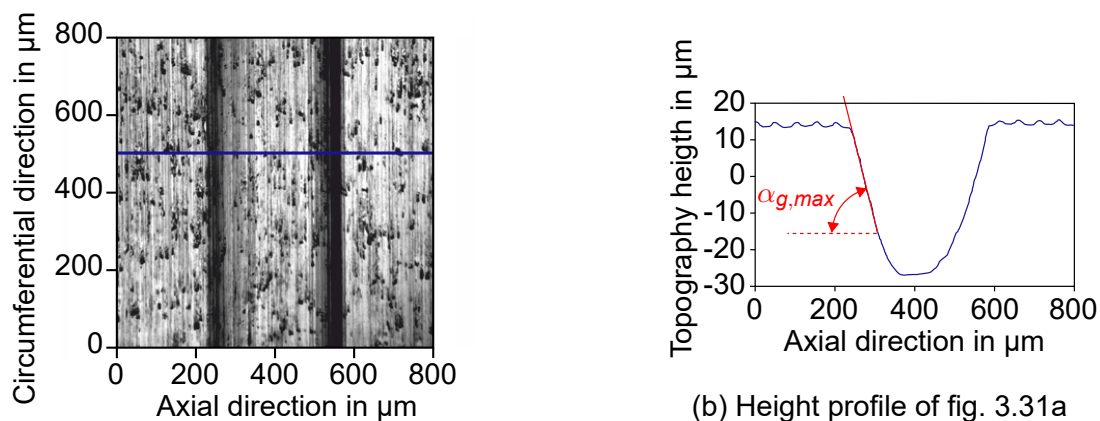
Figure 3.30: L-frame and v-block support

is measured between the cylindrical bearing rollers forming well-defined and reproducible contact points with low surfaces roughness values. The v-block opening angle  $2 \cdot \alpha_V = 120^\circ$  allows for measurements of large shafts. This non-standard opening angle is chosen deliberately as it allows scaling to large shafts without excessive increase in the system's overall size. The downside is a higher sensitivity of topography orientation to local radius variations under the contact points. With this setting the prototype can be used on shafts within a diameter range from 80 to 100 mm.

An important feature is translational alignment in tangential and radial direction. The options for adjustment are highlighted in fig. 3.29a. A precision x-y stage connects L-frame and measuring instrument and makes both adjustments possible. The piezo drive of the measuring instrument is used to fine-adjust radial distance and it governs the stepping motion to record an image stack of the surface. Axial translation is available by simply moving the device on the shaft and does not need to be accounted for by the design. An additional rotation of the field of view by rotating the camera can be used to adjust the camera to circumferential direction. In order to use different types of objectives with different magnification factors, the camera height above the instrument can be changed. It brings the region of maximal modulation depth (the peak of the envelope) into the focal plane. Relating the possible translational and rotatory adjustments to a measured topography all six degrees of freedom are accounted for.

### 3.3.2 Calibration

The shaft's axis is generally not known. Prior to taking meaningful measurements with respect to circumferential direction it has to be calibrated in a calibration procedure. A dedicated turned shaft with a circumferential cut-in with round groove bottom is used as calibration shaft. The shaft has a diameter of 80 mm and is made of well-machinable stainless steel. Its surface is turned to maximum height of the profile  $Rz = 1.9 \mu\text{m}$  and mean spacing of profile elements  $Rsm = 47 \mu\text{m}$  [50, 51]. The surface finish and the groove are manufactured without reclamping. The groove has a width  $b_g \approx 350 \mu\text{m}$  and a depth  $t_g \approx 40 \mu\text{m}$  (cf. fig. 3.11). The largest angle occurring at the edge of the groove  $\alpha_{g,max}$  is  $\approx \pm 30^\circ$  (without considering the surface gradient by short wavelength roughness). A microscopy image of the groove and an axial section through the topography are displayed in fig. 3.31. The microscopy image reveals dark spots on the



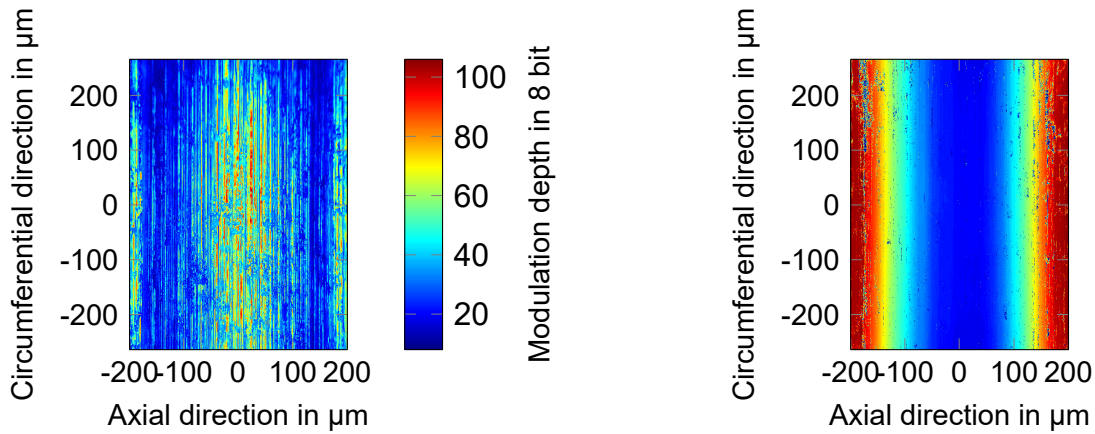
(a) Microscopic image of circumferential groove on the calibration shaft

(b) Height profile of fig. 3.31a

Figure 3.31: Microscopic image and height profile of calibration groove

surface which most likely originate from included material structures. The large number of peaks occurring in the measured topography, and especially on the groove bottom, are most likely caused by effects relating to low reflectivity at these included structures. For CSI instruments low reflectivity results in a low signal to noise ratio translating to low data quality. Looking at the modulation depth of a representative groove measurement in fig. 3.32a confirms a varying signal to noise ratio throughout the groove bottom. The poor ratio at the walls is also visible. The corresponding topography in fig. 3.32b was processed by setting excessive outliers to NMPs. Apart from the low signal to noise ratio other effects offering an explanation for the high number of peaks can be a differing phase change of reflected light in dark pitches and surrounding matrix that can lead to an assumed height difference. However, as phase variations are usually less than  $45^\circ$  [107, p. 105] this effect is unlikely to be visible on the rough surface<sup>9</sup>. Assuming that

<sup>9</sup>With the maximum of the wavelength spectrum at  $525 \mu\text{m}$   $45^\circ$  equals a height difference of  $\approx 0.066 \mu\text{m}$ .



(a) Modulation depth of a groove measurement with the CSI

(b) Topography of groove measurement of fig. 3.32a (colours represent height)

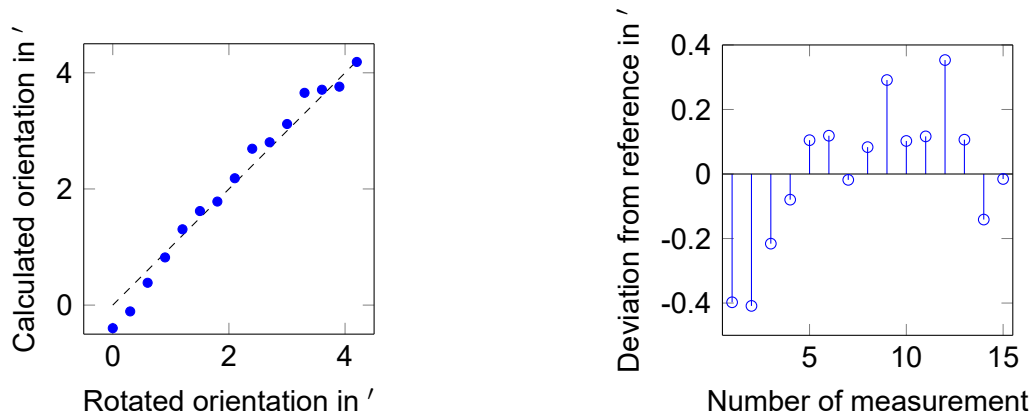
Figure 3.32: CSI measurement's modulation depth and corresponding topography of calibration groove [4]

the inclusions slightly protrude or are lower than the surrounding matrix batwings can occur as well [58].

The measurement procedure from section 3.1.3 has to be modified to account for the high number of peaks. This is done by replacing the excessive height values by NMPs, interpolating the NMPs according to section 4.1.1 and increasing the median filter mask to 9 pixel  $\times$  9 pixel which equals a size of 7.5  $\mu\text{m}$   $\times$  7.5  $\mu\text{m}$ . The goal is to remove all excessive height values that would otherwise hinder the evaluation scheme's work. Tests show that a further increase in the median filter mask does not alter the results further. In accordance with section 3.1.4 the evaluation method profile (i.e. fitting parabolas to each topography section) is applied. The grooves in this section are of significantly worse quality than those in section 3.2.2. For comparison some results obtained by the two other methods (areal and areal robust) are presented as well but only results of the profile method are used.

An important input parameter to the evaluation method is  $\alpha_g$ . The instrument's 20 $\times$ /0.4 objective has an acceptance angle  $\alpha_{NA} = 23.58^\circ$ . With eq. (3.6)  $\alpha_g$  is then  $12^\circ$ . The results of 15 measurements on the shaft rotated around a radial axis (cf. section 3.1.3 and fig. 3.15b) evaluated in this manner can be seen in fig. 3.33a. Figure 3.33b indicates that evaluation scheme and shaft are suited for the task even though values vary more than on other calibration shafts and as a result the resolution is lower. Each deviation from the reference orientation except one is smaller than 0.4'. Deviations include manually adjusting the rotation and uncertainties from the rotary unit itself.

Having obtained the groove orientation of individual circumferential measurements  $\psi_{circ,j}$  with  $j = (1, 2, \dots, M)$  the arithmetic mean  $\bar{\psi}_{circ}$  is calculated as an estimate of



(a) Rotation and ideal linear curve [4]

(b) Deviation from manually set orientation

Figure 3.33: 15 measurements of rotated calibration shaft (cf. section 3.1.3)

$\psi_{circ}$  according to eq. (3.11).

As indicated before, values vary slightly between the evaluation schemes. The results of 36 calibration measurements around the circumference with  $10^\circ$  increments are given in table 3.6<sup>10</sup>. The results for the two areal calibration methods are given for the sake of completeness but are not used any further.

Table 3.6: Results of 36 circumferential calibration measurements of groove orientation with the mobile measuring system

| Evaluation scheme | $\overline{\psi}_{circ}$ | $s(\psi_{circ,j})$ |
|-------------------|--------------------------|--------------------|
| Profile           | 5.66'                    | 2.09'              |
| Areal             | 5.67'                    | 2.11'              |
| Areal robust      | 5.83'                    | 2.49'              |

### 3.3.3 Uncertainty considerations

Applying a calibration measurement to calibrate texture orientation in production, the measurement uncertainty has to be known. In addition to the purely numerical value knowledge of the influencing factors and their respective contributions can aid the development of improved designs.

First, the measurement uncertainty of a single calibration measurement is assessed from experimental observations. Then, a study on the measurement uncertainty of a single calibration measurement reveals the predominant influence factor.

<sup>10</sup>Another series of 33 measurements on the same groove by a another operator and with different optical setup of the CSI evaluated with the identical evaluation scheme led to worse values for  $s(\psi_{circ})$ : 4.05', 4.35', and 4.19' for profile, areal, and areal robust, respectively. The reason for the modifications conducted at MTS was to improve the system's performance. The results cannot be compared directly.

The first question is, how well groove orientation can be estimated from a single measurement of the calibration shaft's groove. A step in the Type A evaluation of standard uncertainty  $u(\psi_{circ})$  according to the GUM [75, p. 10] is the experimental standard deviation  $s(\psi_{circ,j})$  of the measurement results. Evaluating 36 measurements around the shaft with the profile method and an axial groove region with  $\alpha_g = 12^\circ$  the experimental standard deviation  $s(\psi_{circ,j})$  is calculated similar to eq. (3.13):

$$s(\psi_{circ,j}) = \sqrt{\frac{1}{M-1} \sum_{i=1}^M (\psi_{circ,j} - \bar{\psi}_{circ})^2} = 2.09' . \quad (3.16)$$

With absence of other factors influencing uncertainty the combined uncertainty  $u_c(\psi_{circ})$  then equals the standard uncertainty  $u_c(\psi_{circ}) = s(\psi_{circ,j})$ . Adjusting the value to the limited number of samples with a coverage factor  $k_p = 1.01$  [75, p. 78] (a standard uncertainty with a level of confidence of 68.27 % is considered) yields the expanded uncertainty  $U_{68.27}$  for single calibration measurements:

$$U_{68.27} = k_p \cdot u_c(\psi_{circ}) = 2.11' . \quad (3.17)$$

Estimation of shaft orientation is based not on a single measurement only but on several independent measurements at different positions of the groove around the circumference. The corresponding measure is the experimental standard deviation of the mean  $s(\bar{\psi}_{circ})$  (cf. eq. (3.12)). As before  $u_c(\bar{\psi}_{circ}) = u(\bar{\psi}_{circ}) = s(\bar{\psi}_{circ})$ . This value is multiplied by a factor representing the number of measurements and the level of confidence.  $s(\bar{\psi}_{circ})$  has 35 degrees of freedom  $\nu$  and a  $t$ -factor  $t_p(\nu) = 3.23$  at a confidence level of 99.73 % which equals a coverage factor  $k_p = 3$  for a normal distribution [75, p. 70]. The expanded uncertainty  $U_{99.73}$  of the shaft's circumferential direction is then [75, p. 72]:

$$U_{99.73} = t_p(\nu) \cdot s(\bar{\psi}_{circ}) = 3.23 \cdot \frac{s(\psi_{circ,j})}{\sqrt{36}} = 1.14' . \quad (3.18)$$

The circumferential direction can thus be estimated with an uncertainty of 1.14' at a level of confidence of 99.73 %<sup>11</sup>.

The factors that are thought to influence the single calibration measurements and their respective uncertainties will be examined in detail in the following paragraphs. The study is concerned with the uncertainty of a single calibration measurement and the result is compared to  $U_{68.27}$  from eq. (3.17). The quantities  $U_{68.27}$  from eq. (3.17) and  $U_{99.73}$  from eq. (3.18) must not be confused.

<sup>11</sup>See footnote 10: Equivalent evaluation to eq. (3.18) of  $s(\psi_{circ,i}) = 4.19'$  results in  $U_{99.73} = 2.29'$  at a confidence level of 99.73 %.

**Mathematical model** Among the many factors that can influence  $\psi_{circ}$  in a calibration measurement some are thought to contribute significantly to the overall uncertainty. These include roundness  $\Delta\psi_{round}$  and form  $\Delta\psi_{form}$  deviations of the calibration shaft, effects from contact surface roughness  $\Delta\psi_{contact}$ , and influences of the evaluation procedure  $\Delta\psi_{eval}$ . Displacements and rotations caused by thermic effects are disregarded. It is assumed that the set-up expands symmetrically and therefore the resulting rotation is negligible. Measurements should generally only be taken after a running in time, when a stationary temperature distribution of set-up and shaft is reached.

The simple model of the set-up for a single measured circumferential orientation  $\psi_{circ,j}$  can be

$$\psi_{circ,j} = \psi_{circ,j,ideal} + \Delta\psi_{circ,j} . \quad (3.19)$$

$\psi_{circ,j,ideal}$  represents an ideal measurement result without any deviations. The additive relation of the influences is

$$\Delta\psi_{circ,j} = \Delta\psi_{round} + \Delta\psi_{form} + \Delta\psi_{contact} + \Delta\psi_{eval} . \quad (3.20)$$

Correlations are not regarded in this simple model. The expected values of the deviations are all assumed to be zero but they still contribute to the combined uncertainty  $u_{c,theo}(\psi_{circ})$  of a single measurement<sup>12</sup>.

The variances and the yet unknown sensitivities are:

$$u_{c,theo}^2(\psi_{circ}) = c_{round}^2 \cdot u^2(\Delta\psi_{round}) + c_{form}^2 \cdot u^2(\Delta\psi_{form}) + c_{contact}^2 \cdot u^2(\Delta\psi_{contact}) + c_{eval}^2 \cdot u^2(\Delta\psi_{eval}) . \quad (3.21)$$

As stated  $\psi_{circ,j,ideal}$  has no deviations and therefore does not add to  $u_{c,theo}(\psi_{circ})$ . Now, appropriate formulations and values for the uncertainty contributions have to be found.

**Form and roundness deviations of the calibration shaft** Form and roundness deviations can influence the measured orientation  $\hat{\psi}_{ax,ideal}$  (denoted  $\hat{\psi}_{ax}$  for shorter writing) by displacing the measuring system on the shaft to the true axis orientation  $\psi_{ax}$ . The possible situations are displayed in fig. 3.34.

A **roundness deviation** displaces a single contact point between system and shaft in radial direction and rotates the system by

$$\Delta\psi_{round}(\Delta r_c) = \arcsin \frac{\Delta r_c}{2 \cdot L_V \cdot \cos \alpha_V} , \quad (3.22)$$

with  $\Delta r_c$  being a local variation of calibration shaft radius due to roundness deviations.  $L_V$  is the distance between the contact points, and  $\alpha_V$  the half opening angle of the

<sup>12</sup>The subscript *theo* indicates quantities from the uncertainty study in contrast to the experimental values in eqs. (3.16) to (3.18).



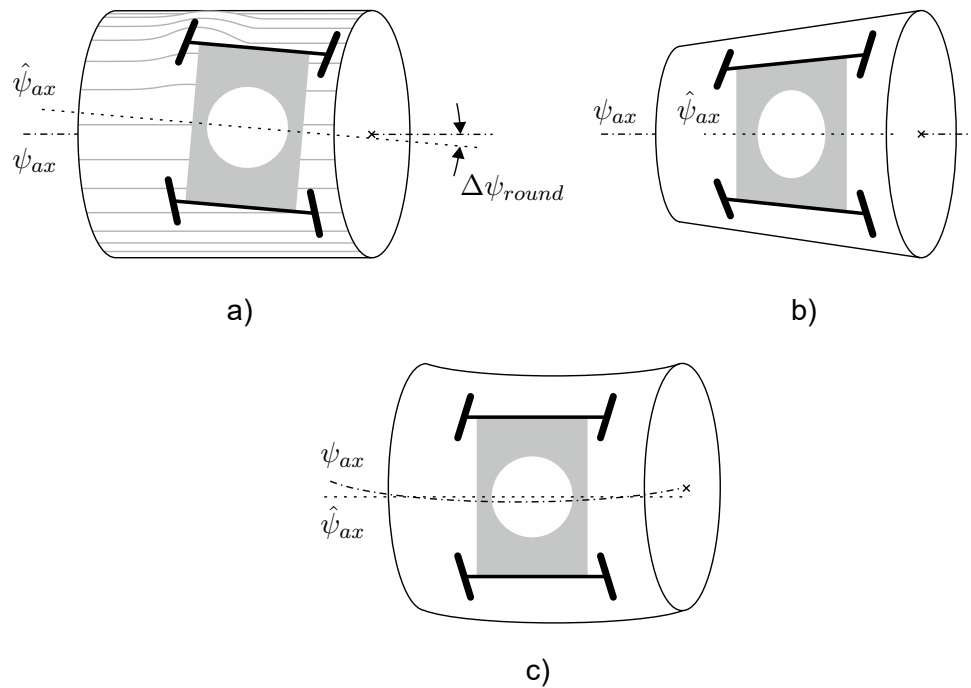


Figure 3.34: Form and roundness deviations and their effects on measured axis orientation; a: roundness deviation; b: cylindricity deviation; c: coaxiality deviation

v-block support. The sensitivity coefficient  $c_{round}$  as a function of  $\Delta r_c$  is then

$$c_{round} = \frac{d\psi_{circ,j}}{d\Delta r_c} = \frac{\frac{1}{2 \cdot L_V \cdot \cos \alpha_V}}{\sqrt{1 - \left(\frac{\Delta r_c}{2 \cdot L_V \cdot \cos \alpha_V}\right)^2}} \quad (3.23)$$

With the assumption of  $\Delta r_c = 0$  this equation simplifies to

$$c_{round} = \frac{1}{2 \cdot L_V \cdot \cos \alpha_V} = \frac{1}{2 \cdot 100 \text{ mm} \cdot \cos 60^\circ} = 0.01 \text{ mm}^{-1} \quad (3.24)$$

To establish an uncertainty budget with realistic values the calibration shaft was measured on a Mahr MMQ 200 form measuring instrument. Five measurements at approx. the contact positions yielded a maximal roundness deviation of  $\approx 1.71 \mu\text{m}$ . A maximal deviation of four times  $\Delta\psi_{round}$  could occur if all four contact points were displaced crosswise with the same sign. The maximal angular displacement is therefore assumed to be  $\Delta\psi_{round,max} = 4 \cdot 1.71 \mu\text{m} = 6.83 \mu\text{m}$ . The displacement can occur in any direction depending on the sign of the local roundness deviation. As most angular displacements will likely be smaller, a normal distribution having a level of confidence of 99 % at  $\Delta\psi_{round,max}$  is assumed. The standard deviation  $u(\Delta\psi_{round})$  is then [75, p. 70]

$$u(\Delta\psi_{round}) = \frac{6.83 \mu\text{m}}{2.58} = 2.65 \mu\text{m} \quad (3.25)$$

The maximal **form deviation** of the calibration shaft in terms of cylindricity was 20  $\mu\text{m}$

on an axial length of 110 mm. To good approximation, the shaft diameter changes linearly, i.e. the shaft has a slightly conical form. A measurement of conicity confirms a deviation of almost 9  $\mu\text{m}$  on an axial measuring length of 108 mm. A likely cause might be a parallelism deviation in the axial feed of the grinding machine. However, such form deviation has no influence on the measured groove orientation because the measuring instrument is adjusted with the optical axis normal to the shaft surface (see fig. 3.34 b). Another deviation from cylinder shape is coaxiality in fig. 3.34 c. It can well result in a deviation of measured groove orientation. In the case of the calibration shaft ten circumferential measurements were made along 100 mm in axial direction. Coaxiality deviations ranged from 0.2  $\mu\text{m}$  to 0.7  $\mu\text{m}$  and apparently did not follow a recognisable shape. Therefore, and because the roundness measurements at the contact position showed a variability of circle centres of the same order of magnitude, the coaxiality deviation is neglected. So the uncertainty from form deviations is

$$u(\Delta\psi_{form}) = 0 . \quad (3.26)$$

**Effects of positioning and contacting** The quality and effects of positioning and re-positioning on the detected groove orientation and the resulting uncertainty are gauged with the help of reference measurements of the turned shaft surface and the evaluation procedure for texture orientation from section 4.2 and [6]. The reference measurements are taken with the rotating measuring system from section 3.1.1 with the confocal microscope and its 20 $\times$ /0.45 objective. Prior to measuring, eccentricity and tilt were adjusted to levels beyond recognition in the evaluated data. 36 confocal reference measurements with its larger field of view yield a standard deviation of 0.36'. A standard deviation of 1.2' is obtained from 34 measurements around the circumference with the mobile CSI sensor. It is known that the variance of the orientation estimation depends on the topography size (see section 4.3.2). The different topography sizes will be adjusted by a correction factor which is calculated as the quotient from the standard deviations of CSI and confocal microscope measurements. As differing lateral resolutions make a direct comparison impossible the correction factor is assessed by simulation. Of both sizes 20 topographies each are simulated and evaluated. The turned surface model consists of two superposed sinusoids with a moderate amount of phase noise perpendicular to propagation direction and a superposed white Gaussian noise. These topographies were then filtered with an areal Gaussian low pass filter with nesting index 16  $\mu\text{m}$ . The modelled topographies visually matched their measured counterparts. From this data the correction factor is found to be  $\approx 2.1$ . The corrected standard deviation of the comparative measurements with a similar topography size is then  $2.1 \cdot 0.36' = 0.76'$ . The interpretation is that a standard deviation of 0.76' can be expected from non-contact measurements around the circumference with the CSI

of the mobile sensor. The difference between contacting and non-contacting standard deviations is seen as the uncertainty of positioning and contacting effects:

$$u(\Delta\psi_{contact}) = 1.2' - 0.76' = 0.44' . \quad (3.27)$$

**Influences of the evaluation procedure** A Monte Carlo simulation [124, pp. 31 sqq.] helps to estimate the evaluation algorithm's uncertainty on the calibration shaft's groove. A large number of topographies containing a simulated groove with several variations is evaluated with the evaluation procedure from section 3.3.2. The variations emulate characteristics found on 34 CSI-measured topographies. Topographies preprocessed by 9 pixel  $\times$  9 pixel median filtering followed by areal Gaussian filtering with 8  $\mu$ m nesting index are taken as input. Each characteristic is modelled individually by a set of parameters. All characteristics are assumed to be additional, i.e. their sum adds up to the measured topography. The characteristics composing a measured topography are identified as cylinder form, calibration groove, deviation from ideal groove shape, small turning grooves, and noise. The parameter values governing these characteristics are taken from a range of values described by individual distributions. For simplicity the distributions are not identified by statistical tests but are rather assigned based on their visual appearance and experience. The composition of the model and the parameters can be found in appendix B and their numerical values in table B.1.

1000 topographies were simulated according to appendix B. In the Monte Carlo simulation step these 1000 topographies are evaluated by the profile method with  $\alpha_g = 12^\circ$  (the same setting as in eq. (3.16)). The results are 1000 estimated orientations of the groove (see fig. 3.35) with mean  $-1.15'$  and standard deviation  $2.00'$ . For comparison the results from the methods areal and areal robust from section 3.1.3 are listed in table 3.7. The uncertainty of the selected evaluation scheme on these topographies is then

$$u(\Delta\psi_{eval}) = 2.00' . \quad (3.28)$$

It is important to mention that on other grooves and calibration shafts the specialised

Table 3.7: Results from Monte Carlo simulation of 1000 calibration topographies

| Evaluation scheme | $\bar{\psi}_{circ}$ | $s(\psi_{circ,j})$ |
|-------------------|---------------------|--------------------|
| Profile           | $-1.15'$            | $2.00'$            |
| Areal             | $-1.13'$            | $2.04'$            |
| Areal robust      | $-1.09'$            | $1.89'$            |

model parameter values of table B.1 will not be appropriate any more and the evaluation scheme will behave very differently.

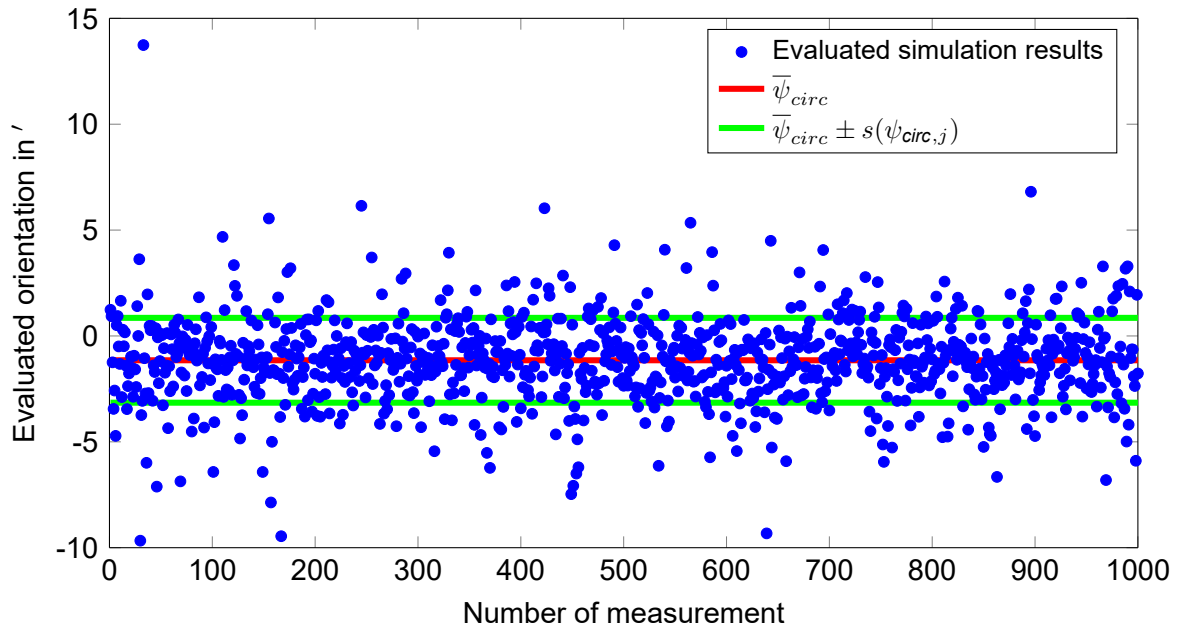


Figure 3.35: Evaluated orientations from the Monte Carlo simulation with evaluation method profile

**The whole picture** Values for the quantities in eq. (3.21) are found in eqs. (3.23) and (3.25) to (3.28). Still unknown are the sensitivity coefficients  $c_{form}$ ,  $c_{contact}$ , and  $c_{eval}$ . They are calculated as

$$\begin{aligned}
 c_{form} &= \frac{d\psi_{circ,j}}{d\Delta\psi_{form}} = 1, \\
 c_{contact} &= \frac{d\psi_{circ,j}}{d\Delta\psi_{contact}} = 1, \\
 c_{eval} &= \frac{d\psi_{circ,j}}{d\Delta\psi_{eval}} = 1.
 \end{aligned} \tag{3.29}$$

With these values eq. (3.21) evaluates to

$$\begin{aligned}
 u_{c,theo}^2(\psi_{circ}) &= c_{round}^2 \cdot u^2(\Delta\psi_{round}) + u^2(\Delta\psi_{form}) \\
 &\quad + u^2(\Delta\psi_{contact}) + u^2(\Delta\psi_{eval}) \\
 &= 0.09'^2 + 0'^2 + 0.44'^2 + 2.00'^2 \\
 &= 4.20'.
 \end{aligned} \tag{3.30}$$

The combined uncertainty of a single groove measurement  $u_{c,theo}(\psi_{circ})$  is estimated as 2.05'. Making this value comparable to the expanded uncertainty from eq. (3.17) requires calculating the expanded uncertainty  $U_{68.27,theo}$  at a level of confidence of 68.27%. The estimated  $u_{theo}(\psi_{circ})$  is a combination of four factors each contributing individual degrees of freedom  $\nu$ :

- $u(\psi_{round})$  is assumed to be reliable to 10% which can be transformed to

$$\nu_{round} = 50 \text{ [75, p. 74].}$$

- $\nu_{form} = 0$  because form influences are disregarded.
- A reliability of 10 % accounts for a possible uncertainty of the correction factor for topography sizes obtained by simulation and therefore  $\nu_{contact} = 50$ .
- The evaluation procedure's uncertainty is governed by the limited number of topography samples used to set up the model and so  $\nu_{eval} = 33$ . It is not 35 because the measurements from footnote 10 were used plus one additional sample.

Calculating effective degrees of freedom  $\nu_{eff}$  according to the Welch-Satterthwaite formula allows approximating the distribution of  $u_{c,theo}$  by a  $t$ -distribution [75, p. 73]:

$$\nu_{eff} = \frac{u_{c,theo}^4}{\sum_{i=1}^4 \frac{u_i^4}{\nu_i}} = \frac{2.05'^4}{\frac{0.09'^4}{50} + 0' + \frac{0.44'^4}{50} + \frac{2.00'^4}{33}} = 36.4 \quad (3.31)$$

The corresponding  $t$ -factor  $t_{68.27}(\nu_{eff})$  is 1.01 [75, p. 78] and therefore

$$U_{68.27,theo} = 2.07' . \quad (3.32)$$

This reveals a difference of roughly 2 % from the expanded uncertainty derived from the experimental standard deviation in eq. (3.17). It indicates that the considered quantities are estimated very accurately and that the model assumptions are correct. Care was taken not to underestimate the uncertainty of the evaluation procedure. The theoretical value from eq. (3.28) is rather an overestimation.

It is clear that the presented uncertainty estimation is not exhaustive. An exemplary shortcoming is apparent in the positioning and contacting paragraph: the uncertainty of the evaluation procedure for texture orientation is not regarded. Additionally, an uncertainty should be added to deal with model deficiencies of the simulated turned surfaces. Looking at other possible contributions it could be beneficial to include thermal effects as well. Neither has the uncertainty of the areal-topographic measuring instrument itself been taken into account and the groove surface models were based on measurements with a suboptimal optical set-up (cf. footnote 10). However, the goal of the study was to regard only major contributions and it was therefore purposely kept simple.

Despite legitimate criticism the study reveals that the evaluation procedure contributes by far the most to  $u_{c,theo}(\psi_{circ})$  and thus to  $U_{68.27}$  and  $U_{99.73}$ . A consecutive study might shed light on the remaining question about the small difference between theoretical and experimental results and address the uncertainty in more detail. But even with its inherent simplifications does it provide a valuable starting point to improve a successive design of the mobile sensor: the quality of the calibration groove. Efforts to improve the groove were made but not at a shaft diameter required for the mobile

sensor.<sup>13</sup> The study provides the encouraging result that the uncertainty from contacting and repositioning effects ranges within reasonable limits.

### 3.3.4 Discussion

It is clear that the system can fulfil the given task of measuring micro lead on large shafts. Its modular concept makes it scalable to accommodate larger shafts if required. Nevertheless, it is still a prototype and dimensions from section 3.3.1 can be seen as examples. For serious application some modifications are possible:

- Increasing the lateral field of view increases lateral sampling distances but can also lead to a lower uncertainty of estimating texture orientation. This is possible by changing the optical configuration.
- Considering mobility and handling requires taking wire length and wire handling into account. Wired components are piezo actuator, light source, and camera. Wiring was not in the focus of this prototype.
- Axial length of the system might be a limiting factor in some applications. Reducing it is an option but comes at the cost of an increased sensitivity to local radius variations influencing the uncertainty component  $u_{round} = c_{round} \cdot u(\Delta\psi_{round})$ . The effects of changing the axial length  $L_V$  can be estimated with the help of fig. 3.36. It displays the expected expanded uncertainty  $U_{99.73,round}$  as a function of  $L_V$  without considering other effects. The graph is based on the roundness uncertainty from eq. (3.30), varying only  $L_V$  in eq. (3.24) and assumes a competence level of 99.73 %. With a shorter  $L_V$  the adjusting screws should be changed

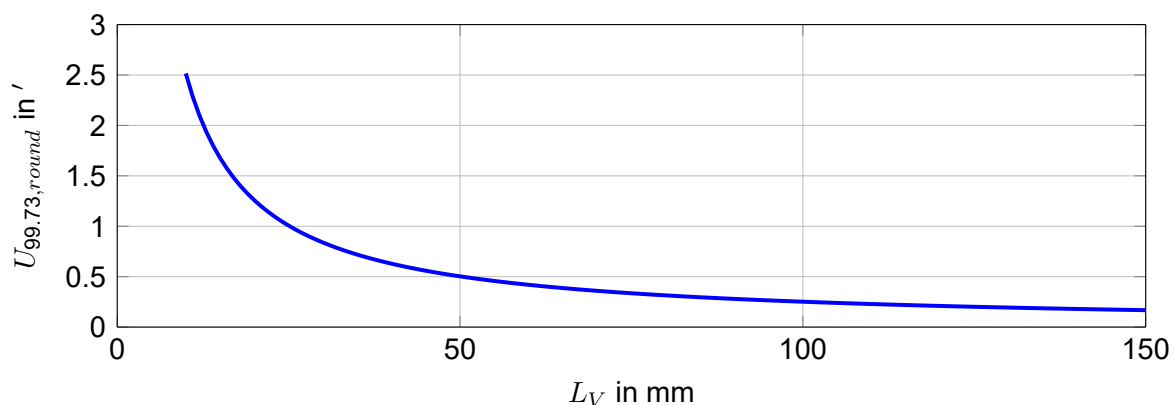


Figure 3.36: Expected roundness uncertainty from local shaft diameter variations for different axial lengths

to a thread pitch smaller than the current 0.5 mm.

<sup>13</sup>In the timeline of developments this system was studied prior the calibration shaft in section 3.1.3.

- Using special objectives with tiltable reference mirror can simplify the design. Care must be taken regarding the accessibility in the constricted space between shaft and v-block support.
- The system's uncertainty can be decreased by increasing groove quality. See section 3.1.3 for details. As an alternative to the circumferential groove the turned surface can be used for calibration directly. If the groove's angle was either measured as macro lead angle in a macro lead evaluation or known from the turning process, the orientation of several topographic measurements evaluated as in section 4.2.2 could reveal the circumferential direction.

### 3.3.5 Summary

The above considerations showed that the prototype of a mobile measuring system was suitable for the given task. It enabled measurements on large shafts with respect to the shaft's circumferential direction. The installed areal-topographic measuring instrument was able to capture a topography section that could be evaluated by the procedure described in section 4.2.2. Shaft orientation was assessed by a calibration procedure and the high reproducibility guarantees low uncertainty from repositioning. The calibration procedure was able to resolve orientation in the sub-arc minute range. Circumferential direction could be estimated with an uncertainty of  $1.14'$  at a coverage factor  $k_p = 3$ . A future concept could address the shortcomings (mainly calibration shaft quality) found in the uncertainty study and result in a mobile system with a significantly lower uncertainty.

## 3.4 Summary

After motivating the use of optical areal surface texture measurement methods three measuring systems were introduced. All of these systems incorporated an areal-topographic measuring instrument and were capable of assessing micro lead structures on ground shafts both in terms of texture orientation and calibration of circumferential direction.

The first system had the areal-topographic measuring instrument aligned horizontally while the shaft was mounted vertically on a rotary table. Rotating the shaft after adjusting eccentricity and tilt, measurements at multiple positions around its circumference could be taken. The calibration procedure used a dedicated calibration shaft with a circumferential groove. Measurement uncertainty of the calibration was found to be in the sub-arc minute range.

The second system used a commonly available areal-topographic measuring instrument set-up with the shaft positioned horizontally under the vertical optical axis. The

shaft was placed in a v-block and the rotation between shaft axis and instrument was calibrated either with the help of a calibration shaft or by measuring geometric structures of the v-block, which were known to maintain a fixed position to shaft axis. The first approach was found to be better suited and offered the advantage that lateral positioning could be kept to a minimum.

The third system was a mobile measuring system for large shafts. It consisted of a v-block support that was placed on the shaft and a CSI mounted on the support with various options for adjusting the alignment. A calibration shaft with a circumferential groove enabled calibration of shaft axis. An uncertainty study of the calibration procedure was conducted that indicated that the expected measurement uncertainty could be decreased by improving the quality of the calibration groove. It also revealed that other sources of uncertainty, e.g. repositioning on the shaft, had a small share in the overall uncertainty and did not oppose the application of the system.



## 4 Texture orientation

Micro lead is defined as a deviation of the main texture orientation of the ground micro texture from the shaft's circumferential direction. Its characterisation requires knowledge of both shaft axis orientation and texture direction. This chapter focusses on the second requirement and presents a method to detect texture orientation with sub-arc minute resolution.

The chapter starts with a motivation for a new procedure before detailing the preprocessing of measurement data. Explaining several Radon transform-based implementations and selecting one suited for high resolution applications paves the way for a practical and computational procedure. Several effects and peculiarities in the results regarding superposed structures, aperture effects, topography sizes, and scale limiting are examined. Finally, procedures and results are discussed and summarised.

### Why is a new method required?

The latest standard on areal surface texture parameters DIN EN ISO 25178-2 [45] defines the parameter surface texture direction  $Std$  to characterise the direction of surface texture on bandlimited topographies. Its calculation is based on the angular spectrum, i.e. the radial integration of the areal power spectral density obtained from the 2D Fourier transform of the measured surface [136, pp. 193,225 sq.]. It is designed to robustly and effectively evaluate texture direction on a wide variety of surfaces [136, pp. 224 sq.]. Its application is limited only by a required level of texture isotropy that is measured by the parameter texture aspect ratio  $Str$  [136, pp. 224 sq., 84, p. 37]. It is obvious to employ the parameter  $Std$  to characterise texture orientation of ground surfaces. A test where a shaft is rotated around a radial axis in 20 increments of  $16.91''$  each and measured after each rotation (c.f. section 3.1.4 and fig. 3.15b) offers information on the resolution of the parameter in its current implementation in a major software package. The results are plotted in fig. 4.1. The calculated orientation clearly does not resolve the rotation of the surface. It rather manifests the need for a dedicated evaluation method for these minute variations in texture orientation. Besides, the sign of  $Std$  defined in [136, p. 227] is inverted to the definition of the micro and macro lead angle in MBN 31007-7 [95].

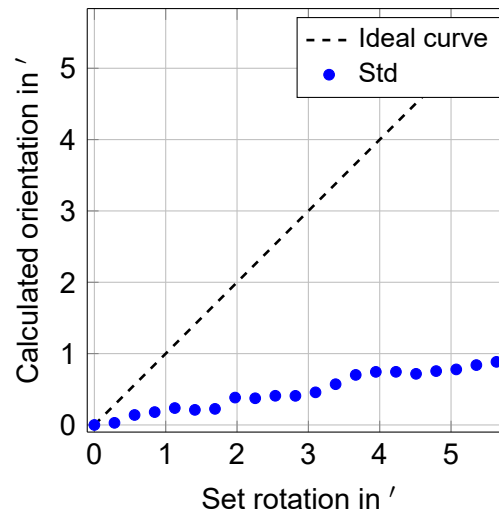


Figure 4.1: Resolved texture orientation with Std parameter in its current implementation (measured curve is adjusted to start at  $0'$ )

In addition to Std several other methods to assess the orientation or directional textures can be found in literature. The following overview is loosely ordered by publication date and by no means exhaustive.

- Beyerer estimated texture orientation of grooves in grayscale images of technical surfaces with the help of their Fourier transform. He integrated the power spectrum radially and interpolated the unknown values by bilinear interpolation with an angular sampling distance of  $0.5^\circ$  [17, pp. 57 sqq.]. Puente appeared to use the same procedure but averaged several images to gain a higher angular resolution [109].
- Lin et al. found the orientation in topographies of milled surfaces by *"tracing the shift of primary peaks using cross-correlation"* [89].
- Krahe and Beyerer [81, 20, 80] evaluated macro lead structures on grayscale images. They used an integral evaluation of the Radon transform to calculate orientation in the range of several degrees. A similar scheme with some modifications was employed by Xin [148, pp. 94 sq.]. For small angles in the arc minute range they correlated characteristics in the Radon domains of successive circumferential images.
- In an overview paper on skew detection in document images Hull discussed four methods: iteratively analysing projection profiles of the image, connecting image features and then analysing the projection profile, the Hough transform, and predefined morphological masks to detect structures matching these masks [69].

- Methods using morphological image processing were explained by Soille in [133, pp. 330 sq.]. They were based on volume measurements after morphological operations with directional structuring elements.
- Cohen et al. used a "*Fourier transform of the data to determine an angular power spectral density of the angle of the marks*" for micro lead evaluation [30]. They provided no further details except this very general description.
- Baitinger extracted and weighted individual grinding marks from topographic measurements and described texture orientation by parameters of the resulting distributions [8].

## 4.1 Preprocessing of measurement data

Areal-topographic measurement data requires preprocessing before it can be evaluated. This step aims first at accentuating relevant structures while suppressing noise and artefacts from the instrument and second it makes the results comparable among different measurement procedures and instruments.

Here, preprocessing is based on the standardised procedure from DIN EN ISO 25178-2 [45] to generate the S-F surface but expanded by several steps. First, non-measured points are interpolated and noise in the form of isolated spikes and holes is removed by a median filter. Based on the surface generated by this non-standardised steps the primary surface according to [45] is calculated by applying the S-filter. The F-operation then finalises preprocessing to the S-F surface. In case evaluation is based on the S-L surface the L-filter is applied to the S-F surface in a last step.

### 4.1.1 Handling non-measured points

Invalid data points can occur in any measurement and are quite common in optically measured topographies. These are often referred to as voids, NMPs, or non-measured points. They typically but not exclusively occur when the local surface slope is in the range of the acceptance angle  $\alpha_{NA}$  (cf. eq. (3.5)). This results in a poor signal to noise ratio at the corresponding pixel. The ratio might not exceed a predefined threshold and the height information at the specific pixel is regarded invalid.

A variety of methods to handle NMPs can be found in literature (e.g. [29, 114]). Their main purpose is to interpolate data from non-uniform grids, mostly in geo sciences. Petzing et al. [107, p. 94] advise caution on the interpolation scheme used on measurement data. He states that using linear interpolation statistical surface parameters will see more mid-height values thus leading to biased arithmetical mean height Sa

and root mean square height Sq parameter values. Therefore, data should be left unchanged and NMPs should only be interpolated when absolutely necessary. However, the algorithms presented in this work rely on a rectangular grid without occurring NMPs. For this work it is therefore advisable to interpolate NMPs.

Here, a simple linear implementation interpolates linearly between valid neighbouring pixels in  $x_t$  and  $y_t$  direction. The unknown pixel value is then the arithmetic mean between the calculated height values in the two directions. Prior to doing so, pixels at the topography borders are processed: in case the unknown value happens to occur in a corner, a square grows iteratively until several pixels lie within its range. The unknown corner pixel is then the arithmetic mean of these pixels. Pixels at the topography edges that are not corner pixels are assigned values linearly interpolated along the respective edge in one dimension.

The ratio of non-measured points to valid points of ground shaft surfaces measured by areal-topographic methods lies typically well below 1 %. Depending on the measurement principle and the instrument used the ratio can be zero in many cases. It is therefore not likely that the application of very advanced interpolation strategies will produce significantly varying results.

#### 4.1.2 Noise removal

A median filter removes unwanted isolated peaks and holes by ordering the height values within the filter mask and selecting the median of the ordered series as pixel value in question. It is a non-linear rank filter that requires an odd side length of the filter mask [133, p. 77]. Median filters keep steep topography edges better than common surface filters [84, p. 195] and they produce less blurring than linear smoothing filters of similar size [57, p. 156].

#### 4.1.3 S-filter

The S-filter's nesting index  $\lambda_s$  constitutes the short cut-off wavelength of lateral structures on the topography. At cut-off wavelength the corresponding amplitude is damped by 50 %. Several recommendations on how to choose a correct  $\lambda_s$  are available:

- $\lambda_s$  can be found by measurements on grating or resolution standards [143]. Such tests are not conducted here.
- VDI/VDE 2655 part 1.1 recommend  $\lambda_s$  as two to three times the value of the optical resolution due to diffraction determined by the Rayleigh-criterion [143, p. 14].
- In DIN EN ISO 25178-3 the nesting index can be selected from a series of values corresponding to the maximal lateral sampling distance [49, pp. 8 sq.]. The

coarsest lateral sampling distance of the instruments used in this work is  $1.5625\ \mu\text{m}$  (see section 3.1.1). The next larger maximal sampling distance in [49, p. 9] is  $2.5\ \mu\text{m}$  and  $\lambda_s$  then  $8\ \mu\text{m}$ .

Following the third recommendation  $\lambda_s = 8\ \mu\text{m}$  is selected.

According to DIN EN ISO 25178-3 the S-filter is an areal Gaussian filter [49, p. 8]. It is implemented according to E DIN EN ISO 16610-60 and -61 [42, 43] as linear planar filter working in the image domain. The scaled impulse response is first convolved in the one and then the other orthogonal direction parallel to topography edges. End effects are handled by mirroring because this processing is simple to implement even though better solutions exist [84, pp. 79 sq.].

#### 4.1.4 F-operation

An F-operation removes the form component from the topography measurement [45] which is in this case the underlying cylinder form.

A least-squares fitted second order areal polynomial is used as F-operation. It is an association operation and therefore the nesting index is the side length of the evaluation area [49, p. 6]. Lemke et al. state that form removal by the areal second order polynomial fit is suited for measurements on a cylinder running surface [87]. Still, they propose a more advanced scheme suited for the removal of possible residual cylinder form deviations. The benefit of the F-operation used here is its simple implementation but it deviates from DIN EN ISO 25178-3 which demands a total least squares procedure [49, p. 9].

#### 4.1.5 L-filter

An L-filter removes large scale components [45]. According to DIN EN ISO 25178-3 the L-filter's nesting index is five times the scale of the largest structure of interest [49, p. 6]. The nesting index is specified in the relevant section where it is applied. The filter is an areal Gaussian filter similar to the S-filter.

#### 4.1.6 Summary

The procedure to preprocess raw measurement data was detailed. It consisted of several steps which were an extension of the standardised bandlimiting steps from DIN EN ISO 25178-2 and -3 [45, 49]. After filling NMPs, isolated noise was removed by an areal median filter. Only now the bandlimits were applied to generate the S-F or S-L surface, depending on the application.

## 4.2 Radon transform-based method

After successful preprocessing, the topography still holds orientation information of the ground micro texture. One way of extracting it is by applying the Radon transform. This approach is detailed in the following section.

In general, the Radon transform can be used to estimate parameters of parametrised curves. The transform simply integrates values from the image domain along predefined curves and maps the result of the integration in the parameter or Radon domain. The dimension of the Radon domain naturally depends on the number of free parameters of the curve in question. By varying these parameters and integrating height values for many combinations the Radon domain fills with samples. After collecting an adequate number of samples the information about the parameters can be extracted from the Radon domain. The generation of the Radon domain is elaborated first, before a way to calculate the orientation is explained.

In the case of texture orientation of ground surfaces the curve in question is a straight line in the two dimensions  $x_t$  and  $y_t$ . A straight line in 2D can be represented by two parameters. Typically, these are slope and y intercept [74, p. 29]. Another possibility to define a line is in Hesse normal form [34, p. 57, 53, p. 292] in the  $(x_t, y_t)^T$  coordinate system from fig. 3.3. The parameters  $\rho$  and  $\phi$  stand for distance from origin and orientation normal to the line, respectively:

$$\rho = y_t \cdot \cos \phi - x_t \cdot \sin \phi . \quad (4.1)$$

Writing eq. (4.1) in parametric form with parameter  $t$  yields [34, p. 57]

$$\vec{x}_l(t) = \begin{pmatrix} x_t(t) \\ y_t(t) \end{pmatrix} = \begin{pmatrix} t \cdot \cos \phi - \rho \cdot \sin \phi \\ t \cdot \sin \phi + \rho \cdot \cos \phi \end{pmatrix} . \quad (4.2)$$

A possible line is plotted in fig. 4.2.

The Radon transform integrates the topography heights  $z_t$  along lines and each line integral is mapped into the Radon domain. The sifting property of the impulse function [103, p. 183] is used to select one line at a time. The Radon transform  $\check{g}(\rho, \phi)$  of the topography  $g(x_t, y_t)$  with the height values  $g(x_t, y_t) = z_t$  is then defined as [34, pp. 58 sq.]

$$\check{g}(\rho, \phi) = \int_{-\infty}^{\infty} g(x_t, y_t) \cdot \delta(\vec{x}_l(t)) \cdot dt . \quad (4.3)$$

Toft termed this form normal Radon transform because it is based on the normal equation of the straight line [140, p. 23]. Here, instead of calculating the Radon transform

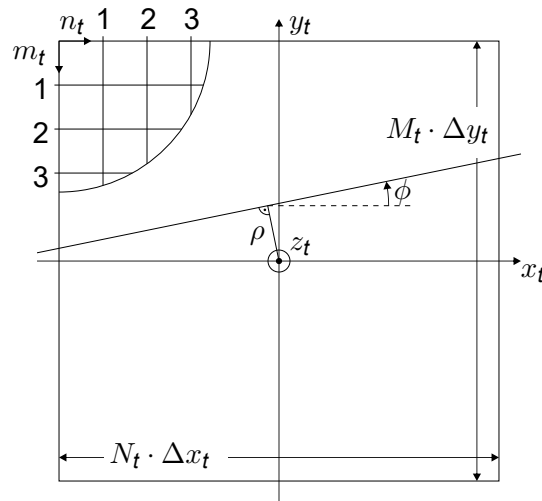


Figure 4.2: Coordinate system based on fig. 3.3 with an exemplary line

via the 2D Fourier transform<sup>1</sup>, Radon domain samples are found by evaluating the line integral.

In the case of sampled topographies (cf. fig. 4.2) the integrals turn into sums that run along the lines within finite limits. The Radon domain then consists of a finite number of sampled  $\rho$  and  $\phi$  values. Such a sampled Radon domain representation of a ground S-F surface is plotted in fig. 4.3.

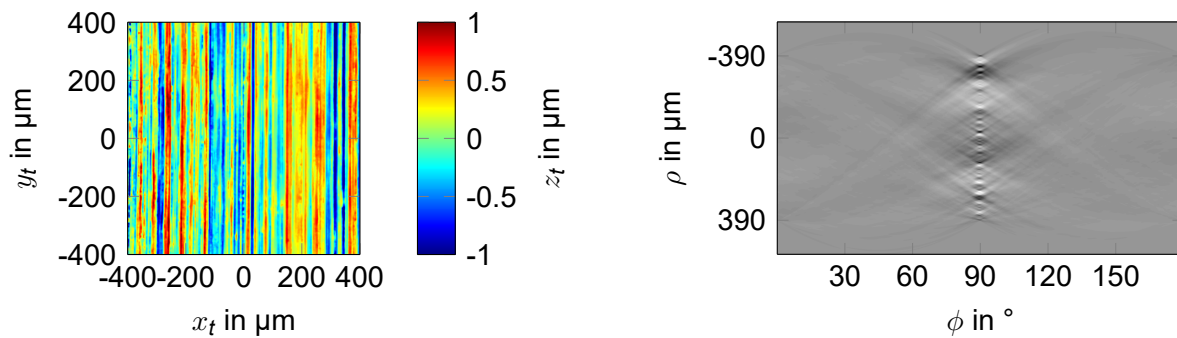
Applying eq. (4.1)  $y_t$  values are selected for each  $x_t$  and vice versa depending on the line's slope. The situation changes with the line's parametric definition in eq. (4.2). Instead of using predefined  $x_t$  or  $y_t$  values the parameter  $t$  chooses these values along the straight line. In most cases these  $(x_t, y_t)^T$  values will not be located at integer  $(m_t, n_t)^T$  positions requiring some kind of interpolation to find the corresponding height value. Several implementations of the Radon transform using different interpolation schemes are described in the following.

#### 4.2.1 Implementations based on different interpolation schemes

The goal is to find  $g(x_t, y_t) = z_t$  height values at  $(x_t, y_t)^T$  on the topography that are close to or lie on the straight line defined by  $\rho$  and  $\phi$ .  $\rho$  and  $\phi$  itself are chosen according to the desired angular resolution and sampling considerations (see section 4.2.4).

Depending on the line's definition 1D and 2D interpolation can be applied. Both interpolations require limiting the number of possible samples to a finite range. For 1D interpolation, either the  $x_t$  or  $y_t$  samples are queried whether they are located within the topography's borders. In 2D it works differently. All 2D interpolating schemes used here

<sup>1</sup>The connection between the Radon transform (or more accurately its 1D Fourier transform) and the 2D Fourier transform is made by the projection slice theorem (other names are Fourier slice or central slice theorem) [34, pp. 128 sqq., 140, p. 95, 57, pp. 374 sq.]. With the help of FFT algorithms for the 2D Fourier transform it enables an efficient calculation of the Radon transform via subsequent interpolation and a 1D inverse Fourier transform [22, pp. 819 sq.].



(a) S-F surface of measured topography

(b) Radon domain of fig. 4.3a

Figure 4.3: An exemplary ground shaft sealing surface and its Radon domain representation

have in common that the lines run across a circular aperture (see fig. 4.4). The aperture

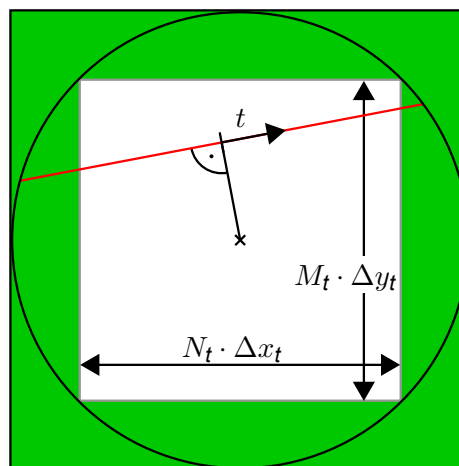


Figure 4.4: 2D interpolation scheme where lines run across a circular aperture with the region outside of the topography filled with zeros

is centred on the topography's centre and has a diameter equal to the longest diagonal of the topography, so that all sample points are included. The region outside of the original topography is filled with zeros. The samples of the parameter  $t$  are equidistantly distributed along the line with their origin at the line's centre. This eliminates the need of querying samples for their position in or outside of the aperture. And the aperture's size could be reduced very easily if desired. But it comes at the cost of summing up more samples than absolutely necessary.

The most straightforward schemes are nearest neighbour and linear interpolation both in 1D and 2D. Cubic spline interpolation in 1D and 2D is also considered and a non-interpolating scheme is presented. They are all implemented to work on an equidistant grid. The non-interpolating scheme does not necessarily require an equidistant grid but changes to the implementation are required in that case.



### Nearest neighbour interpolation

Nearest neighbour interpolation finds integer pixel coordinates close to the straight line by rounding. This also is termed zero-order interpolation [88, p. 496]. The straight line is then represented by a discrete line at integer grid coordinates (see fig. 4.10a). The heights  $z_t$  are all known at integer  $(m_t, n_t)^T$  coordinates and no further calculation is required.

1D nearest neighbour interpolation finds the closest  $y_t$  sample from the ideal line for each  $x_t$  or vice versa (depending on the line's slope). It is straightforward to implement with rounding operations and very fast. Toft offers some examples [140, pp. 8,28].

Nearest neighbour interpolation in 2D [57, pp. 65 sq.] selects the  $m_t$  and  $n_t$  coordinates that are closest to the Euclidean line by rounding. 2D interpolation requires additional sampling of parameter  $t$ .

### Linear/bilinear interpolation

Linear interpolation differs from nearest neighbour interpolation by calculating the desired  $z_t$  from the surrounding samples. In the 1D case the height at the position of interest lies somewhere on the connecting straight line between the two adjacent samples [73, p. 175]. Depending on the line's slope either the  $m_t$  coordinates for each  $n_t$  are regarded or vice versa.

In 2D the position between four neighbouring height values is evaluated linearly first in one direction. Then, the positions are connected by a straight line and evaluated in the orthogonal direction [88, p. 496].

With linear interpolation it can be possible to access a height value outside of the topography's borders to construct the connecting straight line. This case is taken care of by mirroring the second/last but one pixel in the row/column [138].

### Cubic spline interpolation

Cubic spline interpolation finds the unknown sample value on piecewise defined polynomial curves that are two times continuously differentiable [25]. Image processing benefits from the spline interpolation's ability to be described as digital filtering which makes computation very efficient [141, 73, p. 181]. In a first step the samples are mirrored on the topography edges according to Unser and Thévenaz et al. [142, 138] to avoid border effects. The topography size is then almost quadrupled. The application of B-splines for interpolation requires a preprocessing step to correct the cubic B-splines' smoothing effect and to ensure that the interpolated topography heights match the heights at the sample positions [138, p. 745, 73, p. 180]. In this preprocessing step the B-spline coefficients are calculated from the samples and all further processing is based on the B-spline coefficients rather than the original samples. Because the con-

volution of coefficients and the B-spline results in the sampled data, the coefficients are found by inverting the B-spline's transfer function. The B-splines are FIR filters and so the inversion results in IIR filters. Unser [142] calculated the coefficients by recursive filtering of the decomposed transfer function. The procedure is also detailed in another publication by Unser [141, p. 26]. Having obtained the coefficients most literature sources describe interpolating at regular values between the samples (up-sampling or zooming). This step is not performed here but rather are the individual samples of the line found by evaluating an explicit parametric equation in the equidistant grid according to Brombeer [25]. The cubic parametric equation consist of four parts and implements the convolution of the discrete cubic B-spline, which overlaps four samples, with the B-spline coefficients as depicted in fig. 4.5a. An straightforward alternative to evaluating

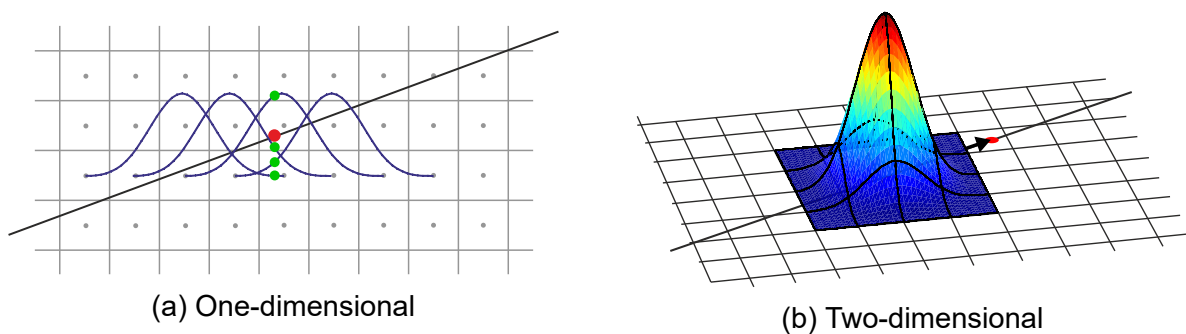


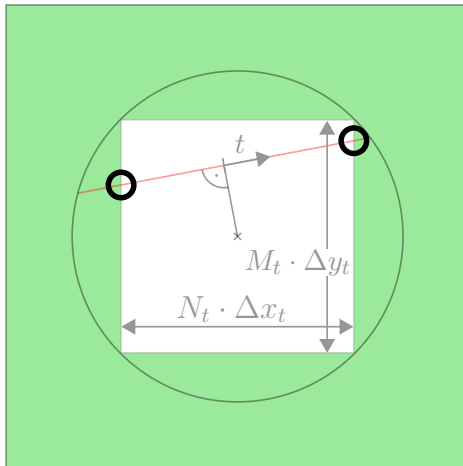
Figure 4.5: Interpolation using cubic B-splines

the explicit expression is the convolution with a densely sampled cubic B-spline via a lookup-table.

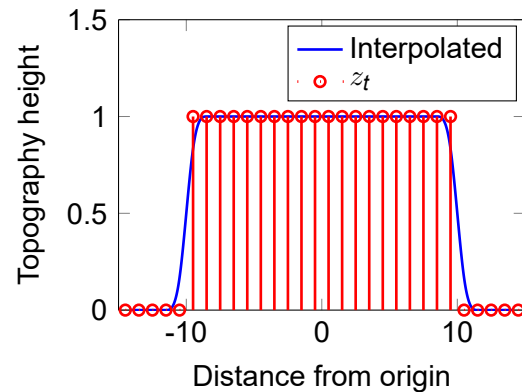
In 1D this procedure is carried out in  $x_t$  and  $y_t$  direction separately, depending on the line's slope.

In 2D it is carried out in both directions successively. Calculation of the B-spline coefficients is done in  $m_t$  and subsequently on the obtained data in  $n_t$  direction. The B-spline coefficients are convolved with the areal B-spline (see fig. 4.5b), whose integral is one: First, the areal B-spline is calculated at the unknown point's position (implemented as successive calculation in two directions) and then all 16 coefficients have to be convolved with the B-spline. The large number of coefficients involved means that more samples outside of the original topography are requested. These coefficients are already available from the mirroring of samples mentioned above.

**End effects** At the topography's borders end effects from spline interpolation occur. The spline coefficients are calculated on the complete mirrored topography. Then, spline coefficients outside of the range of the original topography are set to zero to ensure a correct value of the line integral. Using coefficients overlapping this border (see fig. 4.6a) the convolution with the areal cubic B-spline leads to smoothed interpolated values because some contributions are zero. As a result, both ends of a line



(a) End effects occurring at the marked positions of the line



(b) Topography samples and interpolated values on a line through a topography

Figure 4.6: End effects in the Radon transform implementation using cubic splines

are smoothed around the original topography's edges (see fig. 4.6b for a topography with a constant height and the corresponding interpolated line). A related effect can be observed with lines passing close to the topography. When some coefficients are in the range of the areal B-spline the line's integral is not equal to zero even though the line does not touch the topography. Options to correct this behaviour exist, e.g. subtracting the transform of an increased topography with broader border from the transform of the border alone in the Radon domain or checking each sample to be contained within the original topography's limits. However, both approaches lead to a rougher appearance of the Radon domain and therefore the border effects are accepted as beneficial.

### Non-interpolating approach

A non-interpolating method assumes a specific shape of the pixels and rotates the pixels' coordinates as well as their shapes around the topography's centre. The beams can be thought of as arbitrarily thin. They run through the rotated topography and interact with individual pixels. Because each interaction is calculated within the finite area of a pixel interpolation is obsolete. In contrast to the other methods the beams are stationary and always run from top to bottom. Figure 4.7a depicts the procedure. Rotating the beams counterclockwise is similar to rotating the topography clockwise. The beam direction from top to bottom is a change to the coordinate system from fig. 4.2 that is accounted for by subtracting the initial rotation.

For each pixel hit by the beam the line integral is increased. The intersection length  $l$  between beam and pixel governs the amount of the pixel value (i.e. topography height) added to the line integral. Each pixel is assumed to be a square because this will be the most common case. Other shapes (e.g. rectangular, circular etc.) require slight changes to the implementation. To calculate  $l$  the rotated square (pixel) is separated

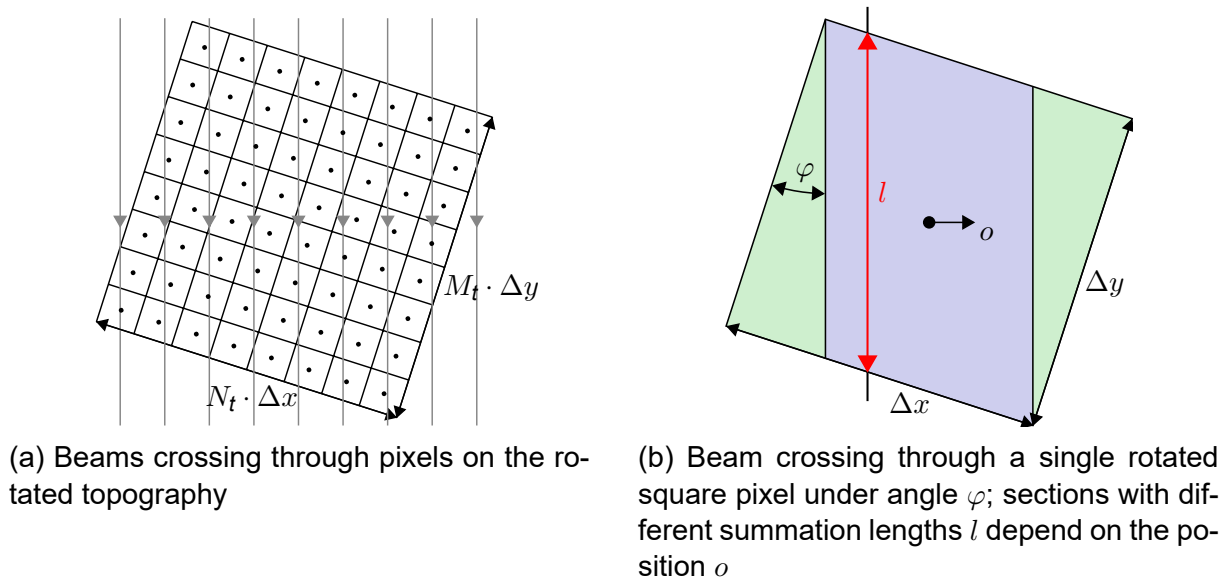


Figure 4.7: Illustration of the non-interpolating method

into three sections (see fig. 4.7b). The fraction of the pixel value added to the line integral is smaller or equal in the outer regions (green) compared to the centre region (blue) simply because  $l$  is shorter.

$l$  changes for each rotation. So for each rotation the region is selected with the help of the coordinate  $o$  that describes the horizontal distance between the beam and the pixel's centre. In order to avoid testing each of the topography's pixels for intersection with each beam a search region around the beam is selected. The search region is adapted for each beam and for each rotation and is based on area considerations. The pixels' coordinates are sorted in horizontal order and the area before and after the beam of interest is calculated. The two areas are depicted in fig. 4.8a with the relevant coordinates  $O_{min}$  and  $O_{max}$ . For safety reasons the area around the beam is slightly larger than absolutely necessary (red and grey areas in fig. 4.8b).

The different running lengths through the topography cause some features appearing exaggerated while underestimating other. In a final step, the different running lengths through pixels and the topography are corrected by normalisation.

A beneficial modification is achieved by saving the lengths  $l$  of each pixel, each beam, and each rotation. This then enables very efficient calculation of the Radon transform of identically sized topographies and reduces calculation time by a factor of more than 15 on topographies with  $50 \text{ pixel} \times 50 \text{ pixel}$  and of nearly 60 on topographies with  $512 \text{ pixel} \times 512 \text{ pixel}$ . The idea is related to algebraic reconstruction techniques outlined in e.g. [34, pp. 142 sqq., 140, pp. 129 sqq., 73, p. 277].

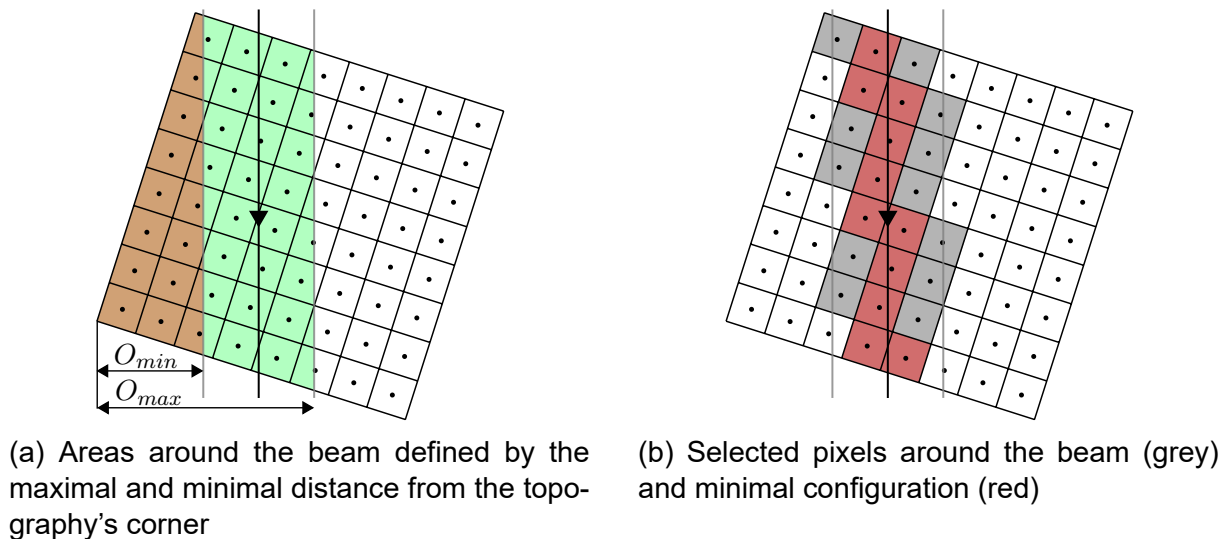


Figure 4.8: Selecting relevant pixels around a beam

### 4.2.2 Main texture orientation

The Radon transform is well suited for the detection of texture orientation because similar parameter values form peaks and these peaks can be read out from the parameter domain. Different methods of processing the parameter domain come to mind. The method's goal is to be applicable to a wide range of directional surfaces and to be independent of changes to the grinding process parameter. So instead of tailoring the characterisation technique to a specified type of surface texture (or peak size in the Radon domain) it needs to be working on most if not all directional surface textures. Each groove on the topography, whose height is lower than the topography's average height, results in a valley in the Radon domain. Vice versa, the same is true for protruding ridges. One of the simplest ways of detecting the peaks is by thresholding the Radon domain [140, p. 3]. However, ground surface texture does not consist of clearly defined lines. Grinding marks rather appear as very noisy lines where noise is not simply normally distributed white noise<sup>2</sup>. Other techniques for detecting local extrema can be based on morphological operators [133, pp. 201 sqq.] or correlation with a sample groove in the Radon domain [17, pp. 77 sqq.]. These extrema then require a weighting scheme, possibly depending on their height or orientation. An integral approach could consider the whole Radon domain or the domain after thresholding and calculate a global centre of mass. Some authors [131, 17, pp. 57 sqq., 80, p. 77] integrated the squared Radon domain along parameter  $\rho$  (representing the distances from the origin) and found the orientation as the resulting maximum.

This latter approach is taken here, too. All samples in the Radon domain are integrated over the parameter  $\rho$  which results in a curve with a distinct peak for unidirectional

<sup>2</sup>Beyerer examined the random process parameters generating ground surface texture [17, pp. 38 sqq.].

surfaces. Multi-directional surfaces will exhibit multiple peaks. This curve is termed orientation curve  $c(\phi)$  and its maximum is evaluated to find an estimate of texture orientation.

Calculation of the orientation curve  $c(\phi)$  is outlined first, before explaining a way of finding its maximum. The best suited approach is found empirically by evaluating artificial and measured topographies (see section 4.2.3).

### Calculating the orientation curve

Integrating over  $\rho$  the orientation curve of the sampled Radon domain can be obtained as the sum over absolute values corrected by the simple sum over  $\rho$  as<sup>3</sup>

$$c_1(\phi) = \sum_{k=\rho_{min}}^{\rho_{max}} | \check{g}(\rho_k, \phi) | + \check{g}(\rho_k, \phi) . \quad (4.4)$$

The other candidate is the squared Radon domain:

$$c_2(\phi) = \sum_{k=\rho_{min}}^{\rho_{max}} \check{g}(\rho_k, \phi)^2 . \quad (4.5)$$

Figure 4.9 shows curves  $c_1(\phi)$  and  $c_2(\phi)$  calculated from fig. 4.3. The correction term of eq. (4.4) leads to better results of  $c_1(\phi)$  but yields no difference in maximum detection when the Radon samples are squared and is omitted in eq. (4.5). The implementations will be examined on artificial and measured topographies on their ability to derive the main texture orientation of the ground texture.

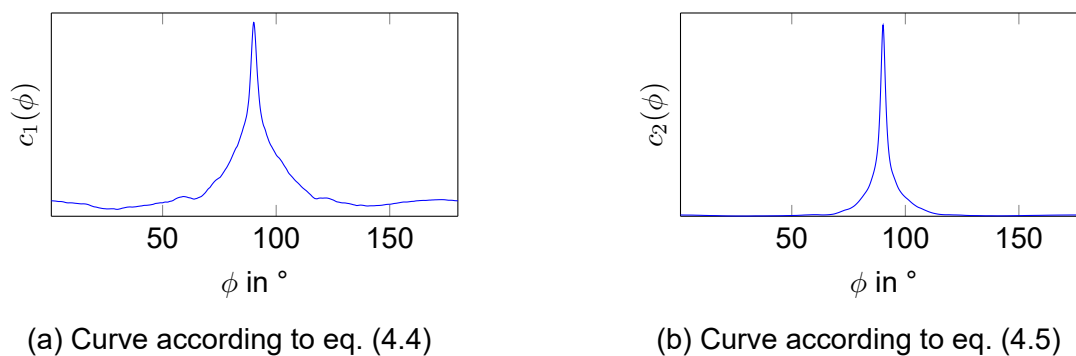


Figure 4.9: Orientation curves of fig. 4.3

### Detecting the orientation curve's maximum

The orientation curve's maximum is detected not in the evaluated curve  $c(\phi)$  with the resolution defined by the angular sampling parameter of the Radon transform but the

<sup>3</sup>A multiplicative term  $\Delta\rho$  from the discrete implementation of the integral over all  $\rho$  is omitted because only the maximum's position is of interest.

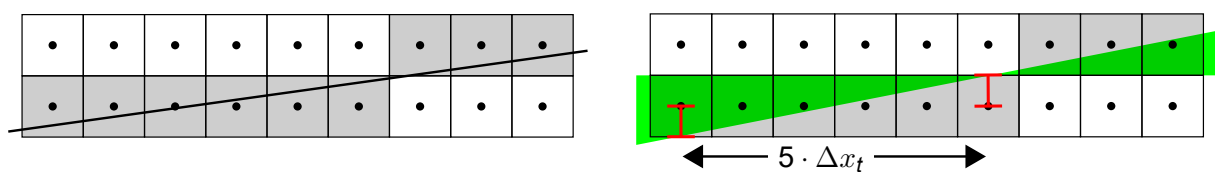
curve is interpolated using cubic spline interpolation. This increases the resolution further. The estimate of main texture orientation  $\psi_t$  is then found on the interpolated curve  $c_{int}(\phi)$  as

$$\psi_t = \arg \max_{\phi} c_{int}(\phi). \quad (4.6)$$

An alternative idea to increase resolution is fitting a Gaussian curve to the orientation curve because after integrating over a large number of local extrema of various shapes,  $c(\phi)$  is assumed to resemble a Gaussian curve (Central Limit Theorem [75, p. 71]). However, this works only in a small central region of the peak or by increasing the number of terms contributing to the fit. It generally increases the variability of the results. Therefore, the method is not applied and all following results are evaluated with cubic spline interpolation of the orientation curve.

### 4.2.3 Comparison with regard to orientation estimation

All implementations can generally be sampled with small angular increments. The angular and radial resolution of nearest neighbour schemes is lower and non-equidistant because the decision, which pixels contribute to a line, varies for each  $\phi$  and  $\rho$ . In contrast to Euclidean lines (the ideal straight lines with arbitrary coordinates) discrete lines can only adopt a limited number of slopes [133, pp. 40 sqq.]. Here, the value of  $\rho$  also influences the decision which discrete samples are selected. It is therefore difficult to state the angular resolution explicitly. Figure 4.10 illustrates the issue by showing an Euclidean line and the corresponding discrete line in fig. 4.10a and the possible range of orientations in fig. 4.10b. The range of orientations is found to reach from



(a) An arbitrary Euclidean line and the corresponding discrete line

(b) Range of possible Euclidean line directions for the discrete line in fig. 4.10a

Figure 4.10: Euclidean lines, discrete lines, and possible angular steps using 1D nearest neighbour interpolation

$0^\circ$  to  $\arctan\left(\frac{\Delta y_t}{5 \cdot \Delta x_t}\right)$  because the horizontal distance between the samples defining the maximal slope is  $5 \cdot \Delta x_t$  and an increase in slope would change at least one discrete sample. It is obvious that this depends on the number of pixels involved (i.e. topography size) and the actual  $\rho$  and  $\phi$ . Linear/bilinear interpolation does not suffer from this effect directly because the height values are interpolated linearly guaranteeing a steady transition and even less does cubic spline interpolation.

To test the implementations topographies with purely sinusoidal wavefront orientation are generated (see fig. 4.11a). Orientation ranges from  $-0.05$  to  $0.05^\circ$  around

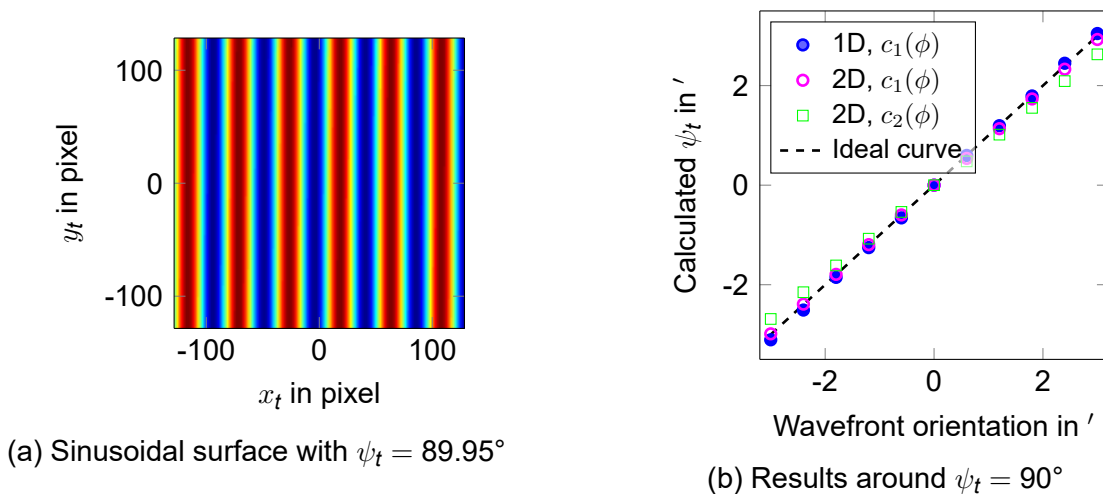


Figure 4.11: Exemplary sinusoidal surface and results from cubic spline implementations and different orientation curves

$\phi = 90^\circ$  with increments of  $36''$ . Only the implementations using cubic splines are able to reflect the wavefront's orientation correctly. The 1D cubic spline implementation did so only for orientation curve  $c_1(\phi)$  from eq. (4.4). In 2D both  $c_1(\phi)$  and  $c_2(\phi)$  could reproduce all increments (see the plots in fig. 4.11b). However, the 2D  $c_2(\phi)$  curve exhibits a slightly lower sensitivity.

The reason that prevents the other schemes from indicating the correct peak position becomes obvious by looking at the peaks of the corresponding orientation curves from either  $c_1(\phi)$  or  $c_2(\phi)$  in fig. 4.12. Using nearest neighbour interpolation and the non-interpolating approach a distinct ripple around  $90^\circ$  can be observed in all plots. By squaring the nearest neighbour implementation's Radon domain the ripple is transformed into a flat top. This flat top is visible using linear and bilinear interpolation as well. Both, the ripple and the flat top hamper the detection of small shifts in the peak's position. Only an indicator with one unique maximum is able to resolve small angular steps. Such a pointer is only present in 1D cubic spline interpolation in fig. 4.12a and in 2D also using cubic splines in figs. 4.12c and 4.12d. For this reason only these implementations are applicable to this kind of high accuracy evaluation. Even though the topographies regarded are synthetic the ripple could be observed on actual measurements with orientations of several arc minutes away from  $0^\circ$ ,  $\pm 90^\circ$ , etc. as well.

Looking for the cause of the distorted peak the projection profiles at  $0'$ , i.e. the slices of the Radon domain that were integrated for one  $\phi$  and all  $\rho$ , are regarded in fig. 4.13. The projection profiles for the non-interpolating approach and nearest neighbour interpolation look almost similar and resemble zero-order hold sampled sequences. The appearance stems from interpolating parallel to the topography borders and therefore



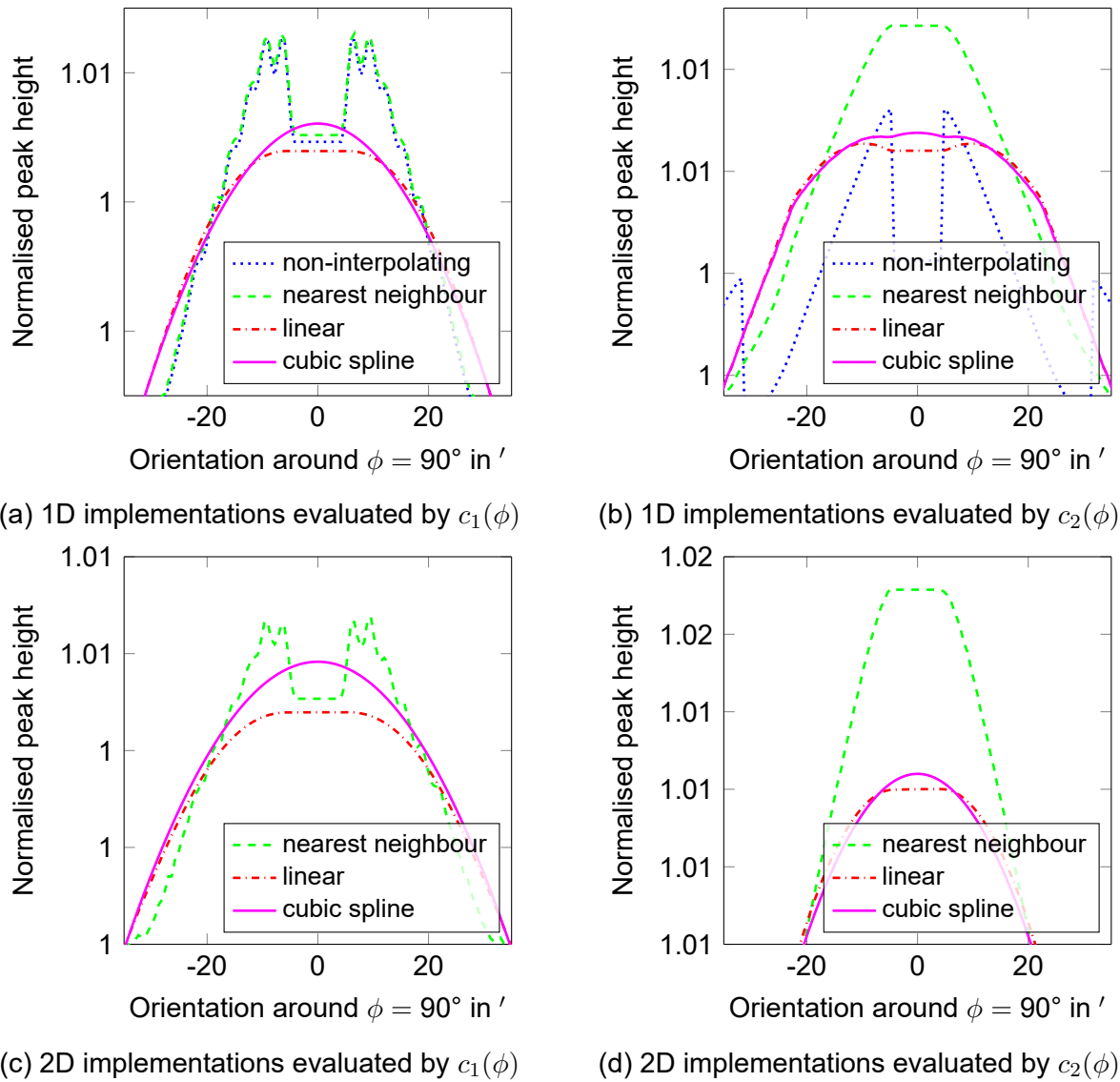


Figure 4.12: Peaks around  $90^\circ$  in orientation curves of the surface from fig. 4.11a for different implementations

to the pixels' edges. At a denser  $\rho$  sampling than the topography's lateral sampling distance neighbouring line integrals yield identical heights. Linear interpolation resembles first-order hold and only cubic spline interpolation produces a smooth projection profile. It is very likely that this somehow leads to the pronounced ripple. The good correspondence of  $\psi_t$  with the manually set rotation similar to fig. 4.1 is depicted in fig. 4.14. It can be clearly seen that the curve  $c_2(\phi)$  follows the theoretical line much better than  $c_1(\phi)$ . Despite the observed slightly lower sensitivity on a simulated sinusoidal topography in fig. 4.11b 2D cubic spline interpolation is the method of choice and all further results are based on  $c_2(\phi)$  from cubic spline interpolation unless stated otherwise.

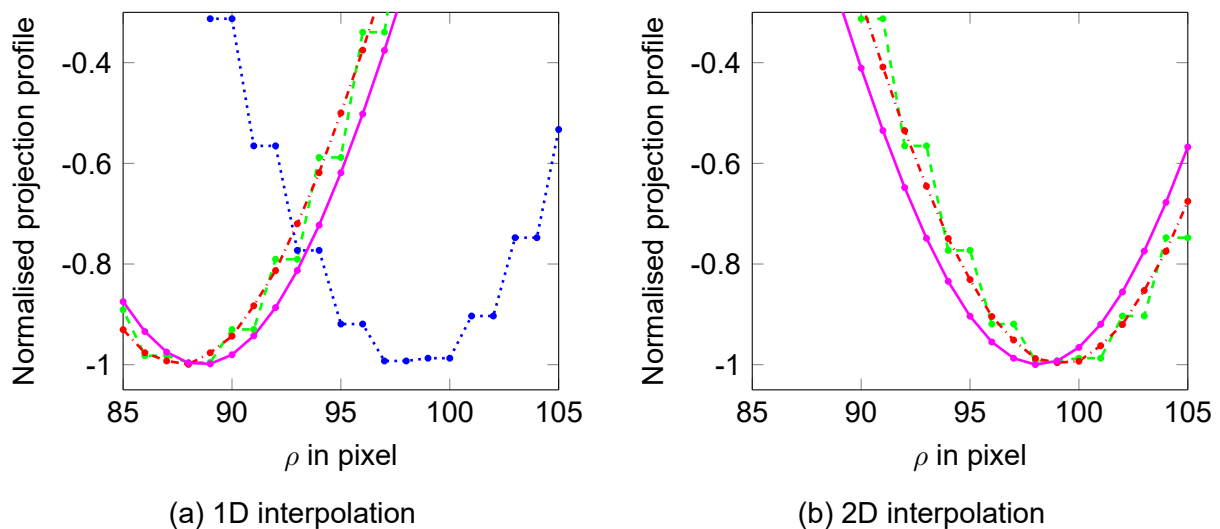


Figure 4.13: Projection profiles of the implementations at wavefront orientation of  $90^\circ$  and  $\phi = 90^\circ$  (colours equal to fig. 4.12)

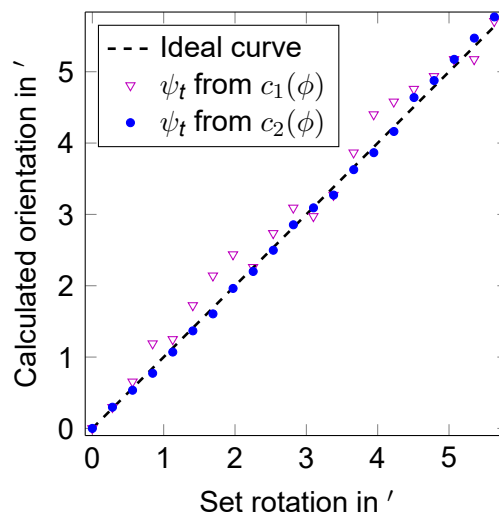


Figure 4.14: Calculated main texture orientation  $\psi_t$  similar to fig. 4.1 with 2D cubic spline interpolation (curves are adjusted to start at  $0^\circ$ )

#### 4.2.4 Sampling considerations

The discrete implementation of the Radon transform requires adequate sampling of the involved variables. Beyerer deduced the angular sampling distance from the sampling theorem of computer tomography by regarding the corresponding 2D DFT [17, p. 48, 21]. Toft derived the sampling distance of the parameter domain as a function of the line's orientation and demanded *“that the change of line positions should be below one sample, when changing either [of the two parameters; note from the author] with their respective sampling intervals”* [140, p. 29]. In other words, both authors demand that the sampling distance has to be small enough to consider each sample. While the maximal sampling interval is self-evident, the effects of finer sampling on

$\psi_t$  are examined similar to [6] on measured topographies and default values are derived.

In one-dimensional interpolation  $y_t$  values are chosen for each  $x_t$  or vice versa. Sampling is then not independent of the line's slope and sampling distances follow a  $\min(|\cos^{-1} \phi|, |\sin^{-1} \phi|)$  relation. This is not a desired behaviour – even though angles of  $\psi_t$  larger than a few degree at most are not expected as topography edges are aligned parallel to surface texture in most cases. As before, only 2D cubic spline interpolation is regarded in the following.

The discrete version of eq. (4.3)  $\check{g}(\rho_l, \phi_k)$  is found according to [140, p. 27] as

$$\check{g}(\rho_l, \phi_k) \approx \Delta t \cdot \sum_{h=t_{min}}^{t_{max}} g(t_h \cdot \cos \phi_k - \rho_l \cdot \sin \phi_k, t_h \cdot \sin \phi_k + \rho_l \cdot \cos \phi_k) \quad (4.7)$$

All sampled variables run from a minimum to a maximum, e.g.  $\phi_{min} \leq k \cdot \Delta \phi = \phi_k \leq \phi_{max}$  for  $k = 0, 1, \dots, K - 1$  and likewise for  $\rho_l$  and  $t_h$ .

### Sampling of $t_h$

The density of samples along the line is governed by parameter  $t$ . The minimal sampling distance of  $t_h$  is  $\min(\Delta x_t, \Delta y_t)$ . With varying slope the distance between the gridded samples changes. This is accounted for by adjusting the minimal sampling distance by a factor depending on the line's slope:

$$\Delta t = \min(|\cos^{-1} \phi|, |\sin^{-1} \phi|) \cdot \min(\Delta x_t, \Delta y_t). \quad (4.8)$$

Not considering eq. (4.8) would lead to broad peaks at  $\pm 45^\circ$  because most samples are regarded in the diagonal direction.

To study the effects of varying sampling distances  $\Delta t$  is multiplied by a factor  $t_f$  with  $t_f = (0.2, 0.3, \dots, 2.5)$ .  $\psi_t$  is evaluated on ten measured topographies of ground shaft surface limited to  $400 \mu\text{m} \times 400 \mu\text{m}$  (for faster calculation). The mean absolute deviations of the topographies are plotted in fig. 4.15a. The offset at higher sampling rates is presumably caused by calculating the average orientation of each measurement as the mean of all  $t_f$  and can be neglected. It can be seen that  $t_f = 1$  is an adequate choice which just corresponds to the sampling demands above. Even slightly coarser sampling distances might be acceptable.

### Sampling of $\rho_l$

The same study is conducted for the sampling of  $\Delta \rho$  but with the difference that  $\Delta \rho_l$  is not a function of  $\phi$ . Here, the expansion factor  $\rho_f$  is varied in the range of  $\rho_f =$

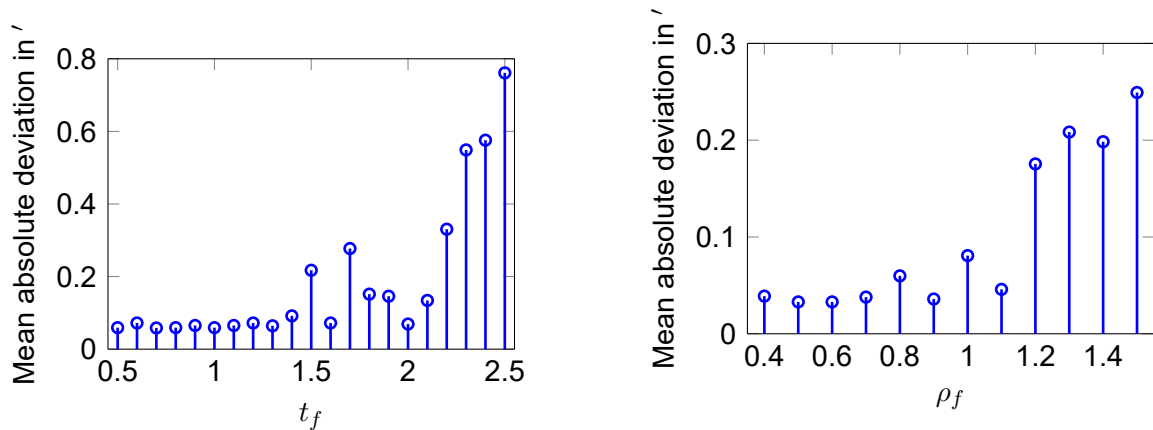
(a) Variation of the sampling distance  $\Delta t$  by  $t_f$ (b) Variation of the sampling distance  $\Delta \rho$  by  $\rho_f$ 

Figure 4.15: Variation of two sampling parameters evaluated as mean absolute deviation from the averaged orientation of each measurement using ten different measurements with topography size limited to  $400 \mu\text{m} \times 400 \mu\text{m}$

(0.4, 0.5, ..., 1.5). The resulting mean absolute deviation is plotted in fig. 4.15b. The curve suggests to  $\rho_f < 1$ . Here,  $\rho_f = 0.5$  is selected. These results concur with [6]. But similar to  $t_f$ , a slightly coarser sampling could be accepted.

### Sampling of $\phi_k$

The parameter  $\Delta\phi$  is an input parameter to the evaluation and, together with the cubic spline interpolation of  $c(\phi)$ , governs the resolution. It is not varied but generally fixed at  $0.6'$ . With this setting, steps smaller than  $0.6'$  can still be resolved, as fig. 4.14 with set rotations of approx.  $0.282'$  indicates.

## 4.2.5 Summary

The Radon transform-based method to assess texture orientation on preprocessed topographic data was studied. Several implementations were examined and a method to extract the orientation information was found in the parametric definition of the Radon transform and its discrete implementation using cubic spline interpolation. Together with the integral evaluation of the squared Radon domain this method was able to reproduce minute differences in texture orientation on rotated topographies very well. The effects of varying sampling distances were examined and recommendations on parameter values were given for the implementation.

## 4.3 Practical realisations

The practical realisation of a method to assess texture orientation using the Radon transform and its respective parametrisation from section 4.2 is regarded in this section. First, two evaluation procedures using the above implementations are described. Then, several characteristics and effects relevant for the proper application of the evaluation are discussed. These regard the effects of varying topography size, changes to the aperture, and effects of dominant structures – namely surface imperfections and superposed periodic structures and macro lead. Two ways to simulate directional structures and two ways to look at different scales are also provided.

### 4.3.1 Evaluation procedures

Calculating the Radon domain with fine sampling distances over a wide range of angles to derive  $c(\phi)$  takes a considerable amount of time. A more practical approach for unidirectional surface texture is based on an iterative procedure. Another idea circumnavigating the costly convolution step in cubic spline interpolation is to use a pre-interpolated topography and calculate the Radon domain samples using faster interpolation schemes, e.g. nearest neighbour or linear/bilinear. Both of these approaches are presented and discussed.

#### Iterative

The iterative procedure incorporates a coarse sampling part using 1D cubic spline interpolation followed by a dense sampling with 2D cubic spline interpolation. Figure 4.16 depicts the procedure. In the coarse part on the left side of fig. 4.16 the Radon domain is calculated over a larger angular range. Before deriving the orientation curve, a high pass filtering removes additional components in the Radon domain. The high pass aids the detection of peaks from ground structures. It does so only in the first few iterations. In case other types of surface texture are regarded it should be switched off. From the filtered or unfiltered Radon domain the orientation curve  $c_2(\phi)$  is derived and the angular width around the maximum is detected as full width at half maximum (FWHM). This angular region then serves as input to the next iteration until the FWHM falls below a threshold. At this point the dense sampling 2D implementation takes over and in the final cycle on the right side of fig. 4.16 the peak's maximum is evaluated as described in section 4.2.2. In its current single-threaded implementation in Matlab the procedure runs approx. 5 min on a standard PC to evaluate a 512 pixel  $\times$  512 pixel topography.

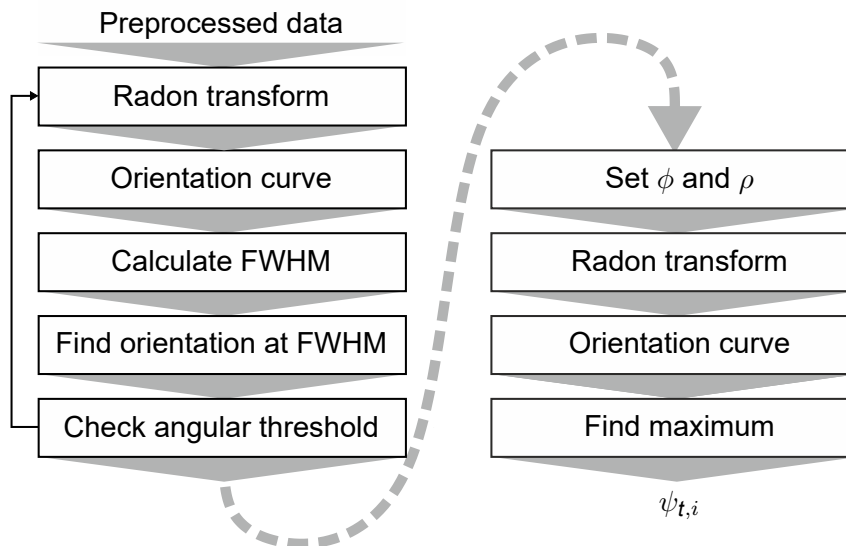


Figure 4.16: Iterative procedure to assess main texture orientation [6]

### Pre-interpolated

The costly step in the Radon implementation is the 2D cubic spline interpolation of each line sample at varying  $(x_t, y_t)^T$  positions. It requires setting up the areal cubic B-spline and convolving it with surrounding samples. Upsampling of the grid on the other hand can be performed efficiently (cf. e.g. [142]). The question arises if a combination of a fast upsampling and a fast interpolation method might be possible.

Doing so, the ripple could be seen to decrease with the upsampling factor in all evaluations. The shape of the curves from evaluating the rotated topographies approached the cubic spline curve in fig. 4.14. Still, the results obtained from the series of sinusoidal topographies from section 4.2.3 find this approach not advantageous with upsampling factors of up to three (i.e. expanding a topography of 512 pixel  $\times$  512 pixel to 4089 pixel  $\times$  4089 pixel). An improvement is only visible in 1D cubic spline implementation. Overall, this approach did not lead to the desired success.

### 4.3.2 Practical considerations and effects

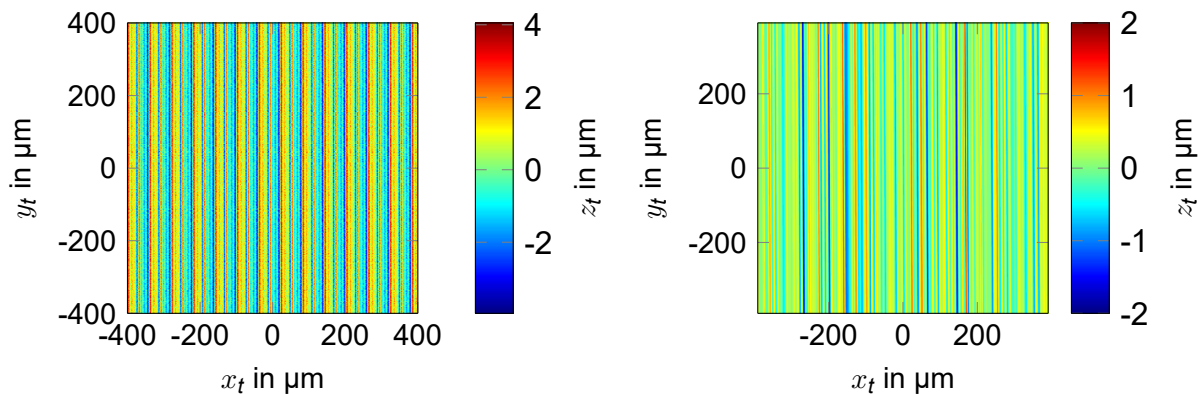
Applying the iterative procedure to assess texture orientation on ground surfaces benefits from some further considerations. Measurement accuracy and resolution were already found to be well suited in section 4.2.3. Here, a look is taken at effects of varying topography size and square and circular aperture, how texture orientation can be assessed at different scales, and how superposed structures influence the evaluation. Studying these effects benefits from artificial surface textures and therefore ways to model directional surfaces are discussed first.

### Simulation of ground surface texture

Modelling topographies enables straightforward testing of evaluation procedures. Several authors simulated topographies with directional surface texture. Among those are Beyerer, who designed surface texture with stochastic grooves [17, pp. 38 sqq., 81 sqq.], and Baitinger, who simulated sinusoidal and sawtooth structures on topographies for fluid simulations [8, pp. 57 sqq.].

Here, two different methods are applied. One uses periodic components. Such simulated topographies were used before to study the Radon-based method in section 4.2.3. They consist of sinusoids whose phase is shifted row- or column-wise. Varying phase delay, amplitude, and wavelength generates different appearances. More components on the topography can be added by considering more frequencies. All input parameter values can be described by probability distributions. Adding additional noise followed by linear or non-linear filtering yields more realistic appearances. Figure 4.17a depicts such a topography.

The second approach uses the inverse Radon transformation of texture designed in the



(a) Simulated topography with  $\psi_t = 90.05^\circ$  constructed of superposed periodic components and additive noise

(b) Simulated topography with  $\psi_t = 90.25^\circ$  modelled in the Radon domain

Figure 4.17: Simulated topographies to empirically assess characteristics of evaluation procedures

Radon domain. The stochastic distribution of grooves and their orientation is visible in the Radon domain. Consequently, it can be modelled there and transformed into the image domain by the inverse Radon transform. Appendix C describes the general procedure and model parameters. A simulated ground surface is displayed in fig. 4.17b. These two types of artificial surfaces are used in the following examinations together with real measurement data.

### Effects of topography size

Topography size has two effects on the detection of linear structures [6]. First, the variability of the angular distribution decreases with the line's length because the longer structures of constant width are, the fewer lines of different angles match them. This situation is depicted in fig. 4.18. The other effect is that the number of local extrema

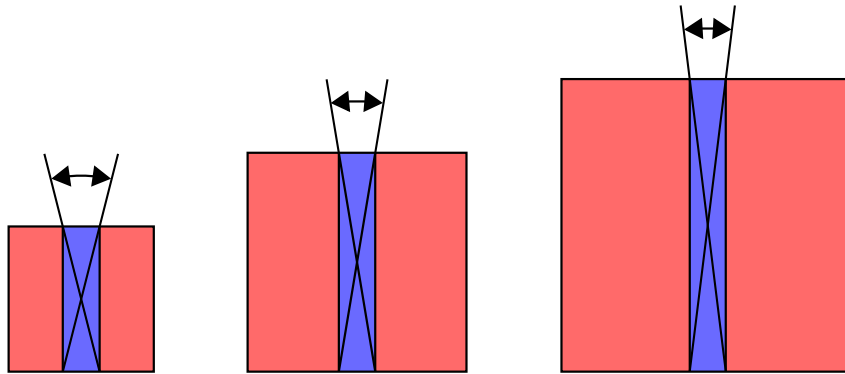


Figure 4.18: Effects of the length of linear structures of equal width on possible orientations

involved in the integration for the main texture orientation increases simply because more structures are present on the topography. This effect also reduces the variability of the orientation curve  $c(\phi)$ .

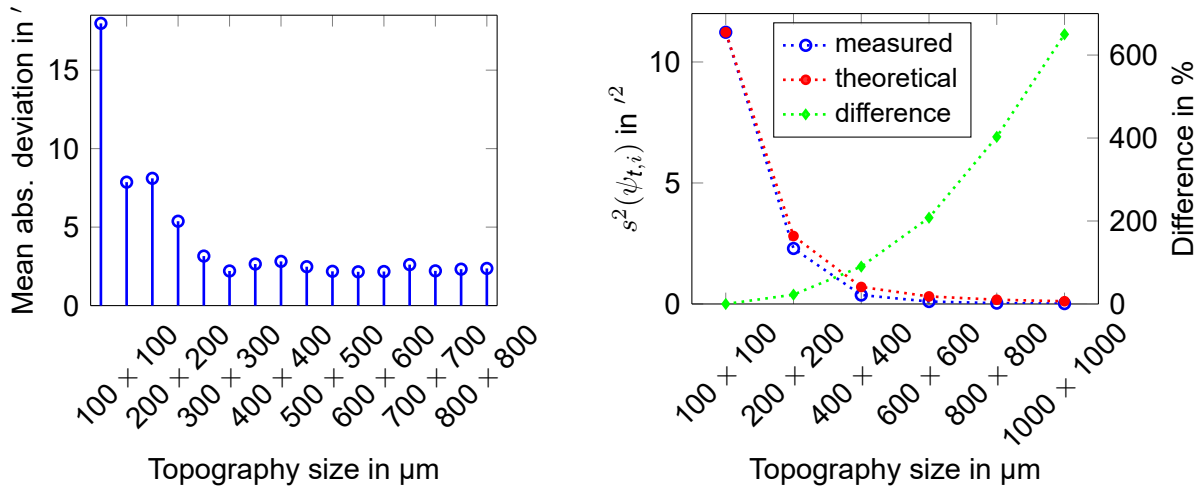
Both of these effects can be observed on measured topographies. Figure 4.19a depicts the resulting curve as mean absolute deviation from the averaged orientation for different topography sizes obtained from ten different measurements of ground surface texture. Topography sizes vary between  $50 \mu\text{m} \times 50 \mu\text{m}$  and  $800 \mu\text{m} \times 800 \mu\text{m}$ . The curve shows that topography sizes larger than  $500 \mu\text{m} \times 500 \mu\text{m}$  result in stable  $\psi_t$  – at least in the current set-up of examined texture and instrument.

Variability of the main texture orientation with varying topography size is examined on simulated topographies similar to fig. 4.17a with considerable superposed noise. The variability is measured by the experimental variance  $s^2(\psi_{t,i})$  and is found to follow approximately  $s^2(\psi_{t,i})/N_s$ , where  $N_s$  is expressed as the ratio of increasing topography sizes. With  $A_p$  being actual size and  $A_1$  the starting size of  $100 \mu\text{m} \times 100 \mu\text{m}$ , the standard deviation at larger topographies  $s(\psi_{t,i})_{A_p}$  can then be approximated by

$$s(\psi_{t,i})_{A_p} \approx s(\psi_{t,i})_{A_1} \cdot \sqrt{\frac{A_1}{A_p}}. \quad (4.9)$$

Figure 4.19b supports eq. (4.9) by showing the good agreement of the *theoretical* curve of  $s^2(\psi_{t,i})_{A_p}$  with experimental *measured* results from simulated topographies. The





(a) Mean absolute deviation from averaged orientations of measured topographies (b) Experimental and theoretical variance and relative difference of simulated topographies

Figure 4.19: Results of topography size variations

green curve *difference* depicts the relative difference as

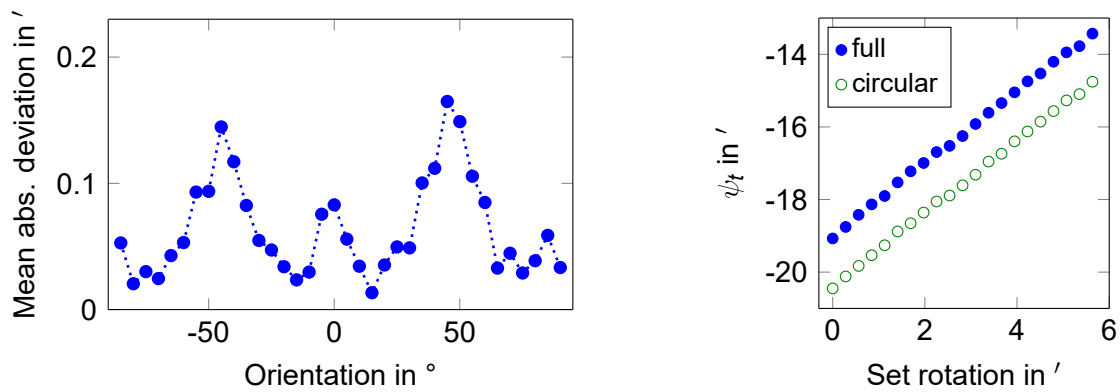
$$\frac{s^2(\psi_{t,i})_{A_p} - s^2(\psi_{t,i})}{s^2(\psi_{t,i})} \cdot 100 \% . \quad (4.10)$$

It shows that the theoretical assumption differs from the measurements to some extent and that the difference increases with topography size. After correcting the relative difference by  $\sqrt{A_p/A_1}$  it progresses almost linear.

### Aperture effects

Using the presented measuring systems ground structures will in most cases be aligned close to parallel/perpendicular to topography edges. They can be captured well by a rectangular or square aperture, which areal-topographic instruments usually provide. The structures run through the complete field of view and are cropped at the perpendicular topography edges only. Still, for some applications it might be of interest to apply a circular aperture.

A simulation of five series of simulated ground topographies similar to fig. 4.17b is examined. The five series contain 36 topographies each ranging from  $-85$  to  $90^\circ$  in  $5^\circ$  increments. Each series is evaluated with its full square aperture of  $500 \text{ pixel} \times 500 \text{ pixel}$  and a circular aperture with a diameter of  $500 \text{ pixel}$ . The mean absolute deviation between square and circular aperture is plotted in fig. 4.20a. Slight differences are observable for all directions. The curve also shows the presence of higher deviations at texture orientations running along the diagonal. However, these differences are still small. They might be caused by structures at the corners being completely left out of consideration with the circular aperture under these angles.



(a) Mean absolute deviation between circular and full aperture on simulated topographies

(b) Different  $\psi_t$  caused by changing the aperture

Figure 4.20: Effects in the detected texture orientation caused by changing from full to circular aperture

In a second test on the measured topographies of fig. 4.1 plotted with full and circular aperture in fig. 4.20b an offset of nearly 1' is visible. The difference is considerably large yet it might look completely different on other topographies. Both tests underline the necessity to include all available information in the evaluation and not to limit the lateral topography any further by choosing a circular aperture.

### Topography's different scales

Areal-topographic measurements of technical surfaces consist of a superposition of structures of different spatial extent. In case of ground sealing surfaces the bandlimited S-F surface from section 4.1 can still incorporate both micro and macro structures. The goal of micro lead evaluation is to characterise micro structures on the surface, while periodic macro structures are taken care of by the macro lead evaluation according to MBN 31007-7 [95]. These micro structures are commonly grinding marks and possibly structures of slightly larger spatial extent. Their scale is usually smaller than that of periodic and circumferential macro lead structures [78, p. 14]. Macro lead evaluation with default settings according to MBN 31007-7 starts to consider structures from an axial period length of 20  $\mu\text{m}$  upwards.

A further limitation of the spatial frequency content of the S-F surface by an L-filter can be necessary to regard small-scale structures only. The L-filter (cf. section 4.1.5) is an areal Gaussian filter according to [43] similar to the S-filter. The structures of interest are of lateral width of between 10 to 20  $\mu\text{m}$  according to [78, p. 14]. The L-filter's nesting index is then chosen as five times the largest structure size from the suggested series in ISO 25178-3 [49] as 0.1 mm (see fig. 4.21).

In case several scales of one topography need to be regarded the topography can be decomposed by the Gaussian filter and each scale can be characterised separately.

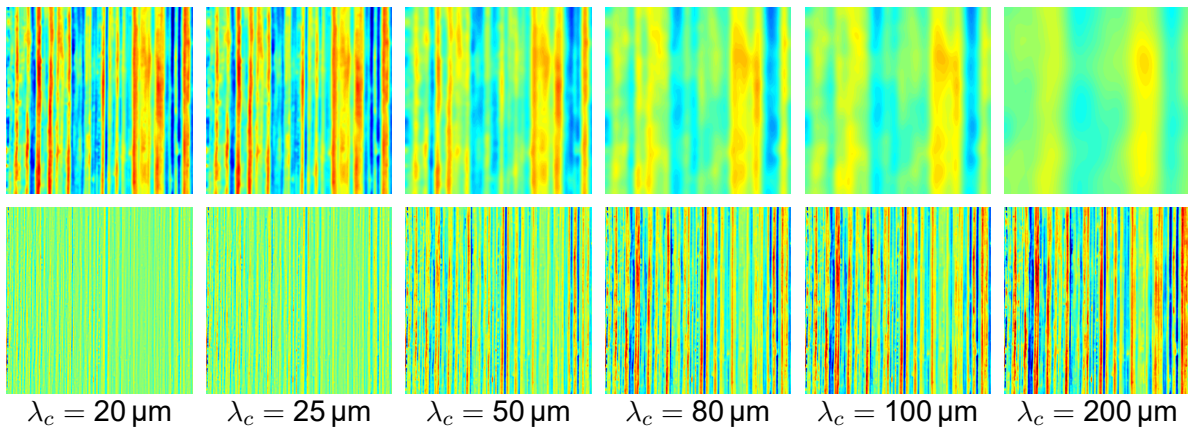


Figure 4.21: Scale-limited surfaces based on fig. 4.3a (upper row: band between S-L and S-F surface, lower row: S-L surface)

Different scales of the bandlimited ground topography in fig. 4.3a are shown in fig. 4.21. Another method to decompose different scales was presented in [5] and uses alternating sequential filters. The benefit of the latter is that the edges remain largely untouched while Gaussian filters smooth details by averaging. An example of the decomposition using alternating sequential filters is given in fig. 4.22. The pictures were obtained by

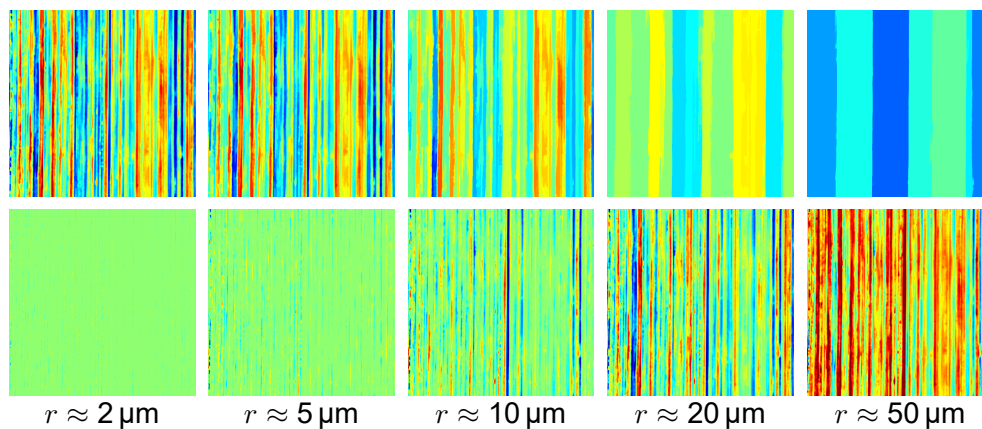


Figure 4.22: Scale-limited surfaces from alternating sequential filtering with morphological reconstruction and circular structuring elements of radius  $r$  (upper row: residual band between S-F and filtered surface, lower row: filtered surface)

open-close filters with circular structuring elements of increasing size using morphological reconstruction. The structuring element's sizes correspond to the suggestion in DIN EN ISO 16610-49 [41] and have radii  $r$  of approximately  $2 \mu\text{m}$ ,  $5 \mu\text{m}$ ,  $10 \mu\text{m}$ ,  $20 \mu\text{m}$ , and  $50 \mu\text{m}$ . Disc-shaped structuring elements are selected because of their high isotropy whereas lines require exact alignment to texture orientation to generate stable results.

### Effects of dominant structures

Several authors describe effects of superposed structures on the pumping rate (cf. section 2.2.2). Generally, the measured topographies should be free of underlying or superposed structures other than ground texture. Surface imperfections should be detected beforehand and the part's acceptance or rejection considered carefully. Still, it is of interest, how the evaluation procedure behaves in case superposed structures or surface imperfections are present.

**Surface imperfections** First, one type of surface imperfection is considered. Simulated topographies of  $781 \text{ pixel} \times 781 \text{ pixel}$  similar to fig. 4.17b are dented by a ball with a diameter of  $\approx 1.5 \text{ mm}$  and a depth of  $\approx 5 \mu\text{m}$ . Such dents were found to be non-leaking by Leis and Hollen [86, pp. 16,49] and their presence could therefore possibly be tolerated on the shaft surface.

Two series of topographies are tested: one with one ball imprint and one with two ball imprints. To mimic real measurements the imprints are distributed randomly and can be located anywhere within the topography and in the topography's border regions. Some of the topographies are displayed in fig. 4.23. In one series five simulated topo-

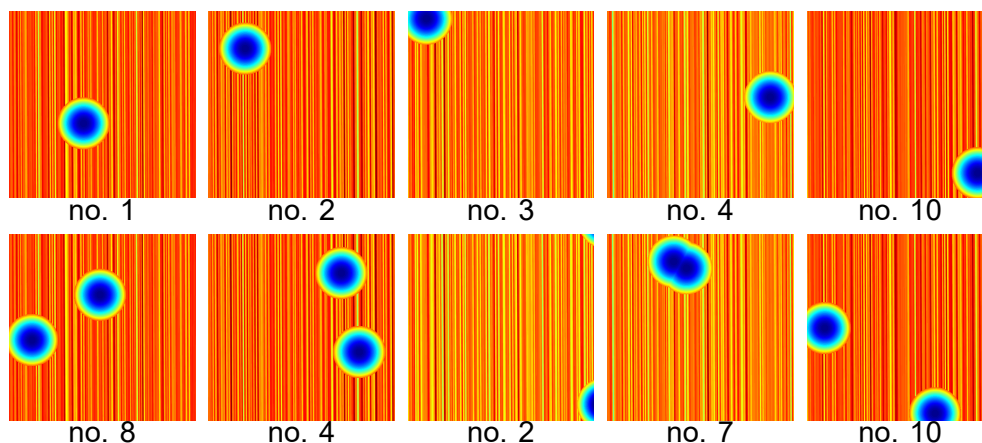
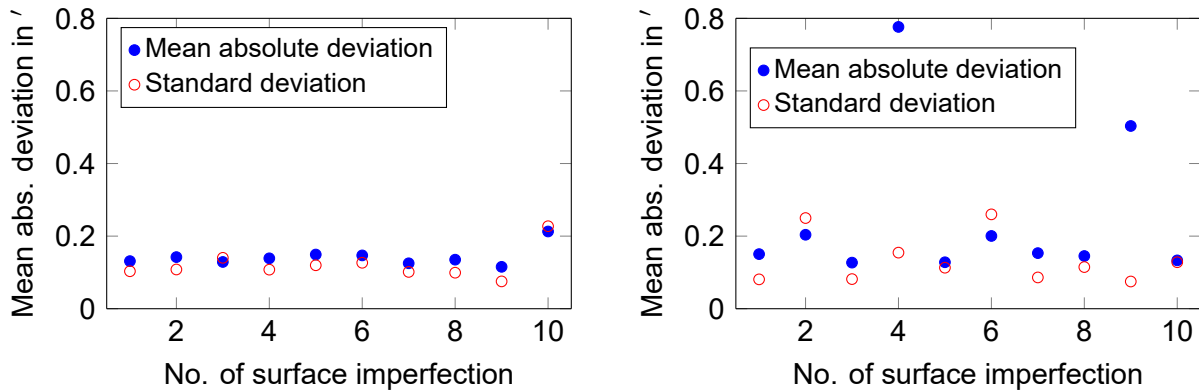


Figure 4.23: Some simulated topographies with one (upper row) and two (lower row) dents produced by ball imprints

ographies are imprinted by ten identical ball imprints each and the resulting main texture orientation  $\bar{\psi}_t$  (cf. eq. (3.3)) is evaluated. With the orientation of the undamaged texture known beforehand, the mean absolute deviation of both series is calculated and plotted in fig. 4.24 together with the experimental standard deviation  $s(\psi_{t,i})$  (cf. eq. (3.2)).

It is apparent from the curves that the mean deviation is generally higher on topographies with two dents with a mean of  $0.25'$  compared to topographies with one dent with a mean of  $0.14'$ . The presence of a single imperfection has minor effects on the detection of texture orientation. The outcome depends of course on the exact type of both surface and imperfection. The small values of the standard deviation show that the main



(a) Mean absolute deviation of topographies with one dent

(b) Mean absolute deviation of topographies with two dents

Figure 4.24: Mean absolute deviation and standard deviation of topographies with one or two dents

texture orientation for each defect on different topographies does not vary excessively. An imperfection overlapping a dominant grinding mark will influence  $\psi_t$  more than if it annihilates a rather shallow section. But the statistical considerations reduce these effects. With two dents present the mean absolute deviation can approach levels that might bias  $\psi_t$  significantly.

**Periodic structure** Having looked at isolated surface imperfections, underlying periodic structures in general are regarded next. The micro structure is a simulated ground texture similar to fig. 4.17b. The texture has an arithmetical mean height of the scale limited surface  $S_a = 0.36 \mu\text{m}$  and a maximum height of the scale-limited surface  $S_z = 3.07 \mu\text{m}$ . The periodic structures are modelled as 2D sinusoids. Wavefront orientation is varied randomly from 0 to  $180^\circ$ , amplitude from 3 to  $1000 \mu\text{m}$ , and wavelength from 8 to  $310 \mu\text{m}$ . Phase is varied randomly, too. 800 variations are generated and the resulting deviation of calculated  $\psi_t$  from the orientation of the bare micro structure is plotted against the amplitude of the sinusoids in fig. 4.25a. The plot shows only the details from  $-4.5$  to  $4.5'$  and omits outliers (the first outlier outside of the plot appears at an amplitude of  $0.68 \mu\text{m}$ ). It shows that deviations are influenced by the amplitude of the sinusoidal texture. A small amplitude does not alter the results significantly.

This result is also confirmed by plotting the three-dimensional parameter space in fig. 4.25b. The deviation from reference orientation as fourth dimension is added in the markers' colour. Here, no outliers are excluded. Dark red spots represent absolute deviations of  $4.5'$  and above. These are found only at higher amplitudes and small wavelengths. A preferred direction is not observable. The reason appears clear. The detection-aiding high pass filter integrated into the evaluation scheme (cf. section 4.3.1) prevents larger wavelength structures to influence the result. But it fails when struc-

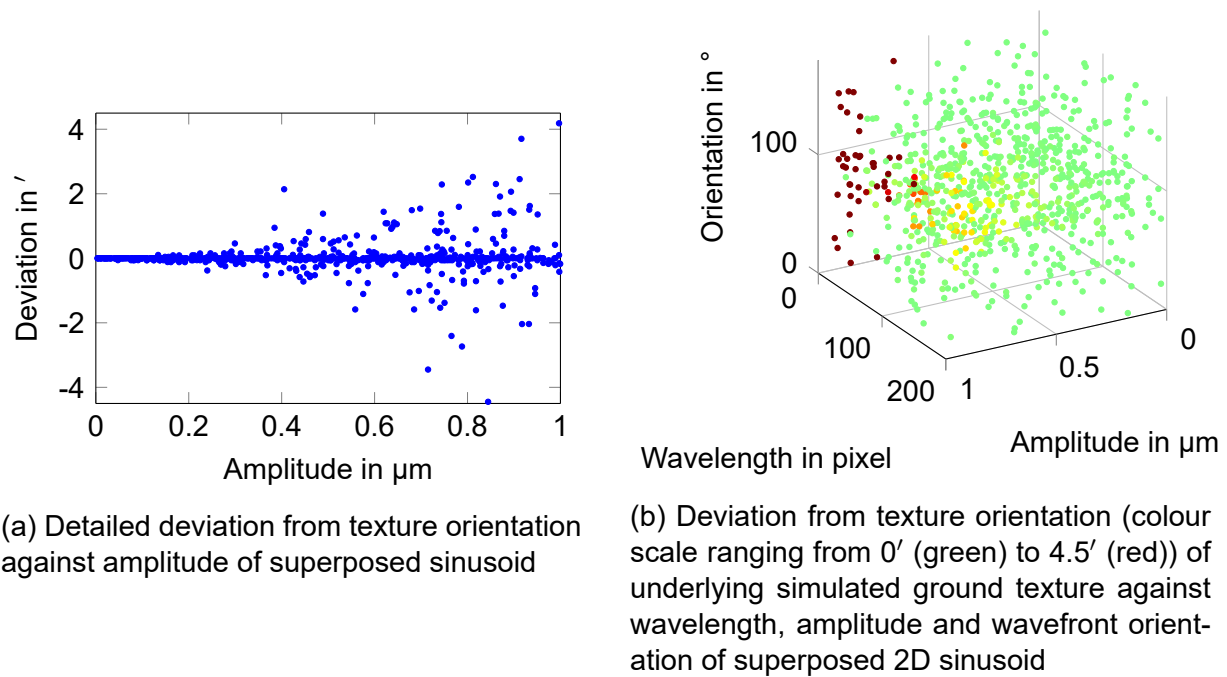


Figure 4.25: Results from superposing simulated 2D sinusoidal and ground texture

tures fall below a certain wavelength and their height exceeds the ground texture. A clustering of yellow and orange samples around 90° indicates that structures running approximately parallel to the ground texture can also deviate  $\psi_t$ . However, this visible clustering might be exaggerated by denser sampling of this region.

**Macro lead** Another study is conducted on the influence of underlying macro lead on the measured topography orientation. The ground texture can be superposed by a periodic structure depending on the dressing of the grinding disc [78, pp. 19 sq.]. This study involves the complete data processing from section 4.1 because the macro lead is added to the raw measurement data of fig. 4.3a before preprocessing to gain realistic results. A sinusoid is designed as macro lead with its properties taken from a report on findings of macro lead structures on ground shaft surfaces by Rau et al. [116]<sup>4</sup>. Parameter values are picked randomly from the values summarised in table 4.1 with a shaft diameter of 80 mm. The curvature of the shaft is neglected in modelling the macro lead structure. 500 random topographies are generated.

A result displayed as surface can be seen in fig. 4.26a. The samples are interpolated using nearest-neighbour interpolation and show lead depth  $D_t$  and number of thread starts  $D_G$  versus absolute deviation from the unchanged texture orientation up to 4.5'. For a low number of thread starts (equals long axial period lengths)  $D_t$  can be varied over a large range without significant effect on texture orientation. On the other hand,  $D_G$  can be varied with minimal effects for a small  $D_t$ . With both  $D_t$  and  $D_G$  increasing

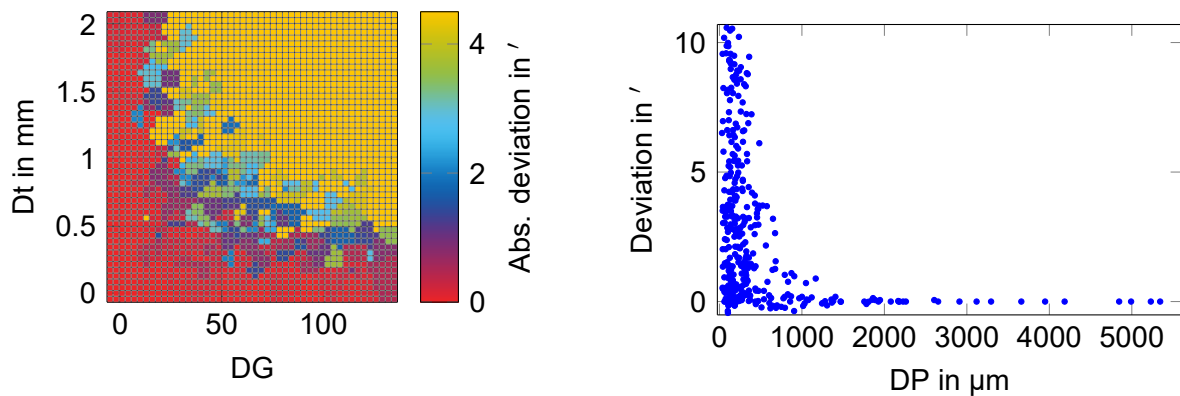
<sup>4</sup>The evaluation in Rau et al. used the first generation macro lead evaluation. Today's values might differ to some extent.



Table 4.1: Parameters of underlying macro lead structures related to [116]

| Parameter | Parameter value |
|-----------|-----------------|
| Dt        | 0.03 to 2 mm    |
| DP        | 0.03 to 20 mm   |
| DG        | 0 to 130        |
| $D\gamma$ | 0.08 to 5°      |

the gradient is steep. A corresponding observation is possible by plotting period length



(a) Deviation from texture orientation as a function of Dt and DG (visualised using nearest neighbour interpolation)

(b) Deviation vs. period length (plot shows detail not full range)

Figure 4.26: Deviation from texture orientation as a result of superposed macro lead structures

against deviation in fig. 4.26b. For long period lengths the deviation is negligible but small axial periods result in high deviations. A dependency of the deviation on  $D\gamma$  is not observable.

Generally, the absence of macro structures is recommended but they might not be avoidable under all circumstances. Short period lengths in axial and circumferential direction can be particularly disruptive. In contrast to the wide range of sinusoidal structures examined above macro lead structures always run somewhat parallel to the ground texture and are therefore even more effective in deviating  $\psi_t$ . Limiting the scale of the topography by an L-filter with the above mentioned 100  $\mu\text{m}$  improves the deviation as fig. 4.27 demonstrates.

### 4.3.3 Summary

In this section two possible realisation of a Radon-based evaluation method were discussed and the iterative evaluation procedure was found to be well suited for the application. With the help of measurements and simulated topographies the effects of topography size and two different apertures were studied. Topographies of

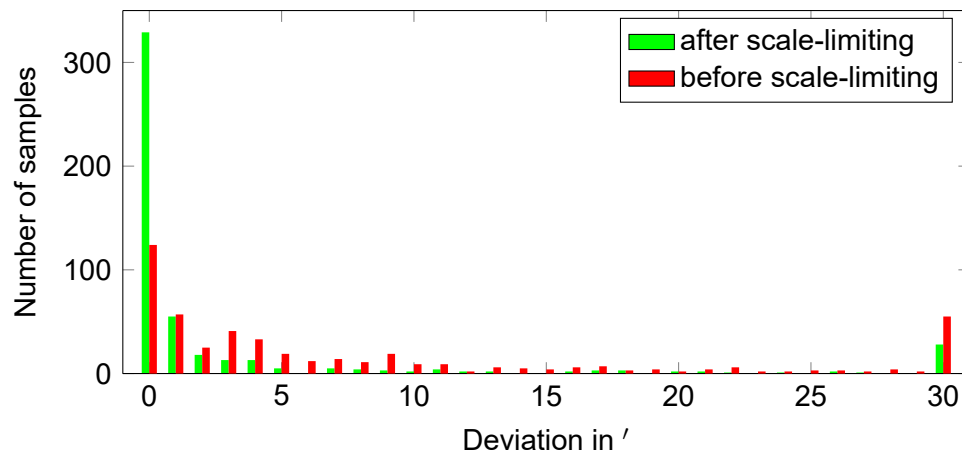


Figure 4.27: Effects of scale-limiting by an L-filter with nesting index of  $100\ \mu\text{m}$  on a measured topography affected by 500 variations of simulated macro lead

$500\ \mu\text{m} \times 500\ \mu\text{m}$  upwards seemed to produce stable orientations. It was recommended to use the largest aperture and topography size available in order not to miss out on relevant features. Finally, the presence of surface imperfections, superposed sinusoidal structures, and macro lead structures on the detected orientation were studied. It became clear that any structure present can deviate the result but for small structures and long wavelengths these effects were considerably smaller.

## 4.4 Discussion

The Radon-based evaluation method performs well on topographies with ground texture. Besides of using the Radon transform, it might be possible to produce comparable results by evaluating the 2D Fourier spectrum and applying interpolating techniques there. Another option is a correlation-based method which was developed at MTS and whose results are well comparable to the Radon-based method (cf. [5, 6]). Further approaches to assess texture orientation were not examined because a stable procedure was already found in the iterative Radon-based method. In case the Radon-based method needs to be applied to non-equidistant samples, e.g. from a point sensor, an interpolation method such as natural neighbour interpolation could be used instead or in combination with cubic spline interpolation.

Regarding the Radon transform-based method and the examinations in this chapter, several points are worth mentioning:

- Sampling considerations from subtracting sloped structures in e.g. the F-operation are not taken into consideration because they are expected to be negligible due to the small field of view and curvature.
- The F-operation for preprocessing uses an ordinary least-squares fit rather than



a geometric fit. A cylinder fit might also be considered. With knowledge of the angular measurement positions on the shaft a cylinder can be fitted to the measured topographies taken around the shaft's circumference and the underlying cylinder shape can be removed. All remaining scales are then really present on the shaft surface and not possible residuals from a preprocessing step.

- A single measurement will not be sufficient to describe the main orientation of ground shaft surface texture. Several measurements are required and texture orientation of the shaft is then adequately described by statistical parameters. Instead of taking several measurements and evaluating  $\psi_t$  individually, averaging Radon domains of a series of measurements and evaluating them for a single orientation might be an option. Expected increases in computation time will however be large if cubic spline interpolation is used. But in this case the non-interpolating approach from section 4.2.1 might be an option, given that the number of measurements and their variability is high enough to provide sufficient smoothing to outbalance the described ripple.
- The height of a peak or the depth of a valley in Radon space is influenced either by the length of structures or their height/depth. Integrating along a longer structure adds up more samples of low amplitude and the resulting peak can be equally high as if the structure is short and high. This information is lost considering the integral parameter  $\psi_t$ . To overcome the ambivalence, modifications to the basic Radon transform are known e.g. the Hough-Green transform [130]. But these techniques are not readily applicable to ground surfaces. Looking at the generation of elevations and depressions the orientation curve  $c_1(\phi)$  from eqs. (4.4) and (4.5) incorporates a weighting of structures according to their length or depth. This is basically a weighting by the volume in the direction of the line. By using  $c_2(\phi)$  the weighting becomes non-linear because the squaring damps shallow peaks and valleys while exaggerating high ones.
- Sampling of  $\rho$  and  $t$  is rather dense and could be relaxed because the lateral extent of structures is usually much larger than topography's lateral sampling distances. This would significantly decrease calculation time. Another way of decreasing calculation time would be implementing the iterative scheme in e.g. C++ and making use of multi-threading. The code in Matlab was written with this application in mind so the effort is expected to be relatively low.

## 4.5 Summary

In this chapter a Radon-based method to assess texture orientation was presented. It is capable of resolving angular steps on rotated topographies as small as a quarter arc minute and possibly smaller. The discrete Radon-transform requires some kind of interpolation of the samples along the line integrals. Several implementations were examined and cubic spline interpolation was identified to be the only approach with high resolution on simulated and measured topographies. Integration of the sampled Radon domain led to the orientation curve indicating texture orientation. The position of the curve's maximal peak represented the main texture orientation  $\psi_t$  of the topography. Sampling considerations were regarded empirically by examining measured topographies. As calculation of the cubic spline interpolation of samples along a line is computationally intensive, an iterative scheme was developed. A straightforward implementation yields an evaluation time of approx. 5 min in the interpreted Matlab language. Finally, several effects were studied regarding topography size and its influence on  $\psi_t$ , regarding the question whether to prefer a circular or square aperture, and how the results behave in case of superposed surface imperfections or sinusoidal or macro lead structures.

Together with the measuring systems from chapter 3 both demands arising from the definition of micro lead can be fulfilled and micro lead can be evaluated.

## 5 Results and Discussion

Combining measuring systems and their calibration from chapter 3 with texture orientation from chapter 4 and assessing micro lead as the deviation between main orientation of the ground texture  $\psi_t$  and circumferential direction  $\psi_{circ}$  leads to

$$\psi_{ml} = \psi_t - \psi_{circ} , \quad (5.1)$$

where  $\psi_{ml}$  is the micro lead angle.

There is of course only one estimate of  $\psi_{ml}$  per shaft. For simplicity, the same symbol  $\psi_{ml}$  represents the measurand and its estimate.

Both  $\psi_t$  and  $\psi_{circ}$  are subject to statistical variations and a reliable description of shaft surface requires more than a single measurement  $\psi_{t,i}$  with  $i = 1, 2, \dots, N$  and  $\psi_{circ,j}$  with  $j = 1, 2, \dots, M$ . Both the expected texture orientation and the expected circumferential direction are described by their arithmetic mean of  $N$  and  $M$  measurements, respectively. There is no need for  $M$  and  $N$  to be equal as the underlying distributions are different. In measurement systems, where eccentricity and tilt can play a role, circumferential measurements equally distributed around the circumference appear indicated. The expected micro lead angle is then defined as

$$\psi_{ml} = \frac{1}{N} \cdot \sum_{i=1}^N \psi_{t,i} - \frac{1}{M} \cdot \sum_{j=1}^M \psi_{circ,j} = \bar{\psi}_t - \bar{\psi}_{circ} . \quad (5.2)$$

The variability of the values of  $\psi_t$  on a shaft and of the circumferential direction  $\psi_{circ}$  can be described by their respective experimental standard deviations of the mean  $s(\bar{\psi}_t)$  and  $s(\bar{\psi}_{circ})$ , which are defined as

$$s(\bar{\psi}_t) = \frac{s(\psi_{t,i})}{\sqrt{N}} , \quad (5.3)$$

$$s(\bar{\psi}_{circ}) = \frac{s(\psi_{circ,j})}{\sqrt{M}} . \quad (5.4)$$

These are measures of the variability of the estimate  $\bar{\psi}_t$  and  $\bar{\psi}_{circ}$  [75, p. 10]. In the best case, without regarding further contributions (e.g. positioning or correlation), the

combined uncertainty follows from eq. (5.1) as [75, p. 19]

$$u_c^2(\psi_{ml}) = c_t^2 \cdot u^2(\bar{\psi}_t) + c_{circ}^2 \cdot u^2(\bar{\psi}_{circ}) . \quad (5.5)$$

The standard uncertainties  $u(\bar{\psi}_t)$  and  $u(\bar{\psi}_{circ})$  of eq. (5.5) are

$$u(\bar{\psi}_t) = s(\bar{\psi}_t) \quad (5.6)$$

$$u(\bar{\psi}_{circ}) = s(\bar{\psi}_{circ}) \quad (5.7)$$

and  $c_t^2 = c_{circ}^2 = 1$ . Therefore,

$$u_c(\psi_{ml}) = \sqrt{\frac{s^2(\psi_{t,i})}{N} + \frac{s^2(\psi_{circ,j})}{M}} . \quad (5.8)$$

In this chapter test shafts and macro lead standards are examined exemplary for micro and macro lead as well as for periodic components on the shaft surface. The subject of micro lead standards is briefly touched on before a discussion and a summary conclude the chapter.

## 5.1 Exemplary evaluations

Exemplary evaluations of two ground test shafts and ground macro lead standards make use of macro and micro lead evaluation procedures explained in previous chapters and eqs. (5.1) to (5.8). Additionally, periodic components on the shaft surface are identified. Band-limiting is demonstrated on macro lead standards with superposed micro and macro structures before first steps towards measurement standards for micro lead structures are taken. Discussions are embedded into the presentation of the results wherever necessary.

### 5.1.1 Ground test shafts

Two ground shafts of approx. 80 mm diameter, which presumably showed leakage in test runs and were reported to exhibit micro lead, were provided by a cooperation partner. The topography in fig. 4.3a shows the surface of one of these shafts. The arithmetic mean deviation of the assessed profile  $R_a$  of test shaft 1 is  $0.36 \mu\text{m}$  and  $0.37 \mu\text{m}$  of test shaft 2, both with a cut-off wavelength  $\lambda_c = 0.8 \text{ mm}$ . As a result of frequent use in different systems and set-ups the shafts' surfaces exhibit several surface imperfections. These are mainly scratches, predominantly in axial direction, and

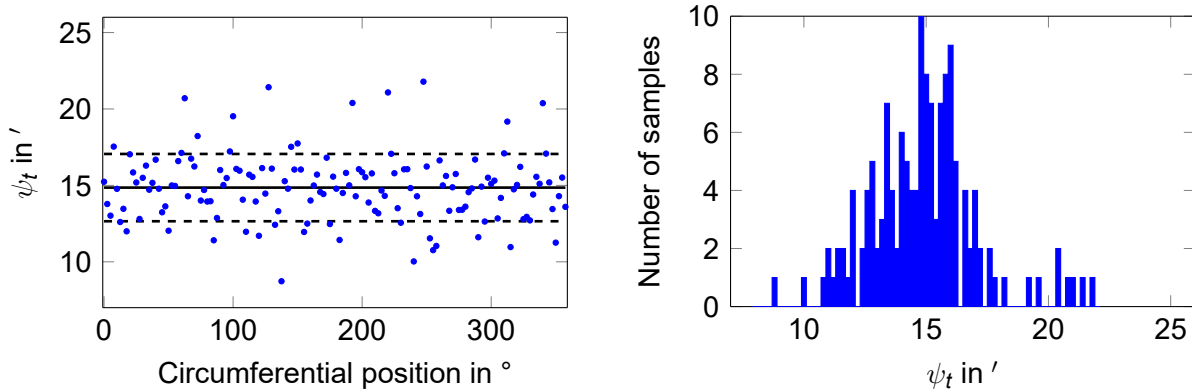
some small dents both caused by handling. Affected topographies are not excluded from evaluation except when marked in the text.

### Micro lead

Micro lead on the two test shafts is examined in several series of measurements. The plain micro lead angle in one axial position is assessed first, followed by an examination of repeatability, measurements at different axial positions, and with different objectives.

**Micro lead angle of ground test shafts** In the first studies the micro lead angle is assessed with the rotating measuring system from section 3.1. The confocal measurements are made in the  $(m_t, n_t)^\top$  coordinate system, but evaluation uses the  $(x_t, y_t)^\top$  system (cf. section 3.1.1). The presented values agree with the definition of MBN 31007-7 [95].

After adjusting eccentricity and tilt beyond recognition, 144 circumferential measurements each were taken in one axial position of test shafts 1 and 2. The resulting curve of texture orientations<sup>1</sup> of test shaft 1 is plotted in fig. 5.1 together with its histogram and in fig. 5.2 for test shaft 2. The results are summarised in the first row of table 5.1.



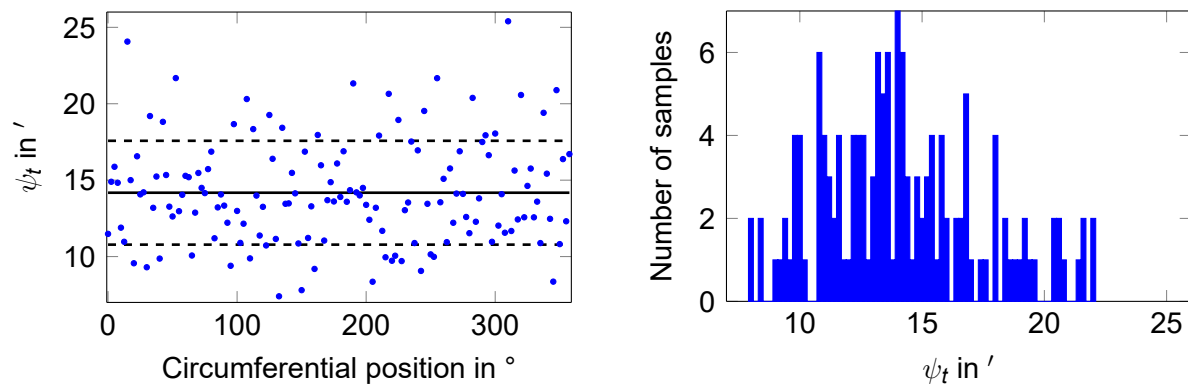
(a) Texture orientation with arithmetic mean (solid line) and experimental standard deviation (dashed line)

(b) Histogram (bin width = 1°)

Figure 5.1: Texture orientation of test shaft 1

The orientations of the calibration measurements with the ultra-precision turned shaft from fig. 3.12 are plotted in fig. 5.3. Because a small three-jaw chuck was used to mount the shafts only the widest groove  $b_{g,3}$  could be reached. The 72 measurements were therefore taken at this groove even though it yields the highest variability of the three calibration grooves (cf. section 3.1.4). Eccentricity and tilt were here also adjusted beyond recognition. The sinusoidal progression in fig. 5.3 presumably stems from

<sup>1</sup>The values ranged around  $\phi = 90^\circ$  but were corrected by this rotation to account for the relative position of instrument and shaft.



(a) Texture orientation with arithmetic mean (solid line) and experimental standard deviation (dashed line)

(b) Histogram (bin width = 1')

Figure 5.2: Texture orientation of test shaft 2

the turning process and is only visible at this groove. The result is summarised in the

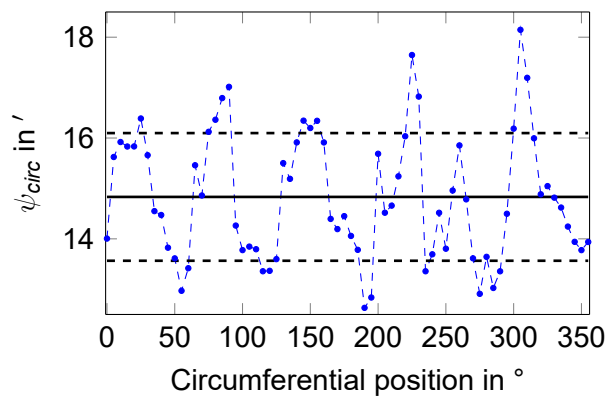


Figure 5.3: Measured calibration orientation of groove  $b_{g,3}$  with arithmetic mean (solid line) and experimental standard deviation (dashed line)

first row of table 5.1. The micro lead angle is calculated according to eq. (5.2) and the combined uncertainty according to eq. (5.8).

Surprisingly, the two shafts – even though they are supposed to differ by 15' – yield almost identical results. Regarding the experimental standard deviation of the mean of  $\psi_{circ}$  of 0.15' and of  $\psi_t$  of 0.18' and 0.28' the values might indeed be similar. Suspecting that the wrong shaft was measured can be rejected on grounds of the higher standard deviation of  $\psi_t$  of test shaft 2 which is also visible in other measurements. These other measurements of both shafts without calibration and at different axial positions revealed a difference of 2.83' with comparable variability.

**Repeatability** Each row of table 5.1 shows the results of repeated consecutive measurements of first the calibration shaft and then test shaft 1. Each row except the first one saw the calibration shaft being mounted, centre and tilt adjusted, measured 36 times

Table 5.1: Results of calibration measurement  $\psi_{circ}$ , texture orientation  $\psi_t$ , micro lead angle  $\psi_{ml}$ , and combined standard uncertainty of test shafts

| Calibration shaft   |                    | Test shaft 1   |                 |             |                  | Test shaft 2   |                 |             |                  |
|---------------------|--------------------|----------------|-----------------|-------------|------------------|----------------|-----------------|-------------|------------------|
| $\bar{\psi}_{circ}$ | $s(\psi_{circ,j})$ | $\bar{\psi}_t$ | $s(\psi_{t,i})$ | $\psi_{ml}$ | $u_c(\psi_{ml})$ | $\bar{\psi}_t$ | $s(\psi_{t,i})$ | $\psi_{ml}$ | $u_c(\psi_{ml})$ |
| 14.8'               | 1.27'              | 14.9'          | 2.20'           | 0.03'       | 0.24'            | 14.2'          | 3.40'           | -0.65'      | 0.32'            |
| 15.1'               | 1.14'              | 14.9'          | 1.94'           | -0.15'      | 0.30'            | -              | -               | -           | -                |
| 15.0'               | 1.46'              | 14.4'          | 2.15'           | -0.59'      | 0.35'            | -              | -               | -           | -                |
| 14.8'               | 1.21'              | 14.8'          | 2.08'           | -0.03'      | 0.32'            | -              | -               | -           | -                |
| 14.7'               | 1.23'              | 14.8'          | 2.21'           | 0.11'       | 0.33'            | -              | -               | -           | -                |

and then test shaft 1 being mounted, adjusted and measured 72 times<sup>2</sup>. The measuring system was not modified and so the measurements were taken at approximately the same axial position. The high repeatability is observable in the results from row one to five. The experimental standard deviation of the means of different measurements in column five is only 0.28'. There are no variations observable in results from 72 or 144 measurements. 72 measurements appear sufficient for stable estimation of  $\psi_t$ .

**Orientation at different positions on the shaft** After all measurements were taken in one axial position, it is of interest whether texture orientation varies at different heights. Test shaft 1 was rotated manually around its axis in twelve increments of  $\approx 30^\circ$  each, while being placed in a high-accuracy v-block. Axial increments were not fixed but rather adjusted between the multiple running tracks of the sealing lip. Across an axial length of 25 mm seven measurements were taken. The results are plotted in fig. 5.4. In fig. 5.4a the means at the seven axial positions of twelve measurements around

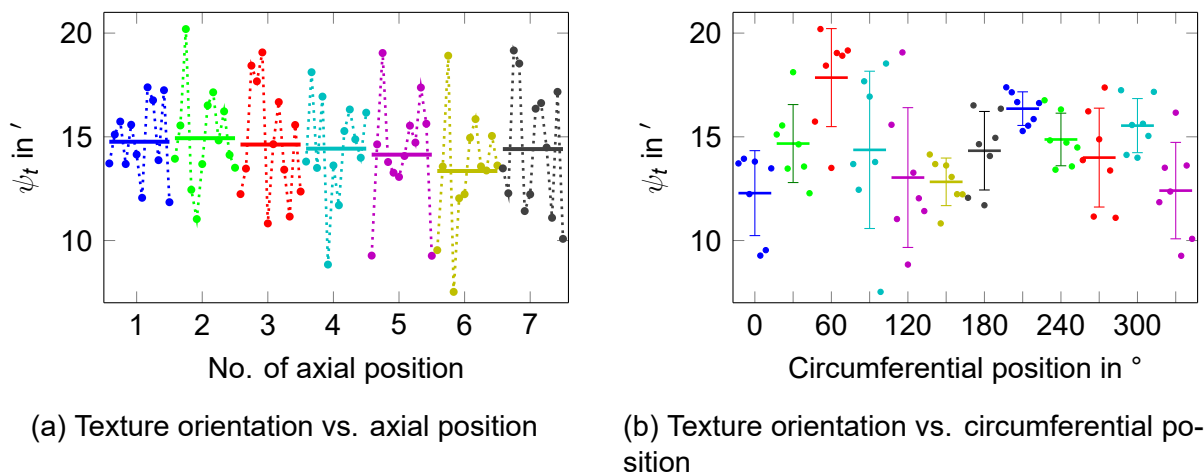


Figure 5.4: Texture orientation of shaft measured at several axial positions in a v-block

the circumference each (solid horizontal bar) have a range of 1.6' from min to max

<sup>2</sup>The first row is based on 144 measurements of both test shafts and 72 measurements of the calibration shaft as detailed before.

and a standard deviation  $s(\bar{\psi}_{t,7}) = 0.52'$ . In other words: the values at different axial positions are considerably homogeneous and it does not matter so much at which axial position a measurement is taken. After looking at the curve progression (dashed lines) reordering the values might be indicated. In fig. 5.4b the values are plotted against their circumferential position. In this case the variability of the means is much higher with a range of  $5.6'$  and a standard deviation  $s(\bar{\psi}_{t,12}) = 1.66'$ . Clearly, these values are not directly comparable because the underlying data base is different. To compare the two values the standard deviations are calculated from the deviations of the means. The standard deviation of the seven axial positions  $s(\bar{\psi}_{t,7})$  is viewed as the standard deviation of the mean of twelve measurements  $s(\psi_{t,7,i})$ :

$$s(\bar{\psi}_{t,7}) = \frac{s(\psi_{t,7,i})}{\sqrt{12}} \quad (5.9)$$

Solving eq. (5.9) for  $s(\psi_{t,7,i})$  yields  $s(\psi_{t,7,i}) = 1.8'$ . Similar calculation for the twelve circumferential positions consisting of seven axial measurements each yields  $s(\psi_{t,12,i}) = 4.4'$ . This indicates that the variability of measurements along axial positions is indeed much higher than measuring around the circumference.  $s(\psi_{t,7,i})$  is in the range of values of table 5.1 but  $s(\psi_{t,12,i})$  is not. The differences are also larger than expected from positioning a nearly deviation-free shaft at different axial positions in the v-block (see section 3.2.3). They are possibly caused by a combination of geometric deviations of v-block and shaft. A further refinement might be achieved by looking at the different uncertainties caused by the limited number of samples (cf. [75, p. 58]). But even without regarding these, it becomes clear that circumferential measurements are recommended over axial measurements at one or few circumferential positions.

**Different objectives** It will be of interest for practical applications if changes to the measuring instrument affect the results. Here, measurements with the  $50\times/0.5$  objective from table 3.1 with a field of view of  $320\ \mu\text{m} \times 320\ \mu\text{m}$  are taken in addition to the known  $20\times/0.6$  objective with  $800\ \mu\text{m} \times 800\ \mu\text{m}$ , which all other measurements are based on. The curves of two consecutive series with 144 measurements each of test shaft 1 are plotted in fig. 5.5. The histograms do not show the micro lead angle but only the texture orientation  $\psi_t$  because they lack a calibration measurement. It can be seen that the distribution of the smaller measuring field is broader with mean  $12.9'$  and experimental standard deviation  $4.1'$  compared to  $\bar{\psi}_t = 16'$  and  $s(\psi_{t,i}) = 2.3'$  from the  $20\times/0.6$  objective. A reason why the means differ is not known. A likely cause is the manual changing of the objectives. Further tests would be beneficial.

Both measurement series contain some topographies with scratches. With section 4.3.2 in mind, where dents and overlaid periodic structures were found to have moderate effects, these topographies were not sorted out. A visual comparison shows that the



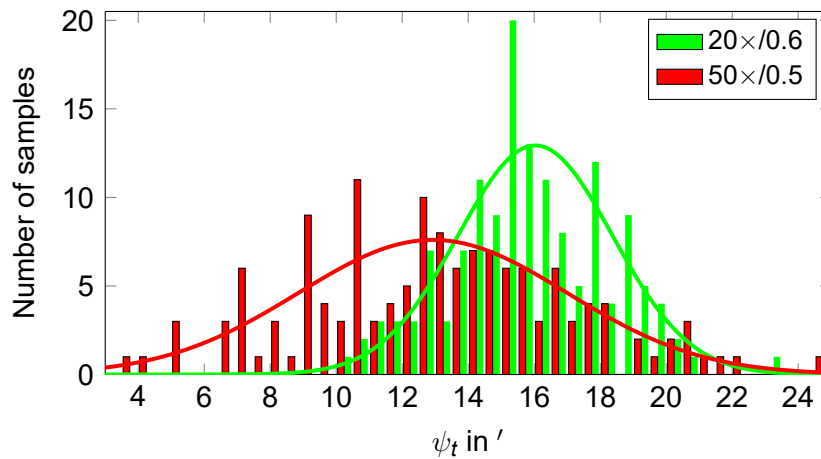


Figure 5.5: Texture orientation measured with two different objectives on test shaft 1 and fitted normal distribution

scratched topographies are not responsible for extreme values. However, they resulted in some invalid values on the small field of view because the iterative scheme failed to converge. Of the 144 measurements with the 50 $\times$ /0.5 objective only 140 could be evaluated and all contained more NMPs than the 800  $\mu\text{m} \times 800 \mu\text{m}$  topographies.

### Macro lead

Both test shafts were tested for macro lead according to MBN 31007-7 [95] (cf. sections 2.1.1 and 2.3.1). Long axial profiles of 25 mm each were measured. These are split into five parts of 5 mm each and analysed separately using both grids. The averaged results of these five sections are summarised in table 5.2. Instead of evaluating

Table 5.2: Arithmetic mean and experimental standard deviation of macro lead parameters of five axial sections of the test shafts

| Parameter | Test shaft 1                         | Test shaft 2                         |
|-----------|--------------------------------------|--------------------------------------|
| $D\gamma$ | $(0 \pm 0)^\circ$                    | $(0 \pm 0)^\circ$                    |
| $Dt$      | $(0.41 \pm 0.07) \mu\text{m}$        | $(0.35 \pm 0.10) \mu\text{m}$        |
| $DG$      | $0 \pm 0$                            | $0 \pm 0$                            |
| $DF$      | $(107.45 \pm 54.25) \mu\text{m}^2$   | $(65.85 \pm 43.47) \mu\text{m}^2$    |
| $DFu$     | $(0 \pm 0) \mu\text{m}^2/\text{rev}$ | $(0 \pm 0) \mu\text{m}^2/\text{rev}$ |
| $DP$      | $(0.52 \pm 0.18) \text{mm}$          | $(0.36 \pm 0.14) \text{mm}$          |
| $DLu$     | $(100 \pm 0) \%$                     | $(100 \pm 0) \%$                     |

only 2 mm of each axial section the valid axial wavelength range is changed from its default setting of 0.02 to 0.4 mm to 0.02 to 0.9 mm.

$DG$  of both shafts is zero and so is the lead angle. There is no distinct axially periodic structure visible on the shaft even though some non-zero values are found for  $Dt$ ,  $DF$ , and  $DP$ . This absence of a distinct periodic macro lead structure also results in a high

variability expressed in the standard deviation of the values. It is helpful in this context to visually compare the automatically generated overlay of reconstructed lead profile and measured counterpart.

### Circumferential waviness

A waviness around the circumference is an undesirable structure on the shaft surface. Symons investigated its effects on the performance of the sealing system [137]. He recommended to keep the height under  $5.08\ \mu\text{m}$  and the number of lobes around the circumference to a minimum. His shafts with seven or 15 lobes showed leakage in test runs depending on the height of structures and the shaft speed. With 45 lobes around the circumference and a height of  $2.54\ \mu\text{m}$  shafts "*leaked excessively on all tests*" [137, p. 373]. The occurrence of waviness from the production process was also spotted by Kersten on ground shaft surfaces [78, pp. 29 sq.] and by Rau et al. on turned shafts [117]. To detect it, Rau et al. measured a densely sampled grid of axial profiles taken every  $0.5^\circ$  around the circumference. This is basically a tenfold extension of the  $36^\circ$  grid of the macro lead evaluation (see section 2.3.1).

Some shafts were checked for the presence of periodic structures around the circumference. The measurement procedure is similar to Rau et al. The 720 axial profiles were taken around the circumference with a roundness measuring instrument equipped with a roughness probe after correcting eccentricity and tilt. The principle is depicted in fig. 5.6a (with the difference that the shaft is aligned upright). A part of the surface of

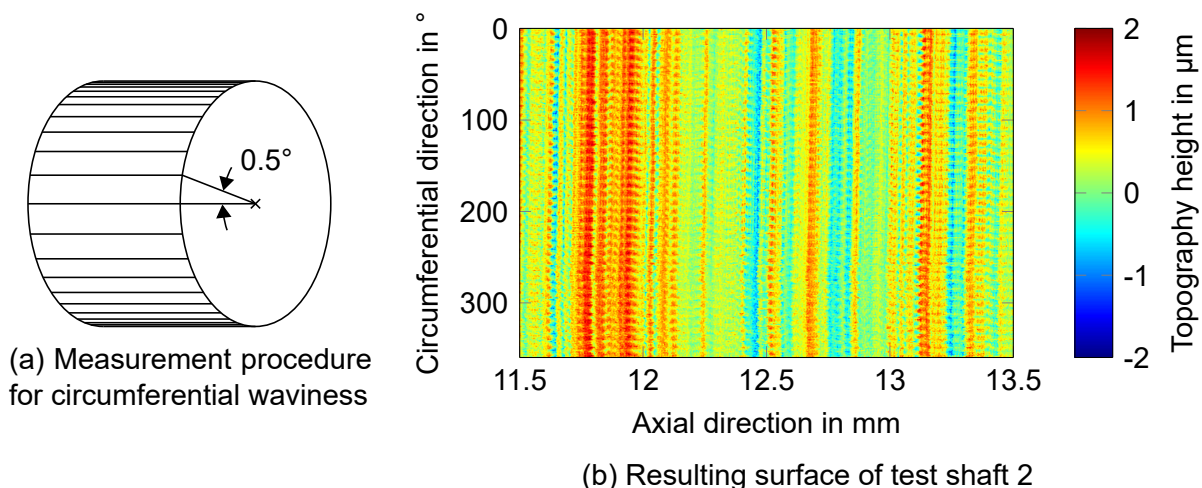


Figure 5.6: Measurements of circumferential waviness

test shaft 2, after subtracting the slope of each axial profile, is depicted in fig. 5.6b. While the structures are non-periodic in axial direction a periodic structure is clearly visible in circumferential direction. The averaged frequency spectra of two shafts in circumferential direction in fig. 5.7 reveal distinct periodic components. Averaging is performed over all 50.000 axial sample points (each axial profile was 25 mm long). The

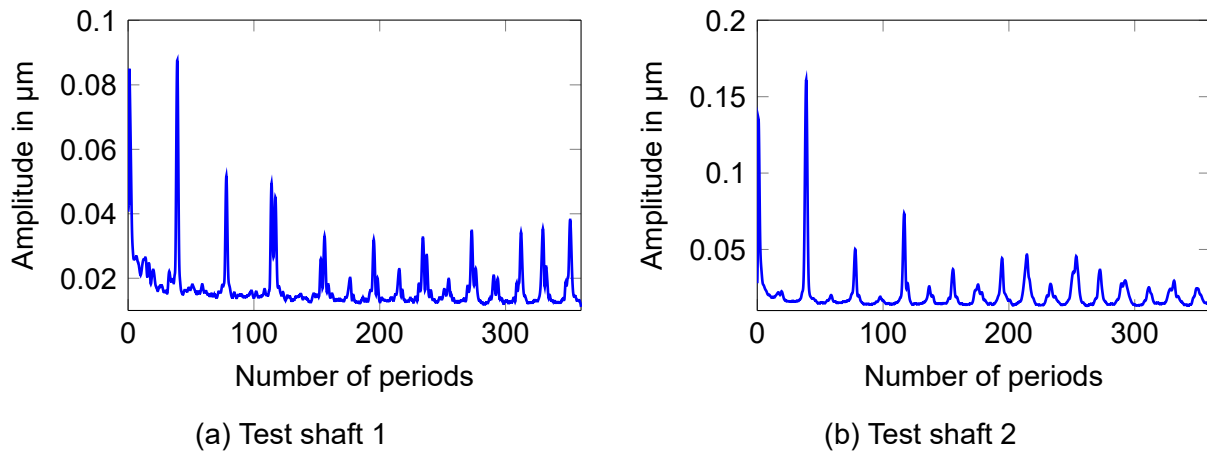


Figure 5.7: Averaged frequency spectra in circumferential direction

dominant peaks of both shafts are located at 39 periods. In terms of height parameters the structures' amplitudes in fig. 5.7 have to be doubled to range from min to max. This waviness around the circumference originates most likely from the manufacturing process. The structures are not commonly classified as lead as they fall in none of the known categories<sup>3</sup>. For further investigation it might be interesting to look at the phases at the dominant frequencies – although no clear relationship appears in fig. 5.6b. This could be well accomplished by regarding the cross-correlation with a sine-wave at the dominant frequency around the circumference.

### 5.1.2 Macro lead standards

Shafts with a known macro lead structure are a demanding test for the micro lead evaluation procedure (see section 4.3.2). Here, two ground macro lead measurement standards with  $DG = 10$  (DN10) and  $DG = 30$  (DN30) are tested. Exemplary measured topographies of DN10 and DN30 are shown in fig. 5.8. Both standards are measured in two axial positions in the rotating measuring system resulting in 144 measurements per shaft. The arithmetic means of the two positions on the shafts differ by less than  $1'$ , which is a small variation considering the standard deviation of around  $5'$  of DN10 and more than  $10'$  of DN30. Because of this small variation of  $\bar{\psi}_t$  72 measurements seem to provide a stable estimate of the distribution of  $\psi_t$  even with macro lead structures present.

To study the effects at different scales similar to section 4.3.2 an L-filter is applied and its nesting index is decreased from 100 to  $20\ \mu\text{m}$ . The curve of the mean of the micro lead angles of all 144 measurements as a function of the nesting index is plotted in fig. 5.9a. As the nesting index decreases the experimental standard deviation decreases. The

<sup>3</sup>Kersten detailed structures caused by oscillations whose arrangement of phases made them appear similar to dressing lead and sorted them into this category [78, pp. 29 sq.].

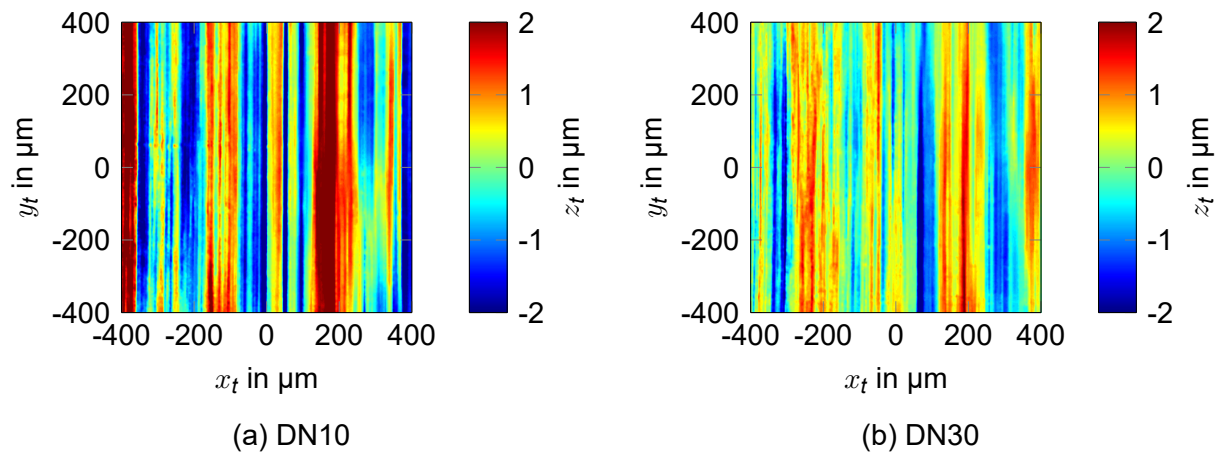
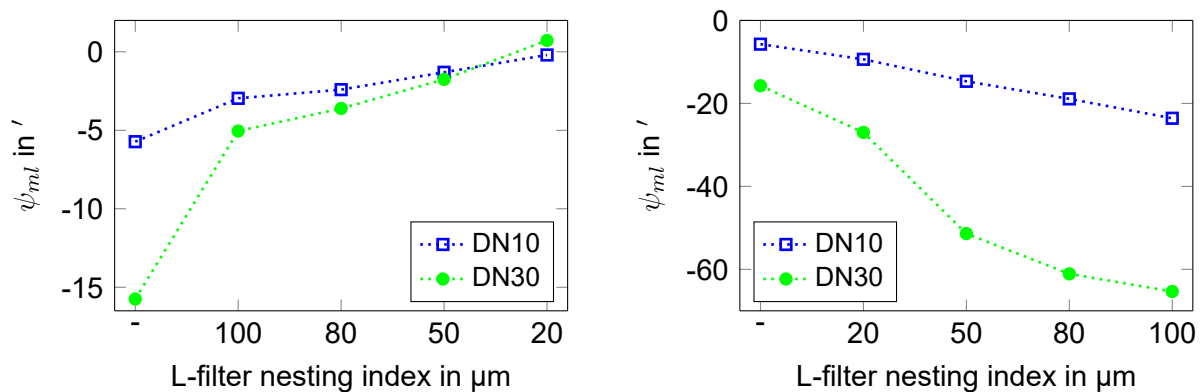


Figure 5.8: S-F surfaces of ground macro lead measurement standards

topographies become more homogeneous because the macro lead structures are suppressed. After suppressing almost all macro structures by applying a nesting index of  $20\ \mu\text{m}$  the fine micro structures emerge and coincide with the circumferential direction of the calibration shaft.  $s(\psi_{t,i})$  of DN10 is then only  $2.8'$  and  $6'$  of DN30. The principle appears clear. Yet, assuming that an L-filter with nesting index of  $20\ \mu\text{m}$  foregrounds the true orientation of the micro structures is based on micro lead-free grinding of the macro lead standards. But this cannot be verified without knowledge of the production process.

Figure 5.9b depicts  $\psi_{ml}$  of the shaft with topographies limited to the band between the



(a) Micro lead angle vs. L-filter nesting index

(b) Micro lead angle of band between L-filter and F-operation vs. L-filter nesting index

Figure 5.9: Measurements of macro lead standard with applied band-limiting

S-L surface and the S-F surface. They were generated by applying the L-filter to the S-F surface, letting low-frequency components pass. The curve progression can be interpreted by looking at the manufacturer's test reports of the macro lead standards<sup>4</sup>. Both

<sup>4</sup>There appears to be a mistake in the test report [67] regarding the sign of one of the results. Instead, the most likely case is assumed.

standards were tested to have negative lead angles and the angle of DN30 has a higher value of  $-38'$  compared to  $-19'$  of DN10 [67, 68]. The superposed macro structures appear to deviate the calculated texture orientation of the micro structures as it could also be observed in section 4.3.2. The observation leads to the question of assessing macro lead orientation from areal topographic measurements. Both curves follow the expected direction but do not converge at the expected macro lead angles. With increasing nesting index the variability rises beyond acceptable limits of more than  $20'$  for DN10 and more than  $30'$  for DN30. This shows that evaluating macro lead angles from such a small aperture does not succeed – at least not with the investigated method. However, this is not necessary anyway because a proven and accepted macro lead evaluation scheme exists in MBN 31007-7 [95]. It offers a wider range of information than a single magnified detail of shaft surface texture. The costs and efforts of generating an indication of the macro structures orientation are much higher than by the macro lead evaluation method according to [95].

### 5.1.3 Measurement standards for micro lead

Measurement results have to be traceable to a reference through a metrological traceability chain [36, pp. 42 sq.]. This requires the use of calibrated measurement standards. The availability of such standards is important to assess measurement uncertainty and to compare measurement principles, methods, and procedures. In the case of micro lead the design of a reference shaft with ground structures or structures resembling a ground surface with low measurement precision would be desired. A gradual inclination to circumferential direction would resemble micro lead structures most realistic. Knowing the structure's orientation from the production process is not a requirement as it can be calibrated later in a reference measurement procedure. The standard should be free of both geometric deviations like roundness or cylindricity deviations and superposed macro lead.

Research on the production of micro lead structures is available. Kersten described, how micro lead could be generated by either grinding with axial feed or by a parallelism deviation of grinding disc axis to shaft axis [78, pp. 14 sqq.]. He employed the latter to generate test shafts.

In an effort to manufacture micro lead measurement standards both methods Kersten described are tried in two series of ten shafts each. The parts were ground at the university's central machine workshop on an universal grinding machine. Grinding with axial feed and several passes in one direction resulted in a very high standard deviation disqualifying this method. Instead, a macro lead structure could be manufactured by grinding with crosswise axial feed<sup>5</sup>. Better results could be produced by tilting the

---

<sup>5</sup>More on the deliberate generation of macro lead can be found in [121].

axis of the grinding disc. All measurements are taken around the circumference with the rotating measuring system. The textures'  $s(\psi_{ml,i})$  of 72 circumferential measurements was only 2.8' on one of the ten test shafts and higher otherwise.  $\psi_{ml}$  varied in a range of more than 10' but the gradual inclination of the grinding disc is not reflected well throughout the series of parts. A main cause is assumed to be the tilting of the grinding disc which could not be adjusted satisfactory due to agglomerations between the slide guide surfaces of the grinding machine. More tests are needed but the preliminary results are promising.

Most stable results are achieved on turned shafts. By turning with small axial feed, the tool marks can be decreased to a minimum and the resulting surface texture resembles a ground surface to some extent (see fig. 5.10). The shaft of fig. 5.10a yields

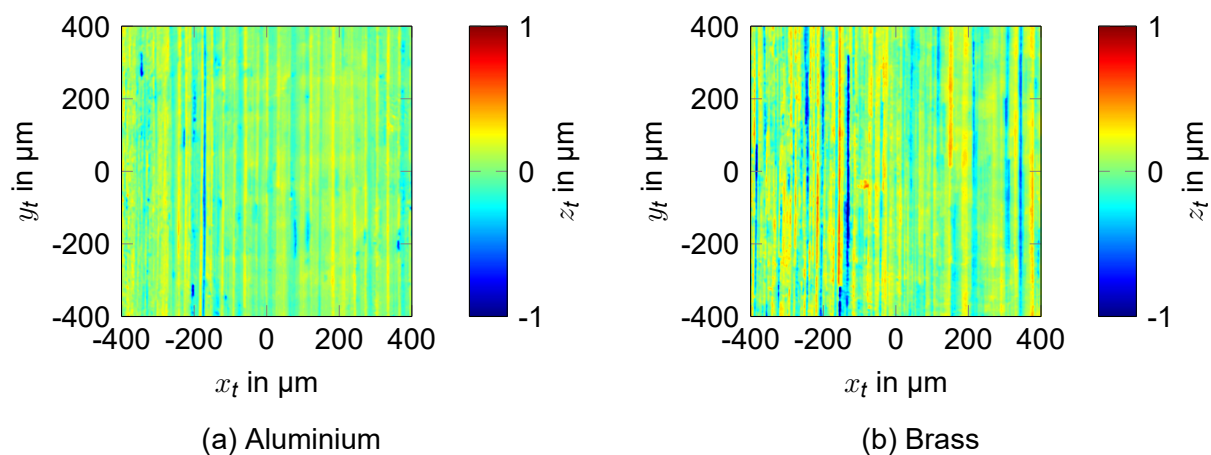


Figure 5.10: Two surface textures of turned shafts made of different materials

an experimental standard deviation of  $< 7'^6$  and fig. 5.10b of  $< 3'$  both with  $N = 72$ . The lowest variability was achieved on turned shafts with distinct turning grooves as shown in fig. 5.11. The brass shaft in fig. 5.11a is the ultra-precision turned surface of the calibration shaft from fig. 3.12. It yields an experimental standard deviation of  $\psi_t$  of 0.8' from 72 measurements and the stainless steel surface in fig. 5.11b of less than 0.5' from 36 measurements.

Besides low variability, turned shafts offer the benefit that with axial feed being controlled tightly or even measured during production, the inclination of the resulting tool marks is known exactly. In a stable turning process the shaft will exhibit only small geometric deviations.

<sup>6</sup>One of the 72 topography measurements exhibited a significant surface imperfection. Excluding it  $s(\psi_t)$  is less than 4'.



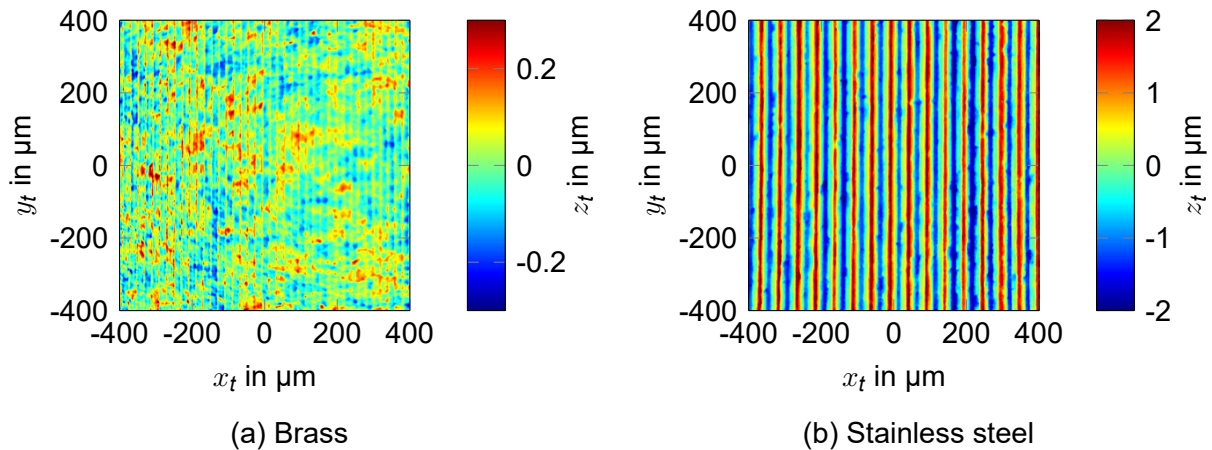


Figure 5.11: Two surface textures of turned shafts made of different materials

## 5.2 Discussion

Generally, micro lead will always be present because there will always be a statistical deviation between  $\psi_t$  and  $\psi_{circ}$  resulting in a non-zero  $\psi_{ml}$ . The results show that it is now possible to measure  $\psi_{ml}$  in an objective way. Limits on the level of acceptable  $\psi_{ml}$  were given by Kersten [78, pp. 101 sq.]. The presented methods can help to establish these limits for state of the art ground sealing surfaces and replace the demand 'free of lead' (cf. section 2.2.2) by tolerable limits.

Still, some points regarding the results are worth mentioning. These appear grouped in the following discussion for better overview.

**Micro lead evaluation** The required number of measurements depends on the desired uncertainty at a defined level of confidence and therefore on the parameters of the underlying distribution. More measurements describe the distribution better than only very few measurements. From the calculations of eqs. (5.5) to (5.7) and the results in table 5.1 it becomes clear that 144 measurements are more than enough for high demands even at a high level of confidence. 72 measurements will be acceptable for most applications and even the twelve measurements in fig. 5.4a provide a rough indication. The uncertainty values will become worse (i.e. possibly more realistic) with more influences on uncertainty regarded, e.g. positioning if applicable. And the values apply only to measurements without visible tilt of the shaft. Tilt will increase the standard deviation when an estimate for  $\psi_{ml}$  is calculated as arithmetic mean according to eq. (5.2). In this case a correction by a Fourier series as shown in fig. 3.21 appears beneficial. In case of non-circumferential measurements that are also subject to tilt, the arithmetic mean will be biased. Circumferential measurements are generally recommended in cases tilt can play a role and – as the measurements at different shaft positions in the v-block showed – can be beneficial in other cases as well. Further investigation into the meas-

measurements at different positions can be done with the help of ANOVA methods (cf. [75, pp. 98 sqq.]).

**Scale limiting** With the results of section 5.1.2 the question arises how scale-limiting affects  $\psi_{ml}$  of test shaft 1 and 2. The application of L-filters with nesting indices 50  $\mu\text{m}$  and 20  $\mu\text{m}$  in fig. 5.12 shows that the effects are much smaller than in the case of superposed macro structures. The limiting of the evaluated band by either of the meth-

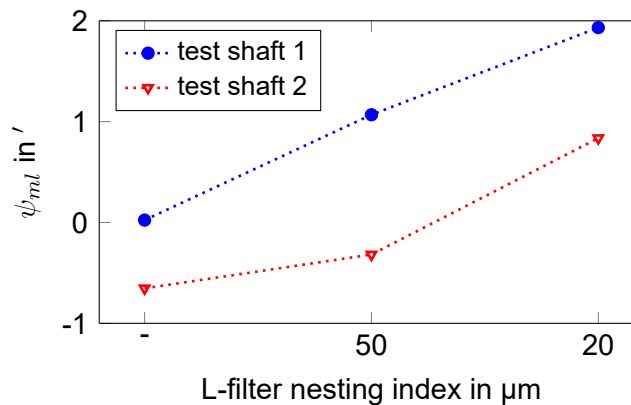


Figure 5.12: Effects of band-limiting of measurements of test shaft 1 and 2 on the micro lead angle

ods presented in section 4.3.2 might be useful in practical test runs when the potential cause of fluid transport is investigated. Kersten reported that fine micro structures, generated by a worn grinding disc, rather enhance axial fluid transport than structures from a freshly dressed disc with the same micro lead angle [78, p. 101].

**Handling of surface imperfections** In none of the above ground topographies scratches and other surface imperfections were sorted out. This approach is arguable because each imperfection changes the outcome to some extent. In industrial applications a method to detect surface imperfections might be available in a preceding or subsequent step. This could be a multi-sensor CMM similar to the set-up of Hollen and Leis [86, 66] or Beyerer [17] and Krahe [81, 80] (cf. section 2.3.3). Imperfection detection could also be included into the evaluation scheme of individual topographies. This could be used to prevent topographies from being evaluated and to automatically characterise individual imperfections that are found. However, the usefulness of characterising imperfections on the basis of random measurement positions on the shaft surface to quality control is limited because the sample size that can be measured with maintainable effort is small<sup>7</sup>.

<sup>7</sup>A shaft diameter of 80 mm requires more than 314 measurements with 800  $\mu\text{m}$   $\times$  800  $\mu\text{m}$  lateral size each to encompass the circumference without overlap.



Approaches to identify imperfections on the surface of ground shafts were and are studied at MTS.

**Measurement methods and procedures** Evaluating micro lead requires some effort. While measurements in v-blocks are comparably cheap regarding hardware costs, the manual workload is high. They appear appropriate for a manageable number of measurements. Measurements with the rotating measuring system are faster and require less manual work. Adjusting eccentricity and tilt can be automated and then only a rigid positioning frame for the measuring instrument is required. The high repeatability found in table 5.1 is promising. Yet, such systems are not readily available and considerably expensive. The mobile measuring system also requires a high manual effort but it might be the only option for measurements of large shafts. Some refinements, especially regarding the calibration shaft, are required before the prototype can be applied to actual measurements.

It is possible and likely that different measurement methods and principles, e.g. based on scattering light, scanning electron microscopy, atomic force microscopy and other might lead to slightly deviating results because they work at a much higher lateral resolution and can capture details that currently remain unresolved. Even with other measuring instruments or other magnification factors than  $20\times$  used as default in this work deviations are expected. Other instruments offer other optical configurations, too. Applying the same set-up for calibration and measurement is paramount.

**Results of the two test shafts** The minimal difference between the two test shafts comes as a surprise. The cooperation partner stated a difference of  $\approx 15'$ . But the stability of the values in table 5.1 and figs. 5.1 and 5.2 inspires confidence into the results obtained in this work. Another supporting fact is that both shafts showed no thread movement in measurements with a thread method according to a company standard by trained and experienced personnel. The difference of  $\approx 3'$  between the test shafts in another measurement without calibration is at the edge of a range that statistical variations can account for. These measurements should be repeated. Yet, both shafts exhibit micro lead structures that are below the limit of  $5'$ , which, according to Kersten, marks the beginning of fluid transport [78]. With neither micro or macro lead present at predominant levels the circumferential waviness detected in section 5.1.1 might be a possible culprit. More work and especially experimental verification with tests of pumping rates needs to be invested into this topic before the relevance of these structures can be confirmed or rejected. From the metrological standpoint it is clear that these structures are present on the shaft surface. They are also visible in macro lead measurements by a common roughness measuring instrument using both a tactile and a confocal chromatic probe.

### 5.3 Summary

In this chapter the two parts of micro lead evaluation, texture orientation and circumferential direction, were joined and the micro lead evaluation procedure was demonstrated on ground test shafts. Comparing both shafts the micro lead angles deviated less than stated by the shaft's provider. The difference also sustained after high-pass filtering of the topographies. Graphic representation of measurements in a v-block at different axial positions indicated that circumferential measurements are to be preferred over axial measurements. Measurements with a higher magnification showed a higher variability and a differing mean. Additionally, the shafts were evaluated for macro lead at different axial positions. Both lead types could not be detected at levels assumed to be significant from literature studies. Instead, periodic components around the shafts' circumference could be identified in macro lead measurements. Their role in axial fluid transport has yet to be assessed.

The effect of scale limiting on micro lead evaluation could be observed on two ground macro lead measurement standards. By letting only fine grinding marks pass the micro lead angle was found to be almost zero. Vice versa, after suppressing the fine texture, the micro lead angle deviated in the direction of the macro lead angle.

In order to test measurement methods and procedures micro lead measurement standards are required. Results of attempts aiming at their production were presented. The effectiveness of grinding with axial feed as a method to produce micro lead standards could be ruled out. Grinding with a tilted grinding disc could not fulfil the demands entirely either. Depending on the texture turned shafts could yield a low variability of orientations and some turned texture was found to resemble a ground texture to some extent. Whether grinding or turning is selected will depend on the intended purpose, i.e. if solely calibration of the micro lead angle is demanded or if other features like appearance or a realistic angular distribution need to be considered as well.

# 6 Conclusion

In this concluding chapter the thesis' contributions to the evaluation of micro lead are summarised and an outlook including current developments is given.

## 6.1 Summary

Lead structures can appear on shaft surfaces in dynamic sealing systems and enhance axial fluid transport under the sealing lip. This generally undesirable behaviour can cause the sealing system to fail by generating leakage or dry run. Besides macro lead, micro lead is one of the lead types that can be present on ground shaft surfaces. It is also known as setting lead and defined as the signed angle between the main texture orientation of the ground micro texture and circumferential direction [95]. It follows from this definition that the two characteristics that need to be assessed in order to quantify micro lead are main texture orientation of the ground micro texture  $\psi_t$  and circumferential direction  $\psi_{circ}$ .

Micro lead evaluation started with measuring the shaft surface. An areal measurement method was required to sample directional processing traces. Three optical areal-topographic measuring systems and the corresponding calibration method for shaft axis orientation were presented and discussed. A major concern was the relation of the chosen coordinate system to the measuring instrument's internal coordinate system to correctly estimate orientation with regard to the signed lead angle. One of the systems was a stationary measuring instrument with the optical axis aligned horizontally. The shaft was mounted on a rotary table in a vertical position enabling simple measurements around its circumference. Positioning of the instrument relative to the shaft could lead to angular deviations caused by the positioning frame but the effects were found to be small. The effects of eccentricity and tilt on texture orientation were studied on a model of the rotating shaft and the stationary instrument. The vertical alignment of the shaft made adjustment of eccentricity and tilt possible and their effects were therefore negligible. To calibrate the measuring instrument's orientation to the shaft's circumferential direction a calibration shaft was designed. Among several alternatives a circumferential groove was found to be well suited, but required a dedicated calibration procedure. The procedure used areal-topographic measurements and

iteratively fitted models of the groove bottom to detect the groove's orientation within a topography. Deviations as small as a quarter arc minute could be resolved easily by the presented procedure. The suitability of the calibration procedure was examined by regarding the metrological properties measurement resolution, sensitivity, accuracy, precision, and uncertainty. An alternative to the rotating measuring system was measuring the horizontal workpiece in a v-block under the upright instrument. In this case calibration could be performed on the v-block's edges or with the help of the calibration shaft. Using the v-block's edges suffered from a high variability, mainly caused by insufficient edge detection. The calibration shaft yielded good results with low variability. An effort to simplify calibration with the help of a grating acting as memory for shaft orientation was not successful, mainly because the mounting of the grating was not repeatable enough. A mobile measuring system was designed as third alternative. It was supposed to enable measurements of large shafts that could not be practically positioned relative to a common measuring instrument. The system had a v-block support and a coherence scanning interferometer as instrument. As before, calibration was conducted with the help of a calibration shaft. In an uncertainty study of the calibration procedure the shaft employed in this case was identified as the main contributor to the system's considerably high calibration uncertainty. The study also revealed that other contributions were small, rendering the system capable of the task.

Besides calibrating the orientation of the instrument to the shaft axis, characterising micro lead required knowledge of the main texture orientation. The discussed measuring instruments generated a microscopic topographic representation of the shaft surface. This topography was preprocessed to extract the relevant processing traces from the measurement and to minimise artefacts evoked by the instrument. To characterise  $\psi_t$  in topographic measurements the available standardised parameter for surface texture orientation could not be used because it was found to have an insufficient resolution — at least in its current implementation. A Radon transform was employed instead to estimate ground texture orientation. Several implementations of the Radon transform-based method were examined and compared and a scheme employing cubic spline interpolation was found suitable. Texture orientation was calculated from the Radon domain in an integral way. The method was made computational in reasonable time by an iterative scheme stepping from coarse to fine orientation. With adequate sampling of the discrete parameters, the method was capable of assessing texture orientation of ground unidirectional topographies in the low sub-arc minute range. Quarter arc-minute deviations could be resolved easily. Some practical applications were studied on simulated and measured topographies with regard to texture orientation, including the effects of varying topography sizes, effects of different apertures, and effects of superposed periodic structures and surface imperfections. Ways to decompose a topography into different scales were shown as well.

With both texture orientation and circumferential direction known, the micro lead angle  $\psi_{ml}$  could be calculated as difference between  $\psi_{circ}$  and  $\psi_t$ . To demonstrate the method's capability exemplary evaluations on test shafts and macro lead standards were presented. The test shafts were found to be free of micro and macro lead but a circumferential waviness was detected. Implications of this structures were not known and further research appeared indicated. Further, it could be shown empirically that measurements in a v-block were better taken around the circumference rather than axially. The usefulness of scale limiting on micro lead orientation estimation could be demonstrated on macro lead measurement standards. Finally, some approaches on the way to micro lead measurement standards were presented and discussed.

The presented method of using areal-topographic measurements with regard to shaft axis enables users to take objective measurements of micro lead on ground shaft surfaces. They are a step towards replacing the demand 'lead free' with objective limits on the extend of micro lead tolerable on shaft surfaces. Micro lead will always be observable to some extend due to statistical variations of involved quantities  $\psi_{circ}$  and  $\psi_t$ . The aim of this thesis was to develop the ability and practical methods and procedures to measure these structures in an objective way. A functional correspondence between micro lead orientation and its influences on the sealing system as well as realistic tolerances should be established in future research.

## 6.2 Further development

Having developed a method to assess micro lead with the help of several measuring systems, a round robin test of this and other measurement and characterisation methods for micro lead by other authors and research groups would be the next logical step. If supervised by an independent agency, e.g. a group of users or a national metrology institute, it can provide developers and users with the objective security and trust necessary for applying the methods. Such a test can also lead to the detection of potential mistakes and shortcomings in either of the methods and helps to improve the schemes. The tests would benefit from dedicated micro lead standards as discussed in section 5.1.3 either focussing on the appearance of ground surface texture or low variability of  $\psi_{ml}$ .

From the standpoint of sealing technology a functional relation between main texture orientation of the processing traces and the effects on axial fluid transport appears desirable. A number of test runs will be required and these need shafts with defined micro lead angles. The shafts should be tested for the presence of macro lead structures and circumferential waviness as well.

The current iterative Radon-based method could benefit from a fast implementation in a compiled programming language such as C++. With multithreading employed the eval-

uation time can certainly be decreased to around or below one minute per topography. A further speed-up can be expected by relaxing the dense sampling conditions. In case another method instead of the Radon-based is employed to assess texture orientation, e.g. the cross-correlation-based method developed at MTS (cf. [5, 6]), the calibration methods for circumferential direction can still be employed and vice versa. These two parts of micro lead evaluation do not depend on each other — as long as the circumferential direction is assessed somehow. The methods developed in this thesis, especially the ones to model ground surface texture and eccentricity and tilt, can be used to generate test schemes and to assess the performance of other micro lead evaluation methods based on areal topographic measurements, e.g. by Cohen [30] and Baitinger [8].

Further developments on the system side are concerned with a fast and robust method to detect micro lead structures in a production-related environment at-line, or even in-line. Instead of areal-topographic measurements an area-integrating method can be employed. It evaluates the scattering light reflected from the shaft. The principle was described by Kersten and the experimental system in fig. 6.1 is a modification of his set-up [78, pp. 78 sqq.] that was designed at MTS. Promising results could already

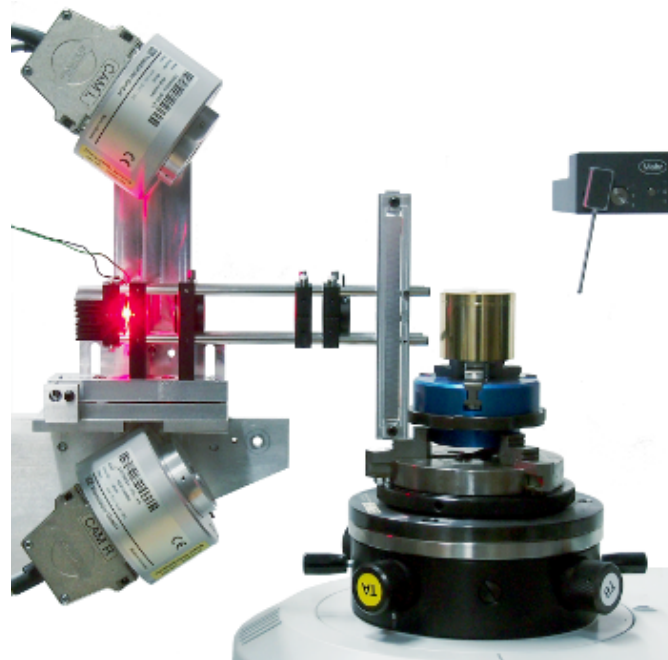


Figure 6.1: Overview of Kersten scattering light sensor mounted close to a roundness measuring instrument

be achieved but further qualifications and of course downsizing steps are required. A different sensor could possibly be set up on the basis of an optical Hough transform (cf. [135]) combined with a flat illumination. Height information would be lost in such a case, though.

Another interesting field is research into the theoretical foundation of the thread

method. This method is well established in industry and still used as comparison in science. It presumably can react on micro and macro lead alike. By understanding the interaction between thread and shaft surface the design of dedicated measuring methods in terms of sampling, resolution, etc. can be possible. It could also provide the community of industrial users with objective forecasts on the behaviour of their individual and proprietary methods. A model of the thread method was developed at MTS and first simulation results indicate realistic behaviour in accordance with measurements by cooperation partners.

# A Model of rotating shaft with stationary measuring instrument

A stationary objective of the measuring instrument sees a rotation of the shaft around the axis of the rotating table. When eccentricity and tilt from fig. 3.6 occur, the aperture is not centred on the shaft axis. This affects each measured topography on the circumference differently. First, the form component of the topography varies and second, the structures and their direction can appear distorted. In order to assess these effects, the rotating shaft is modelled as if it could be seen through a stationary window. The window represents the aperture of an areal-topographic measuring instrument with its optical axis aligned parallel to the  $y$  axis. The window's coordinates are single sample points  $\mathbf{x}_a(x, y, z) = (x_a, y_a, z_a)^T = (x, z, y)^T$ . By changing the window's  $x$  and  $z$  coordinates it can be placed freely on the  $x - z$  plane (see fig. A.1a).

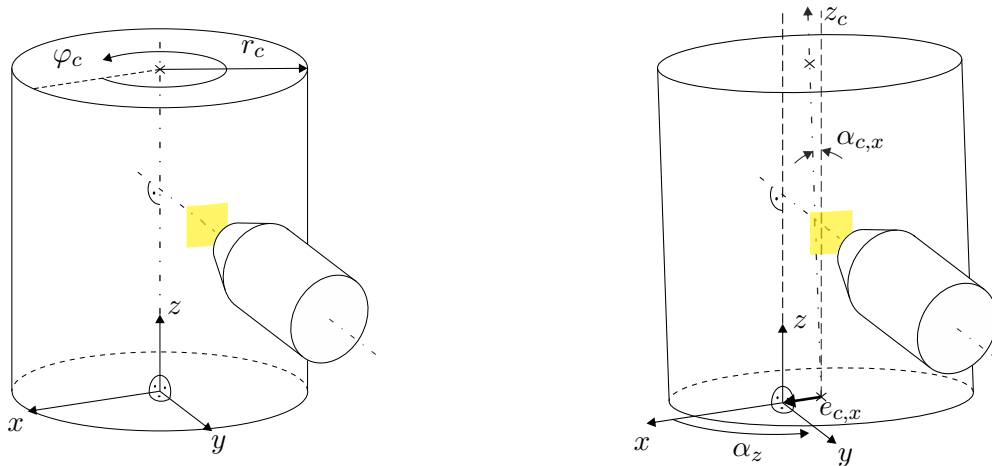
The shaft is modelled as a perfect cylinder in cylinder coordinates with radius  $r_c$  and angular coordinate  $\varphi_c$  as  $\mathbf{x}_c(x, y, z) = (x_c, y_c, z_c)^T = (r_c \cdot \cos \varphi_c, r_c \cdot \sin \varphi_c, z_c)^T$ . The coordinates are rotated around the  $x$  axis to simulate an inclination of  $\alpha_{c,x}$  to the axis of rotation. An eccentricity  $\mathbf{e}_c = (e_{c,x}, 0, 0)^T$  is added and the circumferential rotation with angle  $\alpha_z$  to perform circumferential measurements is applied. The situation is depicted in fig. A.1b. By adding the translation and rotations to  $\mathbf{x}_c$  the new model  $\mathbf{x}_{c,x,z}$  is given as

$$\mathbf{x}_{c,x,z} = \begin{pmatrix} x_{c,x,z} \\ y_{c,x,z} \\ z_{c,x,z} \end{pmatrix} = \begin{pmatrix} \cos \alpha_z \cdot (e_{c,x} + r_c \cdot \cos \varphi_c) - \sin \alpha_z \cdot (r_c \cdot \sin \varphi_c \cdot \cos \alpha_{c,x} - z_c \cdot \sin \alpha_{c,x}) \\ \sin \alpha_z \cdot (e_{c,x} + r_c \cdot \cos \varphi_c) + \cos \alpha_z \cdot (r_c \cdot \sin \varphi_c \cdot \cos \alpha_{c,x} - z_c \cdot \sin \alpha_{c,x}) \\ r_c \cdot \sin \varphi_c \cdot \sin \alpha_{c,x} - z_c \cdot \cos \alpha_{c,x} \end{pmatrix}. \quad (\text{A.1})$$

The model is a simplification of reality for the sake of shorter writing. If a more realistic model was required e.g. a rotation around the  $y$  axis and an eccentricity with  $e_{c,y} \neq 0$  could be added. But the steps detailed in the following stay essentially the same.

The measuring instrument is positioned with its optical axis parallel to the  $y$ -axis. To-





(a) Vertical shaft with areal-topographic measuring instrument

(b) Vertical shaft affected by excentricity and tilt

Figure A.1: Model of rotating shaft with stationary areal-topographic measuring instrument

pography height within the window  $z_a$  is the  $y_{c,x,z}$  coordinate of the shaft. These height values on the cylinder surface can be calculated from eq. (A.1) either analytically or by solving the equation numerically. By substituting  $x_{c,x,z} = x_a$  and  $z_{c,x,z} = y_a$  a solution for  $y_{c,x,z} = z_a$  requires the unknown  $z_c$  and  $\varphi_c$ . These are simply the roots of

$$\begin{aligned} \cos \alpha_z \cdot (e_{c,x} + r_c \cdot \cos \varphi_c) - \sin \alpha_z \cdot (r_c \cdot \sin \varphi_c \cdot \cos \alpha_{c,x} - z_c \cdot \sin \alpha_{c,x}) - x_a &= 0 \\ r_c \cdot \sin \varphi_c \cdot \sin \alpha_{c,x} - z_c \cdot \cos \alpha_{c,x} - y_a &= 0 \end{aligned} \quad (\text{A.2})$$

and they can be calculated with common numerical software. The analytical description has to take into account that a section parallel to the  $x-y$  plane through the tilted cylinder at height  $z_a$  appears as an ellipse rather than a circle. The cylinder coordinates are therefore not directly applicable. The coordinates of an ellipse are  $\mathbf{x}_e = (x_e, y_e, z_a)^T = (r_c \cdot \cos t_e, l_e \cdot \sin t_e, z_a)^T$  with

$$l_e = \frac{r_c}{\cos \alpha_{c,x}} \quad (\text{A.3})$$

and [147]

$$\tan t_e = \frac{l_e}{r_c} \cdot \tan \alpha_z. \quad (\text{A.4})$$

When the rotating ellipse is transformed to a fixed coordinate system the desired values  $\varphi_c$  rotate around the ellipse. The radius of the ellipse  $r_e$  is a function of  $\alpha_z$  [106, p. 117]:

$$r_e(\alpha_z) = \frac{r_c \cdot l_e}{\sqrt{r_c^2 \cdot \sin^2 \arctan\left(\frac{l_e}{r_c} \cdot \tan \alpha_z\right) + l_e^2 \cdot \cos^2 \arctan\left(\frac{l_e}{r_c} \cdot \tan \alpha_z\right)}}. \quad (\text{A.5})$$

The eccentricity  $e_{c,z}$

$$e_{e,z} = y_a \cdot \tan \alpha_{c,x} \quad (\text{A.6})$$

caused by tilt at the height  $z_a$  adds to the given eccentricity  $e_{c,x}$  from eq. (A.1):

$$e_{e,x} = e_{e,z} \cdot \sin \alpha_z + e_{c,x} \cdot \cos \alpha_z \quad (\text{A.7})$$

The  $\varphi_c$  are then calculated by evaluating the parametric equation of an ellipse with some geometric relations and applying a correction for the angular propagation:

$$\varphi_c = \arccos \left( \frac{x_a - e_{e,x}}{r_e} \right) - \arctan \left( \frac{l_e}{r_c} \cdot \tan \alpha_z \right) . \quad (\text{A.8})$$

Care must be taken to stay in the proper quadrant. Therefore, the subtrahend is corrected as

$$\arctan \left( \frac{l_e}{r_c} \cdot \tan \alpha_z \right) + 180^\circ \quad \forall \alpha_{c,z} \in [90, 270] . \quad (\text{A.9})$$

The values for  $z_c$  are found by substituting eq. (A.8) into eq. (A.2):

$$z_c = \frac{y_a - r_c \cdot \sin \varphi_c \cdot \sin \alpha_{c,x}}{\cos \alpha_{c,x}} , \quad (\text{A.10})$$

and finally the height values  $z_a$  on the measured topography are found by substitution of eq. (A.8) and eq. (A.10) into eq. (A.1).

Figure A.2 shows two topographies of a shaft with  $r_c = 40$  mm at  $\alpha_z = (0^\circ, 235^\circ)$ .  $\alpha_{c,x} = 34.38''$ ,  $e_{c,x} = 10$   $\mu\text{m}$ , and the distance from the centre of rotation to the position of measurement is 60 mm. These are the parameters from footnote 2 in section 3.1.2. The lateral field of view is 800  $\mu\text{m} \times 800$   $\mu\text{m}$ .

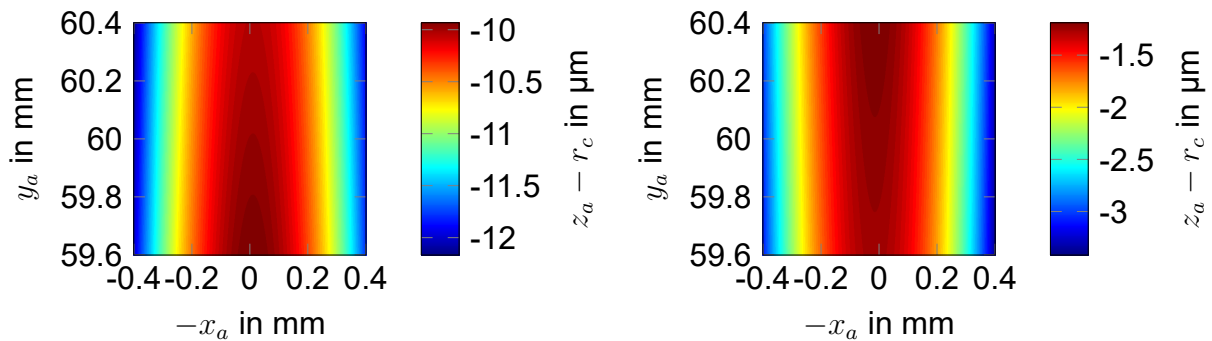


Figure A.2: Two simulated topographies at  $\alpha_z = 0^\circ$  (left) and  $\alpha_z = 235^\circ$  (right)

## B Groove model for uncertainty evaluation

The model of a groove described in the following is used in the Monte Carlo simulation in section 3.3.3 to estimate the uncertainty of the evaluation procedure.

The characteristics composing a measured topography are identified as cylinder form, calibration groove, deviation from ideal groove shape, small turning grooves, and noise. All these five model characteristics are additional. The modelled topography with height values  $z_m$  is then the sum of these individual characteristics:

$$z_m = z_{m_1} + z_{m_2} + z_{m_3} + z_{m_4} + z_{m_5} . \quad (\text{B.1})$$

The parameter values governing their occurrence on a modelled topography are taken from a range of values described by individual distributions. Realistic values were found by inspecting 34 measured topographies. The numerical parameter values and respective distributions are tabulated in table B.1. They are derived from CSI measurements of  $530 \mu\text{m} \times 400 \mu\text{m}$  after preprocessing with a  $9 \times 9$  pixel median filter and an areal Gaussian filter with  $8 \mu\text{m}$  nesting index. Additional steps to extract the information of interest are described below in the corresponding paragraph.

The **cylinder form of the shaft**  $z_{m_1}$  with radius  $r = 40 \text{ mm}$  visible in one areal-topographic measurement includes a circular sector of  $0.76^\circ$ . It is calculated as

$$z_{m_1} = \sqrt{r^2 - y_t^2} - r . \quad (\text{B.2})$$

The cylinder form is not varied in the simulation.

The **calibration groove** is modelled by a ball with radius  $r_g$  passing through a topography. The ball's position is evaluated along a linear path depicted in fig. B.1. The height  $z_{m_2}$  of each sample  $(x_t, y_t)$  is then given by

$$z_{m_2}(x_t, y_t) = z_b + r_g \cdot \cos \left( \arcsin \left( \frac{x_t + \rho_b \cdot \sin \varphi_g - s_b \cdot \cos \varphi_g}{r_g \cdot \cos \left( \arctan \left( \frac{y_t - \rho_b \cdot \cos \varphi_g - s_b \cdot \sin \varphi_g}{x_t + \rho_b \cdot \sin \varphi_g - s_b \cdot \cos \varphi_g} \right) \right)} \right) \right) . \quad (\text{B.3})$$

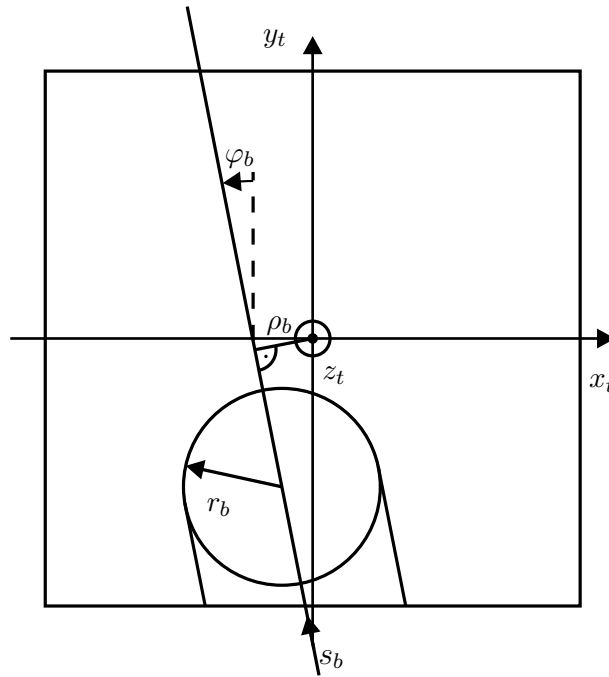


Figure B.1: Path of ball on simulated topography

Providing the parameters groove depth  $t_g$  and width  $b_b$  the ball centre's height above the surface  $z_b$  yields

$$z_b = \frac{b_b^2}{8 \cdot t_g} - \frac{t_g}{2}. \quad (\text{B.4})$$

The ball's radius  $r_g$  is then

$$r_g = t_g + z_b. \quad (\text{B.5})$$

The largest angle  $\alpha_{g,max}$  at the edge of the groove is

$$\alpha_{g,max} = \arccos \frac{b}{r_g} = \arccos \frac{z_b}{t_g + z_b}. \quad (\text{B.6})$$

Realistic values for  $t_g$  and  $b_b$  are found by inspection of the measured topographies. These calibration groove's parameters are seen as fixed and are not varied in the simulation.

A **deviation from the ideal groove shape** is modelled by a sinusoidal oscillation with parameters amplitude  $A_{gs}$ , wavelength  $\lambda_{gs}$ , and phase  $\varphi_{gs}$ :

$$z_{m3}(x_t, y_t) = A_{gs} \cdot \sin(2\pi/\lambda_{gs} \cdot x_t + \varphi_{gs}). \quad (\text{B.7})$$

In the simulation all three are assigned a symmetric normal distribution. Realistic values are obtained from the central part of the grooves from the measured topographies. The groove shape was removed by subtracting algebraic fitted parabolas with a groove angle  $\alpha_g = 20^\circ$  from each topography section perpendicular to the groove. By disregarding the outer parts of the groove in axial direction, distortion from the cylinder sur-

face had no influence on the available frequencies. Mean amplitude and wavelength are found as the average of the highest peak of the magnitude of 1D Fourier transforms for each profile perpendicular to the groove of each topography. Its standard deviation is the standard deviation of the amplitudes/wavelengths of all 34 measured topographies. Distribution of phase is obtained in a similar way by cross correlation of a sine wave with mean amplitude and wavelength.

Low amplitude **turning grooves** run approximately parallel to the groove and are modelled as sine waves:

$$z_{m_4}(x_t, y_t) = A_{tg} \cdot \sin(2\pi/\lambda_{tg} \cdot x_t + \varphi_{tg}) . \quad (\text{B.8})$$

Parameters for  $A_{tg}$  and  $\lambda_{tg}$  are estimated from the measured topographies similar to the deviation from the ideal groove shape. The spectra reveal several peaks so instead of selecting one wave, the second and third peak in the averaged DFT's magnitude are regarded. Thus each modelled topography contains two oscillations each with uniformly distributed amplitude, wavelength, and phase. A uniform distribution is chosen because wavelengths and amplitudes could not be seen to follow a normal distribution. However, no statistical tests were performed. Fringe order errors [107, p. 102] can be ruled out as the cause for the appearance of turning grooves because the evaluation algorithm [126] is set to evaluate each correlogram's envelope without considering phase information.

Trials show the remaining **noise** has a significant influence on the performance of the evaluation algorithm. It is modelled to visually resemble the autocorrelation function and the histogram of the noise on measured topographies. First, three sinusoidal oscillations with uniform distributions of amplitude, wavelength, and phase are superposed. They are added to a normally distributed white noise whose standard deviation is uniformly distributed between topographies but constant on one topography. The resulting topography with height values  $z_{m_5}$  is filtered successively by two orthogonal FIR filters (one runs in  $x_t$  and one in  $y_t$  direction) with fixed order and cut-off index. The FIR filters in  $x_t$  and  $y_t$  direction were empirically designed to match the autocorrelation length in axial direction (perpendicular to the groove) of processed measured topographies. Additionally, a random number of peaks with random height is scattered at random positions across the topography. These three peak parameters are uniformly distributed. Eventually, an areal Gaussian filter with nesting index  $8 \mu\text{m} \times 8 \mu\text{m}$  flattens the surface and broadens the peaks. Realistic parameters were obtained from the measured topographies after removing longer and shorter wavelengths by high- and lowpass filtering with an areal Gaussian filter with nesting indices of  $25 \mu\text{m} \times 25 \mu\text{m}$  and  $8 \mu\text{m} \times 8 \mu\text{m}$ .

Table B.1 lists the model parameters and respective distributions derived.

Table B.1: Parameters of the Monte Carlo simulation to evaluate the evaluation algorithm's uncertainty

| Component                               | Parameter          | Distrib. | Exp. value/<br>low. bound | Std. dev./<br>up. bound |
|---|--------------------|----------|---------------------------|-------------------------|
| Cylinder form                           | Radius             | -        | 80 mm                     | -                       |
| Calibration groove                      | Groove depth       | -        | 40 $\mu\text{m}$          | -                       |
|   | Groove width       | -        | 350 $\mu\text{m}$         | -                       |
|   | Groove orientation | -        | -1'                       | -                       |
| Deviation of shape                      | Amplitude          | Normal   | 1.5 $\mu\text{m}$         | 0.4 $\mu\text{m}$       |
|   | Wavelength         | Normal   | 203.3 $\mu\text{m}$       | 16.1 $\mu\text{m}$      |
|   | Phase              | Normal   | -54.4°                    | 3.8°                    |
| Turning grooves 1                       | Amplitude          | Uniform  | 0.22 $\mu\text{m}$        | 0.64 $\mu\text{m}$      |
|   | Wavelength         | Uniform  | 37.9 $\mu\text{m}$        | 98 $\mu\text{m}$        |
|   | Phase              | Uniform  | 0                         | $2 \cdot \pi$           |
| Turning grooves 2                       | Amplitude          | Uniform  | 0.11 $\mu\text{m}$        | 0.48 $\mu\text{m}$      |
|   | Wavelength         | Uniform  | 22.8 $\mu\text{m}$        | 68.3 $\mu\text{m}$      |
|   | Phase              | Uniform  | 0                         | $2 \cdot \pi$           |
| Noise: oscillation                      | Amplitude          | Uniform  | 0 $\mu\text{m}$           | 0.1 $\mu\text{m}$       |
|   | Wavelength         | Uniform  | 8 $\mu\text{m}$           | 25 $\mu\text{m}$        |
|   | Phase              | Uniform  | 0                         | $2 \cdot \pi$           |
| Noise: Normally distributed white noise | Standard dev.      | Uniform  | 1 $\mu\text{m}$           | 4 $\mu\text{m}$         |
| Noise: FIR filter $x_t$                 | Order              | -        | 100                       | -                       |
|   | Normalised cut off | -        | 0.01                      | -                       |
| Noise: FIR filter $y_t$                 | Order              | -        | 10                        | -                       |
|   | Normalised cut off | -        | 0.2                       | -                       |
| Noise: peaks                            | Number             | Uniform  | 1                         | 100                     |
|   | Height             | Uniform  | 1 $\mu\text{m}$           | 150 $\mu\text{m}$       |
|   | Position $x_t$     | Uniform  | -199.6 $\mu\text{m}$      | 199.6 $\mu\text{m}$     |
|   | Position $y_t$     | Uniform  | -266.25 $\mu\text{m}$     | 266.25 $\mu\text{m}$    |
| Noise: final filter                     | Nesting index      | -        | 8 $\mu\text{m}$           | -                       |

## C Modelling directional surface texture

Directional surface texture can be analysed in the Radon domain. An inversion of the Radon domain is possible using different techniques, see e.g. [140, 73]. The texture's desired parameters can therefore be designed in the Radon domain and transformed back into the spatial domain. This idea was also proposed by Beyerer [17, p. 45].

The parameters of directional surfaces manifest as peaks in the Radon domain. The principal degrees of freedom  $DF_i$  with  $i = (1, 2, \dots)$  are displayed in fig. C.1. Each

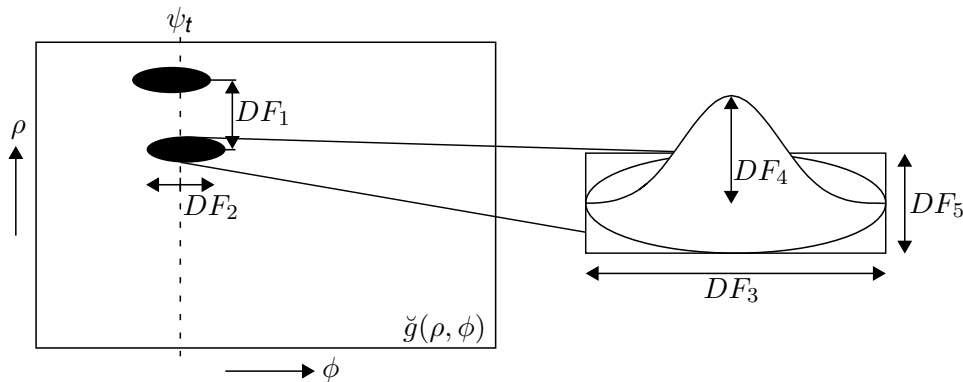


Figure C.1: Several principal degrees of freedom in designing directional surface texture

single peak's position, i.e. its distance from other peaks in  $\rho$  direction ( $DF_1$ ) and its angular position ( $DF_2$ ), can vary as well as the peak's lateral extend in  $\rho$  ( $DF_5$ ). Peaks and valleys can be generated by a Gaussian distribution and vary in height ( $DF_4$ ) and angular width ( $DF_3$ ). Each degree of freedom can be modelled by an adequate probability distributions. Here, only Gaussian and rectangular distributions are used. By adding some kind of noise to the complete Radon domain or selected areas and subsequent filtering with linear or non-linear filters can generate a realistic appearance of the Radon domain of various surface textures. The filtering can also be used to shape the peak's or valley's appearance. By repeating the steps, different distributions can be superposed and several directions can be generated.

Having modelled the topography in the Radon domain its representation is transformed back into the spacial domain. Here, Matlab's filtered back projection algorithm and its conveniently adjustable parameters are used.

In a post-processing step the simulated topography can be adapted to the material's

or the production process's characteristics (e.g. by adding noise etc.) that are more complex to describe in the Radon domain.

A shortcoming of the technique is that the resulting structures all have maximal length. The reason is that the local height of a peak or depth of a valley in Radon space is influenced either by the length of structures or their height/depth in the spatial domain. Integrating along a longer structure adds up more samples of low amplitude and the resulting peak can be equally high as if the structure was short and high. This information is lost when only peaks are considered without regarding the corresponding sinusoidal curve produced by mapping a topography point into the Radon domain according to eqs. (4.1) and (4.3).

An simple exemplified outcome of the procedure is the simulation of a honed-like surface texture in fig. C.2. Parts of the procedure were reiterated to generate two an-

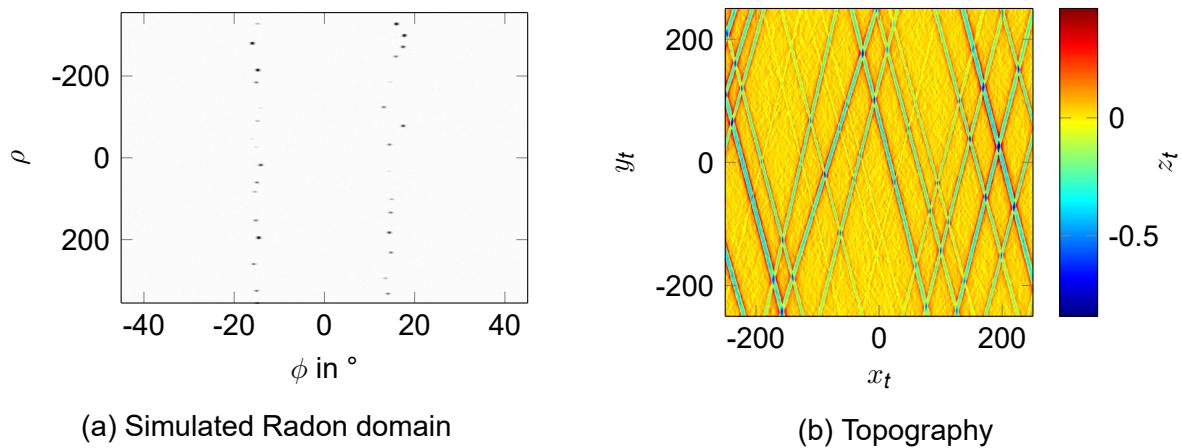
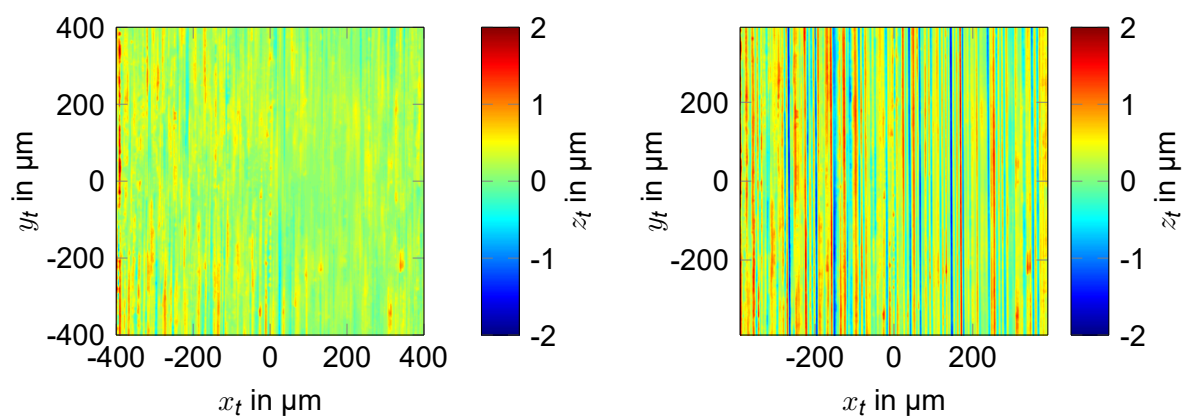


Figure C.2: Simple simulation of a honed surface

gular distributions. The holes at intersections can be removed by further processing in the spatial domain.

Another example is the generation of a ground surface texture in fig. C.3. The non-directional parts in fig. C.3a are taken from the measured topography in fig. 4.3a by applying alternating sequential filters. The superposition of a simulated ground topography from fig. 4.17b with the non-directional part is pictured in fig. C.3b.





(a) Non-directional parts of fig. 4.3a

(b) Superposition of non-directional parts and simulated ground surface texture

Figure C.3: Simple simulation of a ground surface texture

# List of Figures

|      |   |    |
|------|---|----|
| 2.1  | Simplified and exaggerated illustration of lead types . . . . .   | 4  |
| 2.2  | Simplified and exaggerated macro lead structures as developed lateral shaft surfaces according to [95] . . . . .  | 5  |
| 2.3  | Macro lead parameter according to MBN 31007-7 and [3] . . . . .   | 6  |
| 2.4  | Positive micro lead angle $\psi_{ml}$ as deviation of main texture orientation of the ground micro texture $\psi_t$ from circumferential orientation $\psi_{circ}$ according to [4] . . . . . | 7  |
| 2.5  | Axial section through a typical rotary shaft lip-type seal based on [7, p. 348]   | 7  |
| 3.1  | Picture of the rotating measuring system . . . . .  | 24 |
| 3.2  | Set-up of the rotating measuring system . . . . .   | 24 |
| 3.3  | Coordinate system within a topography . . . . .   | 26 |
| 3.4  | Coordinate system of a topography with structures with a positive lead angle (right-handed lead) and their appearance in different coordinate systems . . . . .                               | 26 |
| 3.5  | Measurement of a right-hand threaded screw measured similar to fig. 3.2 to determine topography orientation . . . . .   | 27 |
| 3.6  | Eccentricity and tilt to the axis of rotation in a vertical rotating measuring system . . . . .   | 29 |
| 3.7  | Simulated orientation of circumferential structures on a rotated shaft . .  | 30 |
| 3.8  | Individual variation of either eccentricity, tilt, distance from clamping position, or shaft diameter . . . . .   | 31 |
| 3.9  | Individual variation of distance from clamping position up to maximal limit   | 32 |
| 3.10 | Two simulated orientations of circumferential structures on a rotated shaft   | 32 |
| 3.11 | Sketch of an axial section through the calibration groove . . . . .   | 35 |
| 3.12 | Image of brazen ultra-precision turned calibration shaft . . . . .  | 35 |
| 3.13 | Limiting procedure for one profile . . . . .  | 37 |
| 3.14 | Central groove section of ultra-precision turned shaft . . . . .  | 39 |
| 3.15 | Set-ups with angular adjustment stage to investigate distinguishable variations in structure orientation . . . . .  | 41 |
| 3.16 | Incremental rotation of depth setting standard and identified orientation   | 41 |

|      |  |    |
|------|--|----|
| 3.17 | Deviations from true orientations for three realistic groove models . . . .  | 43 |
| 3.18 | Results for groove $b_{g,1}$ of the calibration shaft for all three methods . . . .  | 44 |
| 3.19 | Results for grooves $b_{g,1}$ and $b_{g,2}$ measured with two objectives . . . . .   | 45 |
| 3.20 | Combined uncertainty of all three evaluation methods . . . . .   | 47 |
| 3.21 | Residuals of a Fourier series with two terms of curves from figs. 3.7<br>and 3.10 . . . . .  | 48 |
| 3.22 | Schematic set-up of non-rotating measuring system . . . . .  | 51 |
| 3.23 | Landmark grating and the actual set-up . . . . .   | 52 |
| 3.24 | Flatness tolerances of the upper and contact surfaces affecting edge<br>orientation according to [5] . . . . .   | 54 |
| 3.25 | Calibration results on the v-block's geometry . . . . .  | 56 |
| 3.26 | Considerations on the required number of measurements on the v-block   | 57 |
| 3.27 | Relation between the number of measurements $M$ and the expanded un-<br>certainty of axis orientation $U_{99,73}$ from measurements on the calibration<br>shaft . . . . .    | 57 |
| 3.28 | Measurements at the landmark . . . . .   | 59 |
| 3.29 | Schematic and prototype of the mobile measuring system . . . . .   | 62 |
| 3.30 | L-frame and v-block support . . . . .  | 63 |
| 3.31 | Microscopic image and height profile of calibration groove . . . . .   | 64 |
| 3.32 | Modulation depth of CSI groove measurement and corresponding topo-<br>graphy . . . . .   | 65 |
| 3.33 | 15 measurements of rotated calibration shaft (cf. section 3.1.3) . . . . .   | 66 |
| 3.34 | Form and roundness deviations and their effects on measured axis ori-<br>entation; a: roundness deviation; b: cylindricity deviation; c: coaxiality de-<br>viation . . . . . | 69 |
| 3.35 | Evaluated orientations from the Monte Carlo simulation with evaluation<br>method profile . . . . .   | 72 |
| 3.36 | Expected roundness uncertainty from local shaft diameter variations for<br>different axial lengths . . . . .   | 74 |
| 4.1  | Resolved texture orientation with Std parameter in its current implement-<br>ation . . . . .   | 78 |
| 4.2  | Coordinate system based on fig. 3.3 with an exemplary line . . . . .   | 83 |
| 4.3  | Exemplary ground shaft sealing surface and its Radon domain repres-<br>entation . . . . .  | 84 |
| 4.4  | 2D interpolation scheme . . . . .  | 84 |
| 4.5  | Interpolation using cubic B-splines . . . . .  | 86 |
| 4.6  | End effects in the Radon transform implementation using cubic splines .  | 87 |
| 4.7  | Illustration of the non-interpolating method . . . . .   | 88 |

|      |   |     |
|------|---|-----|
| 4.8  | Selecting relevant pixels around a beam . . . . .   | 89  |
| 4.9  | Orientation curves of fig. 4.3 . . . . .  | 90  |
| 4.10 | Angular step size using 1D nearest neighbour interpolation . . . . .  | 91  |
| 4.11 | Exemplary sinusoidal surface and results from cubic spline implementations and different orientation curves . . . . .   | 92  |
| 4.12 | Peaks around 90° in orientation curves for different implementations . . . . .  | 93  |
| 4.13 | Scaled projection profiles of the implementations around 90° . . . . .  | 94  |
| 4.14 | Calculated main texture orientation of rotated shaft . . . . .  | 94  |
| 4.15 | Variation of two sampling parameters . . . . .  | 96  |
| 4.16 | Iterative procedure to assess main texture orientation [6] . . . . .  | 98  |
| 4.17 | Simulated topographies to empirically assess characteristics of evaluation procedures . . . . .                         | 99  |
| 4.18 | Effects of the length of linear structures of equal width on possible orientations . . . . .                            | 100 |
| 4.19 | Results of topography size variations . . . . .   | 101 |
| 4.20 | Effects in the detected texture orientation caused by changing from full to circular aperture . . . . .                 | 102 |
| 4.21 | Scale-limited S-F and S-L surfaces . . . . .  | 103 |
| 4.22 | Scale-limited surfaces from alternating sequential filtering . . . . .  | 103 |
| 4.23 | Simulated topographies with one or two dents . . . . .  | 104 |
| 4.24 | Mean absolute deviation and standard deviation of topographies with one or two dents . . . . .                          | 105 |
| 4.25 | Results from superposing simulated 2D sinusoidal and ground texture . . . . .   | 106 |
| 4.26 | Deviation from texture orientation as a result of superposed macro lead structures . . . . .                            | 107 |
| 4.27 | Effects of scale-limiting on a measured topography affected by simulated macro lead . . . . .                           | 108 |
| 5.1  | Texture orientation of test shaft 1 . . . . .   | 113 |
| 5.2  | Texture orientation of test shaft 2 . . . . .   | 114 |
| 5.3  | Measured calibration orientation of groove $b_{g,3}$ with arithmetic mean and experimental standard deviation . . . . . | 114 |
| 5.4  | Texture orientation of shaft measured at several axial positions in a v-block . . . . .                                 | 115 |
| 5.5  | Texture orientation measured with two different objectives on test shaft 1 and fitted normal distribution . . . . .     | 117 |
| 5.6  | Measurements of circumferential waviness . . . . .  | 118 |
| 5.7  | Averaged frequency spectra in circumferential direction . . . . .   | 119 |
| 5.8  | S-F surfaces of ground macro lead measurement standards . . . . .   | 120 |
| 5.9  | Measurements of macro lead standard with applied band-limiting . . . . .  | 120 |

---

- 5.10 Two surface textures of turned shafts made of different materials . . . . 122
- 5.11 Two surface textures of turned shafts made of different materials . . . . 123
- 5.12 Band-limiting effects of test shafts . . . . . 124
  
- 6.1 Overview of Kersten scattering light sensor . . . . . 130
  
- A.1 Model of rotating shaft with stationary areal-topographic measuring instrument . . . . . 133
- A.2 Two simulated topographies at  $\alpha_z = 0^\circ$  (left) and  $\alpha_z = 235^\circ$  (right) . . . 134
  
- B.1 Path of ball on simulated topography . . . . . 136
  
- C.1 Several principal degrees of freedom in designing directional surface texture . . . . . 139
- C.2 Simple simulation of a honed surface . . . . . 140
- C.3 Simple simulation of a ground surface texture . . . . . 141

# List of Tables

|     |   |     |
|-----|---|-----|
| 2.1 | Overview of roughness parameters found in different standards . . . . .   | 9   |
| 2.2 | Macro lead measurement methods sorted by surface texture measurement methods . . . . .  | 15  |
| 2.3 | Overview of publicly available literature on thread methods sorted by time of publication . . . . .   | 20  |
| 3.1 | Objectives and lateral properties of the confocal microscope . . . . .  | 25  |
| 3.2 | Description and results of six series of 50 repeated measurements each after positioning and clamping of the support frame . . . . .                          | 28  |
| 3.3 | Expected advantages and disadvantages of shapes on calibration shafts   | 34  |
| 3.4 | Calculated absolute orientations of the depth setting standard and arithmetic mean $\bar{\psi}_{circ}$ of circumferential measurements of calibration grooves | 42  |
| 3.5 | Measurement precision on circumferentially measured calibration shaft from fig. 3.12 . . . . .  | 44  |
| 3.6 | Results of 36 circumferential calibration measurements of groove orientation with the mobile measuring system . . . . .                                       | 66  |
| 3.7 | Results from Monte Carlo simulation of 1000 calibration topographies .  | 71  |
| 4.1 | Parameters of underlying macro lead structures related to [116] . . . . .   | 107 |
| 5.1 | Results of calibration measurement, texture orientation, and micro lead angle of test shafts . . . . .  | 115 |
| 5.2 | Arithmetic mean and experimental standard deviation of macro lead parameters of five axial sections of the test shafts . . . . .                              | 117 |
| B.1 | Parameters of the Monte Carlo simulation to evaluate the evaluation algorithm's uncertainty . . . . .   | 138 |

# Bibliography

- [1] Ahn, Sung Joon, Rauh, Wolfgang, and Recknagel, Matthias. *Geometric Fitting of Line, Plane, Circle, Sphere, and Ellipse*. 25.-26. 01. 1999.
- [2] Ahn, Sung Joon, Rauh, Wolfgang, and Warnecke, Hans-Jürgen. "Least-squares orthogonal distances fitting of circle, sphere, ellipse, hyperbola, and parabola". In: *Pattern Recognition* 34.12 (2001), pp. 2283–2303. ISSN: 00313203. DOI: 10.1016/S0031-3203(00)00152-7.
- [3] Arnecke, Philipp. *Drall MBN 31007-7: Flyer*. Ed. by Institute for Measurement and Sensor-Technology. 2015. URL: [https://www.mv.uni-kl.de/fileadmin/mts/dokumente/Flyer\\_MBN\\_31007-7.pdf](https://www.mv.uni-kl.de/fileadmin/mts/dokumente/Flyer_MBN_31007-7.pdf) (visited on 12/30/2015).
- [4] Arnecke, Philipp, Boecker, Burkhard, and Seewig, Jörg. "Ein mobiles zur Mikrodrallmessung geeignetes Messsystem und dessen Kalibrierung - accepted, but not yet published". In: *tm – Technisches Messen* (). ISSN: 0171-8096.
- [5] Arnecke, Philipp and Seewig, Jörg. "A Strategy for Micro-Twist Characterization on the Shaft in a Rotary Shaft Sealing System". In: *18th ISC, International Sealing Conference, Internationale Dichtungstagung*. 2014, pp. 653–666. ISBN: 978-3-00-046879-7.
- [6] Arnecke, Philipp and Seewig, Jörg. *Characterisation of texture orientation on ground surfaces with high accuracy*. 15. International Conference on Metrology and Properties of Engineering Surfaces, Charlotte, North Carolina, USA, 03/03/2015.
- [7] Baart, P., Lugt, P. M., and Prakash, B. "Review of the lubrication, sealing, and pumping mechanisms in oil- and grease-lubricated radial lip seals". In: *Proceedings of the Institution of Mechanical Engineers, Part J: Journal of Engineering Tribology* 223.3 (2009), pp. 347–358. ISSN: 1350-6501. DOI: 10.1243/13506501JET473.

- [8] Baitinger, Gert. *Multiskalenansatz mit Mikrostrukturanalyse zur Drallbeurteilung von Dichtungsgegenlaufflächen*. Stuttgart: IMA, 2011. ISBN: 9783936100365.
- [9] Baitinger, Gert and Haas, Werner. "Drallmessung mittels Mikrostrukturanalyse". In: *Sealing systems - cutting edge technology in the smallest envelope*. Frankfurt (Main): Fachverband Fluidtechnik im VDMA e.V., 2010. ISBN: 9783000325236.
- [10] Bätzel, Christian. "Drallmessung mit Methode: Messtechnik gewährleistet sichere Dichtfunktion". In: *Werkstatt und Betrieb* 05 (2008), p. 83.
- [11] Bauer, Frank, Baumann, Matthias, and Haas, Werner. "Scratch & Failure Detection Method for Shaft and Rod Surfaces". In: *Proceedings of 16th Nordic Symposium on Tribology - NORDTRIB 2014*. Ed. by Nielsen, Lars Pleth, Sivebæk, Ion Marius, Stensig Eskildsen, Svend, Lourcing, Sascha, and Larsen, Lone Elly. Danish Technological Institute, 2014, p. 139. URL: [http://orbit.dtu.dk/en/publications/proceedings-of-16th-nordic-symposium-on-tribology--nordtrib-2014\(44f919f6-122b-4455-8f48-458b49213320\).html](http://orbit.dtu.dk/en/publications/proceedings-of-16th-nordic-symposium-on-tribology--nordtrib-2014(44f919f6-122b-4455-8f48-458b49213320).html) (visited on 06/18/2015).
- [12] Baumann, Matthias, Bauer, Frank, and Haas, Werner. "Messung, Analyse und Bewertung von Dichtungsgegenlaufflächen für das Tribo-System Radial-Wellendichtung". In: *18th ISC, International Sealing Conference, Internationale Dichtungstagung*. 2014, pp. 627–639. ISBN: 978-3-00-046879-7.
- [13] Baumann, Matthias, Bauer, Frank, Haas, Werner, and Baitinger, Gert. "How to measure lead in sealing technology?" In: *Sealing Technology* 2013.7 (2013), pp. 8–12. ISSN: 13504789. DOI: 10.1016/S1350-4789(13)70261-7.
- [14] Baumann, Matthias, Novak Erik L., Bauer, Frank, and Haas, Werner. "Fast lead analysis method for shaft counter surfaces of radial lip seals". In: *Society of Tribologists & Lubrication Engineers Annual Meeting & Exhibition 2013*. Red Hook, NY: Curran, 2013, pp. 299–301. ISBN: 978-1-62993-289-7.
- [15] Baumgart, Jörg, Rau, Norbert, and Truckenbrodt, Horst. "Vermessen kleiner, periodischer Welligkeiten in Oberflächen". WO 00/22377. 07.09.1999.
- [16] Berghof, Claus. "Alternative zum Faden: Fertigungsnahe optische Drallprüfung an Rotationsdichtungen". In: *Qualität und Zuverlässigkeit* 57.04 (2012), pp. 45–47.
- [17] Beyerer, Jürgen. *Analyse von Riefentexturen*. Düsseldorf: VDI-Verlag GmbH, 1994. ISBN: 9783183390083.



- [18] Beyerer, Jürgen. "Suppression of stochastically placed, straight toolmarks to enhance objects and defects / Unterdrückung von stochastisch platzierten, geraden Riefen zur Hervorhebung von Objekten und Defekten". In: *tm - Technisches Messen* 59.10 (1992). ISSN: 0171-8096. DOI: 10.1524/teme.1992.59.10.389.
- [19] Beyerer, Jürgen and Krahe, Doris. "Verfahren und Vorrichtung zur Ermittlung einer Drallstruktur in der Oberfläche eines feinbearbeiteten zylindrischen Werkstücks". DE19809790A1. 1999.
- [20] Beyerer, Jürgen and Krahe, Doris. "Verfahren zur Ermittlung einer Drallstruktur in der Oberfläche eines feinbearbeiteten zylindrischen Werkstücks". DE19809790B4. 2005.
- [21] Beyerer, Jürgen and Puente León, Fernando. "Die Radontransformation in der digitalen Bildverarbeitung (The Radon Transform in Digital Image Processing)". In: *at - Automatisierungstechnik* 50.10/2002 (2002). ISSN: 0178-2312. DOI: 10.1524/auto.2002.50.10.472.
- [22] Beyerer, Jürgen, Puente León, Fernando, and Frese, Christian. *Automatische Sichtprüfung: Grundlagen, Methoden und Praxis der Bildgewinnung und Bildauswertung*. Berlin and Heidelberg: Springer, 2012. ISBN: 978-3-642-23966-3.
- [23] Bock, Eberhard. *Dichtungstechnik: Grundlagen und Anwendungen: Lecture*. Technische Universität Kaiserslautern, 2015.
- [24] Böge, Alfred. *Formeln und Tabellen Maschinenbau: Für Studium und Praxis*. revised 3rd ed. Wiesbaden: Springer Vieweg, 2012. ISBN: 978-3-8348-2313-7.
- [25] Brombeer, Rüdiger. *Numerische Mathematik für Ingenieure (lecture)*. winter term 2007/2008.
- [26] BSA Educational Services Committee. *Wear Sleeves & Other Shaft Repair Options*. Ed. by BSA Bearing Specialists Association. 2014. URL: [http://www.bsahome.org/tools/pdfs/Wear\\_Sleeves\\_web.pdf](http://www.bsahome.org/tools/pdfs/Wear_Sleeves_web.pdf) (visited on 04/23/2015).
- [27] Buhl, Steffen. *Oberflächentopographie – Abschlussbericht*. Ed. by Forschungsvereinigung Antriebstechnik e.V. 2000.
- [28] Buhl, Steffen. *Wechselbeziehungen im Dichtsystem von Radial-Wellendichtring, Gegenauflfläche und Fluid*. Stuttgart: IMA, 2006. ISBN: 3936100187.

- [29] Childs, Colin. *Interpolating Surfaces in ArcGIS Spatial Analyst*. Ed. by ESRI Education Services. 2004. URL: <http://www.esri.com/news/arcuser/0704/files/interpolating.pdf> (visited on 01/22/2016).
- [30] Cohen, Donald K., Smith, Stanley N., Novak Erik L., and Masters, Andrew T. "Quantitatively Measuring Surface Texture and Shaft Lead of Dynamic Sealing Systems". In: *Automotive Industries* 191.10 (2011), p. 57. URL: [http://www.ai-online.com/Adv/Previous/show\\_issue.php?id=4401](http://www.ai-online.com/Adv/Previous/show_issue.php?id=4401) (visited on 03/18/2015).
- [31] Confovis GmbH. *Portalsystem zur Messung von Wellen*. Ed. by Confovis GmbH. 2013. URL: <http://www.confovis.com/produkte/confogate-cgdr-100.html> (visited on 12/04/2014).
- [32] Cui, Zheng. *Nanofabrication: Principles, capabilities and limits*. Springer US, 2008. ISBN: 978-0-387-75577-9.
- [33] DaimlerChrysler AG. "Verfahren und Vorrichtung zur Vermessung von Drallstrukturen". DE10150383A1. 2002.
- [34] Deans, Stanley R. *The Radon transform and some of its applications*. New York: Wiley, 1983. ISBN: 047189804X.
- [35] Digital Surf. *Surface Metrology Guide*. URL: <http://www.digitalsurf.fr/en/guide.html> (visited on 02/20/2016).
- [36] DIN Deutsches Institut für Normung e.V. *Internationales Wörterbuch der Metrologie: Grundlegende und allgemeine Begriffe und zugeordnete Benennungen (VIM) ; ISO/IEC-Leitfaden 99:2007 = Vocabulaire international de métrologie = International vocabulary of metrology*. 3 ed. Wissen Messwesen. Berlin: Beuth Verlag GmbH, 2010. ISBN: 9783410200703.
- [37] DIN 2244:2002-05. *Gewinde - Begriffe und Bestimmungsgrößen für zylindrische Gewinde*. DIN Deutsches Institut für Normung e.V.
- [38] DIN 2274:1981-10. *Prüfprismen (Ausführungen, Anforderungen)*. DIN Deutsches Institut für Normung e.V.
- [39] DIN 3760:1996-09. *Radial-Wellendichtringe*. DIN Deutsches Institut für Normung e.V.
- [40] DIN 3761-2:1983-11. *Radial-Wellendichtringe für Kraftfahrzeuge - Anwendungshinweise*. DIN Deutsches Institut für Normung e.V.

- [41] DIN EN ISO 16610-49:2015-12. *Geometrische Produktspezifikation (GPS) - Filterung - Teil 49: Morphologische Profilfilter: Skalenraumverfahren (ISO 16610-49:2015); Deutsche Fassung EN ISO 16610-49:2015.*  
DIN Deutsches Institut für Normung e.V.
- [42] E DIN EN ISO 16610-60:2013-01. *Geometrische Produktspezifikation (GPS) – Filterung – Teil 60: Lineare Flächenfilter: Grundlegende Konzepte (ISO/DIS 16610-60:2012); Deutsche Fassung prEN ISO 16610-60:2012.*  
DIN Deutsches Institut für Normung e.V.
- [43] E DIN EN ISO 16610-61:2013-01. *Geometrische Produktspezifikation (GPS) - Filterung - Teil 61: Lineare Flächenfilter - Gauß-Filter (ISO/DIS 16610-61:2012); Deutsche Fassung prEN ISO 16610-61:2012.*  
DIN Deutsches Institut für Normung e.V.
- [44] E DIN EN ISO 25178-2:2008-03. *Geometrische Produktspezifikation (GPS) - Oberflächenbeschaffenheit: Flächenhaft - Teil 2: Begriffe und Oberflächen-Kenngrößen (ISO/DIS 25178-2:2008); Deutsche Fassung prEN ISO 25178-2:2008.* DIN Deutsches Institut für Normung e.V.
- [45] DIN EN ISO 25178-2:2012-09. *Geometrische Produktspezifikation (GPS) - Oberflächenbeschaffenheit: Flächenhaft - Teil 2: Begriffe und Oberflächen-Kenngrößen.* DIN Deutsches Institut für Normung e.V.
- [46] E DIN EN ISO 25178-3:2008-03. *Geometrische Produktspezifikation (GPS) - Oberflächenbeschaffenheit: Flächenhaft - Teil 2: Begriffe und Oberflächen-Kenngrößen (ISO/DIS 25178-2:2008); Deutsche Fassung prEN ISO 25178-2:2008.* DIN Deutsches Institut für Normung e.V.
- [47] E DIN EN ISO 25178-3:2010-03. *Geometrische Produktspezifikation (GPS) - Oberflächenbeschaffenheit: Flächenhaft - Teil 3: Spezifikationsoperatoren (ISO/DIS 25178-3.2:2009); Deutsche Fassung prEN ISO 25178-3:2009.*  
DIN Deutsches Institut für Normung e.V.
- [48] DIN EN ISO 25178-6:2010-06. *Geometrische Produktspezifikation (GPS) – Oberflächenbeschaffenheit: Flächenhaft – Teil 6: Klassifizierung von Methoden zur Messung der Oberflächenbeschaffenheit (ISO 25178-6:2010); Deutsche Fassung EN ISO 25178-6:2010.* DIN Deutsches Institut für Normung e.V.
- [49] DIN EN ISO 28178-3:2012-11. *Geometrische Produktspezifikation (GPS) - Oberflächenbeschaffenheit: Flächenhaft - Teil 3: Spezifikationsoperatoren (ISO 25178-3:2012); Deutsche Fassung EN ISO 25178-3:2012.*  
DIN Deutsches Institut für Normung e.V.

- [50] DIN EN ISO 4287:2010-07. *Geometrische Produktspezifikation (GPS) - Oberflächenbeschaffenheit: Tastschnittverfahren - Benennungen, Definitionen und Kenngrößen der Oberflächenbeschaffenheit (ISO 4287:1997 + Cor 1:1998 + Cor 2:2005 + Amd 1:2009); Deutsche Fassung EN ISO 4287:1998 + AC:2008 + A1:2009*. DIN Deutsches Institut für Normung e.V.
- [51] DIN EN ISO 4288:1998-04. *Geometrische Produktspezifikation (GPS) - Oberflächenbeschaffenheit: Tastschnittverfahren - Regeln und Verfahren für die Beurteilung der Oberflächenbeschaffenheit (ISO 4288:1996); Deutsche Fassung EN ISO 4288:1997*. DIN Deutsches Institut für Normung e.V.
- [52] DIN 4768:1990-05. *Ermittlung der Rauheitskenngrößen Ra, Rz, Rmax mit elektrischen Tastschnittgeräten*. DIN Deutsches Institut für Normung e.V.
- [53] Dreszer, Jerzy, ed. *Mathematik Handbuch für Technik und Naturwissenschaft*. Thun: Harri Deutsch, 1975. ISBN: 387144149X.
- [54] Engeln-Müllges, Gisela, Niederdrenk, Klaus, and Wodicka, Reinhard. *Numerik-Algorithmen: Verfahren, Beispiele, Anwendungen*. Berlin, Heidelberg: Springer-Verlag, 2011. ISBN: 978-3-642-13473-9.
- [55] Freudenberg Simrit GmbH & Co. KG. *Simmerrings and Rotary Seals: Technical manual*. Ed. by Freudenberg Simrit GmbH & Co. KG. 2007.
- [56] Gao, F., Leach, Richard K., Petzing, Jon, and Coupland, Jeremy Michael. "Surface measurement errors using commercial scanning white light interferometers". In: *Measurement Science and Technology* 19.1 (2008), p. 015303. ISSN: 0957-0233. DOI: 10.1088/0957-0233/19/1/015303.
- [57] Gonzalez, Rafael C. and Woods, Richard E. *Digital image processing*. 3rd ed. Upper Saddle River, N.J.: Prentice Hall, 2008. ISBN: 9780135052679.
- [58] Gräper, Arne, Kraft, Arne, Seewig, Jörg, and Reithmeier, Eduard. "Entwicklung multifunktionaler Kalibriernormale für die optische 3D-Mikroskopie (Development of Multifunctional Standards for Optical 3D Microscopy)". In: *tm - Technisches Messen* 73.1 (2006), pp. 19–25. ISSN: 0171-8096. DOI: 10.1524/teme.2006.73.1.19.
- [59] Group, Winterthur Technology. *All around simply the best: Peripheral-transverse outer diameter grinding*. URL: <http://www.winterthurtechnology.com/en/group/solution-finder/grinding-process/outside-diameter-grinding.html> (visited on 02/20/2016).

- [60] HALLE Präzisions-Kalibriernormale GmbH. *Depth measurement standards: line of products KNT 2060/01 (Conventional design)*. 2009. URL: [http://www.halle-normale.de/pdf/2013/englisch/04\\_Ps-KNT-2060\\_01-B1\\_1-1\\_GB.pdf](http://www.halle-normale.de/pdf/2013/englisch/04_Ps-KNT-2060_01-B1_1-1_GB.pdf) (visited on 10/09/2015).
- [61] HALLE Präzisions-Kalibriernormale GmbH. *Depth measurement standards (with round groove bottom) line of products KNT 4060/03: Calibration standards for contact stylus instruments - Corresponding to PTB-measurement standards: Technical data*. 2015. URL: [http://www.halle-normale.de/pdf/2015/englisch/18%20Ps-KNT%204060-03\\_b1\\_8-1\\_gb.pdf](http://www.halle-normale.de/pdf/2015/englisch/18%20Ps-KNT%204060-03_b1_8-1_gb.pdf) (visited on 09/07/2015).
- [62] Hertzsch, Albrecht. *Optischer Messstand zur automatischen Drallprüfung*. Ed. by INNOVENT e.V. Technologieentwicklung Jena. URL: [www.innovent-jena.de/files\\_db/1402990822\\_6995\\_\\_20.pdf](http://www.innovent-jena.de/files_db/1402990822_6995__20.pdf) (visited on 12/26/2015).
- [63] Hertzsch, Albrecht, Grossmann, Marko, and Kröger, Knut. "Optische Drallerkennung für die fertigungsnahen Qualitätskontrolle". In: *ATZ-Produktion* Volume 3, Issue 5-6 (2010), pp. 40–44.
- [64] Hertzsch, Albrecht, Kröger, Knut, and Grossmann, Marko. "Optical twist measurement by scatterometry". In: *Proceedings OPTO 2013*. 2013, pp. 40–45. ISBN: 978-3-9813484-3-9.
- [65] Hertzsch, Albrecht, Kröger, Knut, and Grossmann, Marko. "Schnelle optische Drallmessung". In: *tm – Technisches Messen* 80.12 (2013). ISSN: 0171-8096. DOI: 10.1515/teme.2013.0049.
- [66] Hollen, Jan von, Leis, Alexander, Poll, Gerhard, and Reithmeier, Eduard. "Einfluss von Beschädigungen der Gegenlauffläche auf das tribologische Verhalten von Radialwellendichtringen und Verfahren zur messtechnischen Charakterisierung". In: *Reibung, Schmierung und Verschleiß : Forschung und praktische Anwendungen*. Ed. by Gesellschaft für Tribologie. Aachen, 2010.
- [67] HOMMEL-ETAMIC GmbH. *Prüfprotokoll Drallnormal DN10*. 2007.
- [68] HOMMEL-ETAMIC GmbH. *Prüfprotokoll Drallnormal DN30*. 2007.
- [69] Hull, Jonathan J. "Document image skew detection: survey and annotated bibliography". In: *Document Analysis Systems II*. Ed. by Hull, Jonathan J. and Taylor, Suzanne L. Vol. 29. Series in Machine Perception and Artificial Intelligence. Singapore: World Scientific Publishing Company, 1998, pp. 40–64. ISBN: 9789812797704.
- [70] INNOVENT e.V. Technologieentwicklung Jena. *Drallinspektor DIO 125 SD: Optical system for automatic twist measurement*.

- [71] ISO 6194-1:2007-09. *Rotary shaft lip-type seals incorporating elastomeric sealing elements – Part 1: Nominal dimensions and tolerances*. ISO International Organization for Standardization.
- [72] ISO 8785:1998. *Geometrical Product Specification (GPS) - Surface imperfections - Terms, definitions and parameters*. ISO International Organization for Standardization.
- [73] Jähne, Bernd. *Digitale Bildverarbeitung und Bildgewinnung*. revised 7th ed. Berlin: Springer, 2012. ISBN: 978-3-642-04952-1.
- [74] James, Glyn. *Modern engineering mathematics*. 3rd ed. Essex: Prentice Hall, 2001. ISBN: 0130183199.
- [75] JCGM 100:2008-09. *Evaluation of measurement data - Guide to the expression of uncertainty in measurement*. Joint Committee for Guides in Metrology. URL: [http://www.bipm.org/utils/common/documents/jcgm/JCGM\\_100\\_2008\\_E.pdf](http://www.bipm.org/utils/common/documents/jcgm/JCGM_100_2008_E.pdf) (visited on 02/17/2015).
- [76] Jordan, Walter and Schütte, Wolfgang. *Form- und Lagetoleranzen: Handbuch für Studium und Praxis*. revised 7th ed. München: Hanser, 2012. ISBN: 9783446430808.
- [77] Jung, S. and Haas, Werner. "Treffsichere Bewertung: Einfluss der Gegenlauffläche auf Dichtgüte und Reibung von Radial-Wellendichtungen". In: *KEM 5* (2011), pp. 20–21. URL: <http://www.kem.de/angewandteforschung/-/article/30599594/32581285/Treffsichere-Bewertung> (visited on 06/12/2015).
- [78] Kersten, Gerhard. *Optische und antastende Prüfung der Gegenlauffläche von Radial-Wellendichtungen*. Düsseldorf: VDI-Verlag GmbH, 1992. ISBN: 3-18-148102-5.
- [79] Klocke, Fritz and König, Wilfried. *Schleifen, Honen, Läppen*. revised 4th ed. Vol. 2. VDI-Buch. Berlin: Springer, 2005. ISBN: 3-540-23496-9.
- [80] Krahe, Doris. *Zerstörungsfreie Prüfung der Textur gehonter und geschliffener Oberflächen*. Düsseldorf: VDI-Verlag GmbH, 2000. ISBN: 3183842084.
- [81] Krahe, Doris and Beyerer, Jürgen. "Quantifizierung von Drallerscheinungen an geschliffenen Wellendichtflächen mit Methoden der Bildverarbeitung". In: *Sensoren und Messtechnik*. Ed. by Meixner, Heinz and Schmidt, C. Berlin: VDE-Verlag, 1998, pp. 639–645. ISBN: 3800723301.
- [82] Krenn, Astrid. "Drall oder nicht Drall... Eine Frage der Oberflächenmessung". In: *Inspect 01* (2008), pp. 75–76.

- [83] Kunstfeld, Thomas. *Einfluss der Wellenoberfläche auf das Dichtverhalten von Radial-Wellendichtungen*. Stuttgart: IMA, 2005. ISBN: 3936100160.
- [84] Leach, Richard K. *Characterisation of areal surface texture*. Berlin and New York: Springer, 2013. ISBN: 978-3-642-36458-7.
- [85] Leach, Richard K. *Fundamental principles of engineering nanometrology*. 1st ed. Micro and nano technologies. Oxford and Amsterdam: William Andrew; Elsevier Science, 2010. ISBN: 978-0-08-096454-6.
- [86] Leis, Alexander and Hollen, Jan von. *Stochastische Strukturen: Auswirkungen stochastischer Strukturen von Gegenlaufflächen auf die Funktion von Radialwellendichtungen: Vorhaben Nr. 281 - Abschlussbericht*. 2009.
- [87] Lemke, Hinrich-Wilhelm, Seewig, Jörg, Bodschwinn, Horst, and Brinkmann, Stefan. "Kenngrößen der Abbott-Kurve zur integralen Beurteilung dreidimensional gemessener Zylinderlaufbahn-Oberflächen". In: *MTZ - Motortechnische Zeitschrift* 64.5 (2003), pp. 438–444. ISSN: 0024-8525. DOI: 10.1007/BF03226709.
- [88] Lim, Jae S. *Two-dimensional signal and image processing*. Prentice Hall signal processing series. Englewood Cliffs, N.J.: Prentice Hall, 1990. ISBN: 0139353224.
- [89] Lin, T. Y., Lu, S. H., and Stout, K. J. "Model-based topography characterisation of machined surfaces in three dimensions". In: *International Journal of Machine Tools and Manufacture* 35.2 (1995), pp. 239–245. ISSN: 08906955. DOI: 10.1016/0890-6955(94)P2378-S.
- [90] Lobera, Julia, Gao, F., Coupland, Jeremy Michael, and Leach, Richard K. "Limitations and innovations in scanning white light interferometry". In: *Proceedings of the 10th anniversary international conference of the European Society for Precision Engineering and Nanotechnology*. Ed. by van Brussel, H. Bedford: EUSPEN, 2008, pp. 287–291. ISBN: 978-0-9553082-5-3.
- [91] Mahr GmbH. "Versteckten Formfehlern auf der Spur: Mit Linear- und Rundheitsprofil dem Drall begegnen". In: *Qualität und Zuverlässigkeit* 52.8 (2007), pp. 48–49.
- [92] Marquart, Matthias, Sauer, Bernd, and Seewig, Jörg. "3D-Oberflächenanalyse einer RWDR-Lauffläche unter Berücksichtigung der DIN EN ISO 25178". In: *Reibung, Schmierung und Verschleiß: Forschung und praktische Anwendungen*. Ed. by Gesellschaft für Tribologie e.V. Aachen, 2009, pp. 61/1–61/13. ISBN: 978-3-00-028824-1.
- [93] Matesy. *STT - Shaft Twist Tester: Optischer Drallprüfer*. Ed. by Matesy.

- [94] The Mathworks Inc. *Curve Fitting Toolbox User's Guide: Matlab R2015b*. 2015. URL: [http://de.mathworks.com/help/releases/R2015b/pdf\\_doc/curvefit/index.html](http://de.mathworks.com/help/releases/R2015b/pdf_doc/curvefit/index.html) (visited on 10/03/2015).
- [95] MBN 31007-7:2009-04. *Geometrische Produktspezifikationen (GPS) - Oberflächenbeschaffenheit - Mess- und Auswerteverfahren zur Bewertung von drallreduzierten dynamischen Dichtflächen*. Mercedes-Benz.
- [96] MBN 31007-7:2002-05. *Technische Oberflächen, Oberflächenbeschaffenheit/Gestaltabweichung. Drallreduzierte dynamische Dichtflächen. Meßverfahren, Kenngrößen, Fertigungshinweise und Zeichnungsangaben*. Mercedes-Benz.
- [97] Merziger, Gerhard and Wirth, Thomas. *Repetitorium der höheren Mathematik*. 5 ed. Springe: Binomi, 2006. ISBN: 3923923333.
- [98] Müller, Heinz Konrad and Nau, Bernhard S. *Fluid sealing technology: Principles and applications*. New York: Marcel Dekker, 1998. ISBN: 0824799690.
- [99] Müller, Heinz Konrad and Nau, Bernhard S. *Kapitel 8: Wellendichtringe ohne Überdruck*. Ed. by [www.fachwissen-dichtungstechnik.de](http://www.fachwissen-dichtungstechnik.de). URL: [www.fachwissen-dichtungstechnik.de](http://www.fachwissen-dichtungstechnik.de) (visited on 05/30/2015).
- [100] NanoFocus AG. *Berührungsloses 3D-Oberflächen-Messsystem: µsurf explorer*. 2007.
- [101] NIST/SEMATECH. *e-Handbook of Statistical Methods*. Ed. by NIST/SEMATECH. URL: <http://www.itl.nist.gov/div898/handbook/> (visited on 10/03/2015).
- [102] Novak, Matthew and Schmit, Joanna. "Corrosion, Friction and Wear: 3D Microscopes Shed Light on Functional Sealing Surfaces". In: *18th ISC, International Sealing Conference, Internationale Dichtungstagung*. 2014, pp. 45–56. ISBN: 978-3-00-046879-7.
- [103] Oppenheim, Alan V. and Schafer, Ronald W. *Discrete-time signal processing*. 3rd internat. ed. Upper Saddle River, N.J.: Pearson, 2010. ISBN: 9780132067096.
- [104] Otto, Volkmar. "Mehr Sicherheit beim Abdichten mit Radial-Wellendichtringen durch optimierten Drall". In: *Goetzwerke-Fachschrift Mai (1978)*, pp. 1–11.
- [105] OWIS GmbH. *Produktinformation: Winkelverstellische: WV 100*. 2015. URL: [http://www.owis.eu/fileadmin/user\\_upload/owis.eu/products/pdf/pi\\_wv\\_100.pdf](http://www.owis.eu/fileadmin/user_upload/owis.eu/products/pdf/pi_wv_100.pdf) (visited on 10/12/2015).



- [106] Papula, Lothar. *Mathematische Formelsammlung für Ingenieure und Naturwissenschaftler: Mit zahlreichen Rechenbeispielen und einer ausführlichen Integraltafel*. revised 11th ed. Vol. 6. Berlin: Springer Vieweg, 2014. ISBN: 978-3-8348-2311-3.
- [107] Petzing, Jon, Coupland, Jeremy, and Leach, Richard K. *The Measurement of Rough Surface Topography using Coherence Scanning Interferometry*. Vol. 116. Measurement Good Practice Guide. Queen's printer and Controller of HMSO, 2010.
- [108] Prem, Erich and Vogt, Rolf. *The Simmerring: Basics for preventing damage*. Ed. by Freudenberg Simrit GmbH & Co. KG. 2008. URL: [http://www.ftl.technology/PDF\\_library/Product\\_Downloads/radial\\_shaft\\_seals.pdf](http://www.ftl.technology/PDF_library/Product_Downloads/radial_shaft_seals.pdf) (visited on 10/24/2015).
- [109] Puente León, Fernando. "Drallerkennung an Gegenlaufflächen von Radialwellendichtringen". In: *Bildverarbeitung im industriellen Einsatz: VDI Berichte Nr. 1572*. Düsseldorf: VDI-Verlag GmbH, 2000, pp. 117–122. ISBN: 3180915722.
- [110] Puente León, Fernando and Rau, Norbert. "Detection of Machine Lead in Ground Sealing Surfaces". In: *CIRP Annals - Manufacturing Technology* 52.1 (2003), pp. 459–462. ISSN: 00078506. DOI: 10.1016/S0007-8506(07)60625-8.
- [111] Qu, Jiajin. "Non-Ra Roughness Parameters of Shaft Surfaces for Radial Lip Seal Applications". In: *SAE 1995 Transactions: Journal of Commercial Vehicles*. Ed. by SAE International. 1996, pp. 14–18. ISBN: 1-56091-878-0. DOI: 10.4271/951195.
- [112] Raab, Henry. *Wellenlaufflächen: Vorhaben Nr. 211 - Einfluß der Wellenlauffläche auf das Dichtverhalten von Radial-Wellendichtringen - Abschlußbericht*. Vol. 239. Forschungshefte. 1998.
- [113] Rahlves, Maik and Seewig, Jörg, eds. *Optisches Messen technischer Oberflächen: Messprinzipien und Begriffe*. 1 ed. Beuth Verlag GmbH, 2009. ISBN: 3410171339.
- [114] Raid, Indek, Kusnezowa, Tatjana, and Seewig, Jörg. "Application of ordinary kriging for interpolation of micro-structured technical surfaces". In: *Measurement Science and Technology* 24.9 (2013), p. 095201. ISSN: 0957-0233. DOI: 10.1088/0957-0233/24/9/095201.
- [115] Raid, Indek, Seewig, Jörg, Frölich, Daniel, Sauer, Bernd, Mayer, Patrick, Schneider, Florian, and Aurich, Jan. "Kinematische Simulation gedrehter Wellenlaufflächen". In: *wt-online* 5 (2014), pp. 279–287. URL: <http://www.wt-online.de>

- [//www.werkstattstechnik.de/wt/article.php?data\[article\\_id\]=78906](http://www.werkstattstechnik.de/wt/article.php?data[article_id]=78906)  
(visited on 02/11/2015).
- [116] Rau, Norbert, Kruppke, Volker, and Seibold, Michael. "Drallstrukturen an geschliffenen Dichtflächen und ihr Einfluss auf die Dichtfunktion". In: *Sealing systems for fluid power applications: balancing leakage, control and performance*. Ed. by Merkel, H. 1999, pp. 393–404.
- [117] Rau, Norbert, Kruppke, Volker, and Seibold, Michael. "Messtechnische Beobachtungen zum Funktionsverhalten von gedrehten Dichtflächen". In: *Sealing systems for fluid power applications: sealing technology - a global challenge*. Ed. by Fachverband Fluidtechnik im VDMA e.V. 2004, pp. 93–105.
- [118] Rau, Norbert and Seibold, Michael. "Drallstrukturen geschliffener Dichtflächen beurteilen". In: *Werkstatt und Betrieb* 130.11 (1997), pp. 1013–1016.
- [119] Rau, Norbert, Seibold, Michael, and Heilbronner, Robert. "Verfahren zur Ermittlung einer Drallstruktur in der Oberflächenrauheit eines feinbearbeiteten Wellenzapfens". DE19740141C1. 12.09.1997.
- [120] Rau, Norbert, Seibold, Michael, Truckenbrodt, Horst, Hertzsch, Albrecht, and Würtenberger, Harry. "Verfahren zur Filterung und Visualisierung periodischer Strukturen auf rauhen zylindrischen Oberflächen". DE10027449B4. 2013.
- [121] Rehm, Fritz. "Einfluss der Abrichtbedingungen auf die Oberfläche geschliffener Gegenlaufflächen (DLF) von Radial-Wellendichtringen (RWDR)". In: *Schleifen und Trennen* 109/110 (1984), pp. 4–7.
- [122] OS-1-1:1999. *OS-1-1: Oil Seal Technical Bulletin - Shaft Requirements for Rotary Lip Seals*. RMA, Rubber manufacturers association.
- [123] Schneider, Petra. "Zelldifferenzierung auf Mikrostrukturen". PhD thesis. Kaiserslautern: Technische Universität Kaiserslautern, 2009.
- [124] Schwenke, Heinrich. *Abschätzung von Meßunsicherheiten durch Simulation an Beispielen aus der Fertigungsmeßtechnik: PTB-Bericht F-36*. PTB-Bericht. 1999. ISBN: 3-89701-373-8.
- [125] Seewig, Jörg. "Method for determining a twist structure". US 2011/0283784 A1. 2011.
- [126] Seewig, Jörg, Böttner, Thomas, and Broschart, Daniel. "Uncertainty of height information in coherence scanning interferometry". In: *Optical Measurement Systems für Industrial Inspection VII*. Ed. by Lehmann, Peter H., Osten, Wolfgang, and Gastinger, Kai. 2011, pp. 0V-1–0V-9.

- [127] Seewig, Jörg and Hercke, Tobias. "2nd generation lead measurement". In: *Fundamental and applied metrology*. Budapest: IMEKO, 2009, pp. 1957–1961. ISBN: 978-963-88410-0-1.
- [128] Seewig, Jörg and Hercke, Tobias. "Lead characterisation by an objective evaluation method". In: *Wear* 266.5-6 (2009), pp. 530–533. ISSN: 00431648. DOI: 10.1016/j.wear.2008.04.080.
- [129] Seewig, Jörg, Jordan, H.-J., Hercke, Tobias, and Volk, Raimund. "Optical High Speed Twist Characterisation". In: *XII. International Colloquium on Surfaces*. Ed. by Dietzsch, M. Aachen: Shaker, 2008, pp. 43–49. ISBN: 3832269126.
- [130] Shapiro, Vladimir. "Accuracy of the straight line Hough Transform: The non-voting approach". In: *Computer Vision and Image Understanding* 103.1 (2006), pp. 1–21. ISSN: 10773142. DOI: 10.1016/j.cviu.2006.02.001.
- [131] Shapiro, Vladimir A., Kavardjikov, V. I., and Atanassov, S. A. "Approach to automatic analysis of Young's fringes in speckle photography". In: *Applied Optics* 32.23 (1993), pp. 4378–4387. DOI: 10.1364/AO.32.004378..
- [132] Shuster, Mark, Combs, Dana, Pillar, Jim, Burke, Doug, and Cohen, Donald K. "Development of the Methodology for 3-D Characterization of Oil Seal Shaft Surfaces". In: *SAE Technical Paper* (2002-01-0661). DOI: 10.4271/2002-01-0661.
- [133] Soille, Pierre. *Morphological image analysis: Principles and applications*. 2 ed. Berlin and New York: Springer, 2003. ISBN: 3540429883.
- [134] Späth, Helmuth. "Least squares fitting with rotated paraboloids". In: *Mathematical Communications* 6 (2001), pp. 173–179.
- [135] Steier, William H. and Shori, Raj K. "Optical Hough transform". In: *Applied Optics* 25.16 (1986), pp. 2734–2738.
- [136] Stout, Ken. *Development of methods for the characterisation of roughness in three dimensions*. Rev. repr. London: Penton Press, 2000. ISBN: 1857180232.
- [137] Symons, J. D. "Shaft geometry - A major factor in oil seal performance". In: *Journal of Lubrication Technology* 2 (1968), pp. 365–374. ISSN: 00222305.
- [138] Thévenaz, Philippe, Blu, Thierry, and Unser, Michael. "Interpolation Revisited". In: *IEEE Transactions on Medical Imaging* 19.7 (2000), pp. 739–758. URL: <http://bigwww.epfl.ch/publications/thevenaz0002.pdf> (visited on 12/12/2014).
- [139] Tipler, Paul Allen, Baumgartner, Michael, Gerlich, Dieter, and Jerke, Götz. *Physik*. Heidelberg: Spektrum, 1994. ISBN: 3860251228.

- [140] Toft, Peter. "The Radon Transform: Theory and Implementation". PhD thesis. Technical University of Denmark, 1996.
- [141] Unser, Michael. "Splines: a perfect fit for signal and image processing". In: *IEEE Signal Processing Magazine* 16.6 (1999), pp. 22–38. ISSN: 10535888. DOI: 10.1109/79.799930.
- [142] Unser, Michael, Aldroubi, A., and Eden, M. "Fast B-spline transforms for continuous image representation and interpolation". In: *IEEE Transactions on Pattern Analysis and Machine Intelligence* 13.3 (1991), pp. 277–285. ISSN: 01628828. DOI: 10.1109/34.75515.
- [143] VDI/VDE 2655 Blatt 1.1:2008-03. *Optische Messtechnik an Mikrotopographien - Kalibrieren von Interferenzmikroskopen und Tiefeneinstellnormalen für die Rauheitsmessung*. Verein Deutscher Ingenieure.
- [144] VDI/VDE 2655 Blatt 1.2:2010-10. *Optische Messtechnik an Mikrotopografien - Kalibrieren von konfokalen Mikroskopen und Tiefeneinstellnormalen für die Rauheitsmessung*. Verein Deutscher Ingenieure.
- [145] Vogt, Rolf and Metzner, Hermann. *Bearbeitung von Wellenoberflächen für Radialwellendichtungen*. Ed. by Freudenberg Simrit KG.
- [146] Weber, Hero and Funke, Erik. "Verfahren und Vorrichtung zur Erfassung von Drallstrukturen". DE102006001799B4. 2007.
- [147] Weisstein, Eric W. *Ellipse*. From *MathWorld—A Wolfram Web Resource*. URL: <http://mathworld.wolfram.com/Ellipse.html> (visited on 07/25/2015).
- [148] Xin, Binjian. "Auswertung und Charakterisierung dreidimensionaler Messdaten technischer Oberflächen mit Riefentexturen". PhD thesis. Karlsruhe: Universität Karlsruhe, 2008.
- [149] Zhang, Ran, Schuber, Andeas, and Zeidler, Henning. "Drallfreie Bearbeitung mittels Start-Stopp-Drehverfahren". In: *ZWF* 12 (2014), pp. 889–894. URL: <http://www.zwf-online.de/ZW111261> (visited on 04/21/2015).

# Relevant supervised theses

|                     |                 |   |
|---------------------|-----------------|---|
| Bastian Barwick     | Diploma thesis  | Modellierung und Simulation der Fadenmethode zur Drallmessung an Wellen   |
| Burkhard Boecker    | Diploma thesis  | Entwicklung eines mobilen optischen Messsystems zur Drallwinkelbestimmung von Dichtungsgegenaufläachen an ruhenden Wellen                       |
| Anna Borsch         | Diploma thesis  | Recherche zu Auftreten, Entstehung und Charakterisierung von Defekten an Wellenaufläachen in dynamischen Dichtsystemen                          |
| Felix Diewald       | Project thesis  | Konstruktion eines Streulichtensors für Mikrodrall  |
| Juri Geringer       | Diploma thesis  | Entwicklung einer Auswertemethode für Topografien basierend auf Granulometrie   |
| Sebahattin Gökkaya  | Project thesis  | Parameterstudie zur Winkelverteilung der Schleifstruktur an geschliffenen Wellendichtfläachen   |
| Tycho Groche        | Project thesis  | Inbetriebnahme und Untersuchungen an einem optischen Sensor zur Charakterisierung der Hauptstrukturrichtung an geschliffenen Wellenoberfläachen |
| Simon Kieß          | Project thesis  | Automatische Defekterkennung an geschliffenen Oberfläachen  |
| Alexander Reinke    | Diploma thesis  | Anbindung eines Weißlichtinterferometers an ein Multisensor-Koordinatenmessgerät mit C++  |
| Marius Stemler      | Bachelor thesis | Modellierung und Simulation eines optischen Sensors zum Nachweis von Mikrodrall   |
| Martin Witzenhausen | Project thesis  | Arbeiten zur Defekterkennung an geschliffenen Oberfläachen  |

# Curriculum vitae

Name Philipp Arnecke  
Place of birth Würzburg, Germany

## Education

2011 – 2015 **Research assistant**  
Institute for Measurement and Sensor Technology  
Department of Mechanical and Process Engineering  
University of Kaiserslautern

2005 – 2011 **Studies of mechanical engineering**  
Department of Mechanical and Process Engineering  
University of Kaiserslautern

2004 **General qualification for university entrance**  
Städt. Mozart- und Schönborn-Gymnasium, Würzburg

## Berichte aus dem Lehrstuhl für Messtechnik und Sensorik

---

### bereits veröffentlicht wurden

- 1 Wendel, M.: Qualifizierung eines Streulichtensors und Untersuchung erster Ansätze zur dreidimensionalen Streulichterfassung  
2015, ISBN 978-3-95974-006-7 € 39,-
- 2 Schäfer, P.: Modellbasierte Entwicklung pneumatischer Abstandssensoren für prozessintegrierte Messungen  
2015, ISBN 978-3-95974-009-8 € 39,-
- 3 Eifler, M.: Modellbasierte Entwicklung von Kalibriernormalen zur geometrischen Produktspezifikation  
2016, ISBN 978-3-95974-027-2 € 39,-
- 4 Arnecke, P.: A measurement method for characterising micro lead on ground shaft surfaces  
2017, ISBN 978-3-95974-047-0 € 39,-

ISBN: 978-3-95974-047-0

ISSN: 2365-9742

## Kurzfassung

Bei der Herstellung von Wellenoberflächen als Gegenaufläachen für Radialwellendichtringe in dynamischen Dichtsystemen können Strukturen auftreten, die Einfluss auf die Funktion des Dichtsystems haben können. Diese Strukturen werden als Drall bezeichnet und können entsprechend ihrer Ausprägung und Entstehung in die Drallarten Makro- und Mikrodrall eingeteilt werden. Im Optimalfall wird Drall bereits während der Herstellung vermieden, zumindest soll er aber erkannt und bezüglich seiner Ausprägung an Hand von Parametern quantifiziert werden. Während Messmethoden und Verfahren zum Nachweis von Makrodrall existieren, wird in dieser Arbeit eine Methode zur Charakterisierung von Mikrodrall, also der Hauptrichtung der Bearbeitungsstruktur bezogen auf die Umfangsrichtung, beschrieben.

Aus der Definition von Mikrodrall folgt direkt, dass sowohl die Umfangs- als auch die Bearbeitungsrichtung hochgenau erfasst werden müssen. Zu diesem Zweck werden geeignete Messsysteme und zugehörige Kalibrierverfahren beschrieben, welche neben der Messung der Wellenoberfläche die Kalibrierung der Umfangsrichtung mit hoher Genauigkeit und niedriger Unsicherheit ermöglichen. Auf Basis dieser flächenhaften Messungen wird ein Verfahren zur Ermittlung der Texturrichtung, dem die Radontransformation zu Grunde liegt, vorgestellt und parametrisiert. Mit der Ermittlung der Texturrichtung und der Kalibrierung der Achslage können damit beide Anforderungen an die Messmethode zur Mikrodrallmessung an geschliffenen Wellenoberflächen erfüllt werden.

## Abstract

The detection and characterisation of undesired lead structures on shaft surfaces is a concern in production and quality control of rotary shaft lip-type sealing systems. The potential lead structures are generally divided into macro and micro lead based on their characteristics and formation. Macro lead measurement methods exist and are widely applied. This work describes a method to characterise micro lead on ground shaft surfaces. Micro lead is known as the deviation of main orientation of the ground micro texture from circumferential direction.

Assessing the orientation of microscopic structures with arc minute accuracy with regard to circumferential direction requires exact knowledge of both the shaft's orientation and the direction of surface texture. The shaft's circumferential direction is found by calibration. Measuring systems and calibration procedures capable of calibrating shaft axis orientation with high accuracy and low uncertainty are described. The measuring systems employ areal-topographic measuring instruments suited for evaluating texture orientation. A dedicated evaluation scheme for texture orientation is based on the Radon transform of these topographies and parametrised for the application. Combining the calibration of circumferential direction with the evaluation of texture orientation the method enables the measurement of micro lead on ground shaft surfaces.